Electrochemical detection of choline at green mediated nanocomposites modified electrode

GE Uwaya
orcid.org/0000-0003-2040-7740

Thesis accepted for the degree Doctor of Philosophy in Science with Chemistry at the North-West University

Promoter: Prof OE Fayemi

Graduation: May 2021

Student number: 30034507

DECLARATION

I, the under signed here with declare that the dissertation submitted to the Department of Chemistry, Faculty of Natural and Agricultural Sciences, North-West University in its totality is my work with exclusion to the citation and that the present study/research has not been submitted by me or anyone else for a degree to the university.

Signed at.....on this.....day of.....2021
GE Uwaya
(Student)

Signed at.....on this.....day of 2021
Prof OE Fayemi
(Supervisor)

DEDICATION

This thesis is dedicated to God the Father, the Son and the Holy Spirit for the gift of life, good health and inspiration to have completed this work.

ACKNOWLEDGEMENT

My sincere and deed gratitude goes first to my supervisor, Prof. OE Fayemi for the opportunity availed to me to research on this topic. I want to say thank you for your patience, encouragement, support, advice, guidance and your motherly role during my research and the writing up of this thesis. Special thanks to Prof. Eno. E. Ebenso for your impact and support.

My profound appreciation also goes to North-West University for the opportunity of a PhD study in Chemistry. I also acknowledge all staff members of the chemistry Department of North-West University (Mafikeng campus) for all their help, and kind words. I will like to appreciate Mr. Enyioma C. Okpara, Mr. Taiwo W. Quadri and Dr. Akinola Stephen for their impact and moral support. Thanks to my entire colleagues in Sensor and corrosion group.

Thanks to my friends who have been of great help and comfort to me during my PhD journey. I am extremely grateful to my big mum, wonderful siblings, nieces and nephews for their love, support, comfort, and sacrifice. Without their immense help and constant encouragement, this work could not have been completed.

I will also like to extend my profound gratitude to Dr. Joseph Adesina, Dr. Abah John, Pastor (Dr.) Olutope P. Fayemi and family, Dr. Wojuola and family, Mr. Maxwell, Prof. Fagbola, Prof. O. Osibanjo, Dr. Adewunmi, Pastor Kehinde Alabi, Pastor Ogbu and Nuhu, Pastor Ibrahim and family, Pastor and Dr. (Mrs.) Momah, Mrs. Oladele and family. I will not fail to acknowledge all members of Deeper Life Campus Fellowship, North-West province. You have all been wonderful.

ABSTRACT

This work describes the successful green synthesis of two metal oxides (MO = Fe_3O_4 and ZnO) nanoparticles from *Callistemon viminalis* leaf and flower extract (Fe_3O_4NPL, Fe_3O_4NPF and ZnONPL, ZnONPF), and modified with functionalized multi-walled carbon nanotubes (f-MWCNT) on glassy carbon electrode (GCE). Total phenol and flavonoids contents (TPC and TFC) of the extracts were determined using UV-Visible spectrophotometer. Successful synthesis of MO nanoparticles (Fe_3O_4NPL, Fe_3O_4NPF, ZnONPL and ZnONPF) and f-MWCNT/MO nanocomposites (f-MWCNT/Fe_3O_4NPL, f-MWNT/Fe_3O_4NPF, f-MWCNT/ZnONPL and f-MWCNT/ZnONPF) were confirmed by characterization using scanning electron microscopy (SEM), transmission electron microscopy (TEM), x-ray diffraction spectroscopy (XRD), electron dispersive x-ray spectroscopy (EDX), Fourier transformed infra-red spectroscopy (FTIR) and ultraviolet-visible (UV-Vis) spectroscopy. Thermal and electrical stability of the metal oxide nanoparticles were also studied via thermogravimetric analysis and zeta potential. Electron transport (ET) properties of the modified electrodes was investigated by cyclic voltammetry (CV) and electrochemical impedance spectroscopic techniques (EIS) in ferricyanide ($K_3[Fe(CN)_6]$) as the redox probe. Electron transport mechanism between the MO nanomaterials/nanocomposites (GCE/f-MWCNT/Fe_3O_4NPL, GCE/f-MWNT/Fe_3O_4NPF, GCE/f-MWCNT/ZnONPL and GCE/f-MWCNT/ZnONPF) and the electro oxidation or reduction of choline at the modified electrode was studied using cyclic voltammetry and electrochemical impedance spectroscopy (EIS). There were differences in the electron transfer rate constant (ks) in terms of the materials, level of catalysis and electrical equivalent circuits used in the fitting or modelling process. The electron transport properties of modified metal oxide electrodes were enhanced in the presence f-MWCNT in comparison with electrodes without f-MWCNTs.

Electrochemical oxidation of choline on a GCE modified with functionalized multi-walled carbon nanotubes doped with metal oxides = Fe_3O_4NPL and Fe_3O_4NPF (GCE/f-MWCNT/Fe_3O_4NPL, GCE/f-MWCNT/Fe_3O_4NPF) was studied using cyclic voltammetry, EIS, square wave voltammetry (SWV) and chronoamperometry (CA) in 10 mM lithium chloride (LiCl) solution at pH 7.3. The results were compared with those obtained from bare GCE, GCE/f-MWCNT and MO GCE modified electrodes (GCE/Fe_3O_4NPL, GCE/Fe_3O_4NPF). The nanocomposite modified electrodes displayed an excellent electrocatalytic activity towards the electrochemical oxidation of choline with high current peak compared to other electrodes investigated. It was found that the multi-walled carbon nanotubes enhanced greatly the reactivity

of Fe_3O_4NP for choline oxidation. Limit of detection for choline in the concentration range studied from square wave voltammetric (SWV) and chronoamperometric (CA) measurement was 0.83 and 0.16; 0.36 and 0.05 μM for GCE/f-MWCNT/Fe_3O_4NPL and GCE/f-MWCNT/Fe_3O_4NPF electrodes respectively. GCE/f-MWCNT-Fe_3O_4NPL was the best electrode in terms of choline current response, electrode selectivity and storage stability GCE/f-MWCNT/Fe_3O_4NPF had the best limit of detection (LoD) towards the analyte (choline). From the selectivity study, there was an absence of interfering signals of 100 mM ascorbic acid (AA) and 0.1 mM dopamine (DA) to choline at 0.1 mM. Successful measurement of choline in choline dietary supplements was performed using the fabricated electrodes.

Similar results were obtained for GCE/f-MWCNT/ZnONPL and GCE/f-MWCNT/ZnONPF) for electrochemical detection of choline with detection limit of 0.06 and 0.45 μA; 0.29 and 0.32 μA from SWV and CA choline measurements.

Keywords: Electrochemical detection, Choline, Functionalized multiwalled carbon nanotube, Green synthesis, Iron (III) oxide, Zinc oxide, *Callistemon viminalis*, Glassy carbon electrode, Cyclic voltammetry, square wave voltammetry, impedance spectroschopy, Chronoamperometry.

TABLE OF CONTENTS

LIST OF ABBREVIATIONS

AA	Ascorbic acid
Ag/AgCl	Silver/silver chloride reference electrode
C. viminalis	*Callistemon viminalis*
CA	Chronoamperometry
C_{dl}	Double layer capacitance
CE	Counter electrode
Cho	Choline
CNS	Central nervous system
CNTs	Carbon nanotubes
CPE	Constant phase element
CV	Cyclic voltammetry
DA	Dopamine
DMF	Dimethylformamide
EDX	Electron dispersive x-ray spectroscopy
EFSA	European Food Safety Authority
EIS	Electrochemical impedance spectroscopy
Epa	Anodic peak potential
Epc	Cathodic peak potential
ET	Electron transport
Fe_3O_4	Iron (III) oxide
Fe_3O_4NPF	Iron (III) oxide nanoparticles from *C. viminalis* flower extract
Fe_3O_4NPL	Iron (III) oxide nanoparticles from *C. viminalis* leaf extract
f-MWCNT	Functionalized multi-walled carbon nanotube
FTIR	Fourier transform infrared
GAE	Gallic acid equivalent
GCE	Glassy carbon electrode
GPES	General purpose electrochemical system software
HT	Serotonin
IOM	Institute of medicine
Ipa	Anodic/oxidation peak current

Ipc	Cathodic/reduction peak current
ITES	Electrochemistry at the interface between two immiscible solutions
LiCl	Lithium chloride
LoD	Limit of detection
MO	Metal oxide
MONP	Metal oxide nanoparticles
MWCNT	Multi-walled carbon nanotube
Ox	Oxidation
PBS	Phosphate buffer
R_{ct}	Charge resistance transfer
RE	Reference electrode
Red	Reduction
R_s	Solution resistance
Sat'd	Saturated
SEM	Scanning electron microscopy
SWCNT	Single-walled carbon nanotube
SWV	Square-wave voltammetry
TEM	Transmission electron microscopy
TFC	Total flavonoids content
TGA	Thermogravimetric analyser
TPC	Total phenol content
USDA	United States Department of Agriculture
UV-Vis	Ultraviolet-visible
Vs	versus
W	Warburg
WE	Working electrode
XRD	X-ray diffraction
ZnO	Zinc oxide
ZnONPF	Zinc oxide nanoparticles synthesized from *C. viminalis* flowers extract
ZnONPL	Zinc oxide nanoparticles synthesized from *C. viminalis* leaf extrac

LIST OF SYMBOLS

α	Electron transfer coefficient
$E_{1/2}$	Formal potential
R	Universal gas constant
K	Kelvin temperature
n	Number of electrons
A	Electroactive surface area (cm2)
ks	Standard rate constant of electron transfer
D	Diffusion coefficient
A	Amperes
ω	Warburg impedance
Z'	Real impedance
Z''	Imaginary impedance
W	Warburg impedance
v	Scan rate
$v^{1/2}$	Square root of scan rate
Γ	Surface coverage area/ surface concentration of electrochemical specie
V	Volts
Hz	Hertz
nm	Nanometer
Mg/g	Milligram/gram
mVs^{-1}	Millivolt/ second
v/mVs^{-1}	Volt/millivolt/second
kHz	Kilohertz
Ω	Ohms
μF	Microfarad
μM	Micromole
$\mu A/\mu M$	Micro ampere/micromole
cm^2s^{-1}	Centimetre square/second
mM	Millimole
ΔE	Peak potential separation

LIST OF FIGURES

LIST OF TABLES

CHAPTER ONE

INTRODUCTION

1.1 Electrochemical senors

The electrochemical sensor gives information about a specimen in the form of an electrical signal (Power & Morrin, 2013). Electrochemical sensor involves chemical interaction of analytes of interest with the sensor resulting in an electrical signal which corresponds to the concentration of the analytes (Power & Morrin, 2013). Researchers in the field of electrochemistry have widely explored electrochemical sensors in detecting several biological substances. Electrochemical sensors possess excellent properties such as very high sensitivity, selectivity, cheap, convenient, fast response, low limit of detection, and simple instrumentation. An ideal electrochemical sensor consists of the cell, electrolyte and the electrodes(Koyun *et al.*, 2012; Power & Morrin, 2013). Electrochemical signals are enhanced by coupling the sensor with nanomaterials such as carbon nanotubes (CNTs), metal oxide nanoparticles, nano composites and conductive polymers in the range of 1-1000 nm (Power & Morrin, 2013). CNTs exhibit high electrical conductivity between biomolecules, promotes high electron transfer, stable (chemical, electrochemical and thermal), have a high surface area with small size and can adhere to the electrode surface (Ahammad *et al.*, 2009; Magar *et al.*, 2017). These distinct properties have led to the application of CNTs in the electrochemical sensor.

There are two categories of CNTs; single-walled carbon nanotube (SWCNT), which is a single graphene tube, and multiwalled carbon nanotube (MWCNTs which are different coordinated graphene tube fitted into another) (Ahammad *et al.*, 2009). Metal oxide (MONP) nanoparticles such as iron (III) oxide (Fe_3O_4), zinc oxide (ZnO), nickel oxide (NiO), molybdenum oxide (MoO_2), manganese (IV) oxide (MnO_2), and zirconium oxide (ZrO_2), synthesize from their metal salts exhibit unique properties such as optical, electrical, and thermal owing to their excellent density, high surface area and are biocompatible (Immanuel *et al.*, 2019; Kecili & Hussain, 2018; Soytaş *et al.*, 2019). These make them hold potential applications in catalysis, and chemical sensor (Immanuel *et al.*, 2019; Rezaei & Irannejad, 2019). Iron (III) oxide (Fe_3O_4) also refer to as magnetite is one of the commonly known forms of iron oxide and it's known to be less toxic, cheap, ferromagnetic, and super magnetic biocompatible with a high surface area/volume ratio (Mphuthi *et al.*, 2017; Ramesh *et al.*, 2018). Zinc oxide nanoparticles

(ZnONP) have wide application in chemical sensor since it is electrically conductive, possesses pyro-electric property and high catalytic effect (Marsalek, 2014; Sagar Raut & Thorat, 2015; Umar *et al.*, 2019). Also, the research on conducting polymers especially polypyrrole (PPy), polyaniline, and poly-3,4-ethylenedioxythiophine (PEDOT) as electrode materials for electrochemical sensors has been of significant attraction because of their excellent stability, conductivity and ease of preparation (de Oliveira *et al.*, 2016; Kanwal *et al.*, 2011; Mahmoudian *et al.*, 2013). Metal oxides nanoparticles in conjunction with CNTs and PPy (nanocomposites) have been used for electrocatalysis and electroanalysis considering their synergic influence and rapid redox processes (de Oliveira *et al.*, 2016; Kumar *et al.*, 2015; Prasanna *et al.*, 2019). CNTs are functionalized/purified using mixtures of acid tetraoxosulphate (VI) and nitric acid (H_2SO_4/HNO_3) or single acid before its application to remove impurities, activate the CNTs surface and enhance its dispersibility property (Ahmed *et al.*, 2013; Atieh *et al.*, 2010; Gupta & Saleh, 2011; Hu & Guo, 2011; Rajarao *et al.*, 2014). In this work, the modified sensors will be applied in the detection of choline, a neurotransmitter precursor, and in the selectivity study of the designed sensor towards choline in the presence of ascorbic acid and dopamine.

Neurotransmitters are biomolecules located in the central nervous system (CNS) and also found as bioactive compounds in food (Banjari *et al.*, 2014; Herlenius & Lagercrantz, 2010; Klein *et al.*, 2019). Acetylcholine produced from choline, serotonin, dopamine, norepinephrine, and epinephrine are made within the body cells and can also be obtained through diets and supplements. They play vital roles in cell membrane signalling, muscle control, methyl group metabolism, healing of wounds, regulation of moods (anxiety, happiness, fear, aggression), motivation, cognition, and regulates the circulatory system (Banjari *et al.*, 2014; Herlenius & Lagercrantz, 2010; Klein *et al.*, 2019). Low level of these neurotransmitters could result in Parkinson, Alzheimer, heart and liver disease, insomnia, depression, and cognitive decline (Banjari *et al.*, 2014; Filik *et al.*, 2014; Manbohi & Ahmadi, 2019; Reddaiah *et al.*, 2018; Shadlaghani *et al.*, 2019). Electrochemical sensors with some electrochemical techniques (cyclic, linear sweep wave, differential pulse, square wave voltammetry, chronoamperometry, and electrochemical impedance spectroscopy) have been used for the detection of neurotransmitters in pharmaceuticals, food, and biological samples.

Choline belongs to the family of water-soluble quaternary amine (trimethyl-β-hydroxyethyl ammonium), and officially, choline is seen by the Institute of Medicine (IOM) as a vital nutrient for human (He *et al.*, 2014b; Phillips, 2012; Zeisel, 2009). Choline plays three major roles in the

body which include the production of acetylcholine (neurotransmitter), phospholipids (promotes signalling across cell membranes), and the main source of methyl groups (Magar *et al.*, 2017; Phillips, 2012; Zeisel, 2013; Zeisel, 2009). Choline aids the development of brain and memory in the foetus. It helps to reduce the possibility of the formation of neural tube defect (NTDs) at the prenatal and periconceptional stage. In contrast, in premenopausal women and men, choline helps to prevent organ dysfunction (Phillips, 2012; Zeisel, 2012; Zeisel, 2013; Zeisel, 2009). Choline deficiency results in alteration of deoxyribonucleic acid (DNA) structure, fatty liver, damage of liver and muscles, increased apoptosis in tissues and neural tube defects (Phillips, 2012; Zeisel, 2012; Zeisel, 2013; Zeisel, 2009). Protracted choline deficiency leads to memory, pancreatic, hepatic, renal, pancreatic and growth disorder (Phillips, 2012). Considering the health implication of choline, food and nutritional board of institute of medicine established adequate intake (AI) of choline as 425, 550, 450, 550, 125-150 and 200-325 in mg/day for men, women, pregnant women, lactating women, infants, and children respectively (Gossell-Williams *et al.*, 2005; Hefni *et al.*, 2015; Panfili *et al.*, 2000; Phillips, 2012). Choline occurs in a free or esterified form (phosphocholine, phosphatidylcholine, glycerophosphocholine and sphingomyelin) in varieties of food, and dietary supplements as choline chloride and choline bitartrate (Phillips, 2012). Choline is acquired through de novo synthesis, which involves phosphatidylethanolamine methylation to phosphatidylcholine (European Food Safety Authority-(EFSA) Panel on Dietetic Products & Allergies, 2016; Phillips, 2012; Zeisel, 2013; Zeisel, 2009). However, to maintain proper functioning of the body and meet the IOM requirement, choline intake from choline-rich containing food (liver, fish, egg, dairy products, whole grains, peanuts, soybeans, brussels sprout and broccoli and lots more in the USDA data), and supplements are recommended (EFSA Panel on Dietetic Products & Allergies, 2016; Phillips, 2012; Zeisel, 2013; Zeisel, 2009). However, excess of choline in the body results in hypotension as well as nausea, diarrhoea, fishy body odour and gastrointestinal effect (Zeisel, 2013). Thus, IOM defined an upper limit (UL) of choline for adults as 3.5g/day, non for infants and children based on the bodyweight (Zeisel, 2013). It is therefore crucial to consider the determination of choline quantitatively in biological, food, and pharmaceutical samples.

Detection of choline is quite challenging because choline lacks an electroactive, a chromophore and fluorophore groups (He *et al.*, 2014b; Jin *et al.*, 2010). However, different analytical techniques such as chromatography (EFSA Panel on Dietetic Products & Allergies, 2016; Fossati *et al.*, 1994; Gossell-Williams *et al.*, 2005; Hefni *et al.*, 2015; Holm *et al.*, 2003; Ikarashi & Maruyama, 1993; Jin *et al.*, 2010; Koc *et al.*, 2002; Laikhtman & Rohrer, 1999), flow injection

(Jin *et al.*, 2010), chemiluminescence (Yao *et al.*, 2002), colorimetry (He *et al.*, 2014b), proton nuclear magnetic resonance (1H NMR) (Holmes *et al.*, 2000), capillary electrophoresis (Carter & Trenerry, 1996), biosensors (Chang-Zhi *et al.*, 2011; Deng *et al.*, 2013; Magar *et al.*, 2017; Pundir *et al.*, 2012; Sajjadi *et al.*, 2012; Zhang *et al.*, 2014a), electrochemistry at the interface between two immiscible electrolyte solutions (ITIES) (Xie *et al.*, 2017), non-enzyme-based electrochemical sensor (Sattarahmady *et al.*, 2014), reneckates method (Glick, 1944) and spectrophotometry (Woollard & Indyk, 2000) have been employed for choline detection. Great attention has been drawn to the use of chromatography and choline biosensors with limited research on the electrochemical sensor (non-biosensor). However, choline biosensors though simple, reliable, with fast response are non-economical owing to the cost of enzymes. Immobilization of enzymes can be quite challenging as some of the biosensors could suffer from poor sensitivity and selectivity (Power & Morrin, 2013; Sattarahmady *et al.*, 2014) while chromatography methods are time demanding, labour intensive, require expertise and expensive (He *et al.*, 2014b; Magar *et al.*, 2017; Pati *et al.*, 2007; Yu *et al.*, 2016). These short comings will in part be overcome with the present study involving the use of electrochemical sensors for sensing of choline in real samples which is more economical, cheaper, convenient, and readily accessible in laboratories with simple instrumentation, superior sensitivity and selectivity as compared to chromatographic and biosensors assays.

1.2 Problem statement

Choline (Cho), an essential nutrient is involved in several body functions such as modulation of deoxyribonucleic acid (DNA) integrity, aiding of memory and brain development at pregnancy, and also in the synthesis of acetylcholine neurotransmitter found in the central nervous system which plays a role in memory function, muscle control, membrane signalling, and methyl group metabolism (Hefni *et al.*, 2015; Phillips, 2012; Zeisel, 2012; Zeisel, 2013). Low levels of choline in the body result in cognitive decline, heart and liver disease, neural tube defect and atherosclerosis (Phillips, 2012; Zeisel, 2013). Choline can be produced within the body cells by taking more of Cho rich food and dietary supplements to meet the daily choline intake and maintain proper functioning of the body (Hefni *et al.*, 2015; Phillips, 2012; Zeisel, 2012; Zeisel, 2013). The health importance of choline makes it imperative to design a fast, sensitive, cheap, selective and reliable technique for choline detection in food and dietary supplements. Different assays employed in the investigation of choline in real samples include; wet chemical, biological, chromatographic, enzyme-based methods, and biosensors (Jin *et al.*, 2010; Pati *et al.*, 2007;

Phillips, 2012) including those previously stated with considerable attention to chromatography and biosensors.

However, they all have their drawbacks. Wet chemistry requires multi-fold extractions and hydrolysis steps, poor specificity and sensitivity is native to bioassays. The chromatographic assays are tedious and time demanding, requires expertise in instrumentation, and uneconomical, which makes them unsuitable for routine analysis. Biosensors are unstable as enzymes are prone to denaturing resulting to reduced sensitivity and selectivity. Immobilization of enzymes could be difficult. There is the risk of fouling of electrodes and it is not readily available in the routine laboratory (Jin *et al.*, 2010; Pati *et al.*, 2007; Phillips, 2012). Most of these setbacks can be addressed at least or in part by introducing the use of electrochemical sensors with electrode nano catalyst (ferromagnetic nanoparticles and multi-walled carbon nanotubes). In this way, selectivity, sensitivity, and response time will be significantly enhanced with a reduced cost. Thus the quest in designing the present electrochemical sensor (non-enzyme based) based on glassy carbon electrode modified with functionalized multi-walled carbon nanotubes/metal oxide (GCE/f-MWCNT/Fe_3O_4NP and GCE/f-MWCNT/ZnONP) nanocomposites for choline detection. Fe_3O_4NP and ZnONP were synthesized via green route from *Callistemon viminalis* extracts.

This study gives literature search on different analytical methods applied in choline detection, which includes wide use of chromatography and choline biosensor with limited use of electrochemical sensors (non-enzyme based). Hence this study seeks to explore the formation of electrochemical sensors base on the synergy of green mediated metal oxide nanomaterials and multi-walled carbon nanotube onto glassy carbon electrode.

1.3 Aim and objectives

This study is aimed at investigating a comparative study of the characterization of green synthesized metal oxide nanoparticles, electrochemical properties of metal oxide nanoparticles doped with functionalized multi-walled carbon nanotubes (MWCNT), and confirm their efficiency in electro oxidation of choline.

1.3.1 Objectives of the study

The objectives of the study are to:

i. synthesize metal oxide nanoparticles of zinc oxide (ZnONP) and (Fe_3O_4NP) from the leaf and flower extracts *of Callistemon viminalis.*

ii. fabricate nanocomposites of f-MWCNT/MONP. Where MO represents metal oxide nanoparticles (ZnONP and Fe_3O_4NP).

iii. characterize the green mediated synthesized metal oxide NPs and their composites using spectroscopic and microscopic techniques such as Transmission electron microscopy (TEM), scanning electron microscopy (SEM), Fourier transform infra-red spectroscopy (FTIR), X-ray diffraction (XRD) spectroscopy and cyclic Voltammetry.

iv. fabricate electrochemical sensor by modifying the working electrode (GCE) with ZnONP, Fe_3O_4NP and their nanocomposites f-MWCNT/ZnONP, f-MWCNT/Fe_3O_4NP.

v. measure the sensor performance of the bare and modified electrodes towards the detection of choline using cyclic voltammetry (CV) and impedance spectroscopy.

vi. investigate electrocatalysis of choline using different analytical techniques such as square wave voltammetry (SWV), electrochemical impedance spectroscopy (EIS), and chronoamperometric method.

vii. determine the performance of the fabricated sensors for real sensing of choline in dietary choline supplements such as CDP choline (citicholine) and choline bitartrate in super B energy injection fizzy tablet (choline bitartrate).

CHAPTER TWO

LITERATURE REVIEW

2.1 Nanotechnology

Nanotechnology deals with the study, development, fabrication and application of nanoscale size material (nanomaterials/nanoparticles smaller than 1 μm and 1 micron according) with ~ 0.2 nm atomic and molecular length scales (Buzea *et al.*, 2007). Nanomaterials are substances with at the minimum 1D (one dimension) less than 100 nm approximately (Alagarasi, 2011; Buzea *et al.*, 2007). The application of nanomaterial in research based on electronics, medicine, sensor, fuel, solar cells, and catalysis is of great interest considering their distinctive qualities such as large surface to volume ratio, high chemical reactivity, their quantum effects which dictates their optical, magnetic and electrical properties (Alagarasi, 2011). Some nanomaterials exist in nature while some are fabricated at nano range, taking advantage of their small size and unique features. Nanomaterials have a high surface atomic fracture, high surface energy, and spatial confinement and small flaw as structural properties (Alagarasi, 2011). Fullerenes, carbon nanotube (CNTs), metal and metal oxide nanoparticles, dendrimers are examples of nanomaterials (Alagarasi, 2011; Buzea *et al.*, 2007; Khan *et al.*, 2017).

2.2 Classification of nanomaterials

The classification of nanomaterials is dependent on size, shape, composition, uniformity, and aggregation of nanomaterials (Alagarasi, 2011; Buzea *et al.*, 2007). Some nanomaterials have one dimension (1D) like the thin films and surface coating. Some are 2D (2D nanostructures films which are applied in the separation and filtration of small particles size when adhered to a substance) with nanopore filters, asbestos fibre as examples and the 3D dimension (Alagarasi, 2011). The morphology/shape of nanomaterials could be flat, spherical, hexagonal, irregular and helical (Alagarasi, 2011). Nanomaterials could comprise a single material or different using varying modulations of dimension such as zero; one; two; and three with atomic clusters, filaments and cluster Assemblies; multilayers; ultrafine-grained over layers or buried layers; and represented in Figure 2.1 (Alagarasi, 2011).

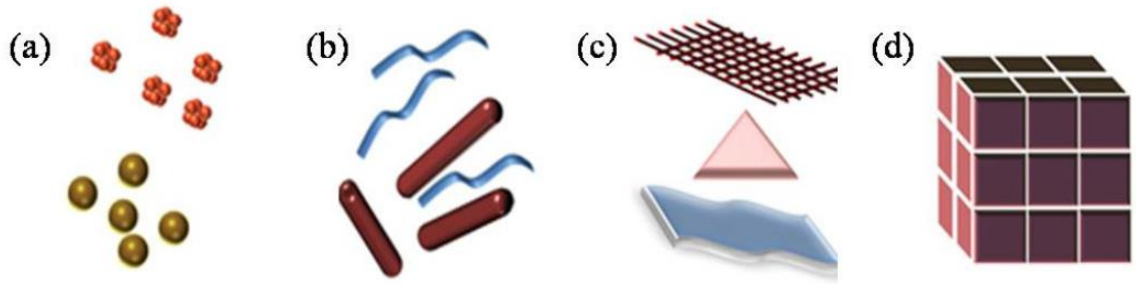

Figure 2.1: Classes of nanomaterials (a) 0D: spheres and clusters (b) 1D: nanofibers, nanowires and nanorods (c) 2D: nanofilms, nanoplates, and networks (d) 3D.

2.2.1 Application of nanomaterials

Nanomaterials have found wide applications in electrochemistry (sensors) for the detection of neurotransmitters (acetylcholine, histamine, glutamate, dopamine, serotonin, epinephrine, norepinephrine, glycine, and gamma-aminobutyric acid), and heavy metals, and also applicable in corrosion inhibition, investigation of forensic drugs, treatment of wastewater, and heavy oil owing to their properties (low toxicity, biocompatibility and small size). For instance, metal oxide nanoparticles doped with phthalocyanine and functionalized multi-walled carbon nanotube (MWCNT/Fe_3O_4/2,3-NC and MWCNT/ZnO/2,3-NC) was employed in the detection of epinephrine and norepinephrine (Mphuthi *et al.*, 2016). Metal oxide nanoparticles doped with multi-walled carbon nanotube (MWCNT/Fe_3O_4 and MWCNT-ZnO), and reduced graphene oxide with polyaniline doped with gold particles (rGO/PANI/AuNPs) was used for serotonin detection (Fayemi *et al*, 2015; Xue *et al.*, 2014).

Besides, reduced graphene oxide doped with palladium nanoparticles (rGO/PdNPs), and NiO and ZnO doped with polyaniline (PANI/ZnO, PANI/NiO) was applied in detecting dopamine (Fayemi *et al.*, 2018). Also, nickel oxide (NiO) nanoparticles and polypyrrole (PPy) was employed for acetylcholine detection (Sacramento *et al.*, 2017; Sattarahmady *et al.*, 2014). In a different study, copper (II) oxide nanoparticles (CuO) was applied in the investigation of histamine (Lin *et al.*, 2018), another experiment used polypyrrole/polyaniline doped with glutamate oxidase (GluX/PPy/PANI) in the study of glutamate (Batra *et al.*, 2014). In a different experiment, terephthalic acid capped with iron oxide (Fe_3O_4-NPs/TA), carbon nano thread (CNT), reduced graphene oxide –magnetic nanocomposites (rGO-Fe_3O_4), and reduced graphene oxide with gold nanoparticle s(rGO/AuNPs) were used for heavy metals detection (Cd^{2+}, Pb^{2+}, Hg^{2+}, Cu^{2+}, Zn^{2+}, As^{3+}, and Fe^{3+}) (Chimezie *et al.*, 2017; Deshmukh *et al.*, 2017; Zhao *et al.*,

2014; Zhu *et al.*, 2017). More so, iron (III) oxide nanorods were utilized in the treatment of heavy oil (Al-Ruqeishi *et al.*, 2019) and zinc oxide nanocomposites (PEG-ZnO, PVP-ZnO and PANI-ZnO), and ferrite pigments zinc ferrite ($ZnFe_2O_4$NPs) in corrosion inhibition (Mahvidi *et al.*, 2017; Quadri *et al.*, 2017).

2.2.2. Synthesis of nanomaterials

Nanomaterials could be synthesized from the wet chemical method of two approaches (top-down/bottom-up) or green assay (Alagarasi, 2011; Khan *et al.*, 2017) as presented in Figure 2.2. The top-down approach is majorly a physical method that involves the use of etching, mechanical grinding, sputtering, and laser ablation to reduce the size of bulk materials (Alagarasi, 2011). In mechanical grinding (MG), nanoparticles are synthesized via the disintegration of the coarse-grained structure due to vehement plastic deformation employing big energy shaker, planetary ball or tumbler. MG is appropriate in synthesizing amorphous/nanocrystalline particles, elemental or compound powders owing to its simplicity, applicability to the synthesis of all types of materials with relatively cheap equipment (Alagarasi, 2011). Mechanical grinding has the possibility of scaling up efficiently to tonnage quantities of materials for different usage as advantage and limitations involve the possibility of contamination within the media/atmosphere, and the consolidation of the product formed without condensing the nanocrystalline microstructures (Alagarasi, 2011).

Sputtering is a type of gas-condensation method with a sputtering target as a source material (Alagarasi, 2011). The target is sputtered using an inert gas with the constituents agglomerating to give nanomaterials. The assay is appropriate for synthesizing ultra-pure and non-agglomerated metal nanoparticles. Lazer oblation involves the use of laser beams as the main source of oblation excitation for producing clusters right from solid material in a vast variety of application (Alagarasi, 2011). This method is an efficient means of producing ceramics particles and coatings. Lazer oblation has the possibility of yielding a small size of particles and forming thick films (Alagarasi, 2011). Chemical etching entails the use of etchants which could be strong acids or corrosive liquids (mordant) to cut into the exposed part of a metal surface in order to make a pattern in the metal (Ayuk *et al.*, 2017). Etching is divided into wet and dry etching. Wet etching entails the use of chemicals/etchants to remove materials from a wafer. For instance, in a study, silicon nanoparticles were synthesized via damp etching with the use of potassium hydroxide as etchants (Ayuk *et al.*, 2017). Also reported was the synthesis of iron oxide. In dry etching, the material to be etched is bombarded with ions which are commonly plasma of un inert (reactive)

gases such like fluorocarbons, oxygen, chlorine, boron trichloride, nitrogen, argon, and helium (Ayuk *et al.*, 2017). The bottom-up approach involves the use of precursors and reducing agents (Alagarasi, 2011). Examples of the different types of bottom-up approach are the liquid phase methods (micro-emulsion, hydrothermal and sol-gel) and the chemical precipitation (Alagarasi, 2011; Dhand *et al.*, 2015). Micro-emulsion is a two-phase method comprising nano-sized water droplets dispersed in an oil phase and stabilized by surfactant molecules which could be cationic anionic or non-ionic. The type of surfactant chosen for use depends on the physicochemical properties of the system (Malik *et al.*, 2012). This method has residual surfactants on the particles and difficulties in scaling up procedure as a limitation (Malik *et al.*, 2012). The hydrothermal method operates at a maintained low or high pressure and temperature conditions in an aqueous media (Huang *et al.*, 2019). The medium is supersaturated by dehydration of metal salts and low solubility of oxides in the aqueous phase. Resulting particle size and morphology of formed nanoparticle is influenced by temperature, the concentration of precursors at the time (Huang *et al.*, 2019). The sol-gel method is majorly applied in the formation of metal oxide nanoparticles, and also composite of mixed oxide. The sol-gel process entails hydrolysis of metal precursor to give a solution of metal hydroxide. The resulting solution is condensed to form gels which are dried through evaporation or supercritical means in order to provide the final product as xerogel or aerogel. The sol-gel method could be aqueous (having water as the medium of reaction) or non-aqueous (organic media) and the press determines the final product obtained after drying (Alagarasi, 2011; Dhand *et al.*, 2015).

Chemical precipitation is widely used to get rid of soluble metals from solution by reacting soluble metal compounds mostly ionic with a precipitating reagent which precipitates out ionic minerals in an insoluble form (Dahman, 2017). Resulting precipitates (nanoparticles) are allowed to settle and then discarded from solution via filtering (Dahman, 2017). pH, type and concentration of precipitating agent together with ionic metals present in solution are factors that influence chemical precipitation (Dahman, 2017). Chemical methods of synthesis are unsafe for human, environment and plant due to the use of toxic chemicals (Kavitha *et al.*, 2017; Seabra & Duran, 2015; Umar *et al.*, 2019). The limitations of the chemical method can be addressed through the green route. Synthesis of nanomaterials using the green approach, also known as a biological method is at present on the upsurge since it is cheap, convenient, environmentally safe, less toxic, and materials are readily available being natural. Green synthesis involves the use of plant extracts (leaves, fruits, seeds, back, and peels of the plant), and microorganisms such as bacteria (Bacillus subtilis), algae (Chlorococcum), and fungi (Aspergillus) which serve as the

reducing agent together with a precursor (Lakshm *et al.*, 2017; Saif *et al.*, 2016; Seabra & Duran, 2015).

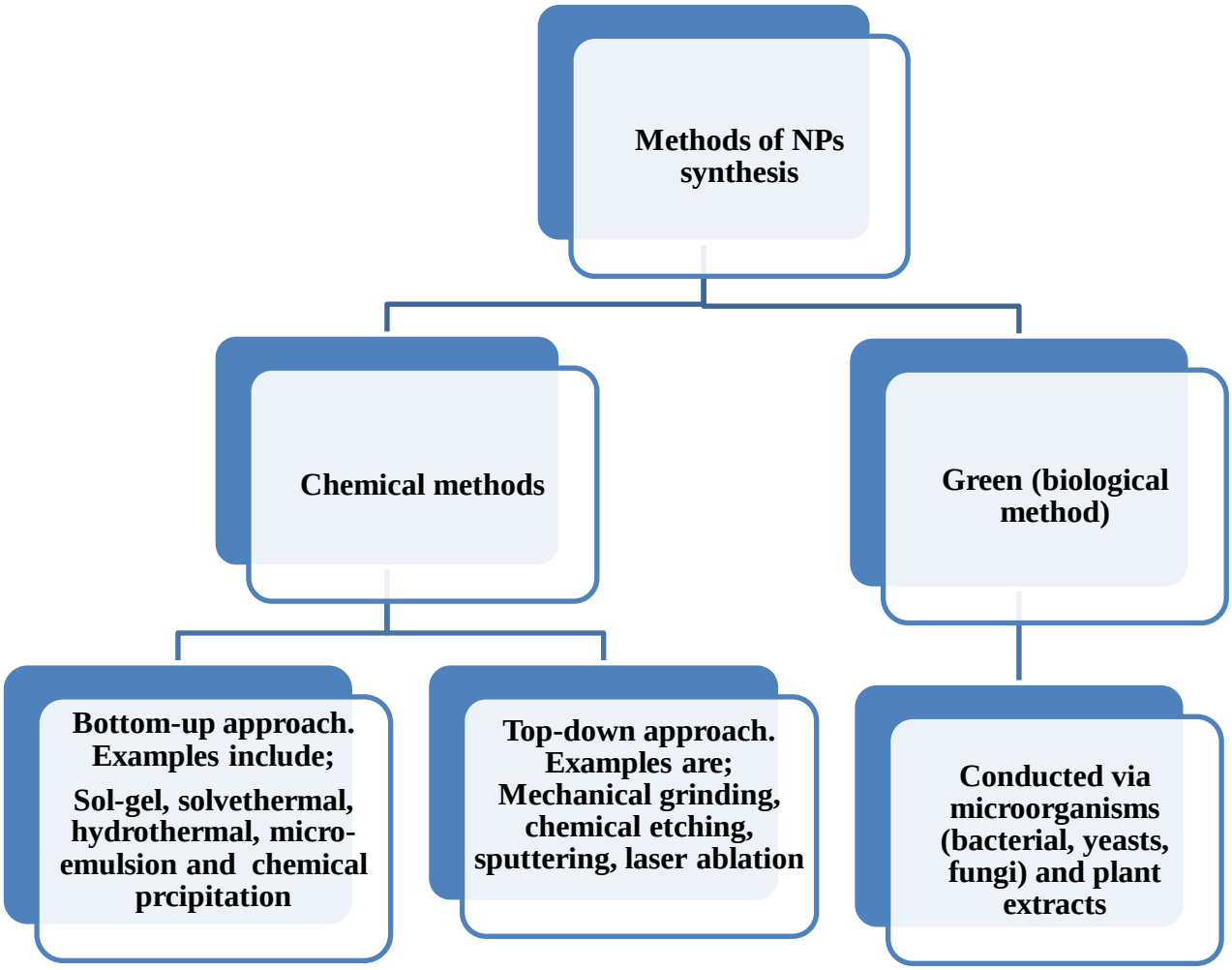

Figure 2.2: Synt]hetic approaches of nanomaterials.

2.3. Metal oxide nanoparticles

Metal oxide nanoparticles (MONPs) formed from their metal salts is significant in the field of physics, chemistry and material science (Immanuel *et al.*, 2019). MONPs possess structural forms with an electronic structure that is capable of revealing semiconductor, metallic and insulator property. They display distinctive properties (optical/electrical/thermal) owing to their excellent density large surface area and are biocompatible (Kecili & Hussain, 2018; Ramesh *et al.*, 2018; Rezaei & Irannejad, 2019). These properties make them applicable in catalysis (photocatalysis, electrocatalysis) (Immanuel *et al.*, 2019) electroanalysis (Rezaei & Irannejad, 2019) transistors, optoelectronic and solar cells (Rezaei & Irannejad, 2019). They display characteristic changes in electrochemical property, in structure and surface character resulting in an alteration of lattice symmetry, cell parameters and increased band gap (Kecili & Hussain,

2018). The increment in band gap affects the conductivity and chemical activity of NPs (Kecili & Hussain, 2018). Examples of some metal oxide nanoparticles are; copper (II) oxide (CuO), zinc oxide (ZnO), Titanium (IV) oxide (TiO_2), magnesium oxide (MgO), tin (IV) oxide (SnO_2), iron (III) oxide magnetite (Fe_3O_4), maghemite (Fe_2O_3), nickel oxide (NiO), silicon (IV) oxide (SiO_2), aluminium (III) oxide (Al_2O_3), and cobalt (IV) oxide (Co_3O_4) nanoparticles. Metal oxide nanoparticles can be synthesized via green and chemical method (Dhand *et al.*, 2015; Seabra & Duran, 2015).

2.3.1 Zinc oxide nanoparticles

Zinc oxide nanoparticle is a non-toxic semiconducting nanomaterial of great research interest due to its characteristic wide direct band gap (3.37) and binding energy (60 meV), stability (electrochemical and thermal) and significant piezoelectric coefficient (Mphuthi *et al.*, 2017). Zinc oxide nanoparticles (ZnONP) are employed in photovoltaic cells, transistors, ultraviolet diodes, painting, coating and cosmetics because of its distinctive properties (optical and electronics) (Umar *et al.*, 2019). Zinc oxide nanoparticles have also found application in chemical sensors (sensing of dopamine and serotonin with 97.8% and 98-104% accordingly) , biosensors, catalysis since they are electrically conductive with high catalytic effect (Kanwal *et al.*, 2011; Mahmoudian *et al.*, 2013). Also, ZnONP is used as an antibacterial and antifungal agent against more resistant bacteria (de Oliveira *et al.*, 2016). Different methods reported in the literature for ZnONP synthesis include; chemical (sol-gel, hydrothermal, precipitate and microemulsion) and green method (Alagarasi, 2011; Dhand *et al.*, 2015; Lakshm *et al.*, 2017; Saif *et al.*, 2016; Seabra & Duran, 2015). The chemical route of synthesis can impact on human health, environment, plant negatively due to the toxic and reactive nature of precursor/reducing agents, and treating of resulting waste products is challenging (Lakshm *et al.*, 2017; Saif *et al.*, 2016; Seabra & Duran, 2015). Recently, zinc oxide nanoparticles (ZnONP) is being synthesized via the green routes which involve the use of different parts of the plant (leaves, flowers, stem, fruits, and stem back), microorganism such like bacteria, fungi and algae (Lakshm *et al.*, 2017; Saif *et al.*, 2016; Seabra & Duran, 2015). The plant extracts play the role of a reducing and capping agent (Lakshm *et al.*, 2017; Seabra & Duran, 2015).

2.3.2 Iron (III) oxide nanoparticles

Iron (III) oxide nanoparticles (Fe_3O_4NP), widely known as magnetite, is one of the most commonly researched forms of oxides. Iron (III) oxide nanoparticles have found application in sensors (for dopamine and serotonin with 90.3 and 96- 98 % respectively), catalysis, medicine,

water treatment, drug delivery, and magnetic resonance imaging. They are biocompatible, economical, super magnetic, and ferromagnetic with the large surface area to volume ratio (Ramesh *et al.*, 2018). The synthesis of iron (III) oxide nanoparticles have been reported in the literature (Dhand *et al.*, 2015; Fayemi OE, 2015; I. Takai, 2019; Saif *et al.*, 2016; Seabra & Duran, 2015; Sun *et al.*, 2015).

2.4 Conducting polymer

Conducting polymers (CPs), also called synthetic metals had drawn great attention to researchers and engineers in the field of science and technology (Nguyen & Yoon, 2016). CPs are polymeric materials with great π-conjugated polymeric chains and exhibit high conductivity, excellent electrocatalytic (electrochemical) activity, biocompatibility, distinct optical, magnetic, mechanical and wetting properties, with simple preparation (Kumar *et al.*, 2015; Nguyen & Yoon, 2016). These properties have earned CPs promising electrode materials for the energy storage device, electrochemical batteries, super capacitors, and electrocatalysts (Kumar & Sharma, 1998; Kumar *et al.*, 2015; Nguyen & Yoon, 2016). Unique properties of CPs result from their possession of conjugated backbone structure which consists of long chains of the alternate single and double bond which permits continual overlapping of p-orbitals and also crucial for polymers to be intrinsically electronically conductive. Examples of the most extensively studied conducting polymers include the polyethenes (polyacetylene) and the polyaromatic conducting polymers with polyaniline, polypyrrole, poly(phenylene vinylene), poly(3,4-ethylene dioxythiophene), and polythiophene as examples (Kumar & Sharma, 1998; Kumar *et al.*, 2015).

Conducting polymers (CPs) are synthesized via (Kumar & Sharma, 1998; Kumar *et al.*, 2015; Nguyen & Yoon, 2016); (a) chemical polymerization which could be condensation or addition polymerization involving the oxidation of monomers in the presence of oxidants to generate polymer of interest, (b) an electrochemical process which involves electrochemical polymerization of CPs using a three-electrode system (working, counter and reference electrode) in a solution containing a monomer, an electrolyte and ideal additives putting electrolyte, deposition time/method, applied potential into consideration. Films of resulted CP are usually thin of approximately 20 nm thickness, (c) photo polymerization/photo initiation method entails polymerization of simple molecules (monomers) exposed to ultraviolet light, visible light, photochemical reaction (laser-generating radicals) or photo electrochemical reactions (holes), (d) pyrolysis is one of the oldest means of synthesizing conducting polymers. Pyrolysis involves the elimination of heteroatoms from the polymer by heating to produce extended aromatic structures

and (e) plasma polymerization, defined as the production of films from a group of organic and organometallic preliminary materials.

2.4.1. Types and application of conducting polymer

There is the existence of various types of conducting polymers (CPs) which include; Polyacetylene, polythiophenes (PTH), polypyrrole (PPy), poly(phenylene vinylene), poly(3,4-ethylene dioxythiophene), polyphenylene, polyaniline, polystyrene, poly (2,3-dimethyl-butadiene), polybutadiene, polyisoprene, poly(p-phenylene-terephthalate), and poly(aniline-CO-O-anisidine) (Kumar & Sharma, 1998; Kumar *et al.*, 2015; Nguyen & Yoon, 2016). Among these, most extensively studied CPs are; polypyrrole (PPy), poly(3,4-ethylene dioxythiophene), and polyaniline (Nguyen & Yoon, 2016). PPy is one of the most widely researched CPs in view of its ease of preparation, unique redox properties, high conductivity, stability, solubility (H_2O), commercially accessible with valuable electrical and optical properties (Kumar *et al.*, 2015). PPy is formed by polymerization (electrochemical or chemical) of pyrrole. Poly (2,3-dimethyl-butadiene) commonly called PEDOT is synthesized from 3,4-ethylene dioxyl thiophene monomer (Kumar *et al.*, 2015). PEDOT possess optical transparency in thin oxidized films, high stability, reasonable band gap, and low redox potential (Kumar *et al.*, 2015). Polyaniline (PANI) is of the family of semi-flexible rod polymer with great importance due to its distinct properties which are conduction mechanism, good environmental stability in the presence of water and oxygen (Kumar *et al.*, 2015).

Conducting polymers mostly PEDOT, PPy, and PANI have a wide range of application as electrode materials in sensors. For example, composites of gold nanoparticles/polyaniline/polydopamine (AuNPs/PANI/pDA), poly (3, 4-ethylene dioxythiophene) (PEDOT), polypyrrole with reduced graphene oxide nanosheets (PPy/rGO), polypyrrole-mesoporous silica molecular sieves (PPy-MCM-48) film, composite of polypyrrole/iron (III) oxide (PPy-Fe_3O_4NPs), polypyrrole/polyaniline doped with glutamate oxidase (GluX/PPy/PANI), and polyaniline with multiwall carbon nanotube (PANI/MWCNT) were applied in the investigation of dopamine and serotonin neurotranamitters (Atta *et al.*, 2011; Batra *et al.*, 2014; Li *et al.*, 2011a; Qian *et al.*, 2014; Sacramento *et al.*, 2017; Uwaya & Fayemi, 2020; Zablocka *et al.*, 2019). Polyaniline-graphene nanoribbons-carbon nanotube (PANI-G-CNT), ternary graphene nanocomposites/metal oxide and conductive polymers (rGO/$MnFe_2O_4$/PPy, rGO/$NiFe_2O_4$/PPy), PEDOT with graphene oxide-carbon nanotube

(PEDOT-GO/CNTs) were applied in super capacitors (Ishaq *et al.*, 2019; Liu *et al.*, 2013; Zhou & Han, 2016).

Polyaniline and graphene films (PANI/G), polypyrrole films, PEDOT, and carbon nanotube/polypyrrole doped with PEDOT (CNT/PPy/PEDOT) were used as electrode materials in solar cells (He *et al.*, 2014a; Lin *et al.*, 2015; Park *et al.*, 2013; Zhang *et al.*, 2014b). Polypyrrole nanoparticles were employed as storage device (Ahn *et al.*, 2015). Composites of zinc oxide polyaniline (PANI/ZnO), PEDOT, and graphene oxide incorporated in PEDOT films were employed in batteries (Guerfi *et al.*, 2014; Trinh *et al.*, 2013; Zhou *et al.*, 2014). Polypyrrole nanotube with quantum dots composites (PPyNT-PbSeQD) in photovoltaic cells (Kim, (2009).). Polypyrrole/ titanium oxide composites (PPy/TiO_2), and PEDOT were used as light-emitting diodes (Ngaboyamahina *et al.*, 2014; Xu *et al.*, 2009). Polypyrrole prussian blue (PPy/PB), polyaniline Prussian blue (PANI/PB), and polypyrrole with PEDOT) in electrochromic cells (Somani *et al.*, 2000; Winther-Jensen *et al.*, 2010), composites of polyaniline/zinc oxide (PANI/ZnO), and polypyrrole films were used for corrosion protection (Fenelon & Breslin, 2002; Quadri *et al.*, 2017).

2.5 Functionalization of multi-walled carbon nanotubes (MWCNT)

Carbon nanotubes (CNTs) has a wide range and growing application in super capacitors, optoelectronics devices, solar cells, biosensors and chemical sensors because it is electrically conductive and stable with small size, CNT enhances high electron transport and has a high surface area (Ahmed *et al.*, 2013; Magar *et al.*, 2017; Rajarao *et al.*, 2014; Sahebian *et al.*, 2016). CNTs could be challenging in application owing to low dispersion ability which is as a result of self-aggregation, bundling between CNTs tubules arising from the existence of van der Waals interaction between the tubules (Ahmed *et al.*, 2013). To enhance dispersion feasibility and activate CNTs surface for efficient applications, there is the need for modifying its surface through functionalization (Ahmed *et al.*, 2013; Gupta & Saleh, 2011; Hu & Guo, 2011; Rajarao *et al.*, 2014). Functionalization of CNTs involves the use of different reagents with varying degree of oxidizing ability under the stirring condition at a specific temperature for some minutes (Ahmed *et al.*, 2013).

In the process of functionalization, functional groups such as O−H, C=O of carboxylic acid are introduced on the CNTs surface (Ahmed *et al.*, 2013; Gupta & Saleh, 2011; Sahebian *et al.*, 2016). Reagents used for functionalization include; a mixture of acids (tetraoxosulphate (VI),

and nitric acid) in 1:3 or 1:1 volume ratio, single acid which could be nitric acid (HNO_3) or tetraoxosulphate (VI) (H_2SO_4). Reagents mixture such as H_2SO_4 in potassium tetraoxomaganate (VII) ($KMNO_4$) or hydrogen peroxide (H_2O_2) in HNO_3 is also use. But for an effective functionalization, HNO_3 or mixture of HNO_3 and H_2SO_4 is preferable (Atieh *et al.*, 2010; Gupta & Saleh, 2011; Sahebian *et al.*, 2016). For CNT/metal oxide composite, functionalization using acid gives room for excellent physical/electrical contact between CNTs and metal oxide nanoparticle, and it is of great importance in designing high performing CNT/metal oxide composite, promoting their dispersion stability, and CNT surface modification (Sahebian *et al.*, 2016).

2.5.1. Utilization of MWCNTs mixed with metal oxide nanoparticles

There is a current innovation in the research of carbon nanotube metal oxide nanocomposites with combined fascinating features and functions of carbon nanotubes (CNTs), and metal oxide nanoparticles (MONP) (Gupta & Saleh, 2011). Different inorganic materials which include metals, metal oxide and semiconducting nanomaterials have been used to dope CNTs owing to CNT fascinating dimensions and high surface areas, and composite materials of CNTs and MONP shows some new qualities such as improved optic, electric and magnetic properties resulting from the synergy between the two materials (Gupta & Saleh, 2011; Hu & Guo, 2011; Sahebian *et al.*, 2016). In the composites, the tendency of agglomeration of MONPs when dispersed on the surface of CNT is resolved (Gupta & Saleh, 2011). CNTs/MONPs composite materials have proved vast application in catalysis, super capacitors, batteries sensors and in wastewater treatment compare to individual MONPs because CNT as a carrier, aids in stabilizing the MONPs and maintain their integrity (Gupta & Saleh, 2011; Hu & Guo, 2011). Examples of reported multi-walled carbon nanotube-metal oxide (MWCNTs/MO) nanocomposites include; multi-walled carbon nanotube/zinc oxide (MWCNT/ZnO), multi-walled carbon nanotube-nickel oxide (MWCNT/NiO), multi-walled carbon nanotube/iron (III) oxide (MWCNT/Fe_3O_4), multi-walled carbon nanotube/Aluminium (III) oxide (MWCNT/Al_2O_3), and multi-walled carbon nanotube/tungsten (VI) oxide (MWCNT/WO_3), multi-walled carbon nanotube /cobalt (IV) oxide (MWCNT/Co_3O_4), multi-walled carbon nanotube-copper (II) oxide (MWCNT/CuO), multi-walled carbon nanotube/tin (VI) oxide (MWCNT/SnO_2) and multi-walled carbon nanotube/titanium (IV) oxide (MWCNT/TiO_2) (Gao *et al.*, 2010; Gelamo, 2009; Gupta & Saleh, 2011; Larrude *et al.*, 2012; Rajarao *et al.*, 2014; Sadegh *et al.*, 2014; Sahebian *et al.*, 2016).

2.6. Neurotransmitters

Neurotransmitters are small molecules/chemicals which act as messengers between neurons and transmit signals within the brain (Herlenius & Lagercrantz, 2010; Klein *et al.*, 2019; Si & Song, 2018). Neurotransmitters are produced endogenously and reserved in vesicles, presynaptic terminals and released into the synaptic cleft in response to an applied potential (Herlenius & Lagercrantz, 2010; Klein *et al.*, 2019; Lozić-Đurić, 2015; Si & Song, 2018). Neurotransmitters are sub-grouped based on their;

- molecular nature such as small organic molecules with acetylcholine, adenosine and adenosine triphosphate as examples; monoamines such as dopamine, serotonin, norepinephrine, epinephrine, and histamine; neuropeptides which include endorphins, methionine-enkephalin and β- endorphin; the amino acid is comprising glycine, glutamate, aspartate and gamma-aminobutiric acid (GABA) and lastly the gastro transmitters with carbon oxide (CO) and nitric oxide (NO) as examples (Klein *et al.*, 2019; Lozić-Đurić, 2015).
- response to an applied electric field (electroactive or non-electroactive) which dictates their direct or indirect namely the monoamines (dopamine, serotonin, norepinephrine, epinephrine, and histamine) can be detected directly using electrochemical methods. In contrast, the non-electroactive is detected indirectly via deposition of enzymes specific to them on sensor sites with the aim of enhancing electron transport between the analyte and electrode. Examples include; glutamate, acetylcholine and adenosine tryphosphate (ADP) (Lozić-Đurić, 2015; Shadlaghani *et al.*, 2019; Si & Song, 2018).
- physiological function (mode of action) as excitatory or inhibitory neurotransmitters. Excitatory neurotransmitters (glutamate, Acetylcholine, histamine, dopamine, norepinephrine, epinephrine, and glycine) stimulate targets cells to action and exhibit fast response to ionotropic receptors. In contrast, inhibitory neurotransmitters (serotonin, gamma-aminobutyric acid) inhibit targets cells, and they respond slowly to metabotropic receptors. Some neurotransmitters could be excitatory and inhibitory like dopamine, Acetylcholine, and glycine as a result of their numerous receptors present on different types of cells (Herlenius & Lagercrantz, 2010; Klein *et al.*, 2019). Most commonly studied neurotransmitters include; Acetylcholine, biogenic moamines (dopamine, norepinephrine, and epinephrine), biogenic indoleamines (serotonin), and the amino acids (glutamate, glycine and gamma-aminobutyric acid) (Shadlaghani *et al.*, 2019). Acetylcholine (Ach) was the first neurotransmitter to be discovered, and it is located in most brain regions with functions, including the transmission of signals from neurons to

muscles (Herlenius & Lagercrantz, 2010; Klein *et al.*, 2019; Lozić-Đurić, 2015). Norepinephrine, also known as noradrenaline, is involved in the regulation of sleep moulds, focus, attention, alertness, learning and memory, fear, anxiety and proper development of the brain (Herlenius & Lagercrantz, 2010; Klein *et al.*, 2019). Epinephrine (adrenaline) rmodulates adrenal glands, sleep, attentiveness and helps in the fight to fight response (Herlenius & Lagercrantz, 2010; Klein *et al.*, 2019). Dopamine regulates motor neurons (Herlenius & Lagercrantz, 2010; Klein *et al.*, 2019). Glycine is involved in sensory and motor functions which permit movement, vision and audition (Herlenius & Lagercrantz, 2010). Glutamate detoxifies the mammalian brain of ammonia and also triggers neuronal receptors (Herlenius & Lagercrantz, 2010; Shadlaghani *et al.*, 2019). Detection of these neurotransmitters has drawn great attention owing to their roles within the body systems.

2.7 Biological analyte

2.7.1 Choline

Choline, a beta-hydroxyethyltrimethyl ammonium hydroxide with 104 $gmol^{-1}$ molecular mass and chemical structure presented in Figure 2.3 is ubiquitously distributed in plants and animal cells mostly, as phospholipids, phosphatidylcholine (lecithin), lysophosphatidylcholine, choline plasmalogens and sphingomyelin (essential components of all membranes) (EFSA Panel on Dietetic Products & Allergies, 2016; He *et al.*, 2014b; Ikarashi & Maruyama, 1993; Koc *et al.*, 2002; Lima *et al.*, 2000; Phillips, 2012; Wiedeman *et al.*, 2018).

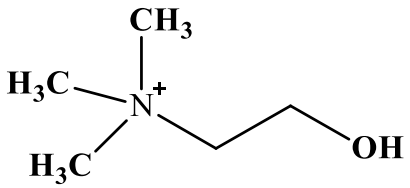

Figure 2.3: Chemical structure of choline.

Choline in its pure form is a colourless, viscous, vehemently alkaline, notably hygroscopic, soluble in polar solvent (water) and non-polar solvent (formaldehyde and alcohol) with boiling point of 113°C, melting point ranging from 244 to 247°C (as chloride salt), refractivity of 42.19 $m^3 \cdot mol^{-1,}$ polarizability of 12.57$Å^3$, polar surface area of 20.23$Å^2$, and predictable water solubility of 3.6 mg/mL (Imming *et al.*, 2006; Lima *et al.*, 2000). Choline can be oxidized to betaine through enzymatic processes involving choline dehydrogenase and betaine

dehydrogenase or hydrolysed to trimethylamine by bacterial deaminase enzyme (Hefni et al., 2015; Holmes et al., 2000; Shadlaghani et al., 2019; Zeisel, 1981; Zeisel, 2013). Choline can also be acetylated to acetylcholine by cytosolic enzyme called choline acetyltransferase and phosphorylated to phosphocholine by choline kinase (Shadlaghani et al., 2019; Zeisel, 1981). Oxidation, hydrolysis, acetylation and phosphorylation reaction of choline is represented with eq 1-4.

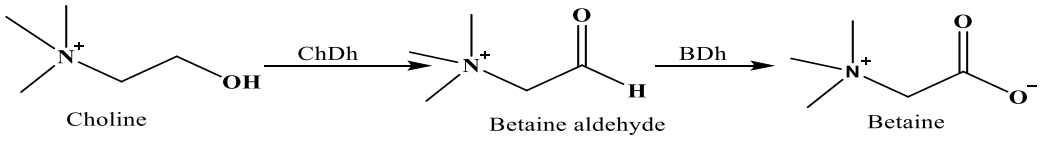

2.1

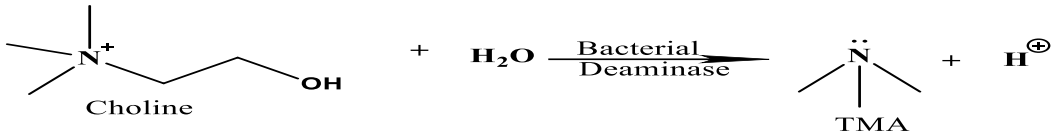

2.2

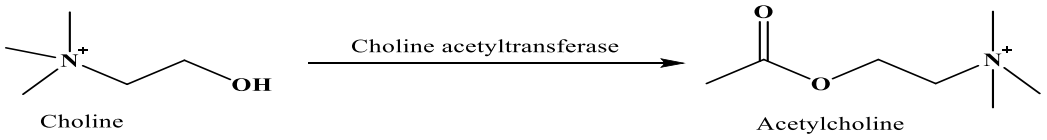

2.3

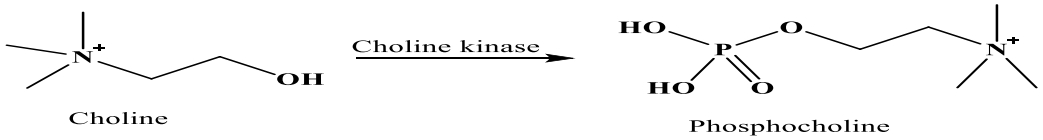

2.4

Choline metabolism is closely related to that of different vitamin B and methionine. The pathways of choline and 1-carbon metabolism intersect at the formation of methionine from homocysteine (Zeisel, 2012; Zeisel, 2013). Methionine is regenerated (re-methylated) from homocysteine in a reaction catalysed by betaine, homocysteine methyl transferase in which betaine, a metabolite of choline, serves as the methyl donor (Phillips, 2012; Wiedeman *et al.*, 2018; Zeisel, 1981; Zeisel, 2006). Choline can be obtained in diets and through de novo biosynthesis which involves methylation of phosphatidylethanolamine (PE) to phosphatidylcholine (EFSA Panel on Dietetic Products & Allergies, 2016; Phillips, 2012; Zeisel, 2013; Zeisel, 2009). However, de novo synthesis alone cannot adequately meet choline requirements in human (Gossell-Williams *et al.*, 2005; Phillips, 2012; Zeisel, 2009). Hence,

there is a need for high consumption of variety of foods rich in choline such as liver, fish, dairy products, brussels sprouts, broccoli, and egg especially egg yolk and choline dietary supplements which can be absorbed into the system by choline transporters (lipoprotein) in order to meet required daily choline intake and to maintain the body's proper function (Gossell-Williams *et al.*, 2005; Phillips, 2012; Wiedeman *et al.*, 2018; Zeisel, 2009). Comprehensive list of choline rich food is found in USDA data base (Patterson *et al.*, 2008). Choline aids normal foetus and brain formation, proper functioning of maternal liver and placental (Phillips, 2012; Wiedeman *et al.*, 2018; Zeisel, 2013; Zeisel, 2009). For premenopausal and postmenopausal females, choline prevents subclinical and organ dysfunction (Wiedeman *et al.*, 2018; Zeisel, 2012).

Choline deficiency or low choline levels results in; atherosclerosis, neurological disorder, cognitive decline, memory loss, kidney failure, heart and liver disease (Phillips, 2012; Zeisel, 2012; Zeisel, 2013; Zeisel, 2009). However, excess choline intake causes hypotension with corroborative evidence on cholinergic side effects (sweating and diarrhoea) and fishy body odour. To prevent hypotension, the tolerable upper intake level (UL) of choline for adults, pregnant and lactating mothers is 3.5 g/day (Zeisel, 2013).

2.7.1.1 Health importance of choline

In human body, choline (Cho) plays vital roles in health structure and function. Hence the necessity of choline is basic. Choline aids the regulation of water transport in and out of the cells (kidney glomerular) and probably mitochondrial functions when converted in the body through oxidation process into osmolyte betaine (Wiedeman *et al.*, 2018; Zeisel, 2013). Cho influences expression of genes through methylation of deoxyribonucleic acid (DNA) and reduces the damage of DNA and apoptosis in white blood cells (Zeisel, 2013; Zeisel, 2009). Cho produces acetylcholine (Ach), an important neurotransmitter involve in neurotransmission in both peripheral and central nervous system (He *et al.*, 2014b). Ach is also important in cortical activation, attention, memory, learning and reward, pain and regulates motor tone and movement (Herlenius & Lagercrantz, 2010; Magar *et al.*, 2017). In addition, choline produces phospholipid which is involve in body metabolism, transport of lipids, signalling and a component of surfactant complex in the lungs (Wiedeman *et al.*, 2018; Zeisel, 2013).

High concentration of choline reduces plasma levels of homocysteine as a result of increased ability of the liver to methylate homocysteine to methionine (Zeisel, 2009). This in turn decreases the risk of some chronic diseases such as cardiovascular diseases, cancer, cognitive decline and bone fractures (Zeisel, 2009). Also, adequate choline intake reduces the volumes of inflammation markers such as C-reactive protein (CRP), interleukin 6, and tumour necrosis factor (Zeisel, 2009). At Periconceptional stage, choline prevents neural tube defects (birth defects of the brain, spinal cord or spine) while in pregnancy/prenatal period, choline aids proper brain and memory formation, maternal placental and liver function, and protects the foetus from environmental abuse such as alcohol that can lead to abnormalities in behaviour, organ structures, foetal loss, and birth defects and also help better cognition in adults (Zeisel, 2013; Zeisel, 2009). Considering the health significance of choline, different analytical techniques have been utilised for choline detection in real samples (physiological, supplements and food).

2.7.1.2 Methods used in choline detection

Choline detection is quite challenging due to the various forms in which it exist, the absence of chromophore, fluorophore group, and also the reason being that choline is non-electroactive. Different methods have been applied for the detection of choline in food from plant and animal origins (cabbage, tomato, melon, lettuce, dairy products, meat/meat products, infant formulas and egg yolk) and clinical samples (Hefni *et al.*, 2015) (plasma, liver, blood and semen) as reported in literature. These methods include chromatography (high performance liquid chromatography (HPLC) (Buchanan *et al.*, 1980; Fossati *et al.*, 1994; Hefni *et al.*, 2015), liquid chromatography with electrochemical detector (LC-ED) (Ikarashi & Maruyama, 1993), liquid chromatography/electrospray ionization-isotope dilution mass spectroscopy (LC/ESI-IDMS) (Koc *et al.*, 2002), thin layer chromatography (TLC) (Sarada & Ramasastri, 1983), tandem mass spectrometry (LC-MS/MS) (Holm *et al.*, 2003), ion chromatography (IC) (Laikhtman & Rohrer, 1999), GC-MS (Hasegawa *et al.*, 1982), GC (Maruyama *et al.*, 1979), biosensor (Deng *et al.*, 2013; Magar *et al.*, 2017; Pundir *et al.*, 2012; Sajjadi *et al.*, 2012; Song *et al.*, 2006) capillary electrophoresis (Carter & Trenerry, 1996), electrochemistry at the interface sensor (Xie *et al.*, 2017) and electrochemical sensor (non-enzyme base) (Sattarahmady *et al.*, 2014).

a.) Conventional methods of choline detection

Example of the conventional methods include chromatography assays which although time-consuming, and labour intensive, have been used for detecting choline in infant formula and dried milk. In a previous study, ion chromatography with a suppressed conductivity was applied

for choline detection in infant formula and powdered milk samples after sample preparation and treatment (Laikhtman & Rohrer, 1999). A good recovery in the range of 85-114 % with 0.9999 regression was obtained (Laikhtman & Rohrer, 1999). Besides, liquid chromatography with electrospray ionization-isotope dilution mass spectrometry (LC-ESI-IDMS) was employed for choline detection in animal and plant tissues obtained from chicken, carrot, cabbage and beef following samples extraction and injection of 10 µl of the aqueous and organic phase supernatant was injected into the chromatograph (Koc *et al.*, 2002). The method gave 104 ± 3.8 % recoveries with 0.9953 regression value (Koc *et al.*, 2002).

Also, a high-performance liquid chromatography–fluorescence detection (HPLC-FLD) was employed for quantitative choline detection in food samples; faba beans, red lentils, whole milk and whole wheat flour highly rich in choline and of high consumption across the globe (Hefni *et al.*, 2015). A 0.25 g of samples was extracted by extraction solvents (chloroform, methanol-water) in 1:2:0.8 volume ratio. Extracts were hydrolysed in 1 m hydrochloric acid- acetonitrile-water. 1-naphthyl isocyanate was employ for choline derivitization (Hefni *et al.*, 2015). Derivatized choline was quantified by HPLC/fluorescence detection. Correlation coefficient was in the range of 2-13 with 83±5 % Recovery for faba beans and for whole-wheat flour (n = 6) (Hefni *et al.*, 2015). In another experiment conducted, choline in human plasma was determined by high performance liquid chromatography coupled with an enzyme reactor and electrochemical detector in plasma of human blood (Fossati *et al.*, 1994). Plasma (0.1 ml) was homogenized, centrifuged with the supernatant heated to dryness and the residue dissolved in 0.5 ml HPLC eluent. 50 µl of the dissolved residue was released into the chromatograph for choline detection (Fossati *et al.*, 1994). Reported percentage recovery independent of concentration of analytes was 86 % with 3.5 to 28.6 M choline level in plasma (Fossati *et al.*, 1994).

In a different study, a high–throughput method based on normal-phase chromatography-tandem mass spectrometry (LC-MS/MS) was applied for choline determination in serum and plasma (Holm *et al.*, 2003). Protein was removed from the samples by adding an internal standard (acetonitrile) followed by centrifuging and removal of the supernatant (Holm *et al.*, 2003). Deproteinized sample (2 µl) was injected into a normal–phase column. Choline was detected in the multiple-reaction monitoring mode of the tandem mass spectrometer using the molecular transitions m/z 104-60 with 0.1 µmol/l LoD and 0.9996 regression value (Holm *et al.*, 2003). More so, free, total and bound choline in plasma was detected using liquid chromatography with an electrochemical detector (LC-ED) (Ikarashi & Maruyama, 1993). A 10 µl portion of the

plasma was enzyme hydrolysed with 100 L of 0.1 M tris-HCl buffer, incubated for 10 min at 37 °C with the reaction stopped by addition of 100 L of 10 M $HClO_4$ (Ikarashi & Maruyama, 1993). The mixture was thereafter filtered and 5 µl of the filtrate was injected into LC-ED for total choline quantification (Ikarashi & Maruyama, 1993). Same step was followed for free choline quantification with exclusion of the incubation step and 50 µl portion of the plasma was hydrolysed (Ikarashi & Maruyama, 1993). Bound choline was obtained from the difference between total and free choline. Concentration of Total, free and bound choline were 1278.7 ± 132.5, 11.5 ± 2.2 and 1267.2 ± 125.6 with 100, 90 and 99 percentage recovery respectively (Ikarashi & Maruyama, 1993). Another experiment investigated choline in plasma with a paired–ion HPLC (Buchanan *et al.*, 1980). Samples were deproteinized by mixing 0.25 ml portion of plasma with 25 µl of 3-hydroxy-NNN-trimethylpropanaminium iodide (internal standard). Precipitation of the protein from the sample was aided by the addition of 0.75 ml of ice cold formic acid/acetone (Buchanan *et al.*, 1980). The mixture was centrifuged and the supernatant removed. Choline was isolated from the deproteinized sample by cation-exchange chromatography and derivative to 3, 5-dinitrobenzoate. Linear range of 1-500 nmole/ml was obtained with ± 6 % reproducibility (Buchanan *et al.*, 1980). Gas chromatography with mass spectrometer detector (Zeisel & DaCosta, 1990) and pyrolysis gas chromatography (Maruyama *et al.*, 1979) was used for choline detection in tissues. Choline concentration of 200 pmol 8.1± 0.98 nmoles was detected (Buchanan *et al.*, 1980; Zeisel & DaCosta, 1990).

A different study employed a thin layer chromatography involving Heyndrickx's reagent in detecting choline in semen samples. Samples were acid hydrolysed (1 N HCl) (Sarada & Ramasastri, 1983). Hydrolysates were analyzed for choline with a resulting parrot green coloured spots of 0.44 RF average value indicating the presence of choline. The method proved simple and specific (Sarada & Ramasastri, 1983). Chromatography methods though accurate and sensitive are time /labour intensive due to sample clean-up, extraction, separation and derivatization processes (Fossati *et al.*, 1994; He *et al.*, 2014b; Hefni *et al.*, 2015). Also they are not economical considering the amount of eluates, samples required and the cost of the instrument. Instrumentation requires expertise (He *et al.*, 2014b; Martinez, 1983). Thus they are not readily accessible to the routine laboratory (Carter & Trenerry, 1996; Hefni *et al.*, 2015; Woollard & Indyk, 2000). However, most or part of these limitations can be controlled by initiating the use of nano-material based-detection techniques such like electrochemical sensor which involve a three electrode electrochemical cell system and transducer (working electrode) surface being modified with nanostructured materials such as CNTs, polymers, metal/metal

oxide nanoparticles of characteristics small surface area, biocompatibility, and high electron transfer between biomolecules and electrode surface (Power & Morrin, 2013). They are convenient, cost effective, and fast due to elimination of extraction, separation and derivatization steps, readily accessible, require very small sample volume, highly sensitive and selective with simple instrumentation.

Some other separation methods employed for choline detection include proton nuclear magnetic resonance (^{1}H NMR) (Holmes *et al.*, 2000), capillary zone electrophoresis with indirect UV detector (CE-UV) (Carter & Trenerry, 1996) , field desorption zone mass spectrometry (Lehmann *et al.*, 1978) chemical and biological methods (Fletcher *et al.*, 1935; Glick, 1944; Martinez, 1983). Choline in vitamin preparations, infant formula, egg yolk and selected foods was determined using CE-UV detection at 214 nm (Carter & Trenerry, 1996). Samples were extracted in methanol, filtered and 50 ml aliquot of the filtrate was heated almost to dryness (Carter & Trenerry, 1996). Near dried filtrate was treated with aqueous calcium hydroxide prior analysis and boiled in a water bath with stirring at intervals for 90 min in order to hydrolyse choline esters and thereafter determined choline in all the samples using a 75 cm x 75 microns uncoated fused silica capillary column with 5 mM 1-methylimidazole electrolyte, pH 4.5, and an operating voltage of 30 kV (Carter & Trenerry, 1996). Choline was released in the electropherograms from other components in less than 3 min with tetramethylammonium ion used as the internal standard (Glick, 1944).

Chemical assay was employed in the investigation of choline in fish (Martinez, 1983) and selected food (Soy beans, oats, barley, bran) (Glick, 1944) respectively following reineckates specified steps. The samples were basic hydrolysed ($Ba(OH)_2$). A 107.5 percentage recovery was obtained for choline in fish (Martinez, 1983). The method proved reliable simple and fast but involve multiple extraction and hydrolysis steps (Glick, 1944; Martinez, 1983; Yao *et al.*, 2002). Also employed was a biological method using ringer tyrodes reagent in detecting choline in tissues (Zeisel *et al.*, 1986). Samples were acid hydrolysed (8 % HCl) (Zeisel *et al.*, 1986). Biological methods have poor specificity and sensitivity as limitation (Yao *et al.*, 2002; Zeisel *et al.*, 1986). In a different study, a proton nuclear magnetic resonance was used to determine choline content in infant formulas, breast milk colostrum after 2-6 day birth delivery and mature milk after 7-22 days birth (Holmes *et al.*, 2000). Samples were hydrolysed (acid hydrolysis) with 0.5 ml of 0.6 M per chloric acid for an hour at 40 °C, centrifuged with the supernatant divided into two and the pH of one adjusted to 2 and the other to 7. The two samples were centrifuged in

order to get rid of the $KClO_4$ precipitate and stored at -70 °C before being lyophilised. lyophilised sample was dissolved in 0.6 ml of water and transferred to a 5 nm OD NMR with chemical shift references 20 µl 20 mm 3- (trimethylsilypropionic-2,2,3d_4 and 50 µl 10 mM-fumarate in water (Holmes *et al.*, 2000). Choline content was quantified with regard to fumerate standard at pH 2 to avoid overlap of NMR carnitine signals. Choline concentration in human milk and full cream milk was found to be 1.28 mM and 0.94 mM respectively (Holmes *et al.*, 2000). The method was precise, void of prolong extraction, chemical modification and standardizations (Holmes *et al.*, 2000).

The aforementioned assays have their limitations. Capillary electrophoresis are expensive, not readily accessible for routine laboratory practices, potential poor specificity; overlapping of NMR signal, unavailable in most laboratory because it is expensive; numerous extraction and hydrolysis procedure; and poor specificity and sensitivity are associated with proton nuclear magnetic resonance (^{1}H NMR), reineckates (wet chemistry), and biological methods. Initiating the use of enzymes (choline oxidase and horseradish peroxidase) in detection schemes could help enhance specificity, sensitivity and reduce analysis time (Phillips, 2012; Woollard & Indyk, 2000; Zeisel *et al.*, 1986).

In addition, the use of enzyme based colorimetry, chemiluminescence, radio scintillation assays for choline detection was also reported. The quantity of choline in milk (human and bovine) and infant formula extracts was conducted using radioactivity aided by liquid scintillation spectrometry employing Bligh and dyer extraction method (Rauch *et al.*, 1997). Obtained percentage recovery was 102±4% with 2.15 precision (Woollard & Indyk, 2000). Enzymatic-colorimetric method was also utilized in determining choline in milk and infant formula (Woollard & Indyk, 2000). Samples were acid hydrolysed in order to release the bound choline. The pH of the hydrolysates was adjusted with $NaOH_{(aq)}$ to 3.5-4.0 (Woollard & Indyk, 2000). Choline phospholipids residual was cleaved with phospholipase D after adjusting the pH and free choline was subjected to choline oxidase resulting in the release of hydrogen peroxide. Choline content was reported as the hydroxide with 0.91 mean value within 0.76 - 1.00 range and a mean RSD value of 0.53 was found. The method proved simple and convenient but cannot be applied to powdered infant formula/milk (Woollard & Indyk, 2000). In another study, flow chemiluminescence sensing device with an immobilized enzyme (choline oxidase and horseradish) to determine choline in cabbage, tomato, melon, lettuce and egg yolk (Dhand *et al.*, 2011). Samples were hydrolysed in 0.2 M tris-HCl buffer of pH 7.4. A 60 µl aliquots of the

hydrolysates was analysed and choline signal was obtained by the generation of luminescent signal (Dhand *et al.,* 2011). Limit of detection with and without luminescent enhancer was 1.2 μm and 3.0 μm respectively.

Besides, an immobilized enzyme base interference-free chemiluminescence technique was likewise used for choline detection in tissue (Yao *et al.,* 2002). In another experiment, choline was determined in urine samples collected from two males and a female via a flow injection enzyme based method with electro chemiluminescence detector (FIA-ECL) which is based on generation of hydrogen peroxide on reaction of choline with choline oxidase (Jin *et al.,* 2010). Enzyme immobilized reactor was prepared by covalently immobilizing choline oxidase on amino propyl-controlled pore glass beads. Amino propyl-controlled pore glass beads was carefully homogenized in 2 ml 2.5% glutaraldehyde solution at room temperature for 90 min thereafter washed with 0.1 M PBS of pH 8.0 and transferred into a 2 ml, 0.1 M PBS which contains choline oxidase for 24 h at 4 ^{0}C (Jin *et al.,* 2010). Enzyme immobilized beads were rinsed with 0.1 M PBS and gently arranged in reactor column. The reactor aided the release of hydrogen peroxide which is directly proportional to choline concentration (Jin *et al.,* 2010). Sample was spiked with choline standard diluted in 10 ml PBS with pH 8.5 and was transferred into a centrifuge tube, centrifuged for 5 min and filtered. Filtrate was moved via a glass column to get rid of interference of (ascorbic acid) filtrate was thereafter released into the FIA system and choline detected by ECL at an applied potent of + 0.8 V (Jin *et al.,* 2010). Concentration of choline detected from samples collected from two males and a female was 12.9, 17.8 and 15.3 with 0.05 M limit of detection (Jin *et al.,* 2010).

The most important advantages of the proposed method over the HPLC for urinary choline are its high sensitivity simplicity and speed (Jin *et al.,* 2010). Radioenzymatic assays are cumbersome and are potential hazard; enzyme based colorimetry suffer from poor stability and sensitivity because enzymes are prone to denaturing; poor stability as a result of enzyme loss from the sensing electrode layer is tied with flow injection analysis enzyme based systems; and enzyme-based chemiluminescence method is expensive and not readily accessible for routine laboratory (Fossati *et al.,* 1994; Hefni *et al.,* 2015; Jin *et al.,* 2010; Phillips, 2012; Woollard & Indyk, 2000; Zeisel *et al.,* 1986). Part of these limitations especially the stability and sensitivity can be improved through incorporating the use of immobilized enzyme base-biosensors. Biosensors (a type of nanosensors) are relatively fast with high specificity and selectivity due to immobilized biological recognition elements (enzymes, protein, DNA). Also integration of

nanostructured materials (nanoparticles) on immobilized enzyme enhances diffusion and particle mobility which greatly impact on catalytic activity of the immobilized enzyme resulting to an increased stability and sensitivity (Power & Morrin, 2013). Summary of the different analytical techniques for choline detection is presented in Table 2.1.

Table 2.1: Analytical methods for choline detection in real samples.

S/N	Methods	Sample	Sample Preparation	LOD (µM)	% recovery	Advantages	Disadvantages	Ref
1	IC with conductivity detection	Infant formula	Acid hydrolysed (1 M HCl)	***	85-114	Accurate, simple and precise	Not readily available to laboratory routine, time demanding and tedious	(He *et al.*, 2014; Laikhtman & Rohrer, 1999; Woollard & Indyk, 2000; Zeisel, 2006)
2	LC-ED	Plasma	Extracted in 0.1 m tris-HCl buffer	***	***	Fast, specific, sensitive and precise	Applicable to small sample size, inability to detect Pcho	(Ikarashi & Maruyama, 1993; Phillips, 2012)
3	LC-ESI-IDMS	Liver, plasma, brain and food	Extracted in mixture of solvents ($CHCl_3$/MeOH/H_2O) in 2:1:0.8	1E-6 to 4E-5	104 ±3.8	No isolation nor derivatization of compounds	Unavailable in most laboratory due to cost	(He *et al.*, 2014; Hefni *et al.*, 2015; Magar *et al.*, 2017; Zeisel *et al.*, 1986)
4	LC-MS/MS	Serum amd plasma	Extracted in acetonitrile containing d9 choline	≤0.3	87-105	Sensitive, specific, high through put	Imprecision, Expensive, Limited to large scale epimologic studies	(He *et al.*, 2014; Hefni *et al.*, 2015; Holm *et al.*, 2003)

S/N	Methods	Samples	Sample preparation	LOD (µM)	% Recovery	Advantages	Disdavantages	Ref
5	HPLC/ED	Plasma	Extracted in acetonitrile containing 0.3 µg/mol of ethylhomocholine IS	***	86	Simple preparation, Sensitive , selective and precise	Expensive, time consuming, tedious And requires expertise	(Fossati *et al.*, 1994; He *et al.*, 2014; Phillips, 2012)
6	HPLC-FLD	Faba beans, milk, whole wheat	Extracted in $CHCl_3$/MeOH/H_2O	***	93 ±9 106 ±5 84 ±6	Precise and accurate	Limited to Cho and Acho, expensive, time consuming and tedious, requires expertise and does not permit the use of internal standards	(He *et al.*, 2014; Hefni *et al.*, 2015; Koc *et al.*, 2002; Pati *et al.*, 2007; Phillips, 2012)
7	Pairedion HPLC/UV	Plasma	Acid Hydrolysis (1 M Formic acid in acetone	***	***	Sensitive	Expensive,time consuming tedious	(Buchanan *et al.*, 1980; He *et al.*, 2014)

S/N	Methods	Samples	Sample preparation	LOD (µM)	% Recovery	Advantages	Disdavantages	Ref
8	Pyrolysis gas chromatography	Tissue	Acid hydrolysis (15% 1 N formic acid in acetone)	***	***	Accurate, sensitive and reproducible	Complex chemical demethylation, time intensive and not readily available	(Buchanan *et al.*, 1980; Hasegawa *et al.*, 1982; Maruyama *et al.*, 1979)
9	GC/MS	Tissue	Extracted in 1 M formic acid/acetone	***	***	readily accessible	Expensive, time and labour demanding, Expertise require , not readily accessible	(Buchanan *et al.*, 1980; Hasegawa *et al.*, 1982; He *et al.*, 2014; Hefni *et al.*, 2015; Maruyama *et al.*, 1979; Zeisel & DaCosta, 1990)
10	TLC	Semen	Acid hydrolysis (1 N HCl)	***	***	Simple and specific	Expensive, time and labour intensive	(Pati *et al.*, 2007; Rauch *et al.*, 1997; Sarada & Ramasastri, 1983)

S/N	Methods	Samples	Sample preparation	LOD (µM)	% Recovery	Advantages	Disdavantages	Ref
11	1H NMR	Milk	Acid hydrolysis (0.6 M per chloric acid, 1 h, 4 ℃)	***	***	High precision, absence of prolong extraction, chemical odification and standardization	Expensive, not readily available in all laboratory, poor sensitivity	(Hefni *et al.*, 2015; Holmes *et al.*, 2000; Rauch *et al.*, 1997)
12	CE-UV	vitamin preparations, infant formula, egg yolk	Extracted in methanol and basic hydrolysed (calcium hydroxide)	8.3E-21	93-119	Convenient, high resolution	Not readily accessible, expensive, potential specificity issue	(Carter & Trenerry, 1996; Woollard & Indyk, 2000)
13	Stable isotope and field desorption mass spectrometry	Tissue	Acid hydrolysis (4 % per chloric acid) 30 min	***	***	sensitive, specific and simple	Expensive	(Lehmann *et al.*, 1978)
14	Radio enzymatic	Milk, infant formulas	Extracted in CH3Cl-MeOH-H2O	***	***	Fast and sensitive	Expensive, cumbersome and a potential health hazard	(Fossati *et al.*, 1994; Holm *et al.*, 2003; Rauch *et al.*, 1997)

S/N	Methods	Samples	Sample preparation	LOD (µM)	% Recovery	Advantages	Disdavantages	Ref
15	chemiluminescence	Cabbage, tomato, melon, lettuce and egg yolk	Hydrolysed in 0.2 M tris-HCl buffer of pH 7.4	1.2 and 3.0 with and without an enhancer	***	Rapid, and void of matrix interference	Expensive, poor stability of enzymes	(Fossati *et al.*, 1994; Magar *et al.*, 2017; Rauch *et al.*, 1997)
16	Chemilumine Scence	Tissue	Extracted in EDTA, EDTA-SDS solution with pH adjusted to 7.2	3×10-8	***	selective	Expensive and poor stability of enzymes	(Fossati *et al.*, 1994; Magar *et al.*, 2017; Yao *et al.*, 2002)
17	Flow injection analysis	Urine	Enzymatic hydrolysis (2 % glutaraldehyde, 90 min, 25 °C)	0.05	***	rapid	Poor stability caused by enzyme from the sensing electrode layer	(Fossati *et al.*, 1994; Jin *et al.*, 2010; Magar *et al.*, 2017)

b) Biosensors

Biosensors are a type of sensor that involve the use of, immobilization surface, biological sensing element such as enzymes, antibodies, proteins, microbes, DNA with an electronic transducer in detection of analytes (Basu *et al.*, 2008; Dhand *et al.*, 2011a; Dhand *et al.*, 2011b). Sensing element aids the release of an electro-active element required resulting to a current response from the transducer (electrical signal) which is proportional to analytes concentration. It also enhances specificity and sensitivity of biosensors (Basu *et al.*, 2008; Dhand *et al.*, 2011a; Dhand *et al.*, 2011b).

bi) Enzyme based biosensor

Enzyme based electrochemical biosensors incorporates bio-recognition enzyme over the immobilization electrode surface (Koyun *et al.*, 2012; Power & Morrin, 2013) The quantity of total, free and phosphatidyl bound choline was determined in untreated milk and dietary samples using a phospholipase D packed bioreactor incorporated in choline oxidase based amperometric biosensor at modified platinum electrode (Pati *et al.*, 2005). Aliquots of the sample were injected via PLD-PBR and PLD-free PBR on selected flow rate (0.2 $mLmin^{-1}$). Up to 0.5 mM linear response was obtained for choline with 0.02 mM limit of detection. Pati et al estimated choline concentration and composition of milk samples using the designed sensor by hydrolysing (acid hydrolysis) an aliquots of the sample. Choline concentration obtained for N = 3 was 0.94± 0.04 mM (Pati *et al.*, 2005) .

Also, a biosensor base on the reaction of choline with immobilized enzyme at modified platinum electrode was used for choline detection in milk hydrolysates (Pati *et al.*, 2007). Enzyme immobilization in the FIA system was achieved by cross linking of glutaraldehyde on a NH_2^- functionalized controlled pore glass support and a total of 0.95± 0.05 mM choline concentration was obtained by liberation of H_2O_2 in a flow-through configuration with 46.9± 0.2 μCmM^{-1} sensitivity and 7 μM LoD (Pati *et al.*, 2007). Designed biosensor was validated by comparing obtained choline concentration with that obtained via an enzymatic colorimetric method and the concentration values were discovered to be quite close (Pati *et al.*, 2007). In addition, the content of choline in milk, soy lecithin, egg powder, yolk and infant formula was detected using a rapid microwave hydrolysis with a choline biosensor (Panfili *et al.*, 2000). The biosensor was based on oxygen (O_2) consumption during the reaction of choline with immobilized choline oxidase (Panfili *et al.*, 2000). O_2-based probe was chosen due to its selectivity and simplicity. Solid and

liquid Samples were hydrolysed in 1M hydrochloric acid (HCl) and 3 M HCl respectively following the Woollard and Indyk method and choline content found were in the range of 10.2 - 2270.0 mg/l00 g in the tested sample (Panfili *et al.*, 2000).

bii) Carbon nanotube/nanomaterials-based electrochemical biosensors

Currently, nanomaterials such as carbon nanotubes (CNTs), nano wires, graphene oxide, and metal/metal oxide nanoparticles such as gold, platinum, zinc oxide, zirconium (IV) oxide (ZrO_2), manganese (IV) oxide (MnO_2), and nickel oxide (NiO), are being incorporated on immobilized biological sensing elements of biosensors due to their possession of a high electrocatalytic effect, biocompatibility fascinating electronic and optical properties, chemical stability and high electron transfer rate between biomolecules and the electrode surface (Bai *et al.*, 2007; Deng *et al.*, 2013; Magar *et al.*, 2017; Power & Morrin, 2013; Pundir *et al.*, 2012; Sajjadi *et al.*, 2012; Zhang *et al.*, 2014). The nanomaterials impact greatly on catalytic activities of the enzymes and increase stability of enzymes which in turn results in an improved sensitivity and specificity of biosensors (Power & Morrin, 2013).

For instance, a novel sensitive amperometric choline biosensor at multi-walled carbon nanotube and gold nanoparticles (Chox/GNP_4/MWCNT/GCE) was designed for choline detection in milk samples using were amperometric and electrochemical impedance spectroscopy (Magar *et al.*, 2017). The designed biosensor with dynamic 3-120 μM linear range gave a good limit of detection (0.6 μM) with 204 μA cm^{-2} mM^{-1}sensitivity (Magar *et al.*, 2017). Also developed was an amperometric aqueous sol-gel biosensor at modified multiwall carbon nanotube platinum (Chox/MWCNT/Pt) electrode for low-potential stable choline detection in serum samples in 0.1M phosphate buffer solution (Song *et al.*, 2006). Chronoamperometry electrochemical methods set at 0.16 V with enzyme-immobilized MWCNT modified Pt electrode as working electrode (WE), platinum spiral wire as counter electrode and a Ag/AgCl 3 M potassium chloride referenced electrode was employed (Song *et al.*, 2006). Obtained amperometric response towards choline at ChOx/MWCNT/Pt was in concentration linear range from 5×10^{-6} to 1×10^{-4} M with a 0.9896 regression value in less than 8s which showed that oxidation current response was proportional to choline concentration. A 1×10^{-7} M limit of detection was found at the electrode (Song *et al.*, 2006). The designed sensor was successfully applied for choline detection in serum (Zeisel & DaCosta, 1990). A different study reported the use of a solid–contact ion-selective electrode based on octanamide cavitand receptor and a non-carbonxylated single-walled carbon nanotube as a solid traducer (GC/SWCNT/ISM) for choline detection.

GC/SWCNT/ISM served as the sensing electrode and Ag/AgCl/KCl (3 M) reference electrode. The designed sensor was characterized via Impedance measurement between 10 KHz and 0.3 Hz frequency range and the stability evaluated with a reversal chronoamperometry while detection limit ($10^{-6.4}$ M) and sensitivity (57.3±1.0 mV/decade) was obtained through potentiometric detection over 10^{-5} to 10^{-1} M linear choline concentration range (Ampurdanés *et al.*, 2009). In another study, choline detection was conducted on an amperometric choline biosensor based on nanocomposites film of choline oxidase (ChOx)-multi-walled carbon nanotube- gold nanoparticles and poly diallyldimethlammonium (PDDA) on platinum electrode (MWCNTs-GNP-ChOx-PDDA/Pt) at 0.35 V applied potential in 0.1 M phosphate buffer solution (PBS) pH 7.6 over a dynamic Cho concentration range of 0.001 -0.5 mM (Qin *et al.*, 2010). Detection limit, correlation coefficient and sensitivity of the sensor was found to be 0.3 μM, 0.992, and 12.97 μA/mM respectively (Qin *et al.*, 2010). Also, choline was detected on a choline biosensor designed using layer by layer assembly of multilayer film consisting of choline oxidase (ChOx), PDDA on electrodes modified with MWCNTs/poly (vinyl sulphate)/polyallylamine (ChOx/PDDA)n/$(PVS/PAA)_3$/MWCNTs/Pt) (Qin *et al.*, 2009). Choline detection was conducted by amperometry at +0.56 V potential in 0.1 M PBS pH 8.0 in a dynamic range from 5×10^{-7} – 1×10^{-4} M. Designed sensor gave a sensitivity value of 10.89 μA/mM with 2×10^{-7} M and 0.9932 M limit of detection and correlation coefficient (Qin *et al.*, 2009).

In a previous study, a choline biosensor fabricated through the deposition of a bio-composites (chitosan hydrogel/choline oxidase/manganese (IV) oxide nanoparticles unto a glassy carbon electrode (ChOx/MnO_2/Chit/GC) was employed for choline detection using SWV in 0.2 M borate buffer solution pH 7.8 with 1.0×10^{-5}-2.1×10^{-3} M linear range (Bai *et al.*, 2007). Regression value of the electrode was found to be 0.9989 (Bai *et al.*, 2007). In a different experiment, choline was detected on a choline biosensor designed by assembling of functionalised MWCNTs and polyaniline on glassy carbon electrode with choline oxidase D (MWCNT/PANI/GCE/CHOD) using amperometry at 0.4 V applied potential in PBS pH 6.98 (Qu *et al.*, 2005). The developed sensor displayed a linear choline response range of 1×10^{-6} - 2×10^{-3} with 0.3 μM and 0.997 values for LoD and regression (Qu *et al.*, 2005). Another choline biosensor fabricated by a sol–gel method with choline oxidase (ChOx) immobilized in composite immobilization membrane matrix comprising Au nanorods and polyvinyl alcohol on platinum electrode (PVA/Au/ChOx/Pt) was used for choline detection in 0.1 M PBS pH 8 at 0.4 v detection potential using amperometry over a linear range from 0.02 -0.4 mM (Ren *et al.*, 2009).

Obtained sensitivity and LoD values at the designed electrode were 15.7 $\mu AmM^{-1}cm^{-2}$, 10 μM accordingly (Ren *et al.*, 2009).

In a different experiment, a choline biosensor designed via immobilization of choline oxidase on prussian blue modified iron phosphate nanostructure immersed in PDDA onto glassy carbon electrode (ChOx-PDDA-PB-FePO4/GCE) was applied for choline detection using amperometry technique in PBS at 0.05 V detection potential (Zhang *et al.*, 2012). A 75.2 $\mu AmM^{-1}cm^{-2}$ sensitivity was found in a linear choline concentration range of 2-3200 μM with 0.4 μM LoD (Zhang *et al.*, 2012). More so, a structured biosensor by immobilization of choline oxidase on nanostructure poly(N-butylbenimidazole)-graphene sheets (PBBIns-GS)-gold electrode (ChOx-PBBIns-GS/Au) was used for choline determination employing chronoamperometry technique at an applied potential of -0.5 V (Chen *et al.*, 2013). The electrode showed a linear range from 0.1 μM - 0.83 mM with 494.9 $\mu AmM^{-1}cm^{-2}$ sensitivity and 0.02 μM LoD (Chen *et al.*, 2013). In addition, a choline biosensor base on synergetic effect of multi-walled carbon nanotube/zinc oxide nanoparticles (MWCNT/ZnO) and immobilization of choline oxidase (ChOx)- poly diallyldimethlammonium (PDDA) unto a pencil graphite electrode (PDDA/ChOx/ZnO/MWCNTs/PGE) was utilized for choline detection in 0.1 M PBS pH 7.8 using amperometry (Zhang *et al.*, 2014). A linear response choline range (1.0-0.8 mM), sensitivity (178 $\mu AmM^{-1}cm^{-2}$), and 0.3 μM detection limit was obtained at the electrode. The biosensor was evaluated for choline determination in plasma and a range of 95-106 percentage recovery was obtained (Zhang *et al.*, 2014).

In another study, ferrocene-chemically reduced graphene oxide, horseradish peroxidase and choline oxidase aided by chitosan (Chox/HRP/FC-CRGO/GCE) on GCE platform was employed for choline investigation using amperometry at a very low applied potential (-0.10V) (Deng *et al.*, 2013). A detection limit of 0.35 μM with 1-400 μM linear range was obtained (Deng *et al.*, 2013). Choline detection was also carried out on a nanocomposites modified electrode (functionalized MWCNT and ionic liquid (1-butyl-3-methylimidazolium tetrafluoroborated) and immobilized with choline oxidase -ChOx/RTIL/NH_2-MWCNT/GCE) using amperometry in PBS (0.2 M, pH 7) (Sajjadi *et al.*, 2012). Amperometric response of the designed biosensor towards choline was linear from 6.9×10^{-3} - 6.7×10^{-1} mM with 0.998 regression value. LoD and sensitivity value were found to be 2.7 μM and 2.59 μA/mM (Sajjadi *et al.*, 2012). An amperometric choline biosensor developed by immobilization of ChOx onto nanocomposites of bamboo-like MWCNT, ionic liquid, prussian blue on GCE surface (Chox/Ni-PB/BG/GCE) was used for

choline detection in PBS pH 7.4 (Keihan *et al.*, 2014). The biosensor displayed a linear response to choline from 4.5×10^{-7} to 1.0×10^{-4} with a high sensitivity of 345.4 $\mu AmM^{-1}cm^{-2}$ and LoD of 4.5×10^{-7} M. Percentage recovery range from 96.2-105.0 was obtained at the biosensor in real sample application (sample not mentioned) (Keihan *et al.*, 2014).

More so, a fabricated amperometry choline biosensor (AChE-Cho/c-MWCNT/ZrO_2NPs/GCE) designed by immobilizing acetylcholinesterase and ChOx onto a nanocomposites of carboxylated MWCNT and zirconium oxide nanoparticle deposited on the surface of GCE was used for evaluation of choline (Pundir *et al.*, 2012). LoD and working linear range values were 0.01 μM and 0.05-200 μM. Biosensors though reproducible, fast, sensitive and selective to choline amidst interfering element are not economical considering the cost of biological sensing element. More so, the instability of the biological sensing element which results from their denaturing have the possibilities of affecting the sensitivity of the electrode and immobilization steps are quite challenging and are not readily accessible to the routine laboratory (Koyun *et al.*, 2012; Power & Morrin, 2013). These limitation can be address by the use of non-enzyme base electrochemical methods (non-biosensors) coupled with nanomaterials such as nanowires, ferromagnetic nanoparticles, which possess an inherent enzymatic activity similar to that seen in natural peroxidase (He *et al.*, 2014; Magar *et al.*, 2017; Power & Morrin, 2013) Recently, employed the use of electrochemical method called electrochemistry at the interface between two immiscible electrolyte solutions (ITIES) and nanomaterials based electrochemical sensor was used for choline detection respectively (Sattarahmady *et al.*, 2014; Xie *et al.*, 2017).

c) Electrochemistry at liquid/liquid interface based method

Electrochemistry at liquid/liquid interface is an electrochemical process that studies the transfer of charge (electron or ions) at a liquid/liquid (water/organic) interface, or an oil and water interface, or interface between two immiscible electrolyte solutions (ITIES) of low mutual miscibility using electrochemical techniques such as cyclic voltammetry, differential pulse stripping voltammetry, and chronoamperometry (Girault, 2010; Toth & Dryfe, 2015). The liquid/liquid interface and ITIES method have found great attraction in different aspect of electroanalysis owing to their sensitivity, selectivity and fast response (Toth & Dryfe, 2015; Xie *et al.*, 2017). The working principle of electrochemistry at liquid/liquid interface depends on the difference in solvation energies of ions in two adjacent phase which result to ionic current signals (Xie *et al.*, 2017). Organic solvents widely used for the study of charge transfer across liquid/liquid interface and they include; 1,2-dichlorobenzene (DCB), 1,6-dichlorohexane,

nitrobenzene (NB)1,1-dichlorobutane, and 1,2-dichloroethane (DCE) (Girault, 2010; Toth & Dryfe, 2015). These solvents are highly toxic and 1,2-dichloroethane (DCE) is suspected to be carcinogenic, which limits their use in electroanalysis (Toth & Dryfe, 2015). Other solvents used include; mixed organic solvent, 2-nitrophenyl octyl ether (NPOE), and ionic liquids which seems to be appropriate are expensive and their preparation challenging (Toth & Dryfe, 2015).

A portable amperometric ion sensor called a nano-wire gel (nano-W/gel) interface was fabricated by incorporating silica isoporous membrane (SIM) and organogel which consist of polyvinylchloride (PVC) and 1,2-dichloroethane (DCE) on a 3D polymer chips (Xie *et al.*, 2017). The nano-W/gel interface array was formed between SIM and silica nitride (SiN) chips boundary. Designed sensor was applied for choline detection using differential pulse stripping voltammetry over 1-100 μM dynamic choline concentration range with magnesium (II) chloride ($MgCl_2$) and bis(triphenylphosphoranylidene) ammonium tetrakis(4-chlorophenyl borate) (BATPBCl) as supporting electrolytes in the aqueous and organogel phase accordingly (Xie *et al.*, 2017). A 9.02 μM LoD, and 4.65±0.22 $nAmM^{-1}$ sensitivity values were obtained at the designed sensor (Xie *et al.*, 2017). Practical applicability of the fabricated sensor was proven by detecting choline in milk and urine over 2-200 μM dynamic range, and 1.12 and 3.62 μM detection limit was obtained for the respective samples (Xie *et al.*, 2017). However, 1,2-dichloroethane (DCE) is toxic and a suspected carcinogen (Toth & Dryfe, 2015).

d) Electrochemical sensor

Considerable attention has been drawn to electrochemical sensor for detection of species in biological, environmental and pharmaceutical samples due to their simplicity, stability, highly sensitive and selective, rapid response and low cost (Power & Morrin, 2013). Electrochemical sensor consists of electrodes such as working, auxiliary, reference electrodes and electrolytes. The sensing or working electrode could be glassy carbon, gold, carbon paste, or platinum electrode and is the reaction point. The counter or auxiliary electrode maintains the potential applied at the sensing electrode, the reference electrode prevents the performance of the sensor from deteriorating over long period of time while the electrolytes is for efficient transport of ions across the electrode (Koyun *et al.*, 2012; Power & Morrin, 2013). The principle of electrochemical sensor is based on the reaction of analytes of interest at the sensing electrode with a resulting electrical signal which corresponds to the concentration of analytes (Power & Morrin, 2013). Signals, of electrochemical sensors are amplified by modifying sensing electrode surface with nanocatalyst such as carbon nanotubes (CNTs), metal, metal oxide nanoparticles,

conducting polymers owing to their high electrocatalytic effect, tensile strength, chemical stability and high electron transport rate within biomolecules and the electrode surface due to large surface area (Fayemi *et al.*, 2017; Luo *et al.*, 2014; Power & Morrin, 2013).

There is a minimal research on choline sensing in real samples using non-enzyme base electrochemical sensor. An electrochemical sensor was utilized for choline detection (flower-like nickel oxide nanostructure modified carbon paste electrodes) and the kinetics of the electrocatalytic oxidation of choline (10 mM) on the modified electrode was studied using cyclic voltammetry (CV), steady-state polarization curve and chronoamperometry in 100 mM sodium hydroxide solution as the supporting electrolyte (Sattarahmady *et al.*, 2014). Choline oxidation peak was noticed at about 0.47 V from CV measurement. Choline was determined on modified CPE using amperometric measurement with working potential set at 550 mV over 0.25-6.98 mM linear range. A 60.5 $mAmol^{-1}Lcm^{-2}$ sensitivity and 25.4 µM LoD was obtained (Sattarahmady *et al.*, 2014). The sensor proved simple, stable, sensitive, repeatable and reproducible (Sattarahmady *et al.*, 2014). However, there was no demonstration of a practical application for choline detection at the designed sensor. Summary of the surveyed electrochemical methods (biosensor, electrochemical at liquid/liquid interface and electrochemical sensor) is seen in Table 2.2.

Table 2.2: Electrochemical methods of different working electrodes for choline detection.

Choline biosensors	Techniques	Linearity (µM)	LoD (µM)	Application	Ref
Phosphlipase D bioreactor coupled with a choline amperometric sensor	Amperometry	10-500	20	Milk/dietary supplement	(Pati *et al.*, 2005)
Microwave hydrolysis and a choline biosensor	Amperometry	5-50	NR	Milk, soy lecithin, egg powder, yolk and infant formula	(Panfili *et al.*, 2000)
Flow injection immobilized enzyme reactor coupled to a selective hydrogen peroxide amperometric sensor	Flow injection system	Upto 1000	7	Milk	(Pati *et al.*, 2007)
Chox/GNP_4/MWCNT/ GCE	EIS	3-120	0.6	Milk	(Magar *et al.*, 2017)
Chox/MWCNT/Pt	Amperometry	5-100	0.7	Serum	(Song *et al.*, 2006)
ChOx-PDDA-PB-FePO4/GCE	Amperometry	2-3200	0.4	NA	(Zhang *et al.*, 2012)
PVA/Au/ChOx/Pt	Amperometry	20-400	10	NA	(Ren *et al.*, 2009)
MWCNT/PANI/GCE/ CHOD	Amperometry	1-2000	0.3	NA	(Qu *et al.*, 2005)
ChOx/MnO2/Chit/GC	SWV	10-2100	NR	NA	(Bai *et al.*, 2007)
ChOx/PDDA)n/(PVS/PAA)3/MWCNTs/Pt	Amperometry	0.5-100	0.2	N/A	(Qin *et al.*, 2009)
MWCNTs-GNP-ChOx-PDDA/Pt	Amperometry	1-5000	0.3	NA	(Qin *et al.*, 2010)
ChOx-PBBInS-GS/Au	Amperometry	0.1-800	0.02	NA	(Chen *et al.*, 2013)
PDDA/ChOx/ZnO/MW CNTs/PGE	Amperometry	1-800	0.3	Plasma	(Zhang *et al.*, 2014)
ChOx/HRP/FC/CRGO/ GCE	Amperometry	1-400	0.35	NA	(Deng *et al.*, 2013)

Choline biosensors	Techniques	Linearity (µM)	LoD (µM)	Application	Ref
GC/SWCNT/ISM	Potentiometric	10-100	0.398	Biological	(Ampurdanés *et al.*, 2009)
ChOx/RTIL/NH2-MWCNT/GCE	Amperometry	6.9-670	2.7	NA	(Sajjadi *et al.*, 2012)
ChOx/Ni/PB/BG/GCE	Amperometry	0.45-100	0.45	NR	(Keihan *et al.*, 2014)
AChE-ChO/c-MWCNT/ZrO2NPs/GCE	Amperometry	0.05-200	0.01	Serum	(Pundir *et al.*, 2012)
Non- choline biosensors					
MCPE/NiO	Amperometry	250-6980	25.4	NA	(Sattarahmady *et al.*, 2014)
Electrochemistry at liquid/liquid interface					
Nano-W/Gel/SIM	DSPV	1-100	0.92	Urine, blood	(Xie *et al.*, 2017)

Note: No application (NA), not reported (NR)

2.7.2 Dopamine

Dopamine, a substituted phenethylamine addressed as 2-(3,4-dihydroxypheny) ethylamine is a precursor for norepinephrine and epinephrine (Klein *et al.*, 2019). Figure 2.4 gives the molecular structure of dopamine.

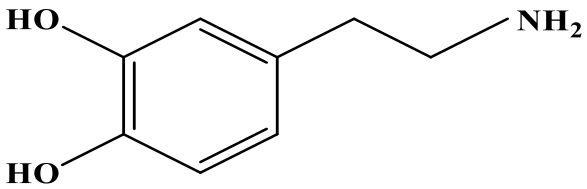

Figure 2.4: Chemical structure of dopamine.

Dopamine (DA) is one of the key catecholamine neurotransmitter found in the human central nervous system. Dopamine is catecholamine due to the presence of catechol, phenyl group with two hydroxyl group and an ethylamine side chain (Liu *et al.*, 2019; Liu *et al.*, 2014). DA is

secreted in the midbrain and hypothalamus by neurons (dopaminergic), and from tyrosine by an enzyme called tyrosine hydroxylase (Klein *et al.*, 2019; Ma *et al.*, 2012). DA plays a crucial role in cognition, memory (working and learning), concentration, motor control, and motivation (Immanuel *et al.*, 2019; Klein *et al.*, 2019). An imbalance of dopamine in the human body causes Parkinson disease, and schizophrenia disease, respectively. The symptoms are with fatigue, apathy, moodiness, insomnia, memory loss, low motivation with a challenge in concentrating as symptoms (Gao *et al.*, 2013; Jiang *et al.*, 2015; Ma *et al.*, 2012; Manbohi & Ahmadi, 2019; Zhang *et al.*, 2016). DA concentration level increases via frequent exercise, sufficient sleep, meditation, supplements and intake of food rich in tyrosine with banana, avocados, almond, eggs, beans, fish and chicken as examples (Banjari *et al.*, 2014).

2.7.2.1 Health importance of dopamine

DA plays a pivot role in the function of renal, mammalian central nervous (CNS), hormonal and cardiovascular systems, and in the interaction between anti-natriuretic and natriuretic systems in renal system. DA modulates fluid homeostasis, blood pressure, and redox balance (between the free radicals and highly reactive oxygen species) (Choi *et al.*, 2015). Imbalance of the redox process results in hypertension (increased blood pressure) which is a significant risk for stroke, heart and kidney failure (Choi *et al.*, 2015). In the CNS, dopamine, modulates cognition, learning, motor control, pain perception, mood, reward, working memory, and reproductive behaviours (Klein *et al.*, 2019; Rubí & Maechler, 2010). In the hypothalamus, dopamine neurons influence the secretion of prolactin by the anterior pituitary, and this promotes the secretion of insulin (Banjari *et al.*, 2014). Also, in the cardiovascular system, dopamine controls cardiovascular processes (heart/blood pressure rate, shock), and impedes the secretion of pro-coagulant Von Wille brand factor from the endothelial cells as high will brand factor level is a risk factor for heart disease (coronary) (Banjari *et al.*, 2014). Besides, DA in the cardiovascular system reduces vascular permeability which is the ability of the blood vessels walls to permit the flow of small molecule (nutrient, water, drugs etc) in and out of the vessels (Banjari *et al.*, 2014). DA in the hormonal system regulates the function of pancreatic endocrine and the action of insulin in various tissues (Banjari *et al.*, 2014).

2.7.2.2 Methods used in dopamine detection

There is an on-going interest in the design of different techniques for dopamine detection looking at its importance in human systems. Methods used for DA detection in pharmaceutical and biological samples include; chromatography HPLC/FD/UV, (HPLC/ED, HPLC-CL, in

tissues and serum (Muzzi *et al.*, 2008; Van Valkenburg *et al.*, 1982; Wu *et al.*, 2016), flow injection (Zhu *et al.*, 2002), chemiluminescence (Guo & Dong, 2005; Li *et al.*, 2011; Zhao *et al.*, 2010), colourimetry (Zheng *et al.*, 2011), fluorimetry (Chen *et al.*, 2011), and capillary electrophoresis (Park *et al.*, 1999). in DA injection, urine, and serum as examples owing to their speed, sensitivity, selectivity. Some of the reported chromatography methods include; the use of HPLC combined with mass spectrometry detection containing methanol-3 gl acetic acid pH 2.8 and 0.75 mL/min flow rate to determine DA in bovine chromaffin cells (Carrera *et al.*, 2007). Chromatographic separation was conducted via direct injection of the sample into the HPLC system with a reversed analytical column of 150 mm 4.6 id with no sample pre-treatment. DA was detected by atmospheric pressure chemical ionization mass spectrometry with signals recorded in the chosen ion mode and 6.474 ng/ml LoD with 0.301 ng/ml limit of quantification was found (Carrera *et al.*, 2007).

Also, high-performance liquid chromatography with fluorescence and ultraviolet detection (HPLC/FD/UV) was applied in the detection of DA within 66 pmol –211 nmol and 6.25 –423 nmol linear range for fluorescence and UV detection following the derivatization of samples with 1,2-diphenylethylenediamine (DPE) (Muzzi *et al.*, 2008). Emitted fluorescence from DA was detected by measuring the native fluorescence using fluorimetric detector while UV detector though less sensitive finally used to exclude interfering substance and naturally fluorescent (Muzzi *et al.*, 2008). In a different experiment, reversed-phase high-performance liquid chromatography with fluorescence detection (HPLC/FD) was utilized for DA determination in porcine after pre-column derivatization using O-phthaladehyde (OPA) and 2-mercaptoethanol (2-ME), which transform DA to a substituted indole, thus permitting fluorescence detection (Zhao *et al.*, 2011). The method in a linear range of 0.001 – 8 μg/ml gave 4 μg/kg LoD. In addition, high sensitive HPLC with silver (III) complex ($[Ag(HI0_6)_2]^{5-}$)-luminol chemiluminescence detection was employed for DA investigation in the brain in the linear range between 3.8-624 ng/ml with 1.9 ng/ml LoD and percentage recovery was 96.1% (Wu *et al.*, 2016). HPLC with electrochemical detection and gas chromatography combined with mass spectrometry in the single ion monitory mode (HPLC/ECD and GC-MS-SIM) was likewise employed for DA determination in food sample (soy sauce and banana pulp) (Duncan *et al.*, 1984). Obtained DA concentration for GS-MS-SIM and HPLC-ED in soy sauce/ banana pulp was 796, 2.1×10^3 and 2.13×10^5 and 6.63×10^5 pmol/kg with the assay (Duncan *et al.*, 1984).

A spectrophotometry assay was employed to determine DA using surface plasmon resonance band of silver nanoparticles which allows quantitative spectrophotometric determination in the company of polyvinylpyrrolidone stabilizing agent (Nezhad *et al.*, 2010). The proposed method with a linear range from 3.2×10^{-6} – 2.0×10^{-5} M and maximum absorbance at 440 nm wavelength yielded 9.7×10^{-7} M LoD (Nezhad *et al.*, 2010). Also reported assay for determination of DA in the pharmaceutical injection is flow injection assay based on its inhibition of electrochemiluminescence luminal Under experimental condition (0.7 V electrode potential, luminal concentration, pH 11of luminal, the concentration of potassium chloride, and 2.0 mL/min flow rate), the intensity of electrochemiluminescent reduced with linear DA concentration range 5.0×10^{8} – 1.0×10^{-5} nmol/l and 30 nmol/l limit of detection (LoD) (Zhu *et al.*, 2002). Capillary electrophoresis with 257 nm excitation and native fluorescence detection was employed for the study of DA within 1400- 120 nm linear range (Park *et al.*, 1999). Determination of DA at designed assay was achieved by maintaining separation conditions (optimization of pH independently within the separation capillary and detection region, and 50 mm of borate buffer pH 7.8) and an acidified buffer sheath (Park *et al.*, 1999). Microchip electrophoresis with chemiluminescence resonance energy transfer based on chemiluminescence detection was employed for DA determination with 3.5×10^{-8} – 350×10^{-8} and LoD of $10^{3}\times 10^{-8}$ M (Zhao *et al.*, 2010).

Electrogenerated chemiluminescence at carbon nanotube /Nafion-Ru(bpy)2/3+ composite film modified glassy carbon electrode (Guo & Dong, 2005) and also chemiluminescence at quantum sized gold nanoclusters (AuNCs ECL) was used for DA determination (Li *et al.*, 2011). DA determination in the former was in the linear range of 1.6×10^{-7} to 3.2×10^{-5} M in 0.1 M phosphate buffer solution (PBS) pH 7.5. A colourimetric biosensor with a recognition element (58-mer dopamine –binding aptamer) and unmodified gold nanoparticles as the probe was designed for DA detection (Zheng *et al.*, 2011). LoD of 3.6×10^{-7} M was found using the designed colourimetry with a linear range of 5.4×10^{-7} – 5.4×10^{-6} M (Zheng *et al.*, 2011). DA was quantitatively determined based on GO-based photoinduced charge transfer (PCT) label-free near-infrared fluorescent biosensor in buffer solution (5.0 mM Tris-HCl pH 5) with DA linear range of 0 –50 μM. A 94 nM LoD was found with 98 -115% (Chen *et al.*, 2011).

Currently, dopamine is widely being detected via electrochemical methods owing to the fascinating properties of electrochemical methods with instances of a graphene oxide modified glassy carbon electrode (GME) in 0.01 mM DA with supporting electrolyte (0.1 M PBS, pH 7)

using cyclic voltammetry (CV) over 2.5 – 100 μM concentration range and LoD, correlation coefficient values of 0.5 μM and 0.9984 (Ma *et al.,* 2012). The designed sensor was sensitive, selective to DA and applicable for DA determination in drug and serum with percentage recovery range (98-103 and 96.2 – 100.2) for respective samples (Ma *et al.*, 2012). Vanadium-substituted polyoxometalates, copper oxide and chitosan–palladium (PEI/[(P2W17V–CuO)/(CS–Pd)]7/(P2W17V–CuO) composite film modified electrode designed by layer-by-layer self-assembly assay was applied for the determination of DA (Zhang *et al.*, 2016). Values of sensitivity, LoD and regression of the electrode using amperometry were 0.92 $\mu A/\mu M^{-1}$, 0.045 μM and 0.99861 with 0.25 –217 μM linearity (Zhang *et al.*, 2016). The developed sensor was sensitive, selective, reproducible, stable, reliable, and practicable for the detection of DA in blood serum yielding a good range of percentage recovery (97.2 –100.27) (Zhang *et al.*, 2016). Furthermore, DA was determine by a fabricated modified polypyrrole-mesoporous silica molecular sieves film (PPy-MCM-48/Au) gold electrode in 0.1M PBS pH 7.4 containing 1 mM DA using cyclic and square wave voltammetry in 10-1200 μM and 2–250 μM dynamic linear range, LoD 2.5 μM; 0.7 μM, and 0.9989; 0.9996 correlation coefficient respectively (Zablocka *et al.*, 2019).

Microfluidic sensor based on paper (EμPAN) was applied in the investigation of DA using differential pulse voltammetry (DPV) technique (Manbohi & Ahmadi, 2019). Concentration linearity was from 0.5 -120 μM and 0.01 μM LoD, 0.9902 regression value was found. The designed sensor was found applicable in real sample analysis for DA with 98-105recovery (Manbohi & Ahmadi, 2019). DA was also investigated using an immobilized mercapto-terminated binuclear copper (II) complex on gold electrode surface employing the use of DPV over detection concentration range of 0.2 –30 μM yielding LoD and regression values of 0.08 μM and 0.9978 (Jiang *et al.,* 2015). Proposed electrode was successfully applied for DA investigation in urine and dopamine hydrochloride injection yielding a range of percentage recovery (92-102) for urine and (96.2 –102) for dopamine hydrochloride injection (Jiang *et al.*, 2015). Graphene oxide modified electrode (GO/GCE) was over 1.0 – 15 μM concentration range (Gao *et al.,* 2013). Respective LoD and regression values were found to be 0.27 μM 0.9980 (Gao *et al.*, 2013). A reduced graphene oxide/palladium nanoparticles composites modified glassy carbon electrode (GCE-RGO-PdNPs) was likewise employed for sensing of DA in saturated 0.5 M H_2SO_4 pH 7 using linear square voltammetry (LSV) (Palanisamy *et al.,* 2013). The electrode in a linear concentration range of 1–150 μM gave 0.233 μM LoD and 0.997 correlation coefficient. Application of the electrode on dopamine hydrochloride injection yielded a range of

97.5 –100.2 recovery (Palanisamy *et al.*, 2013). An electrochemical sensor (poly (O-phenylenediamine) electrochemically reduced graphene oxide modified electrode-PoPD/E-RGO/GCE) was applied for DA determination using DPV in 10 – 400 μM linear detection range (Liu *et al.*, 2014). A 0.996 and 7.5 μM were obtained as respective regression and LoD values. The developed sensor was successfully applied for DA real sensing in urine. A range of 94.6 - 106.7 recovery was found indicating the reliability of electrode for real DA sensing (Liu *et al.*, 2014).

In another study, tyrosinase-chitosan, and reduced graphene oxide modified screen-printed carbon electrode (tyrosinase/chitosan/rGO/SPCE) was used for DA detection using CV with a broad linearity (0.1 – 500 μM) and 20 nM LoD (Liu *et al.*, 2019). Recovery range (93.0 – 97.6) proved the efficacy of the modified electrode of DA detection in the real sample (Liu *et al.*, 2019). A different experiment reported the use of nanocomposites of high conducting polymer (polyaniline) modified glassy carbon electrode (GCE/PANI/NiO, GCE/PANI/ZnO, GCE/PANI/Fe_3O_4) for electrochemical determination of DA at physiological pH 7.0 using DPV. Linear range of DA detection was from 2.0×10^{-5} – 2.4×10^{-6} M with 0.0153, 0.0166 and 0.0176 μM LoD for the respective electrodes (Fayemi *et al.*, 2018). Designed electrodes were employed for real sample (dopamine hydrochloride injection) analysis and recovery of 102.5, 104.3 and 100.6 was found at the various electrodes, respectively (Fayemi *et al.*, 2018).

In addition, a nanocomposites of iron oxide reduced graphene-modified GCE (Fe_3O_4/rGO/GCE) was used for DA detection using DPV in concentration range from 0.5 – 100 μM (Peik-See *et al.*, 2014). A sensitivity and LoD of 2.733 μA/μM and 0.12 μM was found (Peik-See *et al.*, 2014). Besides, an electrochemical sensor fabricated with nanocomposites of zinc oxide and copper oxide decorated with polypyrrole on glassy carbon electrode (ZnO-CuxO/PPy/GCE) was utilized for detection of DA in 0.1 M Britton –Robison buffer solution (B-R) pH 4.0 (Ghanbari & Hajheidari, 2015). The developed sensor in the linear range of 1–130 μM gave 0.04 μM LoD with 09922 regression value (Ghanbari & Hajheidari, 2015). The modified electrode was found applicable for DA determination in injectable medicine yielding a 98.5 –101.1 percentage recovery (Ghanbari & Hajheidari, 2015). Table 2.3 shows a summary of some of the reported electrochemical method.

Table 2.3: Detection of Dopamine at different working electrodes/electrochemical sensors.

Working electrodes	Methods	Lineraity (µM)	LoD (µM)	Ref
GME	CV	2.5 - 100	0.5	(Ma *et al.*, 2012)
[PEI/P2W17V-CUO	CV	0.25 - 217	0.045	(Zhang *et al.*, 2016)
PPy-MCM-48/Au electrode	CV SWV	10 - 1200 2 - 250	2.5 0.7	(Zablocka *et al.*, 2019)
EUPAN	DPV	0.5 - 1 20	0.01	(Manbohi & Ahmadi, 2019)
GO/GCE	DPV	1.0 - 15.0	0.27	(Gao *et al.*, 2013)
Binuclear CUO /Au	DPV	0.2 - 30	0.08	(Jiang *et al.*, 2015)
RGO/Pd-NPs	LSV	1 - 150	0.233	(Palanisamy *et al.*, 2013)
Tyrosinase/Chitosan/rGO/SPCE	CV	0.1 - 500	0.02	(Liu *et al.*, 2019)
GCE/PANI/NIO	SWV	0.2 - 24	0.015	[79]
GCE/PANI/ZnO	SWV	0.2 - 24	0.016	(Fayemi *et al.*, 2018)
GCE/PANI/Fe_3O_4	SWV	0.2 - 2 4	0.017	(Fayemi *et al.*, 2018)
GCE/MWCNT/NiO	SWV	4×10^{-5} - 6.25	7.9×10^{-6}	(Fayemi OE, 2015)
GCE/MWCNT/ZnO	SWV	4×10^{-5} - 6.25	0.374	(Fayemi OE, 2015)
GCE/MWCNT/Fe_3O_4	SWV	4×10^{-5} - 6.25	1.39	(Fayemi OE, 2015)
Fe_3O_4/rGO/GCE	DPV	0.5 - 100	0.12	(Peik-See *et al.*, 2014)
ZnO-CuxO/PPy/GCE	DPV	1 - 135	0.04	(Ghanbari & Hajheidari, 2015)

2.7.3. Serotonin

Serotonin, often called 5-hydroxytryptamine (5-HT) is one of the major neurotransmitters and bioactive component found in animals and food with $C_{10}H_{12}N_2O$ molecular formula and 176.215 $gmol^{-1}$ molecular mass (Huang & Mazza, 2011; Reddaiah *et al.*, 2018; Sidhu & Zafar, 2018; Szeitz & Bandiera, 2018). Figure 2.5 shows the molecular structure of serotonin.

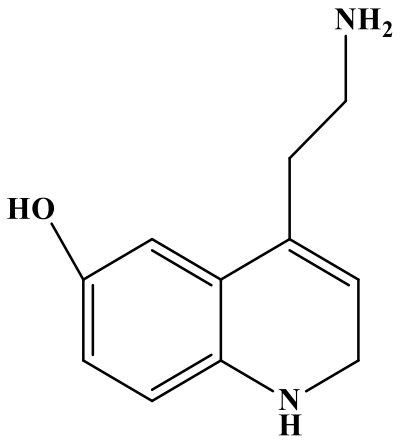

Figure 2.5: Chemical structure of Serotonin.

Serotonin (5-HT) is located in central nervous system (CNS), gastrointestinal tracts of the digestive system, blood, and platelets (Babaei *et al.*, 2013; Fayemi *et al.*, 2017; Mazloum-Ardakani & Khoshroo, 2014). Serotonin is a bioactive component found in fruits (Banjari *et al.*, 2014; Sidhu & Zafar, 2018; Tekes, 2008) and it plays a significant role in wounds healing, appetite, sexuality, mood (anxiety, happiness, fear, aggression and alertness), and it induces sleep (Babaei *et al.*, 2013; Fayemi *et al.*, 2017; Mazloum-Ardakani & Khoshroo, 2014). Summarily, serotonin has great impact on human well-being. Serotonin deficiencies in the body system leads to insomnia, eating disorders, depression fibromyalgia, anxiety, migraine head ache, post menstrual syndrome (PMS), and hormone dysfunction (Fayemi *et al.*, 2017; Filik *et al.*, 2014; Özcan & İlkbaş, 2015). Low levels of serotonin in the body system could be ascribed to poor digestion of food body metabolism and unbalanced diet, hormonal changes, drugs with caffeine, alcohol and nicotine content, and stress (Filik *et al.*, 2014; Huang & Mazza, 2011; Reddaiah *et al.*, 2018; Sidhu & Zafar, 2018). In the body, serotonin concentration could be boosted by exercise, high water consumption and eating tryptophan rich food (bananas, eggs particularly the yolks, cheese, pineapples, salmon, soy products, nuts, and seeds) (Banjari *et al.*,

2014; Szeitz & Bandiera, 2018). 5-HT is believed to be biosynthesized from tryptophan by L-aromatic amino acid decarboxylase (Banjari *et al.*, 2014; Klein *et al.*, 2019).

2.7.3.1 Health importance of serotonin

In vascular biology, serotonin (5-HT) regulates vascular impediment, blood pressure, haemostasis, and function of the platelet by covalent attachment of an independent receptor to proteins (Berger *et al.*, 2009). In the role of the heart, serotonin controls electrical conduction, valvular closure and improvement of the post –MI. 5-HT is also is involved in cardiac valvulopathy resulting from appetite suppressant fenfluramine within the human gastrointestinal system (Berger *et al.*, 2009). Serotonin regulates the secretion of pancreatic enzymes in the intestine. Serotonin influences the reshaping of the pulmonary artery by explicit covalent fitting into intracellular signalling protein in smooth vascular cells (Berger *et al.*, 2009). Also, 5-HT helps maintain energy balance in the endocrine system and metabolism, regulates the development of the mammary gland, the release of milk in the mammary gland and also controls epithelial tight joints (Berger *et al.*, 2009). Serotonin modulates breathing; respiratory drive through effects on brainstem regulatory control centres, pain perception, and nociceptive processing at multiple levels within the central and peripheral nervous system (Berger *et al.*, 2009). It is therefore of great interest to measure serotonin in body fluids, food and pharmaceutical samples.

2.7.3.2 Methods used for serotonin detection

Different techniques are being employed for serotonin detection in various samples (biological, aquatic and plants). For example, chromatography methods such as HPLC-FL/ED, UPLC-MS/MS, HPLC-ED was reportedly used in detecting serotonin in urine, cerebrospinal fluids, gastrointestinal tissue, plasma and fruits respectively (Chau & Patel, 2009; Huang & Mazza, 2011; Suominen *et al.*, 2013; Zydroń *et al.*, 2005). The use of high-performance liquid chromatography with electrochemical detection (HPLC/ED) was reported for serotonin detection. The separation was carried out on a supercoil LC 18DB stationary phase with mixtures of 48 mM citric acid, 28 mM sodium phosphate dibasic, 0.027 nM Na_2EDTA, and 3 % methanol (pH 3.18) as mobile phase at 25 °C and optimal potential of 0.65 V. 3.7 pg/mol limit of quantification over 10 - 200 pg/mol linear range was obtained (Tekes, 2008). A reversed-phase HPLC with fluorescence detection (HPLC-FD) following homogenization and centrifugation of supernatant over the range 0.35 - 7 ng of 5-HT. LoD of the procedure was found to be 0.35 ng (Umeda *et al.*, 2005).

Enzyme immunoassay (EIA) based on the competition of an enzymatic tracer (N-succinyl 5-HT-acetylcholinesterase) and N-succinyl-glycinanide-serotonin (N-SGA-5HT) acquired through the acylation of 5-HT in a sample of interest (Chauveau *et al.,* 1991). LoD (0.5 $nmol^{-1}$) over concentration range 5 - 1000 $nMol^{-1}$ with 99 recovery was found (Chauveau *et al.,* 1991). Radioimmunoassay (RIA) was reportedly used for detection of serotonin in cerebrospinal fluid, plasma and serum. A minimum detectable 5-HT concentration within the range of 5 - 14 nM was 2 nM/l in a 200 µl sample with 109 and 101 percentage recovery for cerebrospinal fluid and plasma, respectively (Engbaek & Voldby, 1982). Capillary electrophoresis–electrospray ionization-time-of-flight spectrophotometer (CE-TOFMS) using a solid-phase extraction on homogenized mode cation-exchange solvents [88]. LoD of 0.15 µM was obtained with % recovery greater than 71.6 (Peterson *et al.*, 2004). These methods are tedious, and labour intensive, especially when derivatization of analytes of interest is needed. It also entails multiple steps, extraction and separation from interfering compounds (Jin *et al.*, 2010; Pati *et al.,* 2007).

There are current reports on the utilization of electrochemical sensor for 5-HT detection since they are reliable, fast, less expensive and highly sensitive with an easy instrumentation and elimination of separation, extraction and derivatization steps (Karabiberoğlu *et al.,* 2016). Electrochemical detection of serotonin have been reported at metal oxide nanoparticle/MWCNT modified glassy carbon electrode (GCE/MWCNT/NiO, GCE/MWCNT/ZnO, GCE/MWCNT/Fe_3O_4) in PBS pH 7 using SWV in dynamic range for 5-HT detection from 5.98×10^{-3} – 62.8 µM. LoD (118, 129, and 166 nM) and sensitivity (9.96, 29.53, 13.93 µA/µM) values were found at respective electrodes (Fayemi *et al.,* 2017). A range of percentage recovery for 5-HT sensing in the real sample (urine) at GCE/MWCNT/NiO, GCE/MWCNT/ZnO, GCE/MWCNT/Fe_3O_4 was 104-114, 96-104 and 92-98 respectively (Fayemi *et al.*, 2017).

Also, serotonin was detected on polypyrrole-3-carboxylic acid modified pencil graphite electrode (p(CP3CA-PGE) by adsorptive differential stripping voltammetry (AdDPSV) in PBS pH 5 as supporting electrolyte with dynamic serotonin concentration range 0.01 - 1.0 µM (Özcan & İlkbaş, 2015). Regression and LoD values were found to be 0.9917 and 0.0025 µM [83]. The designed sensor was successfully applied for 5-HT investigation in a biological sample (blood and urine), and a percentage recovery in the range of 97.7 – 100.6 and 93.8 - 97.4 was obtained accordingly (Özcan & İlkbaş, 2015). More so, 5-ht was investigated with poly-alizarin red S multi-walled carbon nanotubes-glassy carbon electrode (Poly-AzrS-MWCNTs-GCE) in 0.1 M

PBS pH 6 by differential pulse voltammetry (DPV) (Reddaiah *et al.,* 2018). A 0.18 μM LoD, 1.752 μM LoQ with a dynamic range from 0.5 - 11 μM was obtained. The designed electrode was used for 5-HT determination in blood serum, and a good range of percentage recovery (97.35 - 98.85 %) was obtained (Reddaiah *et al.,* 2018).

In another study, 5-HT was detected at polysafranine glassy carbon electrode (Poly(SFO)-GCE) in acetate buffer pH 4 by square wave adsorptive stripping voltammetry (SW-AdSV) with 0.03 - 1 μM 5–HT linear concentration range, 5×10^{-3} μM LoD and 0.9993 correlation coefficient (Filik *et al.,* 2014). Fabricated sensor was utilized for detecting 5-HT in blood serum, and a recovery range of 96 - 109.8 was obtained (Filik *et al.,* 2014). A cobalt hydroxide nanoparticles/multi-walled carbon nanotubes modified carbon ionic liquid electrode (Nafion/$Co(OH)_2$-MWCNTs-CILE) was likewise applied in detecting serotonin by DPV (Babaei *et al.,* 2013). Anodic oxidation potential 0.35 V and 0.023 μM limit of detection in concentration range of 0.05 - 75 μM was obtained (Babaei *et al.,* 2013).

Besides, serotonin was detected at a carbon nanofibers modified electrode (CNF/GCE) using DPV from 1 - 10 μM linearity (Rand *et al.,* 2013). The electrode yielded 250 nM LoD for 5-HT with 0.9970 correlation coefficient (Rand *et al.,* 2013). A different study reported the detection of 5-HT with nanocomposites of benzofuran derivative functionalized multi-walled carbon nanotubes and ionic liquids on glassy carbon electrode (IL-DC-CNT/GCE) in 0.1 M PBS pH 7 with 5 - 900 μM linear dynamic 5-HT concentration range (Mazloum-Ardakani & Khoshroo, 2014). The sensor gave a 2 μM LoD value, and a good percentage recovery (99.3 - 102.0 in serum (Mazloum-Ardakani & Khoshroo, 2014). Also, different graphene-modified electrodes (GO/GCE, RGO1/GCE, RGO2/GCE, RGO3/GCE, GO-SH/GCE, and GO-S-$(CH_2)_4$-SH/GCE) in 0.1 M PBS pH 7.4 using the amperometric technique at an applied 0.35 V potential (Kim *et al.,* 2012) were applied for serotonin detection. LoD with sensitivity values at the various electrode for 5-HT 1 - 100 μM concentration linear range were 0.18, 0.032, 0.046, 0.052, 0.038 and 0.16 μM with 0.568, 0.626, 1.155, 0.872, 0.824, 0.815 $mAcm^{-2}/mM^{-1}$ respectively (Kim *et al.,* 2012).

Also, reducing graphene oxide/PANI/gold nanoparticles modified GCE was used to detect 5-HT using DPV electroanalytical technique (Xue *et al.,* 2014). LoD (11.7 $nMol^{-1}$) and regression value (0.998) over 0.2 - 10 μM linear range was found. The designed sensor was successfully applied for 5-HT detection, and a percentage recovery range of 98.7 - 102.5 was obtained (Xue *et al.,* 2014). 5-HT was likewise detected at a calixarene-based voltammetric sensor by SWV

over a linear range of 1.0×10^{-7} 1.0×10^{-5} mol^{-1} with an LoD 3×10-8 Mol^{-1} (Wang *et al.,* 2013). Efficacy of the electrode was proved by determining serotonin in blood serum which gave 98-114recovery range (Wang *et al.,* 2013). In addition, serotonin was detected by a GCE doped with electrochemically reduced graphene oxide (GCE/ERGO-P) in 0.1 MPBS pH, 7.4 using DPV across linear range of 0.1 – 300 μM and 4.9×10-3 μM LoD with 0.9903 correlation coefficient was obtained (Han *et al.*, 2014), and GCE modified with graphene oxide grafted poly(lactic acid) with palladium nanoparticles (GCE-GO-g-PLA-Pd) in 0.1 M PBS pH 7.4 by amperometry measurement at an applied potential of 0.35 V over a dynamic 5-HT linear concentration range of 0.1 - 100 μM. Designed sensor gave 0.996 correlation coefficient and 0.08 μM LoD (Han *et al.*, 2013). Summary of the different electrochemical sensor is presented in Table 2.4.

Table 2.4: Electrochemical methods of different working electrodes for 5-HT detection.

Working Electrodes	Methods	Linearity(µm)	LoD	Ref
GC-GO-g-PLA-Pd	Amperometry	0.1 - 100	0.08	(Han *et al.*, 2013)
GCE/Poly-Arzrs/MWCNT	DPV	0.5 – 11	0.18	(Reddaiah *et al.*, 2018)
CNF electrode	DPV	1 – 10	0.25	(Rand *et al.*, 2013)
Calixarene-based voltammetric sensor	SWV	0.1 – 10	0.03	(Wang *et al.*, 2013)
P(P3CA)/PGE	AdDPSV	0.01 - 0.1	0.002	(Özcan & İlkbaş, 2015)
Poly(SFO)/GCE	SW-AdSV	0.03 – 1	5×10^{-3}	(Filik *et al.*, 2014)
IL-DC-CNT/GC	DPV	5 – 900	2	(Mazloum-Ardakani & Khoshroo, 2014)
GCE-MWCNT-NiO	SWV	5.98×10^{-3} - 62.8	0.118	(Fayemi *et al.*, 2017)
GCE-MWCNT-ZnO	SWV	5.98×10^{-3} - 62.8	0.129	(Fayemi *et al.*, 2017)
GCE-MWCNT-Fe3O4	SWV	5.98×10^{-3} - 62.8	0.166	(Fayemi *et al.*, 2017)
GO/GCE	Amperometry	1 – 100	0.18	(Kim *et al.*, 2012)
RGO/GCE	Amperometry	1 – 100	0.032	(Kim *et al.*, 2012)
RGO2/GCE	Amperometry	1 – 100	0.046	(Kim *et al.*, 2012)
RGO3/GCE	Amperometry	1 – 100	0.052	(Kim *et al.*, 2012)
GO-SH/GCE	Amperometry	1 – 100	0.038	(Kim *et al.*, 2012)
GO-S-(CH2)4-SH/GCE	Amperometry	1 – 100	0.16	(Kim *et al.*, 2012)
GC-rGO/PANI-AuNPs	Amperometry	1 – 100	0.011	(Xue *et al.*, 2014)
GC-ERGO-P	Amperometry	1 - 100	0.03	(Han *et al.*, 2014)

2.8 Electrochemical sensor studies

Electrochemical sensor studies are conducted in an electrochemical cell as illustrated by Figure 2.6), which comprises the electrodes and electrolyte (Koyun *et al.*, 2012; Nnamchi & Obayi, 2018; Power & Morrin, 2013) using electrochemical methods that measures current, potential, and resistance and relate them to the concentration of analyte, which is displayed inform of electrical signals on the monitor. There are three types of electrodes which are vital in the performance of electrochemical sensor; the working, counter and reference electrode.

The **working electrode** (WE) also known as sensing electrode is the site of reaction of analytes within an electrochemical system and it is sensitive to the concentration of the analytes (Aoki & Chen, 2018; Honeychurch, 2012; Koyun *et al.*, 2012). Working electrode could be called the anode or cathode depending on the reaction (oxidation or reduction) occurring at the electrode. Platinum, glassy carbon, gold, silver and carbon paste electrodes are examples of the working electrode. An excellent WE possesses a good signal to noise ratio, it's response is reproducible with high stability (electrical), it is economical, available, and less toxic (Aoki & Chen, 2018; Honeychurch, 2012; Koyun *et al.*, 2012). The **counter electrode** also known as the auxiliary electrode regulates the possibility of applying current to the working electrode (Aoki & Chen, 2018; Honeychurch, 2012; Koyun *et al.*, 2012) .

Reference electrode helps to enhance the performance of the sensor by maintaining a stable and constant potential applied to the WE (Aoki & Chen, 2018; Honeychurch, 2012; Koyun *et al.*, 2012). Reference electrode is placed in proximity with the sensing electrode (WE) so as to reduce drop caused by cell resistance (iR). Ag/AgCl and saturated calomel electrode (SCE) are the commonly known reference electrodes. The most frequently used is the Ag/AgCl electrode in high concentration of KCl due to stable voltage at the interfaces of Ag-AgCl and AgCl-KCl via rapid charge transfer steps irrespective of current density magnitude. The stable voltage is supported with high concentration of KCl (Aoki & Chen, 2018; Honeychurch, 2012; Koyun *et al.*, 2012).

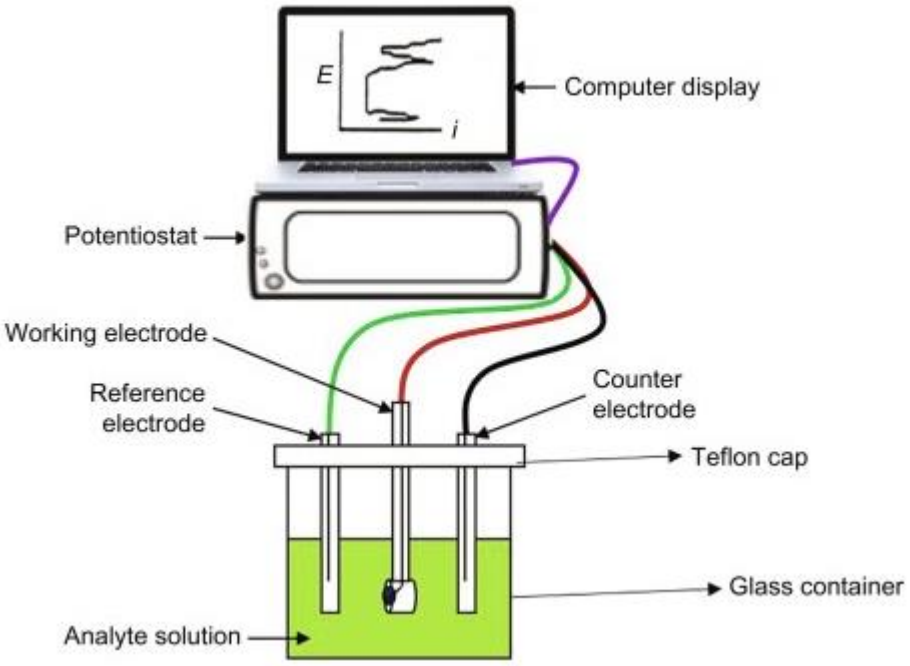

Figure 2.6: Electrochemical cell system (Nnamchi & Obayi, 2018).

The electronic device that drives these three electrodes is called a potentiostat, which concurrently generates an appropriate voltage and determine the current involved in the system (Aoki & Chen, 2018). The potentiostat has three terminals. The first is void of current with a voltage follower for RE, current feeder at CE and current converter (converts current to potential) (Aoki & Chen, 2018). **Electrolytes** are chosen based on the type of analytes of interest. The electrolyte aids the promotion of reaction within the cell and transport efficient ionic charge across the electrodes. Good electrolytes must be compatible with materials within the cells, it should not be volatile as that could lead to decline in the sensor signal and it should form a stable reference potential with the reference electrodes (Koyun *et al.*, 2012).

Electroanalytical methods employed in electrochemical studies include, cyclic voltammetry, square wave voltammetry, differential pulse voltammetry, chronoamperometry, electrochemical impedance spectroscopy (EIS).

2.8.1 Electrochemical methods

Experiments conducted using electrochemical methods are aimed at obtaining a current response which corresponds to concentration of analyte of interest. This aim is achieved by observing transferred electron (s) during the redox reaction of analyte. $Red - ne^- \rightleftharpoons Ox$

2.8.1.1 Cyclic voltammetry

Cyclic voltammetry (CV) is a vital and commonly used electrochemical technique in obtaining quantitative information about electrochemical reactions. In principle, it works by varying an applied potential at a working electrode at some scan rate (v) in both forward and reverse direction while observing the current (Honeychurch, 2012). Cyclic voltammetry is used in the investigation of redox processes (oxidation and reduction reaction), the stability of reactions, the diffusion coefficient of analytes, and rate constant (Mirceski *et al.*, 2018). CV measurement is carried out in quiescent (unstirred) solution to ensure diffusion control (Honeychurch, 2012). The curve obtained by measuring the current at the working electrode during the potential scans is called a cyclic voltammogram (Mirceski *et al.*, 2018) as shown in Figure 2.7a,b. The following Epa, Epc, Ipa, Ipc, $E_{1/2}$ ($\frac{Epa+Epc}{2}$) and SE represents the anodic, cathodic peak potential, anodic, cathodic peak current, formal reduction potential, and switching potential (the point at which the scan is reversed and run in the negative direction) concurrently. The shape of a voltammogram is a reflection of interfacial process and it depends on the time taken to record the voltammogram (scan rate), interfacial electron transfer rate characterized by K^o, diffusion of the reduced and oxidized forms of analyte, charge transfer coefficient (α), degradation rate or other chemical transformation that depletes electrochemically formed specie, electrode surface, concentration and type of the analytes (Espinoza *et al.*, 2019). For instance, the voltammogram in Figure 2.7 a could be said to have occurred at a fast scan rate with a reversible redox electrochemical process while Figure 2.7 b could be attributed to slower scan rate and nature of the analyte since some analyte like serotonin shows oxidation irreversible electrochemical process.

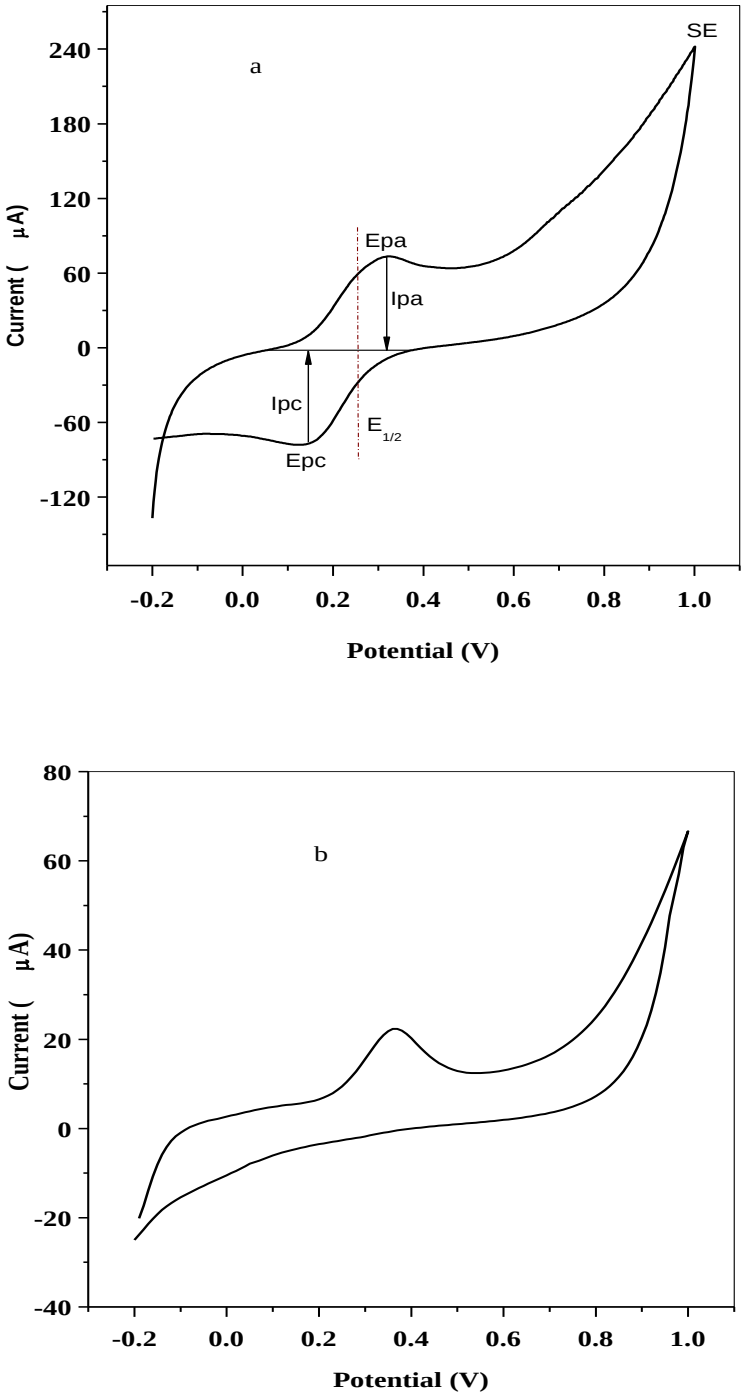

Figure 2.7: Shapes of cyclic voltammograms- a,b.

For a perfect reversible process, voltage separation (ΔE) between current peaks is represented by equation 2.1 (Kounaves, 1997).

$$\Delta E = /Epa - Epc /= \frac{2.303RT}{nF} \qquad (2.1)$$

There is no alteration in peak positions with voltage scan rate, and the ratio of the peak currents (Ipa to Ipc) is equal to one. The peak current for a reversible system which is related to concentration is described by the Randles-Sevcik equation 2.2 (Kounaves, 1997)

$$\mathrm{lp} = 2.686 \times 10^5 n^{3/2} ACD^{1/2} v^{1/2} \qquad (2.2)$$

Where lp is peak (A), A is the area of the electrode (cm^2), D is the diffusion coefficient (cm^2/s), C_o is a concentration ($molcm^{-3}$) and v is scan rate potential (Vs^{-1}).

Properties of an irreversible process include high voltage peak separation greater than $\frac{0.0592}{n}V$ which is due to the slow rate of electron transfer between the electrode and the analytes. Only one peak is observed in one of the potential scan. The peak current for an irreversible system for one number of electrons transferred is described by equation 2.3.

$$\mathrm{Ip} = 2.999 \times 10^5) n[1-\propto]n]^{1/2} ACD^{1/2} v^{1/2} \qquad (2.3).$$

In a cyclic voltammetry experiment, the parameter determined include; anodic and cathodic peak current (Ipa, Ipc), anodic potential (Epa), cathodic peak potential (Epc), and $E_{1/2}$ (formal potential) (Mirceski *et al.*, 2018).Others parameters such as number and coefficient of electron transferred (n; α) are determined based on the slope values of linear plots of Ep (peak potentials) versus logarithm of scan rates (log v) equal to $\frac{-2.3RT}{\propto nF}$ and $\frac{2.3RT}{(1-\propto)nF}$ assigned to cathodic and anodic peak respectively by Lavarion (Laviron, 1979).

2.8.1.2 Square wave voltammetry

Square wave voltammetry (SWV) is commonly used pulse electroanalytical assay with high sensitivity and rapid measurement. The sensitivity of SWV results from its ability to reject background current in measurements and this give room for quick analysis (Mirceski *et al.*, 2018). SWV combines the high sensitivity of the pulse techniques and CV electrode mechanism. SW voltammogram as can be seen in Figure 3 can be obtained by measuring current at the working electrode while sweeping the potential between working and reference electrode over a wide range of set voltage. Parameters determined in SW voltammogram include; increment of scan rate (ΔE), the peak height of the SW pulse (Esw) which corresponds directly to the

concentration of analytes present in solution, and potential pulse time (Kounaves, 1997; Mirceski *et al.*, 2018).

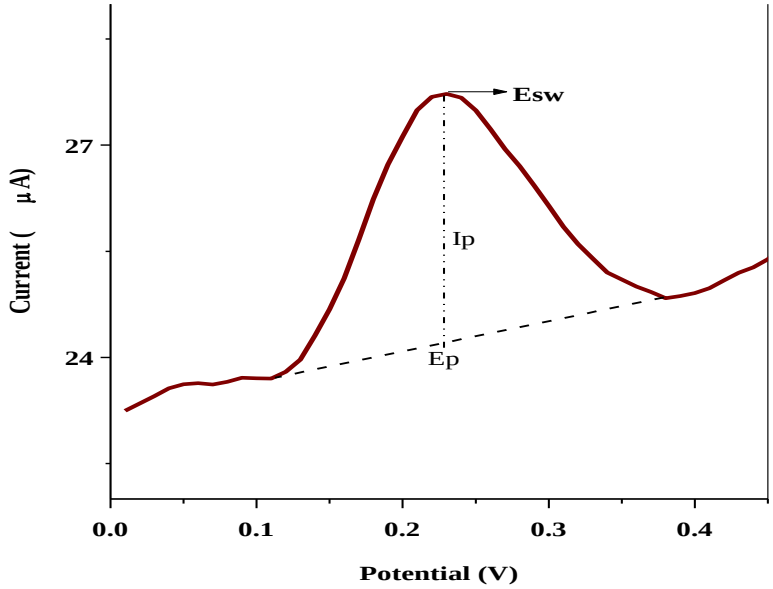

Figure 2.8: Typical square wave voltammogram.

2.8.1.3 Chronoamperometry

Chronoamperometry is a sensitive amperometric technique that functions with time. It involves stepping the potential applied to the working electrode initially held at a value at which analyte of interest had not undergone any electrochemical reaction to that (potential) at which the surface concentration of the electroactive specie is zero (Brownson & Banks, 2014; Rezaei & Irannejad, 2019). The current passing through the cell is measured versus time as depicted by Cottrell equation.

$$\mathrm{I(t)} = \frac{nFACD^{1/2}}{\sqrt{\pi T}} \qquad (2.4)$$

Where, D is diffusion coefficient in ms^{-2} from the redox reaction, Co is the concentration of specie ($molcm^{-3}$), F is the faraday's constant (C) and A the area of electrode in cm^2.

Chronoamperometry measures current-time dependent diffusion controlled processes occurring at the electrode (Guy & Walker, 2016). Change in current is seen in response to rise and fall in the diffuse layers of analyte at the WE surface (Rezaei & Irannejad, 2019). Thus, the principle of mass transport process all through is based on diffusion (Brownson & Banks, 2014). The change in concentration at the electrode surface is reflected by the current time curve (Brownson &

Banks, 2014; Rezaei & Irannejad, 2019). There are two different forms of carrying out chronoamperometric measurements: Single and double potential step (Brownson & Banks, 2014; Rezaei & Irannejad, 2019).

Single potential step involve the application of a forward potential step and recording the resulting current (Kounaves, 1997; Rezaei & Irannejad, 2019) as shown in Figure 2.9.

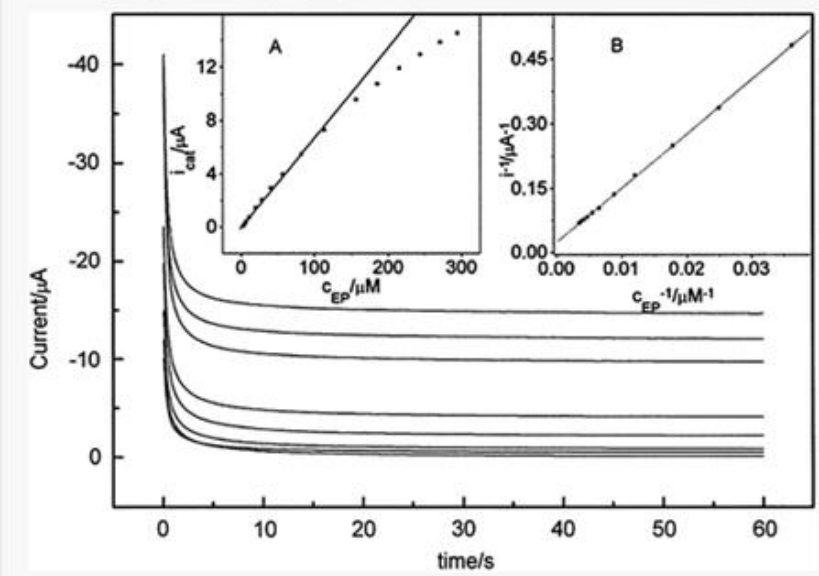

Figure 2.9: Single potential step chronoamperometric curves (Brownson & Banks, 2014).

There could also be a variant on the single potential step chronoamperometric experiment when the potential which instigate the desired electrochemical reaction is kept at a value and aliquots of analyte are made and at each time, and (Brownson & Banks, 2014) a convective flow insures species are transported to the surface of the electrode and transformed electrochemically which is recognized by a step in current as depicted in Figure 2.10 (Brownson & Banks, 2014). The current increases or decreases as all the electroactive species are used up. A calibration plot is obtained by analysing the step in (Brownson & Banks, 2014).

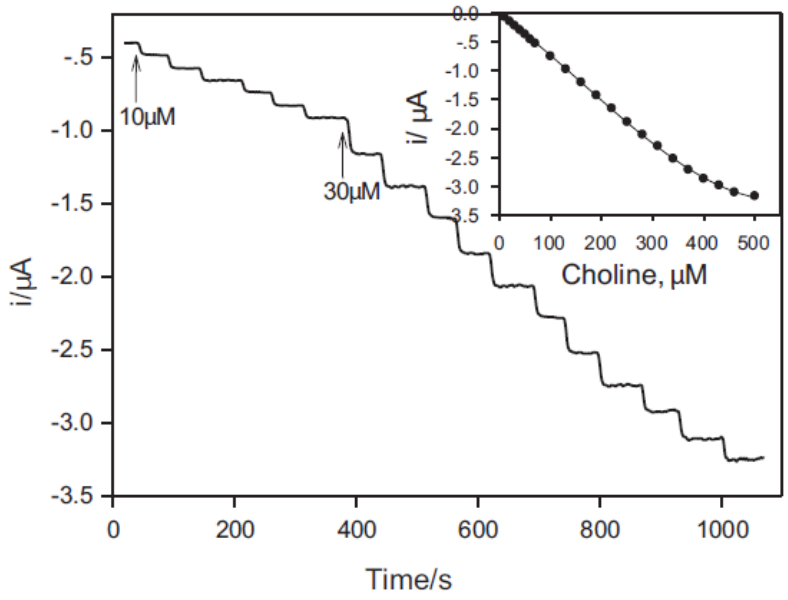

Figure 2.10: Current-time response curve of double potential step chronoamperometric measurement (Deng *et al.*, 2013).

2.8.1.4 Electrochemical impedance spectroscopy (EIS)

This is an electrochemical technique conducted in order to investigate the occurring electrochemical processes, rate of electron transfer, and capacitive behaviour of the system. EIS is applied in studying corrosion in metals, electrochemical synthesis of metals, adsorption and desorption at the electrode (Randviir & Banks, 2013). In principle, current is measured in response to an applied sinusoidal (voltage) perturbation (Randviir & Banks, 2013). Electrochemical impedance is the response of an electrochemical cell to an applied potential. EIS is conducted within specific frequency range (100000 - 0.1 Hz). The frequency reveals underlying chemical reactions. Impedimetric data are presented graphically via Nyquist (Figure 2.11), which provides information on possible active reaction mechanism and Bold's plots (Figure 2.12) helps to monitor phase margins in which a system becomes unstable (Choi *et al.*, 2020; Randviir & Banks, 2013). In Nyquist plot, a real part of impedance (Z") versus an imaginary aspect (Z') is plotted.

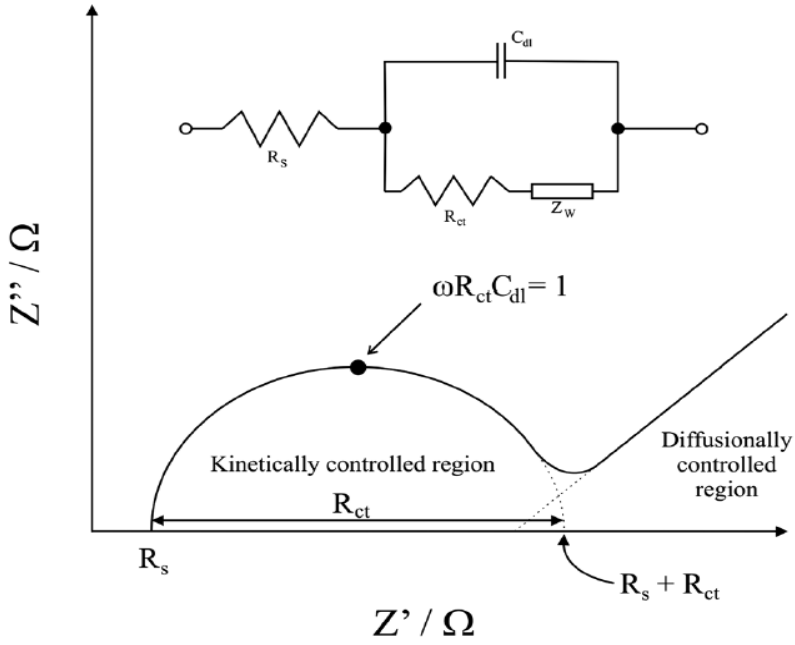

Figure 2.11: Nyquist plot (Randviir & Banks, 2013).

Parameters deduced from Nyquist plot are, solution resistance calculated from the spectra of EIS, Cdl (double layer capacitance) obtained from Z"max of the semi -circle and Rct (resistant charge transfer), and warburg impedance (ω) (Randviir & Banks, 2013). In Bold's plot (Figure 2.12) impedance (opposition of an electrical system to the flow of electrons in Ohms, Ω), which results from Cdl, Rs and Rct is plotted against the phase angle and the influence of capacitor and inductor is determined from the plot (Randviir & Banks, 2013).

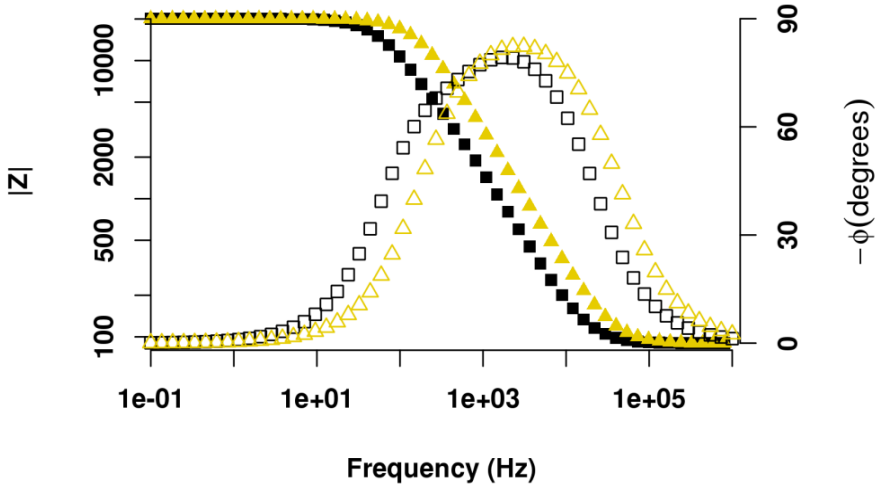

Figure 2.12: Bold's plot (Bardini, 2015).

Combination of Rct, Cdl, Rs and ω gives rise to a Randle's circuit which is use in the simulation of EIS experiments (Randviir & Banks, 2013). See insert in Figure 2.11.

Warburg impedance (ω): This is resistance to mass transfer or diffusion control, which depends on diffusion of reactants to or away from the surface particularly at low frequency. It exhibits 45^0 phase shift in the diffusion controlled region which appears as a straight line under semi-infinite conditions (Choi *et al.*, 2020; Randviir & Banks, 2013). Thus, the diffusion of ions in solution during electrochemical reaction is explained by **ω** (Randviir & Banks, 2013).

Charge transfer resistance (R_{ct}): This is a real quantity connected to heterogeneous electron transfer rate constant which deals with opposition encountered to the flow of electrons. R_{ct} results from charge transfer reactions and ions diffusing from the electrolyte to the interface. R_{ct} occurs in regions that are kinetically controlled at high frequency (Choi *et al.*, 2020; Huang *et al.*, 2016; Randviir & Banks, 2013).

Constant phase element (Q): Q represents the capacitive element of an electrochemical cell with a constant phase angle of -90.n degree. Constant phase element gives information on factors that affect the capacitance of a system such as in homogeneity of surface leading to different rate of reaction upon the surface which initiates a number of time constants (Randviir & Banks, 2013). The property of Q is regulated by exponent (n) irrespective of frequency (Bardini, 2015). Q acts like a capacitor (C), resistor (R) and an inductor (L) when n = 1, 0 or -1 with phase angles as 90.n = 90, -90.n = 0 and -90.n = 90o accordingly (Bardini, 2015). The emergence of constant phase element is caused by different reaction rates on the electrode (GCE), uneven time constant (RC) from the centre to the electrode edge, roughness of electrode surface, and different composition and thickness (Bardini, 2015).

Double layer capacitance (C_{dl}): C_{dl} is the charging of the interfacial capacitor which is linked with flow of current (charging current) (Mirceski *et al.*, 2018) which indicates the frequency at which capacitive current of an experimental system becomes limited by ohmic resistance and it occurs at the surface of conductive materials (electrode) situated in an electrolyte (Bardini, 2015; Randviir & Banks, 2013). The formation of C_{dl} results from excess of charge at the surface of electrode, the corresponding response of the counter, electrolyte ions and orientation of molecules of polar solvent at the interface (Mirceski *et al.*, 2018). The value of obtained Cdl is dependent on the type of ions and the formed layer (Bardini, 2015; Randviir & Banks, 2013).

Solution resistance (R_s): This is the opposition to flow of current through the electrolyte by the immigration of ions depending on the type/ concentration of ions, temperature, and geometry area in which current is carried. R_s is noticed at the highest frequency where the real axis is intercepted (Randviir & Banks, 2013).

2.9. Characterization techniques and their principles

2.9.1 Ultraviolet-visible spectroscopy

This is absorption spectroscopy that investigates the alterations in electronic energy levels within a molecule resulting from the transfer of electrons from pie or non-bonding orbitals. UV-Vis employs the use of electromagnetic radiations in the range of 190 to 800 nm (Kumar, 2006). Electromagnetic radiation in the range of 190 nm to 400 nm is referred to as the UV region while 400 to 800 nm in the visible region. UV-Vis determines the intensity of light passing through a specimen (I) and relates it with the intensity of light before passing via the sample (I_0). The ratio of I/I_0 is referred to as transmittance in percentage (%T). The absorbance A with equation 2.5 is based on transmittance (Kumar, 2006).

$$A = \frac{-log\%T}{100\%} \quad (2.5)$$

UV-Visible also determines reflectance (equation 2.6). The intensity of light reflected from a specimen (I) and relates it to the intensity of light reflected from a reference material (I_0)

$$\text{Reflectance} = \frac{I}{Io} \quad (2.6)$$

The principle of UV-Visible operation is anchored on beer- lamberts Law which states that "when a beam of monochromatic light is passed through a solution of an absorbing substance, the rate of decrease in intensity of radiation with a thickness of the absorbing solution is proportional to the incident radiation as well as the concentration of solution (Kumar, 2006). The law is represented with an equation 2.7.

$$A = Log\frac{Io}{I} = \varepsilon Cl \quad (2.7)$$

Where A = absorbance

I_0 = intensity of light striking on the sample

I = is the intensity of light leaving the sample

Ɛ = molar absorptivity

C is molar concentration of solute

L is the length of sample cell

Essential parts of the UV-Visible include the; light source widely used lamps are hydrogen – deuterium and tungsten filaments, sample/reference cell, monochromator which consists of the prism, and the slit. The prism disperses emitted radiation from the source while he slit selects different wavelength separated by the prism (Kumar, 2006). The cuvette (sample/reference cell)

must be transparent to radiation and the detector. Notable detector use is the photomultiplier since they are sensitive to both UV and visible radiation with rapid response (Kumar, 2006). Commonly used terms in UV-Visible spectrophotometer are; **auxochromes** which do not absorb UV radiation but their presence results in a shift of absorption maximum to longer wavelengths. **Bathochromic/red shift** is a shift in absorption maximum to a longer wave length or lower energy (Kumar, 2006). **Hypsochromic/blue** shift is referred to a shift of maximum absorption to a shorter wave length or higher energy while **hypochromic** and **hyperchromic** effect respectively leads to decreased and increased absorption intensity (Kumar, 2006).

2.9.2 Fourier transform infrared (FTIR) spectroscopy

FTIR is a routinely used analytical technique for characterization of produced materials (organic/inorganic), whose principle involves passing infrared radiation through a specimen (Chakraborty, 2016; Ferrer, 2012). Interaction between the IRR and samples results in absorption and transmission of some IR resulting to a spectrum (fingerprints of the specimen with absorption) assigned to the vibrationa frequencies of the bands (functional groups) present in the sample (Chakraborty, 2016; Ferrer, 2012). FTIR is fast, precise, sensitive with simple instrumentation and optimum optical throughput (Ferrer, 2012). It is applied in medicine, herbal medicine, food and environmental samples for diagnosis of tissue/cells, determination of the quantity of active ingredients present, and for investigation of pollutants and contaminants respectively (Ferrer, 2012; Mostaço-Guidolin, 2011; Siregar, 2018).

2.9.3 X-ray diffraction (XRD) spectroscopy

XRD is a non-destructive tool use in characterizing crystalline materials which could be polymers, plastics, pharmaceuticals, semiconductors and metals. The principle is based on constructive interference of monochromatic X-rays and a crystalline specimen which results in x-ray diffraction peaks (Bunaciu *et al.*, 2015). The distribution of atoms within the lattice of the samples determines the intensity of peaks. The pattern of the x-ray diffraction pattern connotes the finger part of the periodic atomic distribution in the sample. When the interaction of the incident ray with the sample satisfy Bragg's law ($n\lambda$), constructive interference is produced where n, λ, d, θ connotes an integer, wavelength, inter planar spacing which produces the diffraction, and diffraction angle (angle of incidence) respectively (Bunaciu *et al.*, 2015). Bragg's law correlates the wavelength of electromagnetic radiation in the diffraction angle and the lattice spacing in a crystalline material. XRD helps to characterized crystalline materials,

identify fine-grained minerals and unknown crystalline materials, measure the purity of the sample, studies the structure of crystals and their atomic spacing (Bunaciu *et al.*, 2015).

2.9.4 Scanning electron microscopy (SEM)

SEM studies the structural and physical properties of the specimen at the highest magnifications. The principle involves discharging beams of an electron from the electron gun at the target specimen. Interaction of the sample with a beam of electrons liberates signals which are collected. Collected signals are amplified and digitized properly while maintaining a firm relationship between the sample scan point and the image point (Kwiecińska *et al.*, 2019). This is to ensure the generation of a real-time image beheld in a monitor and stored in a computer. The SEM consist of the electron gun which generates beams of the electron, the magnetic lenses that scan the sample surface by the formation of fine convergent electron beams, sample chamber claps the specimen and expels interference of undesired particles while the detectors detect the signals (SE, BSE and X-rays) and magnify the image. Signals reveal information on the surface morphology, composition, and crystallographic structure of sample (Kwiecińska *et al.*, 2019). The point at which different signals are produced due to the interaction between streams of electron and samples is called the area of excitation (area of interaction).

The constituent that makes up the sample and the accelerating voltage determines the size and shape of the excitation volume (Kwiecińska *et al.*, 2019). SEM is employed in the investigation of the structure of highly metamorphosed organic matter (coals, graphite, and coke), carbonaceous substances and their transformation (pyrolysis, coking, oxidation and weathering) at processing stage (Kwiecińska *et al.*, 2019). SEM is also applied in analyzing fractures of different carbon materials giving room for enhanced prediction of their property during the processing stage (Kwiecińska *et al.*, 2019). In material science, SEM is used to study the surface structure and shape of synthesized materials.

2.9.5 Energy dispersive spectroscopy (EDS)

Energy dispersive x-ray spectroscopy (EDS) is a qualitative and quantitative x-ray micro analytical technique which give information on the elemental composition of a specimen with an atomic number greater than 3 using an x-ray mapping (Ebnesajjad, 2014; Gibson, 2005). EDS is qualitative as it identifies the lines in the spectrum and quantitative because it determines the amount of element present. In principle, EDS involves the use of generated x-ray spectrum by a

solid specimen hit with a focused electron beam to obtain a localized chemical analysis. The generated x-rays are detected with the ED spectrophotometer, which splits the x-rays into various energy levels. In instrumentation, x-rays are emitted when an electron beam bombards the sample (Gibson, 2005). Emitted x-rays hit the detector resulting in a charge pulse which is converted to a voltage pulse with an amplitude which reflects the energy of the x-ray detected (Gibson, 2005). The voltage pulse, in turn, is converted to a signal with an additional one more count synonymous to the energy channel. EDS has application in identifying materials as well as evaluation of components of materials (Ebnesajjad, 2014; Gibson, 2005). EDS application stems from the direct relationship that exists between the generated x-ray by every element present in a sample and the amount of the element (Ebnesajjad, 2014; Gibson, 2005) .

2.9.6 Transmission electron microscopy (TEM)

TEM is a microscopy technique with high spatial resolution due to a short de Broglie wavelengths employed in studying the size, shape of materials and crystal structure. In principle, transmission electron microscopy involves the passing of electron streams produced from thermionic emission in the electron gun, accelerated at a high voltage of about 300 kV through a sample (Series & Heath, 2014). Some of the electron beams interact with the sample while some are transmitted. The objective lens focuses the transmitted electrons on an imaging device creating an image. The image is magnified while passing through the intermediate and projector lenses. The images are then projected on a fluorescent screen where they are recorded (Series & Heath, 2014). The application of TEM, include; examining structural units of carbonaceous materials which reveal the topography, morphology, composition and crystallographic characteristics of the material. Tem is used as an XRD complementary tool and also for analysing particle size, the shape of synthesized particles (Series & Heath, 2014).

2.9.7. Zeta potential

Zeta potential which could also be referred to as electrokinetic potential with a Greek symbol (ζ) is a characteristic of nanoparticles suspended in or dispersed in fluid and is based on the interaction of dispersed or suspended particle in the fluid between the charged particle and applied field on the application of electric field (Bhattacharjee, 2016). Zeta potential gives an insight into the type of electrical charge on the particle negative or positive (surface charge) and also the stability of nanoparticles. Positive surface charge of nanoparticles is attracted to the negative plate on the electric field while negative surface charge particle of nanoparticles to the

positive plate of the electric field thus dictating positive or negative dimension of zeta potentials (Bhattacharjee, 2016)

CHAPTER THREE

EXPERIMENTAL

3.1 Reagents and materials

Fresh *Callistemon viminalis* (*C. viminalis*) leaves and flowers were harvested from herbarium of the North-West University, Mafikeng, South Africa. Reagents used include; Potassium hexacyanoferrate (III) ($K_3[Fe(CN)_6]$) purchased from Sigma-Aldrich (Germany) was prepared in 0.1 M phosphate buffer solution (PBS) pH 7.4 using 0.1 M sodium phosphate dibasic (NaH_2PO_4 - 99% purity) and sodium phosphate monobasic (Na_2HPO_4; - % purity (99)) from LABCHEM Edenvale, and Glass World South Africa accordingly. Other reagents include iron (III) chloride hexahydrate with 99% purity, methanol, 10% aluminium (III) chloride ($AlCl_3$) solution, 7.5% sodium trioxocarbonate (IV) solution (Na_2CO_3), 5% sodium nitrite ($NaNO_3$), 5% sodium hydroxide solution, gallic acid, quercetin, 10% Folin–Ciocalteu reagent (FCR), dimethylformamide ($(CH_3)_2NC(O)H$), methanol (HCOH), 10 mM lithium chloride (LiCl) solution pH 7.3, choline chloride ($C_3H_{11}CINO$), and dopamine hydrochloride ($C_8H_{11}NO_2.HCl$). All reagents were of analytical grade. Choline dietary supplements (ReVite(R) super B and energy injection fizzy tablet) product of pharm mark South Africa, CDP choline (dietary supplement) manufactured by RT Labs Ltd South Africa were used for real sample analysis. All solution were prepared using distilled water. Multi-walled carbon nanotube (MWCNT) procured commercially from Sigma-Aldrich (USA), 773810-25G MWCNTs was used in this study. The Purity of MWCNT was $\geq$ *98%,* outside and inside diameters were 10 nm ± 1nm and 4.5 nm ± 0.5 nm respectively with a length 3 – 6 μm). Iron (III) oxide and zinc oxide nanoparticles (Fe_3O_4NPL, Fe_3O_4NPF, ZnONPL, and ZnONPF) were synthesized from *Callistemon viminalis* (*C. viminalis*) leaf and flower extract. glassy carbon electrode (GCE) of 3 mm diameter, silver/silver chloride (Ag/AgCl) in staurated (sat'd) 3 M potassium chloride (KCl) electrode and a platinum disk were used as the working, reference and counter electrode accordingly.

3.1.1 Preparation of *C. viminalis* leaf and flower extracts

Harvested leaves and flowers from *C. viminalis* plant were washed thoroughly with tap water rinsed with distilled water and dried under sunlight for 48 h. About 5 g of dried ground leaves was weighed and boiled with 100 ml distilled water for 15 min at 80 $^{\circ}$C (Kanagasubbulakshmi, 2017). Leaf extracts was allowed to cool under room temperature and filtered using a vacuum

pump with a Buchner funnel and 125 mm Whatman filter paper. Colour of the leaf extracts was an orange-colour with pH of 5.32. The same procedure was followed to obtain red-colour flower extracts which gave pH of 3 .89.

3.2. Phytochemical test of extracts

In order to determine the presence of flavonoids and phenolic compounds in *C. viminalis* leaf and flower extracts which are active components in the formation of nanoparticles, phytochemical test on flavonoids and phenols was conducted on leaves and flowers extract with the specified reported procedure (Balamurughan, 2014). The presence of flavonoids in the extracts of the plant was carried out using alkaline reagent test (treating 2 ml of the extracts with four drops of 10% aqueous sodium hydroxide solution (10 g of NaOH in 90 g of distilled water)) and lead acetate test (adding few drops of 0.1 M lead acetate solution to 2 mL of the extract) . The test for the presence of phenolic compounds in extracts was determined by a ferric chloride test using four drops of 0.1 M of alcoholic iron (III) chloride hexahydrate.

3.2.1 Determination of total phenol content (TPC)

Standard proceure method with some modification was employed in estimating phenol content of *C. viminalis* leaf, and flower extract using gallic acid as an internal standard as reported in the literature (Hossain *et al.*, 2019). Five milligrams (5 mg) of dried ground *C. viminalis* leaves and flowers was dissolved in 5 ml methanol. 10% folin ciocalteu's (FCR) and 6% sodium trioxocarbonate (IV) (Na_2CO_3) solutions were prepared by the addition of distilled water in separate 100 ml volumetric flasks. A 300 µl of each extract was taken into a glass test tube followed by the addition of 1.5 ml of 10% FCR solution. The mixture was sonicated for 5 min. Thereafter, 1.5 ml of 6% Na_2CO_3 solution was added, and the test tubes were kept in a dark place for 2 h at room temperature. Gallic acid standard of various concentrations (750, 650, 550, 450, 350 and 150 µg/ml) was prepared following same procedure as described in extracts (Hossain *et al.*, 2019). *C. viminalis* extracts and gallic acid standard solutions were measured at 760 nm with a UV-visible spectrophotometer after blank measurement (methanol). Total phenol content of the extracts was estimated using the gallic acid standard calibration curve expressed as microgram of gallic acid equivalent (GAEmg) per 5 g of dry extract.

3.2.2 Determination of total flavonoids content

Extracts were prepared following the same procedure in phenol content. 5% sodium trioxonitrate (V) ($NaNO_3$), 5% sodium hydroxide (NaOH) and 7% aluminium (III) chloride ($AlCl_3$) solution

were prepared separately by dissolving 5 g and 7 g of the salts in 100 ml volumetric flasks and made up to mark with distilled water. Leaf and flower extracts (300 µl) were taken into a glass test-tube, 75 µl of 5% $NaNO_3$ was thereafter added and left for 5 min after which 1.25 ml of $AlCl_3$ and 0.5 ml NaOH were added. The mixture was sonicated for 5 min and incubated for 5 min at room temperature (Hossain *et al.,* 2019). Concurrently, quercetin standard of different concentrations (500, 300, 100, 50, and 25 µg/ml) were prepared in the same protocol (stated in the first three lines of this section (3.2.2)) as described in extracts (leaf and flower). The absorbance of all working solution and the standard solution were measured at 510 nm against blank (methanol).

3.3. Synthesis of metal oxide nanoparticles from extracts

3.3.1 Synthesis of zinc oxide nanoparticles (ZnONP)

ZnONPL was prepared from *C.viminalis* leaf extracts following a method reported in the literature with some modifications (Kavitha *et al.,* 2017). 180 ml of 0.1 M zinc trioxonitrate (V) hexahydrate salt solution (prepared by dissolving 14.85 g of the salt in 500 ml volumetric flask and made up to mark with distilled water) was added to 60 ml of leaf extracts in 3:1 (v/v) while stirring condition with the pH was adjusted to 12 with the addition of 65 ml 0.1 M sodium hydroxide which resulted in the formation of a cream coloured precipitate. The solution was stirred for 2 h, quantitatively transferred into a 50 ml centrifuge tube and centrifuged for 5 min at 25 °C and 6000 rmp. Upper liquid portion was discarded. The precipitates were washed thrice with distilled water to ensure the purity of nanoparticles formed and dried at 65.5 °C for 10 h. The same procedure was followed in the synthesis of ZnONPF from the flower extract (ZnONPF) (Kavitha *et al.,* 2017).

3.3.2 Synthesis of iron (III) oxide nanoparticles (Fe_3O_4NP)

Fe_3O_4NPL and Fe_3O_4NPF was synthesized from *C. viminalis* leaf and flower extracts, respectively. Iron (III) chloride hexahydrate (10 mM) solution of 99% purity (prepared by dissolving about 0.67575 g of salt in 250 ml standard flask containing distilled water and thereafter made up to mark with distilled water) was added to the leaf and flower extracts in 1:1 (v/v) (100 ml each) in separate beakers with a resulting colour change from light yellow/red (colour of leaf and flower extracts) to black indicating the formation of Fe_3O_4NPL and Fe_3O_4NPF. The mixture was stirred at room temperature for 3 h and allowed to stand for an hour so as to obtain a colloidal suspension which was thereafter centrifuged at 25 °C, rmp of 6000, at

9 m s^{-2} acceleration for 30 min, washed severally with ethanol, and oven dried for 2 h at 40 °C (Kanagasubbulakshmi, 2017).

3.4 Functionalization of multi-walled carbon nanotubes (MWCNTs)

Multi-walled carbon nanotubes 773810-25G MWCNT were used in this study. The Purity of MWCNT was ≥ 98%, outside and inside diameters were 10 nm ± 1nm and 4.5 nm ±0.5 nm, respectively, with a length 3 – 6 μm. MWCNT functionalization was carried out following a prescribed method with slight modification using mixture of concentrated acid (H_2SO_4/HNO_3) in a 3:1 (v/v) (Chao *et al.*, 2019). 0.5 g of MWCNT were mixed with 100 ml acid mixture, stirred at constant temperature (50 °C) for 30 min and centrifuged. The supernatant was discarded, and the MWCNTs suspension washed several times using a sintered glass until a pH of 7 was obtained. The black solid was dried for 12 h at 70 °C (Chao *et al.*, 2019).

3.5. Preparation of catalyst and solutions

3.5.1. Preparation of functionalized multi-walled carbon nanotube –metal oxide nanocomposites (MWCNT-Fe_3O_4, MWCNT-ZnO)

Nanocomposites of functionalized multi-walled carbon nanotube metal oxide (f-MWCNT-MO) catalysts were prepared following a specified method in the literature (Fayemi *et al.*, 2015) with slight modification. A 4.5 mg of Fe_3O_4NPL and 1.5 mg of functionalized MWCNT was weighed into a glass vial and 1 ml dimethylformamide (DMF) was added. The mixture was sonicated for 72 h at 25 °C and dried in an oven at 55 °C for 2 h to give f-MWCNT/Fe_3O_4NPL. Same step was followed in the preparation of f-MWCNT/Fe_3O_4NPF, f-MWCNT/ZnONPL, and f-MWCNT/ZnONPF.

3.5.2 Preparation of electrolyte solution

Phosphate buffer solution (0.1 m) was prepared by weighing 1.0322 g of monobasic (NaH_2PO_4) and 2.3274 g of dibasic (Na_2HPO_4) into a 250 ml volumetric flask and made up to mark using distilled water.

A 5 mM ($K_3[Fe(CN)_6]$) was prepared by dissolving weighed gram (0.16462 g) of potassium hexacyanoferrate (III) into a 100 ml standard flask and made up to mark with 0.1 M PBS solution (phosphate buffer solution), pH 7.4.

Lithium chloride solution, pH 7.3 was prepared by weighing 211.95 mg of the salt into a 500 ml standard flask and made up to mark using distilled water.

3.5.3 Preparation of analytes solution

A 2 mM of choline chloride solution was prepared by dispersing 27.924 mg of salt in 100 ml standard flask containing 10 mM lithium chloride solution, pH 7.3 which was thereafter made up to mark with same solution. 0.1 mM of the analyte (choline) was also prepared using LiCl solution as the solvent in 100 ml volumetric flask.

A 100 mM ascorbic acid was prepared by dissolving 1.7613 g of AA salt in a 100 ml volumetric flask containing 10 mM lithium chloride solution of pH 7.3 and made up to mark with same solution (LiCl).

Dopamine solution (0.1 mM) was prepared by dissolving 1.8964 mg of dopamine hydrochloride salt in a 100 ml flask containing 10 mM lithium chloride solution of pH 7.3 and made to mark using lithium chloride solution .

3.5.4. Preparation of real sample (choline supplements)

An opened capsule (powder) of CDP choline (citicholine) was dissolved in 2 ml LiCl solution and diluted 100 times using LiCl solution of pH 7.3. Same step was followed in the preparation of super B energy injection fizzy tablet containing choline bitartrate. A 2 ml of the diluted samples were further diluted in 100 ml standard flask and spiked with different concentrations of choline using addition methods. The amount of the analyte (choline) present in the pharmaceutical samples was determined at GCE/MWCNT/Fe_3O_4NPL, GCE/MWCNT/Fe_3O_4NPF, GCE/MWCNT/ZnONPL and GCE/MWCNT/ZnONPF electrodes using SWV.

3.6. Characterization of metal oxide nanoparticles and their composites

Optical properties of synthesized nanoparticles and nanocomposites were investigated using ultraviolet visible spectroscopy (Uvline 9400 SCHOTT instrument produced in EU), energy band gap of synthesized nanoparticles was estimated from UV-VIS absorption peaks using Taucs plot, morphology of nanoparticles and nanocomposites was studied with scanning electron microscopy (SEM), elemental compositions of nanoparticles (Fe_3O_4NP and ZnONP) were

determined with energy dispersive spectroscopy (EDS), fourier transform infrared (FTIR) spectroscopy (Opus Alpha-P, Brucker corporation, Billerica, MA, USA) was employed in examination of bioactive compounds responsible for bio reduction of nanoparticles and the functional groups present in the extracts and synthesized nanoparticles/nanocomposites. Crystallinity of nanoparticles were examined with the aid of Röntgen PW3040/60 X'Pert Pro X-ray diffractometer (XRD), (Germany) having Ni-filtered Cu Kα radiation (λ = 1.5405 Å) at a rate of scanning of 2° min^{-1} and 2θ ranging from 20^0 to 80^0. Thermal and electrical stability of synthesized nanoparticles were investigated with SDT Q600 V20.9 Build 20 thermogravimetric analyser of DSC-TGA (TGA) and Malvern zetasizer, respectively. Shapes of the synthesized nanoparticles were obtained with transmission electron microscopy (TEM)-JEOL2100 instrument (Joel Ltd, Peabody, MA, USA) fitted with a LaB 6 electron while the and particle size distribution was obtained using image J software.

Electrochemical experiments (voltammetry and chronoamperometry) were conducted with an AUTOLAB Potentiostat PGSTAT 302 (Eco Chemie, Utrecht, The Netherlands) driven by the GPES software version 4.9. Electrochemical impedance spectroscopy (EIS) measurements were performed with metrohm AUTOLAB, potentiostat PGSTART 302, frequency response analyser (FRA) 32 using NOVA 1.10.1.9 software between 100 kHz - 0.1 Hz sinusoidal modulation in 0.1 M phosphate buffer solution (PBS) containing $K_3Fe(CN)_6$ at potential of +0.2 V versus Ag/AgCl in saturated (sat'd) KCl (reference electrode). Bare GCE disk (d = 3.0 mm in Teflon) was used as the working electrode and platinum as the counter electrode.

3.7. Pre-treatment and modification of electrodes

3.7.1 Pre-treatment of electrodes

The glassy carbon electrode was cleaned by gently polishing it in aqueous slurry of alumina nano powder on a micro cloth pad followed by ultrasonication in methano and thereafter in distilled water. This was to remove particles of alumina nano powder and obtain a mirror like surface. The electrode was further sonicated in methanol and finally in distilled water and dried at 40 °C for 3 min.

3.7.2. Modification of electrodes

A drop-drying method (Figure 3.1) was applied in electrode modification using the separate suspensions of metal oxide nanoparticles (MONP) and nanocomposites (f-MWCNT/MONP = f-

MWCNT /Fe_3O_4NP and f-MWCNT/ZnONP) were prepared in 1 mL of DMF and sonicated for 4 h to form a paste. Prepared pastes were dropped on the bare glassy carbon electrode (GCE) and dried in an oven at 40 °C for 5 min to obtain GCE/f-MWCNT, GCE-ZnONP, GCE-Fe_3O_4NP, GCEf-MWCNT/ZnONP, GCE/f-MWCNT-Fe_3O_4NP.

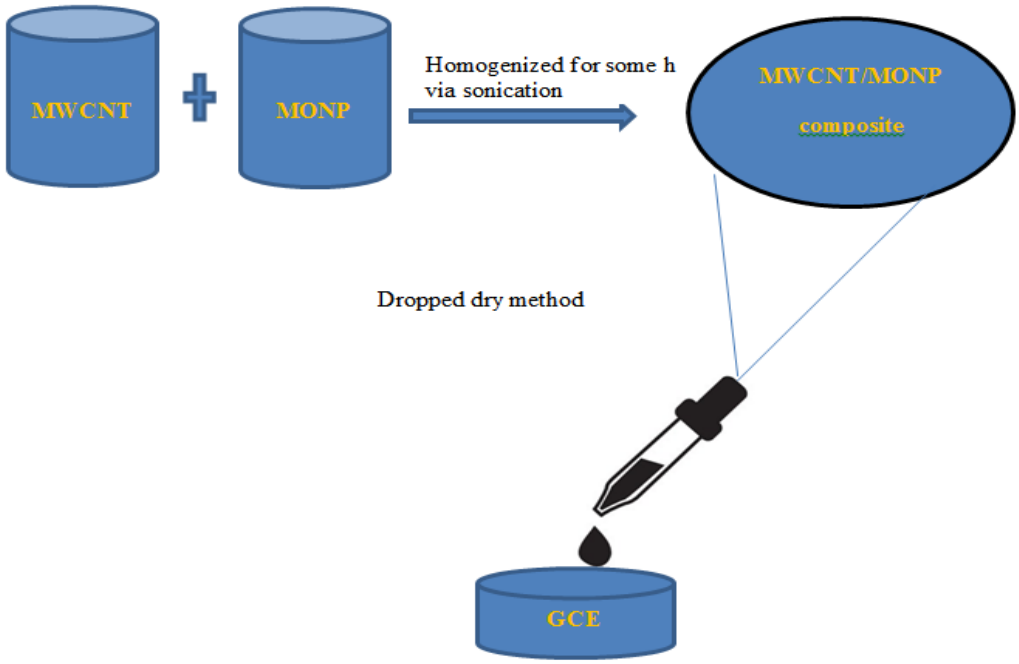

Figure 3.1: Electrode modification process.

3.8. Electrochemical studies

Electrochemical sensor studies were carried out in an electrochemical cell with three set of electrodes: working electrode (glassy carbon, gold, platinum), reference electrode (Ag/AgCl, saturated calomel) and auxiliary or counter (carbon, copper, stainless steel and platinum) electrode. Glassy carbon electrode was used as the working electrode due to its low cost, availability, stability and ability to easily modify the morphology of carbon while Ag/AgCl in sat'd 3 M KCl and platinum were used as the refenece and counter electrodes, respectively. Cyclic voltammetry being a general way to study the electrochemical properties of analytes in a solution was employed in studying the electrocatalytic behaviour of the bare and modified electrodes towards the detection of the analyte (Allen & Larry, 2001). The parameters determined from the cyclic voltammogram include the formal redox potentials ($E_{1/2}$), peak separation potential (ΔE), anodic and cathodic peak currents (Ipa, Ipc). Also, electrochemical impedance spectroscopy (EIS) was conducted to study the behaviour of the electrodes in redox

probe and towards the detection of the analytes at 0.2 and 0.5 V applied potential, respectively vs. Ag/AgCl in sat'd KCl. Other evaluations such as electro analysis, sensitivity, selectivity (simultaneous/interference) study were carried out using square wave voltammetry (SWV) and chronoamperometry (CA).

3.8.1. Electron transport of experiment

Electron transport experiment was carried out prior to electrocatalytic and electro analysis experiments at the bare and modified electrodes in order to evaluate the successful modification of the electrodes and the electrical properties of the redox-active nanomaterials (MWCNT, ZnO, Fe_3O_4, MWCNT/Fe_3O_4, and MWCNT/ZnO). Electrochemical technique used was cyclic voltammetry and the parameters estimated were peak potential separation (ΔE), formal reduction potential ($E_{1/2}$), peak potential, peak current (Ip) and $\frac{Ipa}{Ipc}$ (the ratio of anodic to cathodic peak current).

3.8.2 Electrocatalytic and electro analysis experiments

3.8.2.1 Electrocatalysis

Investigations on the comparative electrocatalytic behaviour of designed electrodes in response to analytes were conducted using cyclic voltammetry and electrochemical impedance techniques. Cyclic voltammetric experiment was run at 25 mVs^{-1} scan rate with -0.2 to 1.0 V potential window. Parameters measured from the experiment were; ΔE, $E_{1/2}$, Ip, and Ep. EIS analysis of analyte at bare and modified electrodes was conducted at 0.50 V fixed potential within 100000 - 0.1 frequency range in Hz and amplitude of 0.0100 V. Double layer capacitance (C_{dl}), charge transfer resistance (R_{ct}), waburg (W) and solution resistance (R_s) were estimated. Also, SWV at 25 Hz frequency, amplitude of 0.019 V, 0.005 V potential step at an applied 0.58 V potential (choline peak obtained from cyclic voltammetry experiments) in potential windows of 0.2 to 0.8 V and chronoamperometry with 4 s equilibration time at an interval of 50 s was employed to determine the sensitive, LoD of choline (Cho) at modified nanocomposite electrodes with optimum performance with response to the analytes.

The effect of interfering ascorbic acid (AA) and dopamine (DA) in the presence of choline was likewise examined using same techniques (SWV and CA). The bare GCE and modified GCE, silver/silver chloride in saturated potassium chloride and platinum electrodes were used as working, reference, and counter electrode, respectively in all the electrocatalytic experiments. In

addition, scan rate influence on the electrochemical response of choline at best electrodes (nanocomposite modified electrodes) was investigated using CV within 25 - 400 mVs^{-1} scan rates. A direct proportional relationship exists between the peaks potential and scan rates. Plots of current (Ip) versus square root of scan rate $(v/mVs^{-1})^{1/2}$, Ip against scan rate (Vs^{-1}), and peak potential versus log of scan rate (v) were obtained. The graphs showed diffusion controlled electrochemical processes. Kinetics parameters examined include; tafel slope (b), number of electron transferred (n), electron transferred coefficient (α), diffusion coefficient (d) in cm^2s^{-1}, surface concentration of electro active specie (choline) (Γ) in $molcm^{-2}$, and electrode reaction standard rate constant (ks) in s^{-1}.

3.8.2.2 Electroanalysis

Comparative electroanalysis experiment of analyte at electrode of optimum performance was carried out via concentration studies using square wave voltammetry (SWV) measurement in LiCl solution (pH 7.3) containing 3×10^{-7} to 2.2×10^{-6} M choline concentrations prepared in LiCl at same parameters (25 Hz frequency, amplitude of 0.019 V, 0.005 V potential step at an applied 0.58 V potential) earlier mentioned in 3.8.2.1 within 0.2 to 0.8 V potential windows. Chronoamperometry was also used. Sensitivity, limit of detection (LoD), and standard deviation were derived from the plot of peak current and analyte concentrations.

3.9. Electroanalytical performance of modified electrodes for choline determination in pharmaceutical samples

Investigation was conducted on practical potential of the modified electrodes (designed sensors) for choline (Cho) detection in real sample of choline dietrary supplements using square wave evoltammetry following dilution with no other treatment and spiking with different concentrations of choline using addition methods. Percentage recovery and relative standard deviation was found and compared with previously studied biosensor electrodes.

3.10. Validation of results

Statistical tool such as t-test, F-test and Q test were used to validate obtained results at modified electrode in real sample analysis.

CHAPTER FOUR
RESULTS AND DISCUSSION

4.1 Leaf and flower extracts of *C. viminalis*

A red and light orange colour extract with a pleasant smell was obtained for *C. viminalis* leaves and flowers accordingly on boiling specific gram (5 g) of the leaves and flowers separately in a beaker containing 100 ml of distilled water for 15 min. A pH of 5.32 and 3 .89 pH was found for leaves and flowers extract.

4.1.1 Phytochemical test

On treating leaf and flower extracts of *Callistemon viminalis* (*C. viminalis*) with alkaline reagent of sodium hydroxide, a brown and an orange colour precipitate was formed respectively with a yellow colour precipitate and blue colour precipitate when leaf and flower extracts were treated with 0.1 M lead acetate solution indicating the presence of flavonoids. A grey black and black solution was formed on adding few drops of 0.1 M alcoholic iron (III) chloride hexahydrate on flower and leaf extracts indicating the presence of phenols.

4.1.1.1 Determination of total phenolic content (TPC) in *Callistemon viminalis*

Total PC of leaves and flowers extracts of C. viminalis was estimated from gallic acid standard calibration plot using equation 4.1

$$\mathrm{C} = \frac{cV}{m} \qquad 4.1$$

Where C mg/ml is the total phenolic content in gallic acid equivalent (GAE), c is the concentration of gallic acid established from the calibration curve, V is the volume of extract and m is the mass of extracts used. The linear plot (Figure 4.1) gave 0.9998, 0.002 μg/ml, and 0.1066 regression, slope, and intercept values accordingly.

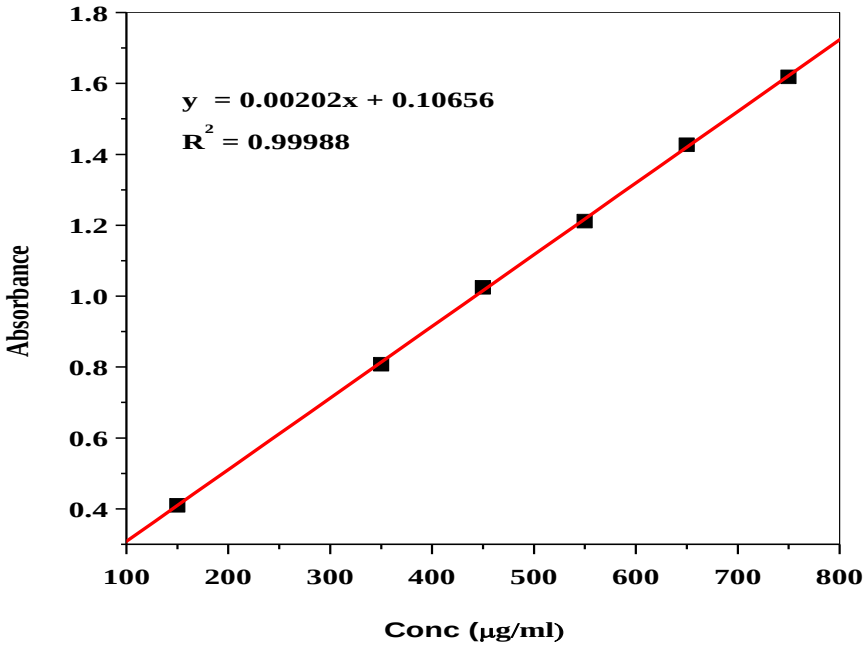

Figure 4.1: Gallic acid standard calibration curve.

Table 4.1: Total phenolic content of *C. viminalis* leaf and flower extracts

Extracts in methanol	Concentration of extract	Absorbance	TPC (mg of GAE/g dried sample
Leaf	5 mg/5 ml	0.532	12.636
Flower	5 mg/5 ml	1.093	29.320

4.1.1.2 Determination of total flavonoid content (TFC) in *Callistemon viminalis*

Total flavonoids composition of *C. viminalis* leaves and flowers extract from quercetin standard calibration curve as presented in Figure 4.2 were 19.371 and 0.634 QE mg/g (Table 4.2) using equation 1. QE is total flavonoids content in quercetin equivalent. The content of flavonoids was higher in *C. viminalis* leaf extract than in the flower. Calibration curves obeyed Beer-lamberts. Regression, slope, and intercept values obtained from the curve were 0.9647, 0.0007 µg/ml, and 0.5701 respectively. Comparing TFC of leaf and flower extracts of *C. viminalis*, the content of phenol in flowers was higher than in leaf.

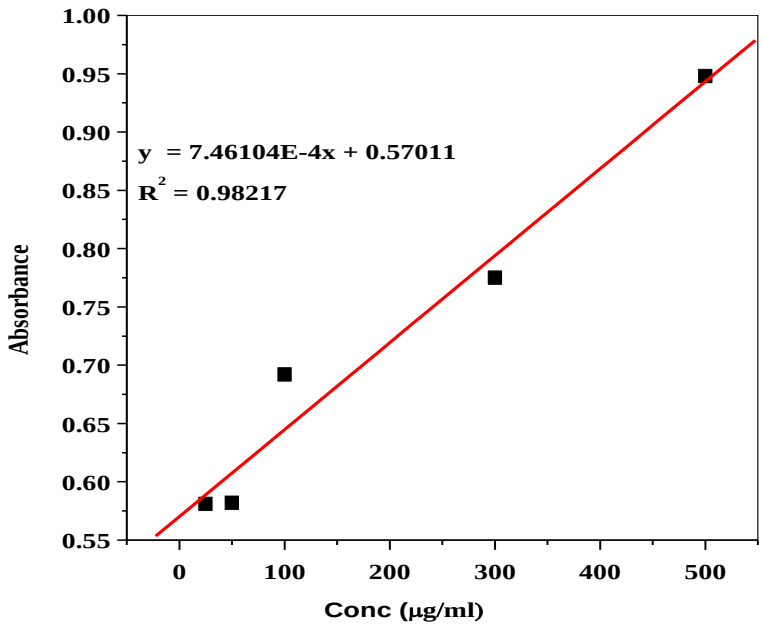

Figure 4.2: Quercetin standard calibration curve.

Table 4.2: Total flavonoid content of *C. viminalis* leaf and flower extracts.

Extract in methanol	Concentration of extract	Absorbance	TFC (mg of QE/g dried sample
Leaf	5 mg/5 ml	0.811	19.371
Flowers	5 mg/5 ml	0.578	0.634

The higher TFC in leaves than flower is supposedly due to the abundant shikimic acid in the leaf compared to other organs while the lower TFC in flowers is indicative of the depletion of the flavonoids due to colour development in the flower petals. Shikimic acid is a precursor in the flavonoids biosynthetic pathway and has been reported to be higher in leaves than other organs due to the photosynthetic activities in the leave (Andersen, 2006; Saboonchian *et al.*, 2014; Sone *et al.*, 2015). The higher TPC in flower from this study could have been influenced by the developmental phase, the associated colour change of the petals due to oxidation resulting in the easy rupture and release of the cell wall bonded phenolic compounds in the flower. The higher TPC in this study corroborates the report on groundcover rose flower (Sone *et al.*, 2015). An increased in total phenol content have been reported to be influenced by stages of development and colour change (Schmitzer *et al.*, 2010).

4.1.2 Characterization of iron (III) oxide nanoparticles

4.1.2.1 Fourier transform infrared spectroscopy

Fourier transform infrared (FTIR) analysis was carried out on extracts and synthesized iron (III) oxide nanoparticles (Fe_3O_4NP) in order to determine compounds and the bonding properties present. In the FTIR spectra (Figure 4.3a) leaf and flower extracts (Figure 3b) spectrum displayed important vibrations peaks at about 3300 and 1729,1724 cm^{-1} which are assigned to O-H stretch of alcohol/phenol and C = O of carbonyl group (aldehyde, and ketone). These peaks are possible reducing agents that are responsible for the formation of iron (III) oxide nanoparticles. The observed peak at 1735 cm^{-1} in $FeCl_3.6H_2O$ is ascribed to deformation of water molecules, suggesting the existence of physio sorbed water on surface of ferric chloride (Inam *et al.*, 2018). The FTIR spectrum of Fe_3O_4NP synthesized by *C. viminalis* leaf extract (Fe_3O_4NPL) showed a reduced intensity in the vibration peaks at 3205, and 1735 cm^{-1} corresponding to O-H stretch of alcohol/phenol group, O-H stretch of carboxylic acid group, aldehyde, and ketone (Figure 4.3a). While peaks at 508 and 578 cm^{-1} are Fe-O stretching of Fe_3O_4NP respectively (Figure 4.3a). For Fe_3O_4NP synthesized by *C. viminalis* flower extract (Fe_3O_4NPF) as shown in (Figure 4.3b), peaks corresponding to the presence of phenol, aldehyde, and ketone, were identified while peaks at 600 and 520 cm^{-1} corresponds to bending and Fe-O stretching of Fe_3O_4NPF respectively. Asymmetry and symmetry stretching vibration of COO^-(carboxylate group) that proved the combination of protein with nanoparticles was noticed at 1575; 1421 and 1597;1431 cm^{-1} on Fe_3O_4NPL and Fe_3O_4NPF spectra.

The elongation of the peaks of aldehyde, ketone, carboxylic acid C = O stretch, C = C aromatic bending, C- O alkoxy stretch, C = C aromatic bending and a broad band of alcohol/phenol O-H stretch in both spectra (Figure 4.3a, b) indicates good interaction of plant the extracts and the precursor. Vibrational bands of green mediated Fe_3O_4NPs are quite close to reported vibrations (Patra & Baek, 2017; Yang *et al.*, 2006). Figure 4.3c, d depicts FTIR of raw MWCNT, f-MWCNT, MWCNT/Fe_3O_4NP while the observed vibrational band (cm^{-1}) and their assignment are given in Table 4.3.

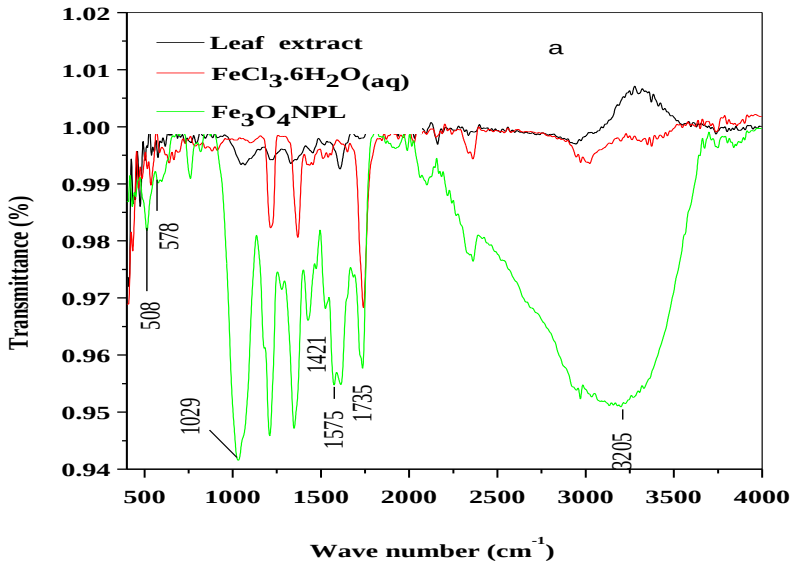
a
Leaf extract
FeCl3.6H2O(aq)
Fe3O4NPL
Transmittance (%)
Wave number (cm-1)
508
578
1029
1421
1575
1735
3205

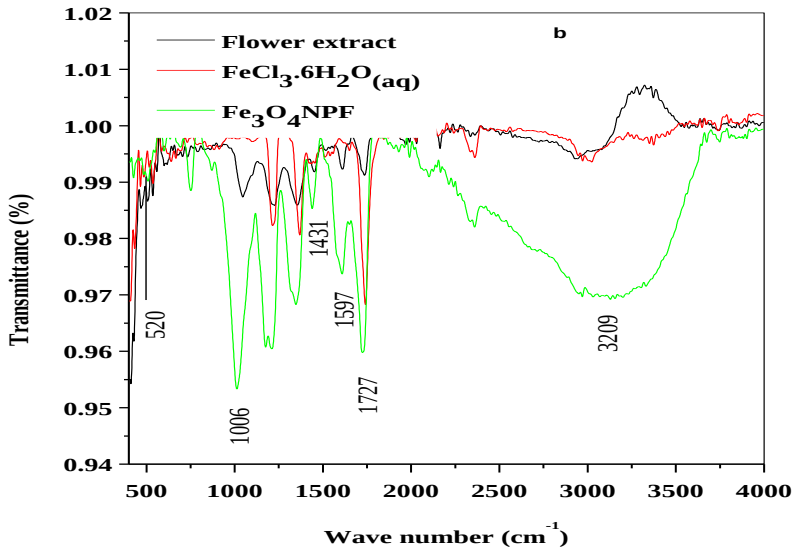
b
Flower extract
FeCl3.6H2O(aq)
Fe3O4NPF
Transmittance (%)
Wave number (cm-1)
520
1006
1431
1597
1727
3209

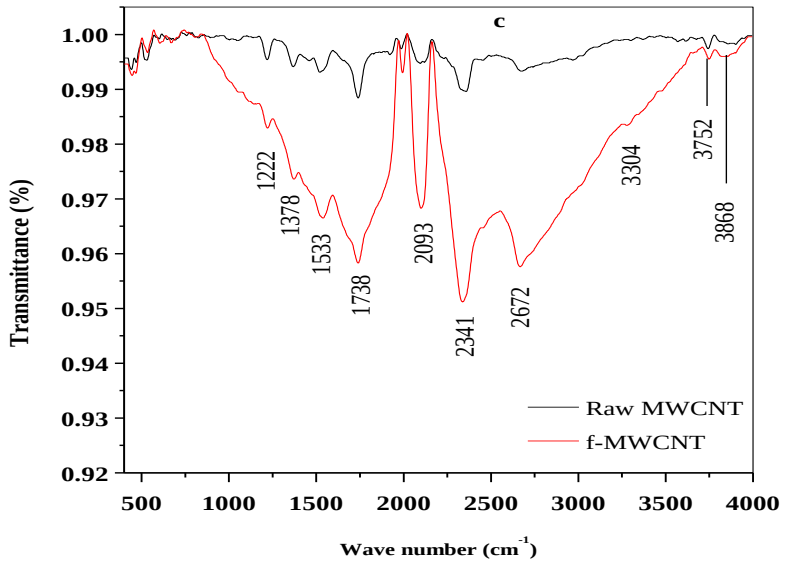
c
Transmittance (%)
Wave number (cm-1)
1222
1378
1533
1738
2093
2341
2672
3304
3752
3868
Raw MWCNT
f-MWCNT

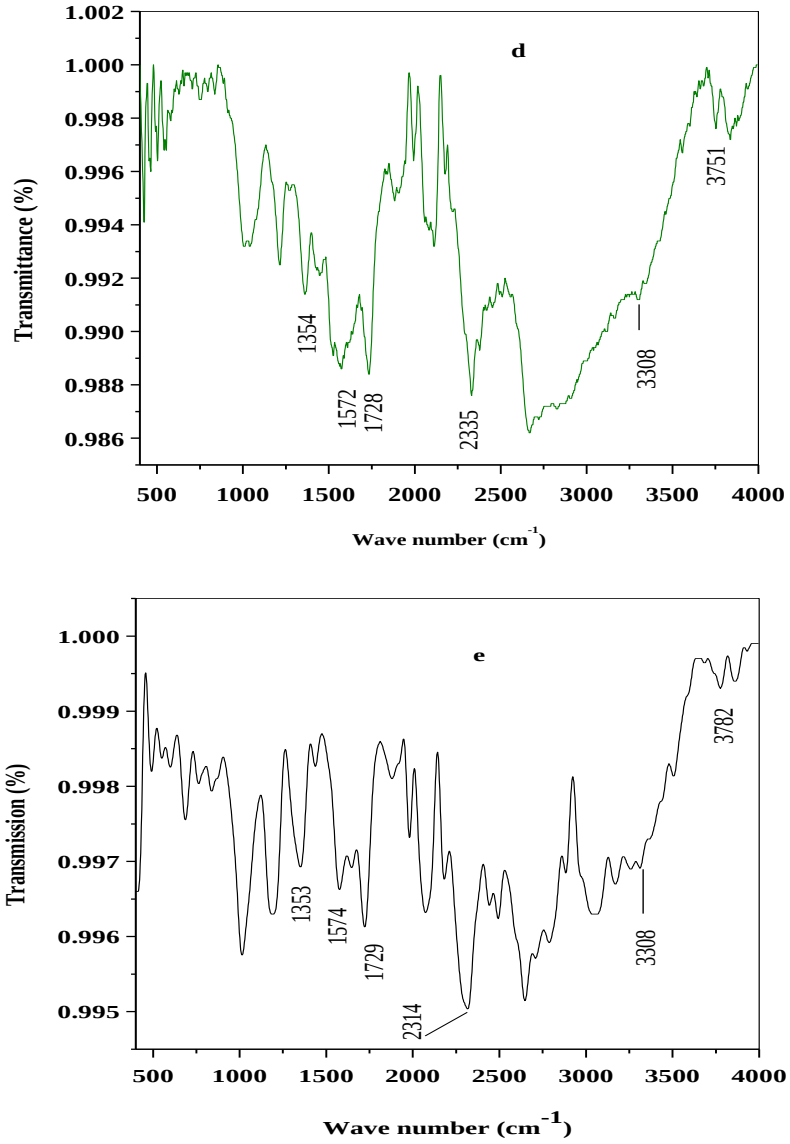

Figure 4.3: FTIR spectra of (a, b) Fe_3O_4NP synthesized from *C. viminalis* leaves anf flowers extracts (c) Raw and f-MWCNT (d) f-MWCNT/Fe_3O_4NPL (d) f-MWCNT/Fe_3O_4NPF accordingly.

Table 4.3: Summary of the FTIR vibration bands.

Raw MWCNT	**f-MWCNT (cm^{-1})**	**f-MWCNT/ Fe_3O_4NPL (cm^{-1})**	**f-MWCNT/ Fe_3O_4NPF (cm^{-1})**	**Assignment** (Atieh *et al.*, 2010)
3743	3772	3751	3782	Free hydroxyl group O-H
3298	3304	3308	3308	O-H stretch mode from carboxyl groups (O=C-OH and C-OH)
2351	2341	2335	2314	O-H stretch from strongly hydrogen –bonded-COOH
1735	1738	1728	1729	Stretching vibration of carboxylic group (C=O)
1510	1533	1572	1574	O-H deformation vibrations
1370	1378	1354	1353	Bending deformation in carboxylic groups (-COOH) due to the formation of CN bond in amino functional group.

The slight red shifts of the O-H, -COOH, and C=O in raw and f-MWCNT spectra and higher intensity is attributed to increased number of these groups on MWCNT surface after functionalization (Figure 4.3c). In Figure 4.3d, e, the red and blue shifts of distinct major peaks found in the f-MWCNT and the presence of new peaks around 553 - 1214 cm^{-1} is an evidence of successful formation of MWCNT/Fe_3O_4NP composite.

4.1.2.2 Ultraviolet visible (UV-Vis) spectroscopy

UV-Vis spectroscopy was used to determine the optical property of synthesized Fe_3O_4NP and its electrical conductivity (insulator, semiconductor or a conductor) through energy band gap of UV absorption spectra. The UV-Vis spectra for Fe_3O_4NP synthesized from leaf extract (Fe_3O_4NPL) and flower extract (Fe_3O_4NPF) of *C. viminalis* is shown in Figure 4.4a with maximum absorbance observed at 297 and 304 nm. *C. viminalis* leaves and flowers extracts

showed absorbance at 307 and 299 nm respectively (graph not shown). The UV-Vis result for *C. viminalis* extracts and synthesized nanoparticles (Fe_3O_4NPL and Fe_3O_4NPF) indicate a shift in vibrations towards shorter/higher wavelength which suggest a good interaction of *C. viminalis* extract (leaf and flower) and precursor in the formation of Fe_3O_4NP (Sathishkumar *et al.*, 2018). The energy band gap of Fe_3O_4NP synthesized by *C. viminalis* leaves and flowers extracts was obtained by Tauc's formula; $(\alpha hv)n = B(hv-Eg)$ (Khashan *et al.*, 2017) using the absorption peak 297 and 304 nm respectively. The energy band gap values for Fe_3O_4-NPL and Fe_3O_4NPF were 2.79 and 2.89 eV using the absorption peaks 297 and 304 nm respectively. Values are quite close to 2.87 eV reported in the literature (El Ghandoor *et al.*, 2012) inferring synthesized Fe_3O_4NPL and Fe_3O_4NPF as semiconductors since values are less than 5 eV. The UV-Vis spectra of the nanocomposites (Figure 4.4b) exhibits a blue shift as compared with the nanoparticle spectra indicating a good synergy between the Fe_3O_4NP and f-MWCNT.

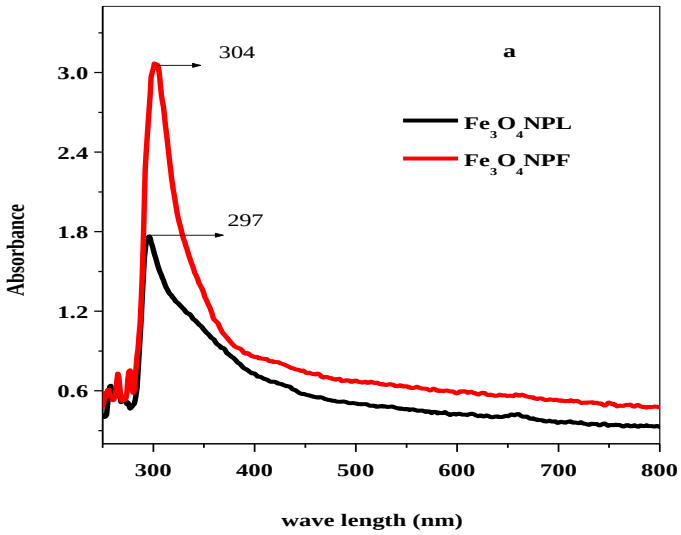

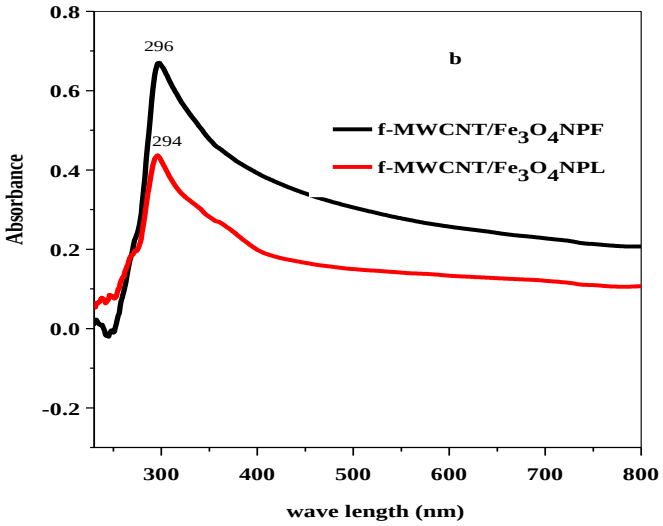

Figure 4.4: UV-Visible spectra for (a) nanoparticles of Fe_3O_4 synthesized from leaves and flowers extract and (b) nanocomposite of f-MWCNT/Fe_3O_4.

4.1.2.3 Scanning electron microscopy

The SEM images of Fe_3O_4NP and Fe_3O_4NPF respectively revealed a uniformly dispersed, agglomerated (Khashan *et al.*, 2017) and nearly spherical in shape Fe_3O_4NP with rough surfaces (Figure 4.5a, b). Rough surface suggests the absorption of carboxylate group existing in protein and acting as surfactant to adhere on nanoparticles surface resulting in the Fe_3O_4NP stabilization as can be seen in Figure 4.5a, b. Mechanism of absorption is presented in the Figure 4.5f.

Figure 4.5c,d,e represents the morphology of SEM image of f-MWCNT, f-MWCNT/Fe_3O_4NPF and f-MWCNT/Fe_3O_4NPL investigated by scanning electron microscopy (SEM). The micrograph revealed functionalized MWCNT (f-MWCNT) to be tube-like in shape, the attachment of Fe_3O_4NP particles on f-MWCNT surface, and the formation of inter particle agglomeration by Fe_3O_4NP due to the inter particle magnetic (Rahmawati *et al.*, 2018).

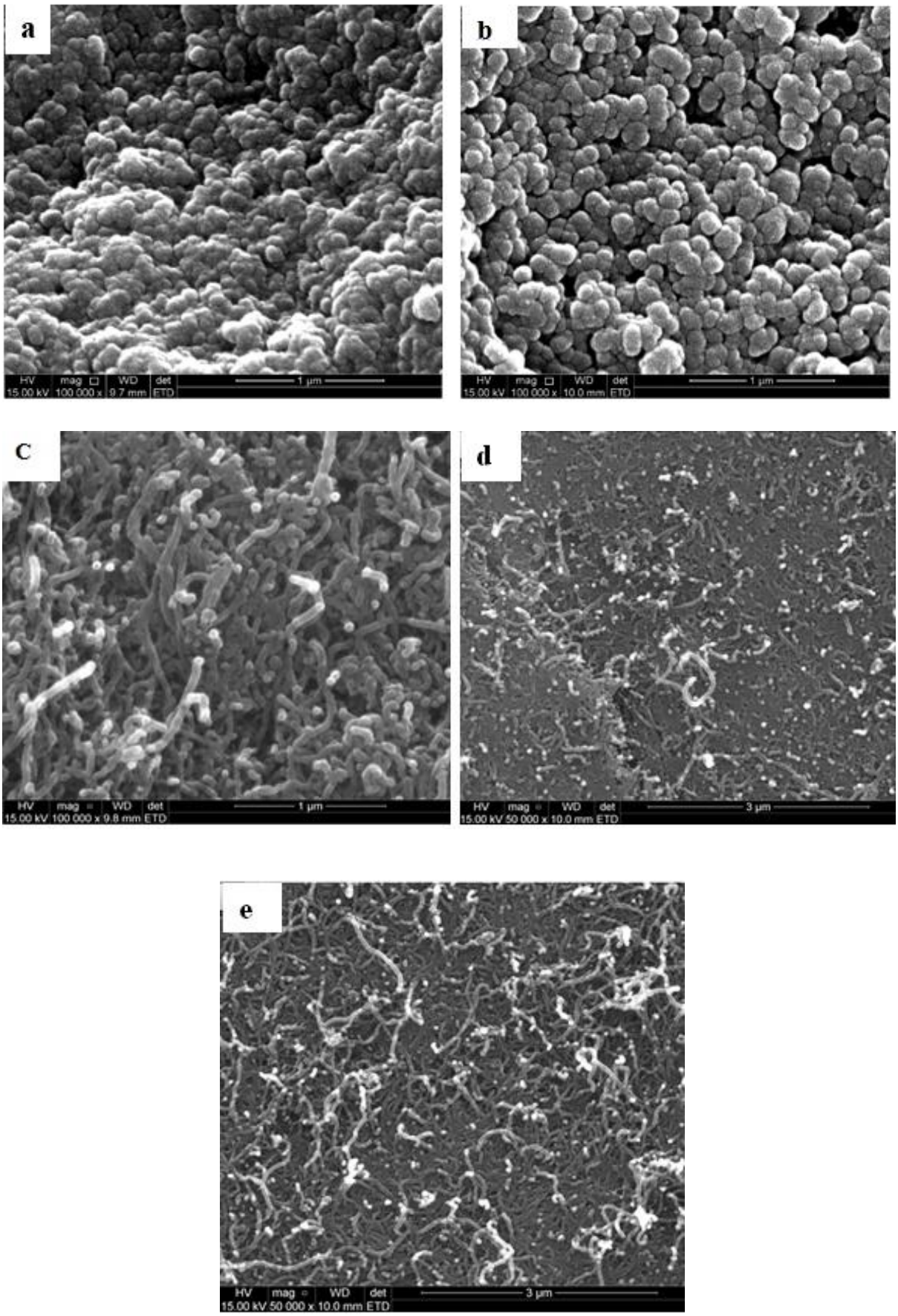
a
HV mag WD det
15.00 kV 100 000 x 9.7 mm ETD
1 µm
b
HV mag WD det
15.00 kV 100 000 x 10.0 mm ETD
1 µm
c
HV mag WD det
15.00 kV 100 000 x 9.8 mm ETD
1 µm
d
HV mag WD det
15.00 kV 50 000 x 10.0 mm ETD
3 µm
e
HV mag WD det
15.00 kV 50 000 x 10.0 mm ETD
3 µm

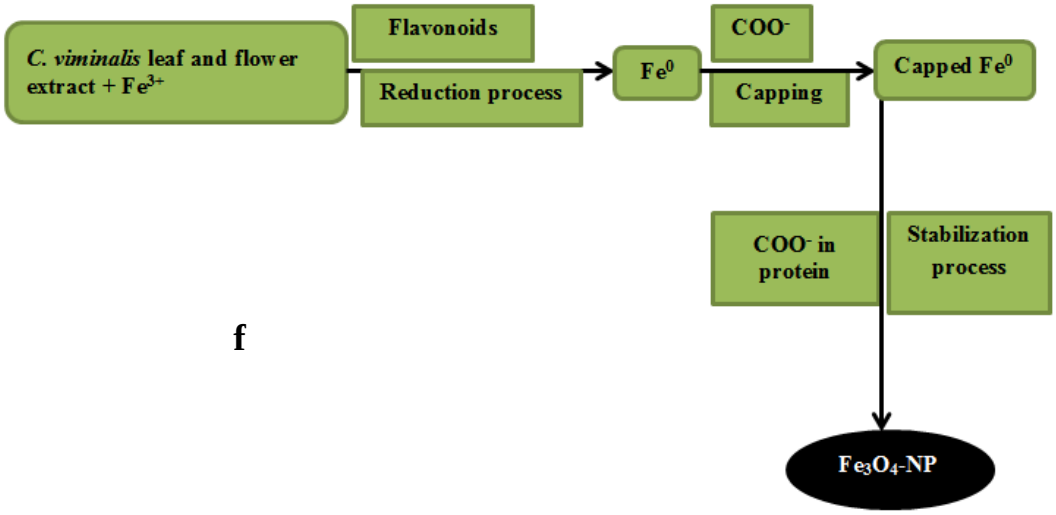

Figure 4.5: Scanning electron microscopic image of (a) Fe_3O_4NPL (b) Fe_3O_4NPF of (c) f-MWCNT (d) f-MWCNT-Fe_3O_4NPL and (e) f-MWCNT-Fe_3O_4NPF accordingly; (f) possible absorption mechanism of bio-reduced Fe_3O_4NP.

4.1.2.4 Energy dispersive X-ray

The EDX results shown in Figure 4.6a, b revealed the presence of iron and oxygen in the Fe_3O_4NP synthesized from the leaves extract (Fe_3O_4NPL) with mean value of iron and oxygen as 43.68 and 56.32 respectively. Mean value of iron and oxygen for Fe_3O_4NPF was 33.58 and 66.42.

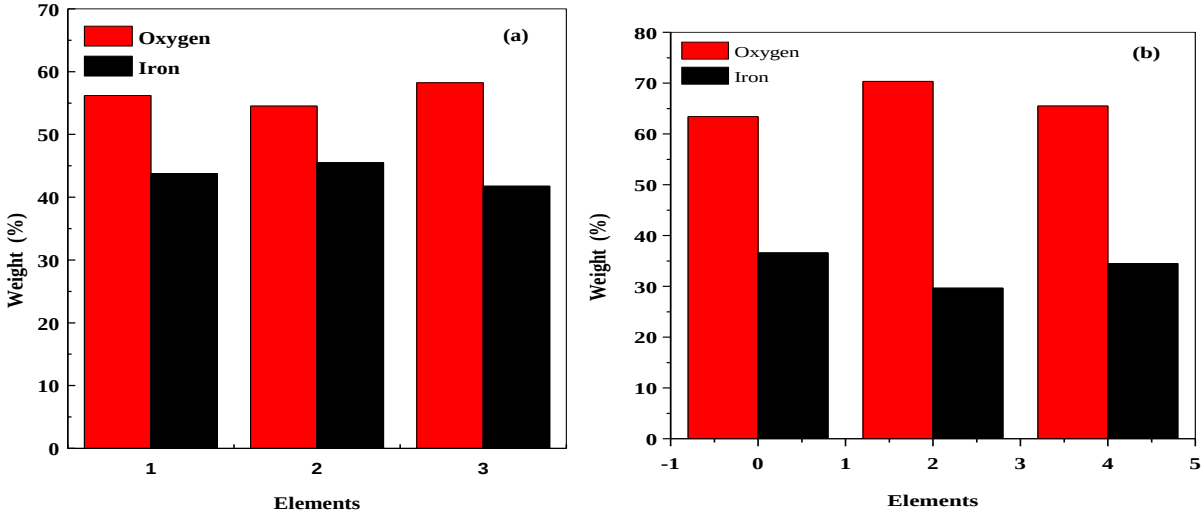

Figure 4.6: Energy dispersive X-ray bar chart of (a) Fe_3O_4NPL and (b) Fe_3O_4NPF.

4.1.2.5 Transmission electron spectroscopy (TEM)

TEM image of Fe_3O_4NP synthesized from *C. viminalis* leaves extract (Fe_3O_4NPL) shown in Figure 4.7ai showed the shape of iron Fe_3O_4NPL nearly spherical, spatially distributed with some particles agglomerated and the size distribution is shown in Figure 4.7aii using image J software application. Mean diameter, and average particle size, for N = 237 of the synthesized particle (Fe_3O_4NPL) was 5.313 nm, 5.3 ± 1.9. Figure 4.7bi is the TEM image of the Fe_3O_4-NPF synthesized from flowers extract of *C. viminalis*. A well dispersed, spherical in shape nanoparticles was observed. Figure 4.7bii is the size distribution of Fe_3O_4NPF with mean diameter and average particle size of 1.127 nm, and 1.1 ± 0.8 for N = 2163 (N = number of counts).

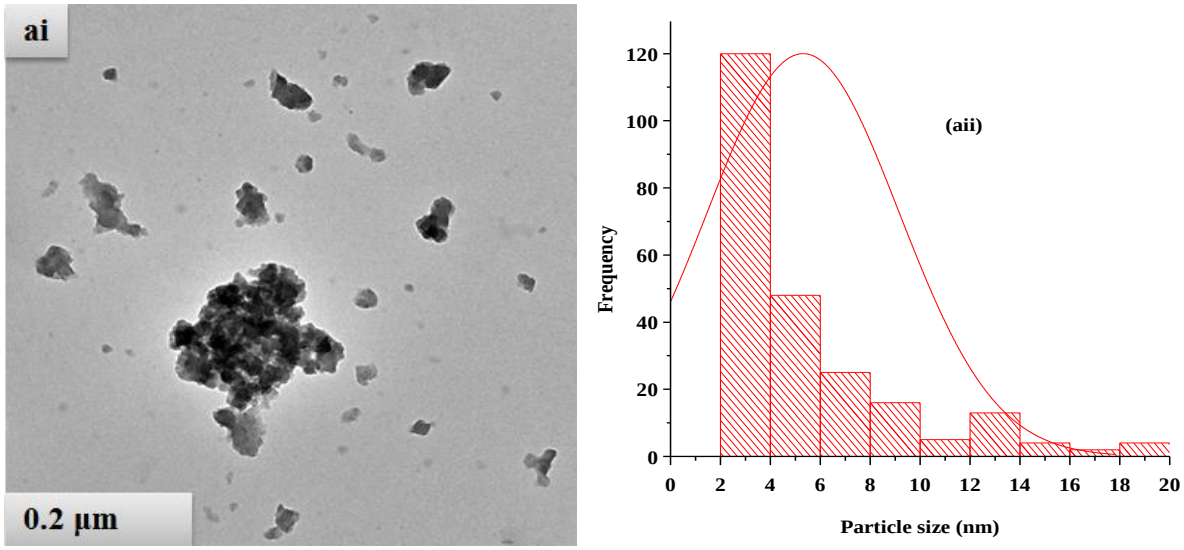

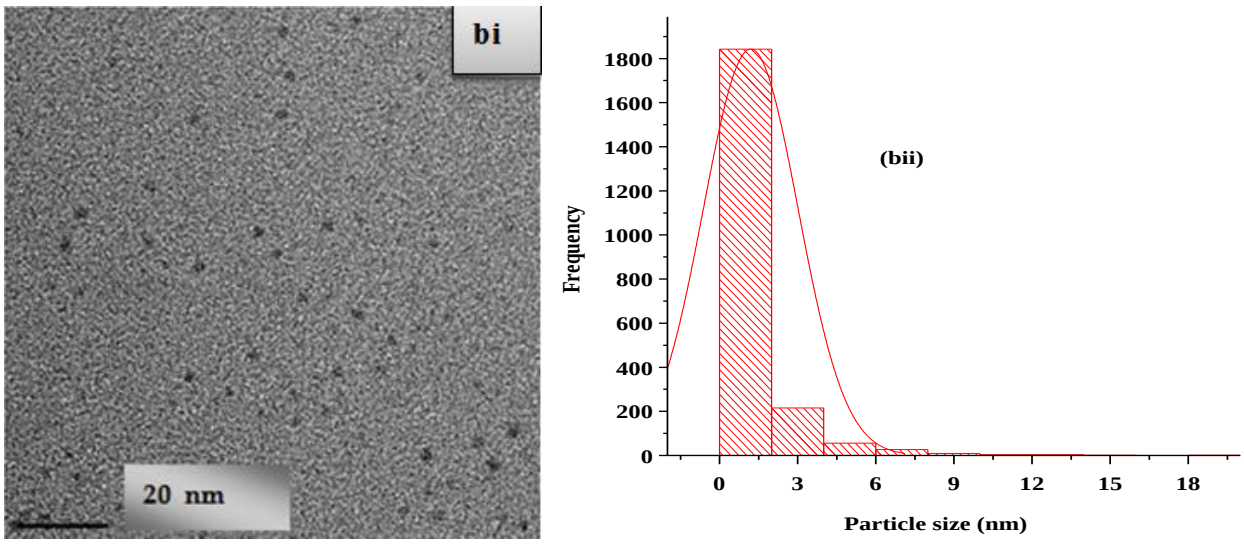

Figure 4.7: TEM image of (ai) Fe_3O_4NPL (bi) Fe_3O_4NPF; particles size distribution of (aii) Fe_3O_4NPL (bii) Fe_3O_4NPF.

4.1.2.6 Zeta potential analysis

Zeta potential analysis of Fe_3O_4NP was conducted to obtain information on the surface charge of dispersed particles (Fe_3O_4NP). Particles with zeta potential values within the range of ±30 mV are widely considered stable (El Ghandoor *et al.*, 2012; Senthilkumar *et al.*, 2017). The zeta potential values obtained for Fe_3O_4NP synthesized from leaves (Fe_3O_4NPL) and flowers extract (Fe_3O_4NPF) were -20.0 mV and -28.4 mV respectively. The values are well comparable to that published in the literature (Bhattacharjee, 2016). Figure 4.8a and b gives summary of the zeta potential analysis of Fe_3O_4NPL and Fe_3O_4NPF respectively. The result of the zeta potential analysis showed good stability for Fe_3O_4NP. A higher stability was observed for Fe_3O_4NPF than Fe_3O_4NPL due to greater surface charge (-28.4 mV), which could be attributed to the existence of more dense electrostatic forces within the synthesized particles and compositions of the reducing agent phenol compounds present in the flowers extract (Senthilkumar *et al.*, 2017).

(a)

Results

	Mean (mV)	Area (%)	St Dev (mV)
Zeta Potential (mV): -20.0	Peak 1: -20.0	100.0	4.12
Zeta Deviation (mV): 4.12	Peak 2: 0.00	0.0	0.00
Conductivity (mS/cm): 0.0656	Peak 3: 0.00	0.0	0.00
Result quality: Good			

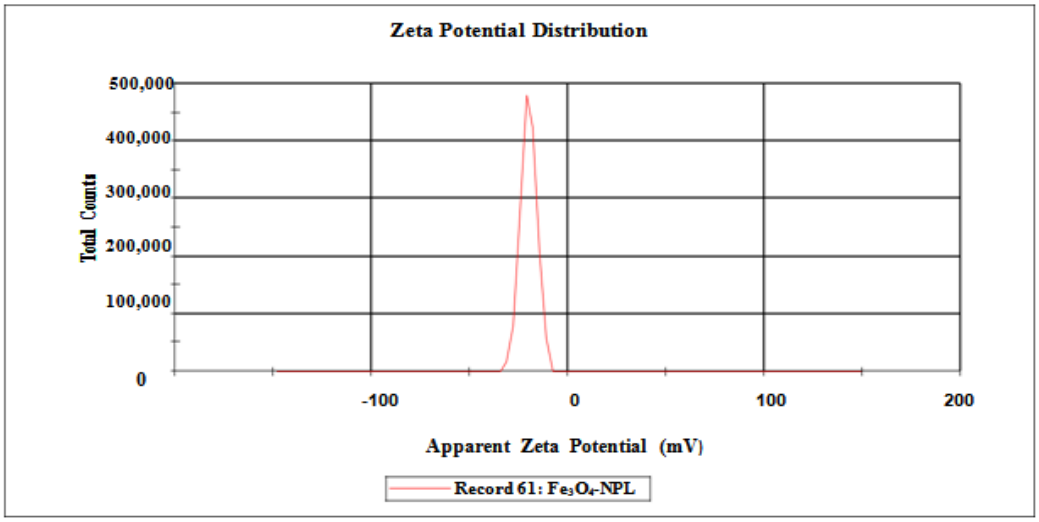

(b)

Results

	Mean (mV)	Area (%)	St Dev (mV)
Zeta Potential (mV): -28.4	Peak 1: -28.4	100.0	4.93
Zeta Deviation (mV): 4.93	Peak 2: 0.00	0.0	0.00
Conductivity (mS/cm): 0.0654	Peak 3: 0.00	0.0	0.00
Result quality: Good			

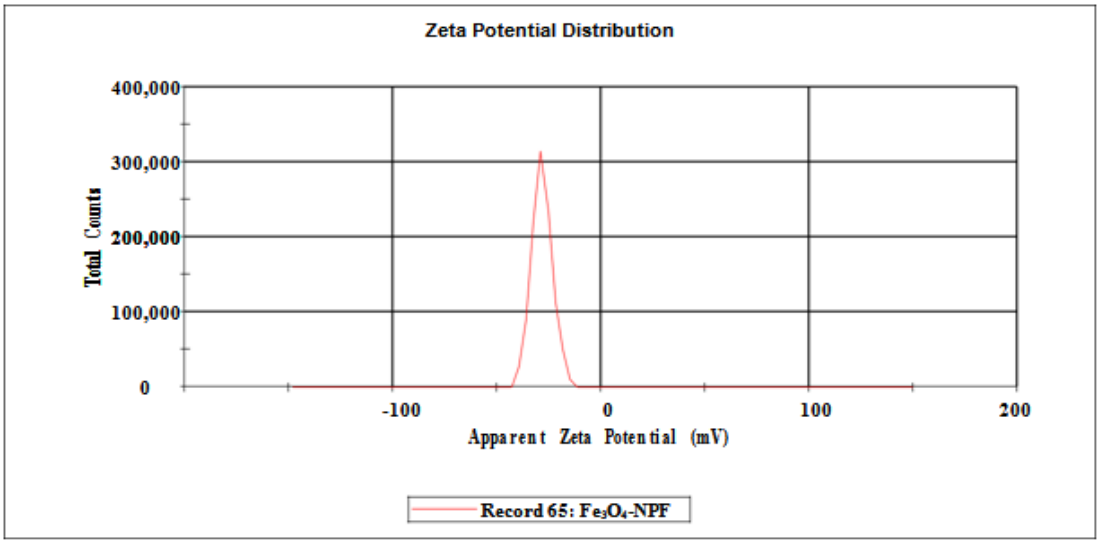

Figure 4.8: Zeta potential of (a) Fe_3O_4NPL (b) Fe_3O_4NPF.

4.1.2.7 Thermogravimetric analysis (TGA)

TGA analysis of Fe_3O_4NP was conducted with SDT Q600 V20.9 Build 20 thermogravimetric analyser of DSC-TGA standard in an unreactive nitrogen gas environment at a high furnace temperature using RAMP method and a heating rate of 10 °C min^{-1}. The thermogravimetric curves of Fe_3O_4NP synthesized from *C. viminalis* leaves (Fe_3O_4NPL) and flowers extracts (Fe_3O_4NPF) are shown in Figure 4.9 with three stages of weight loss. In Fe_3O_4NPL and Fe_3O_4NPF, the first stage lies within 25°C - 65 °C, and 29 - 58 °C with an insignificant weight loss (1%) which could be attributed to loss of water, volatile solvents. The second stage started at 65 °C and 58 °C for Fe_3O_4NPL and Fe_3O_4NPF respectively and ended at 197 °C with weight loss of 13% and 10% respectively and is assigned to loss of water of crystallization and gas desorption. Finally, the third stage at 636 °C and 654 °C for Fe_3O_4NPL and Fe_3O_4NPF had a significant weight loss of 44% and 50% which is assigned to transition phase of Fe_3O_4 to FeO since FeO is stable (thermodynamically) at temperatures greater than 570 °C (Mahdavi *et al.*, 2013) with a reaction formula at possible equilibrium phase :

$$Fe_3O_{4(s)} \rightleftharpoons 3FeO_{(s)} + \frac{1}{2}O_{2(g)}$$

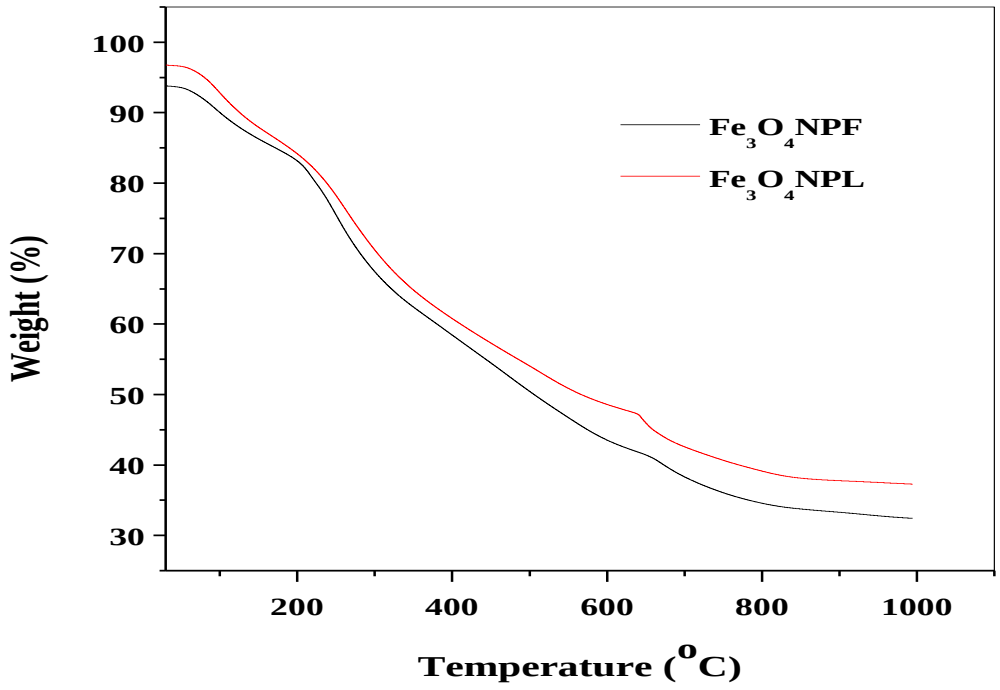

Figure 4.9: Thermogravimetric curves of Fe_3O_4NP from leaves and flowers of *C. viminalis* extracts.

4.1.2.8 X-ray diffraction study (XRD)

XRD spectra (Figure 4.10a) of synthesized Fe_3O_4NP from *C. viminalis* leaves and flowers (Fe_3O_4NPL and Fe_3O_4NPF) extracts conducted from 20^o to 80^o at 2 theta. The presence of a hump instead of a peak observed at 28.560 and 26.620 for Fe_3O_4NPL and Fe_3O_4NPF respectively could possibly be due to the covering of Fe_3O_4NP with organic substances (Kouhbanani *et al.*, 2018). Therefore, the XRD pattern for the Fe_3O_4NP showed deficiency in distinctive peaks which suggest the amorphous nature of Fe_3O_4NPL and Fe_3O_4NPF and proof that surface of the iron oxide is coated by organic materials (Kouhbanani *et al.*, 2018). Similar XRD pattern was reported in the literature (Kouhbanani *et al.*, 2018; Kouhbanani *et al.*, 2019). The XRD spectrum depicts Fe_3O_4NP as confirmed from the colour of the precipitates formed during the synthesis (Figure 4.10b) as opposed to brick red/brown colour expected for Fe_2O_3 (heamatites).

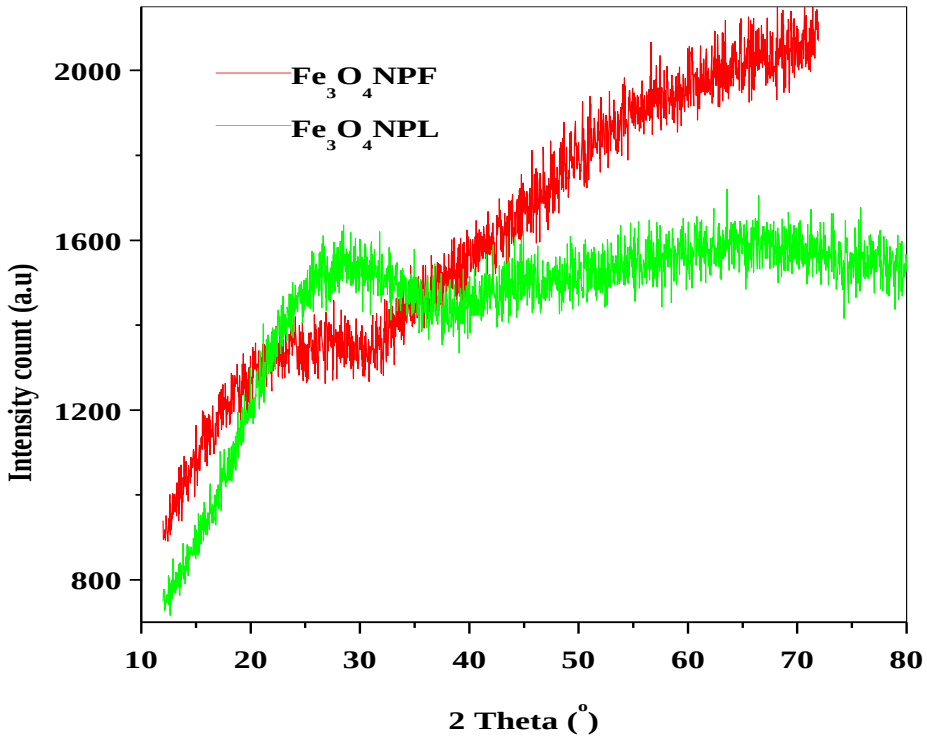

Figure 4.10a: X-ray diffraction pattern of Fe_3O_4NP from leaves and flowers of *C. viminalis* extracts.

Figure 4.10b: Colour formation of Fe_3O_4NPF and Fe_3O_4NPL with $FeCl_3.6H_2O$ during synthesis.

4.1.3 Electrochemical studies

4.1.3.1 Cyclic voltammetric characterization of MWCNT/Fe_3O_4NP composite

The investigation of charge transfer properties of bare GCE, GCE/f-MWCNT, GCE/Fe_3O_4NPL, GCE/Fe_3O_4NPF, GCE/f-MWCNT/Fe_3O_4NP (GCE/f-MWCNT/Fe_3O_4NPL, and GCE/f-MWCNT/Fe_3O_4NPF) electrodes were carried out using cyclic voltammetry in 5 mM $K_3[Fe(CN)_6]$ (probe) prepared in 0.1 M phosphate buffer solution (PBS) pH 7.4 at scan rate 25 mVs^{-1}. The voltammogram obtained over a potential window of -0.2 - 1. 0 V with 0.02 V potential steps is shown in Figure 4.11. The multi-walled carbon nanotube/metal oxide (f-MWCNT/Fe_3O_4) nanocomposites modified electrodes gave greater current response as compared to other electrodes which was attributed to a successful modification of the nanocomposites electrodes, good synergy between f-MWCNT and Fe_3O_4NP with an improved electron transport properties, with high electronic conductive nature. Thus, GCE/f-MWCNT/Fe_3O_4 nanocomposites electrodes demonstrated greater charge transfer properties. However, electron transport properties were optimal at GCE/f-MWCNT/Fe_3O_4NPL than GCE/f-MWCNT/Fe_3O_4NPF considering its current response which was approximately two times higher. All the electrodes displayed redox peaks of $K_3[Fe(CN)_6]$ solution with the exception of GCE/Fe_3O_4NPL and GCE/Fe_3O_4NPF which could be due to fast electron transport at the electrodes or overlap between $K_3Fe(CN)_6$ and Fe_3O_4 redox peaks (Fayemi *et al.*, 2017).

The sequence of oxidation peak current response is GCE/f-MWCNT/Fe_3O_4NPL (0.32V 74.3 μA) > GCE/f-MWCNT/Fe_3O_4NPF (0.26V 44.1 μA) > GCE/f-MWCNT (0.25V 27.7 μA) > GCE (0.26V 17.3 μA). The electrochemical process at the nanocomposites modified electrodes was

quasi reversible since anodic to cathodic peak current (Ipa/Ipc) ratios were greater than 1 (1.05 and 1.14) for GCE/f-MWCNT/Fe_3O_4NPL and GCE/f-MWCNT/Fe_3O_4NPF respectively. Potential peak to peak separation (ΔE) values (163, 102 mV) at the respective nanocomposites modified electrodes applying equations 2.1 were greater than the theoretical value (59 mV) expected for a fast one-electron transport (Haque *et al.*, 2013; Zangeneh Kamali *et al.*, 2014).

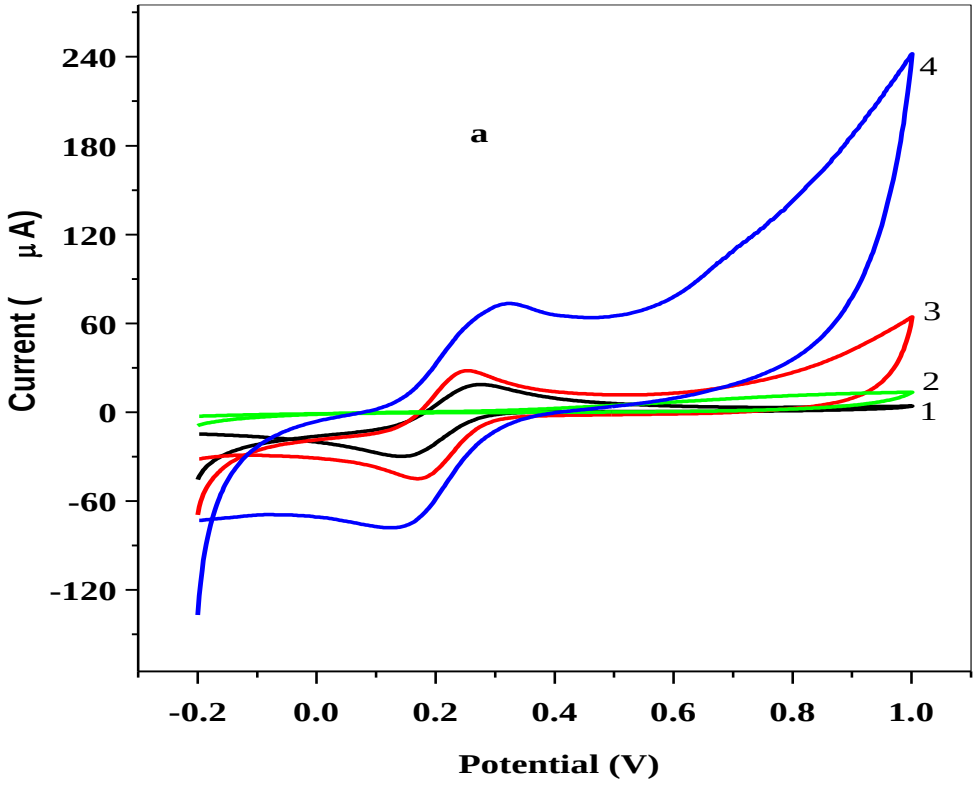

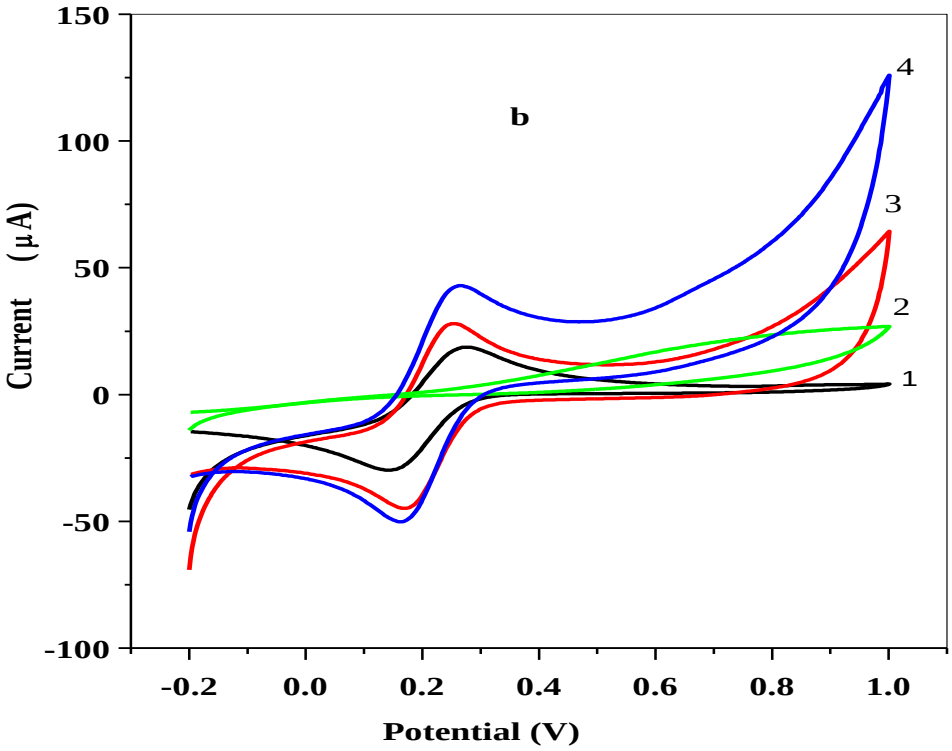

Figure 4.11: Cyclic voltammogram of (a,b1) bare GCE (a2) GCE/Fe_3O_4NPL (b2) GCE/Fe_3O_4NPF (a,b3) GCE/f-MWCNT (a4) GCE/f-MWCNT/Fe_3O_4NPL and (b4) GCE/f-MWCNT/Fe_3O_4NPF in 10 mM PBS solution pH 7.4 containing 5 mM $K_3[Fe(CN)_6]$.

4.1.3.2 Effect of varying scan rate at GCE/F-MWCNT/Fe_3O_4NP electrodes

The influence of scan rate on potential, and current peaks was conducted on nanocomposites modified electrodes (GCE/f-MWCNT/Fe_3O_4NPL and GCE/f-MWCNT/Fe_3O_4NPF) by cyclic voltammetry in 5 mM K3[Fe(CN)6] prepared in 0.1 PBS, pH 7.4 in the range of 25-500 mVs^{-1}. Increase in current response and a shift of anodic potential to the right was observed with increasing scan rate as shown in Figure 4.12a, b. Potential peak separation (ΔE) increases with increasing scan rate confirming quasi-reversible electrochemical process. The plot of current versus square root of scan rate gave 0.99213 and 0.9968 regression value for GCE/f-MWCNT/Fe_3O_4NPL and GCE/f-MWCNT/Fe_3O_4NPF electrodes as shown in Figure 4.12c, d respectively, indicating diffusion controlled processes expected for a direct proportional relationship. Active surface area for the GCE/f-MWCNT/Fe_3O_4NPL and GCE/f-MWCNT/Fe_3O_4NPF modified electrodes were found to be 4.7×10^{-2} and 1.0×10^{-1} cm^2 respectively using Randles-Sevick equation (2.2) from the slope values in Figure 4.12c, d.

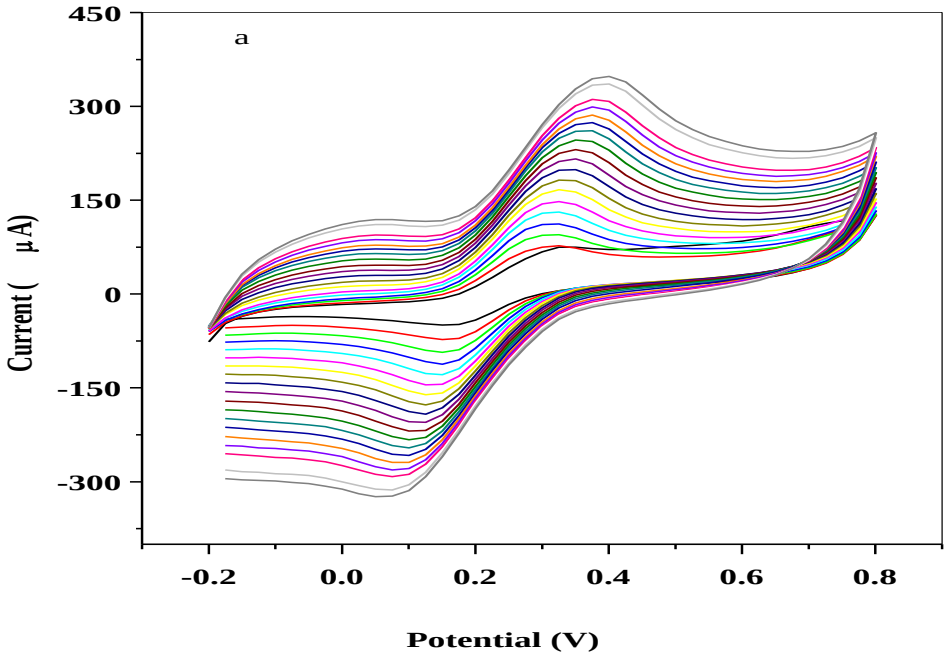
a
450
300
150
0
-150
-300
Current (µA)
-0.2
0.0
0.2
0.4
0.6
0.8
Potential (V)

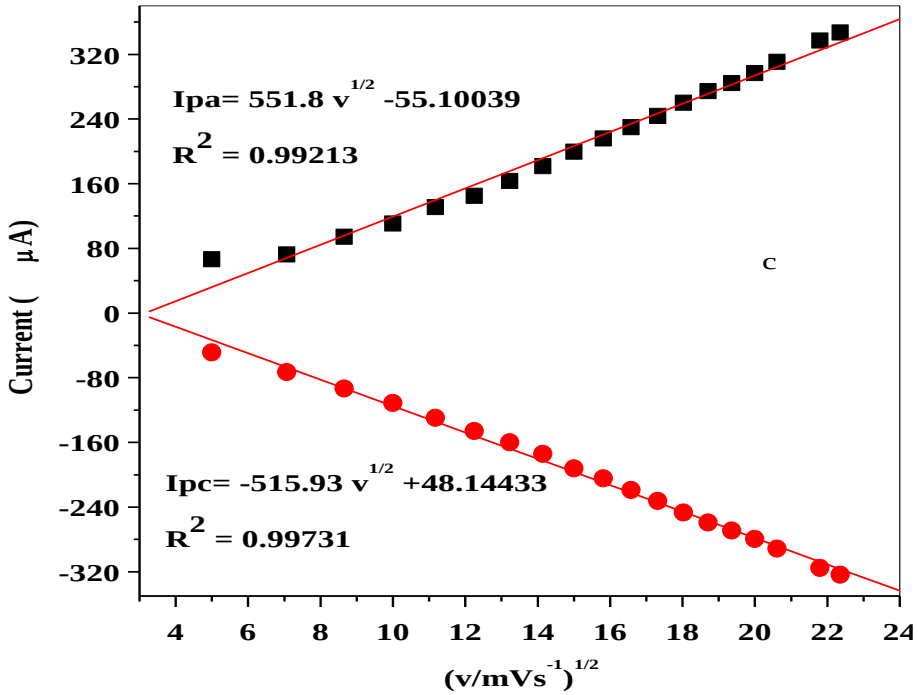
Ipa= 551.8 v 1/2 -55.10039
R2 = 0.99213
c
Ipc= -515.93 v 1/2 +48.14433
R2 = 0.99731
320
240
160
80
0
-80
-160
-240
-320
Current (µA)
4
6
8
10
12
14
16
18
20
22
24
(v/mVs-1)1/2

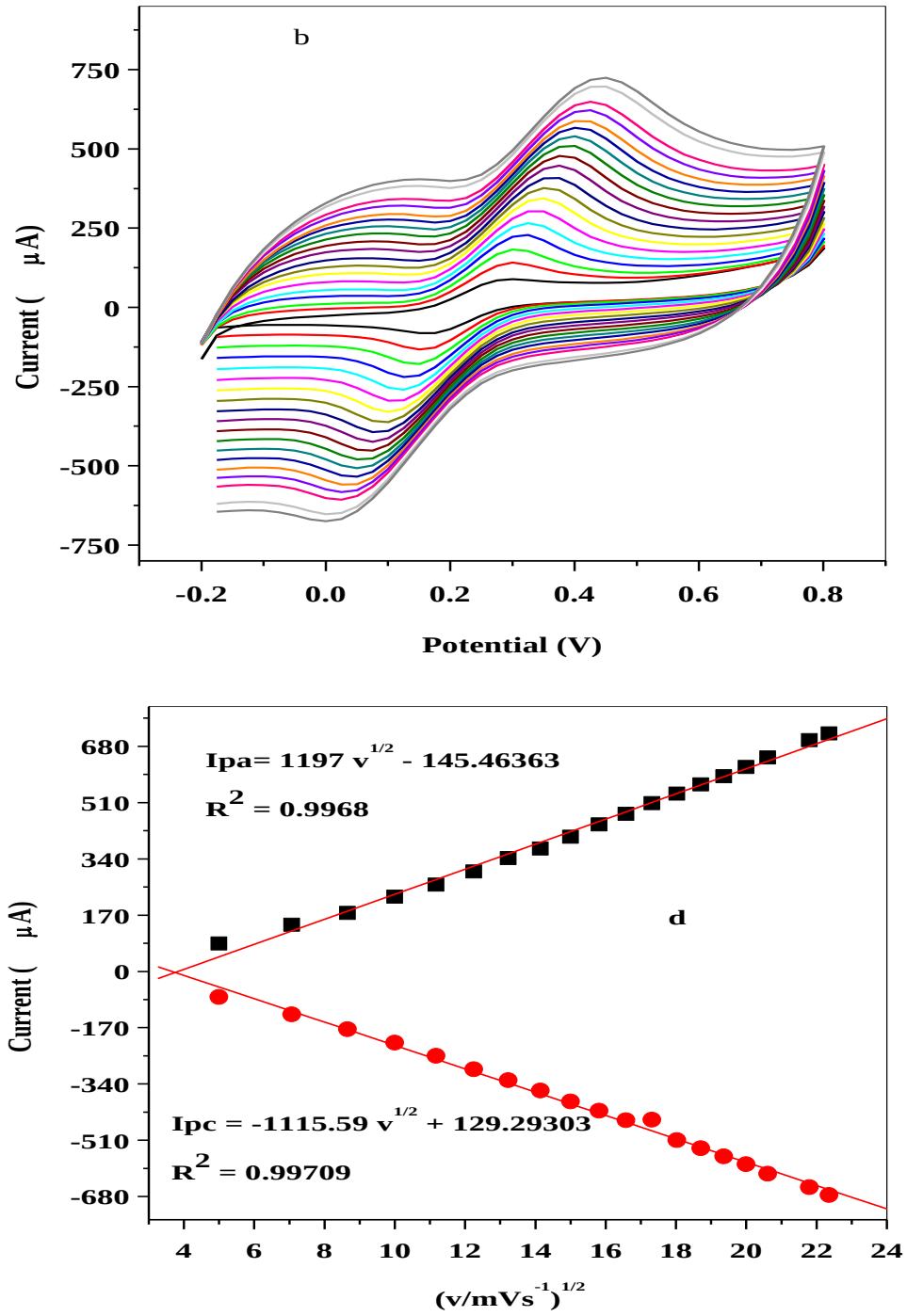

Figure 4.12: Cyclic voltammogram of (a) GCE/MWCNT/Fe_3O_4NPL and (b) GCE/MWCNT/Fe_3O_4NPF in 10 mM PBS (pH 7.4) containing 5 mM $K_3[Fe(CN)_6]$; linear plot of current against square root of scan rate $(v/mVs^{-1})^{1/2}$

Rate determining step in the electrolyte at the electrode-electrolyte solution was investigated from the plot of variation of peak potentials (Ep) against logarithm of scan rate (v) (graph not

shown) with slope of linear equation equal to $\frac{-2.3RT}{\propto nF}$ and $\frac{2.3RT}{(1-\propto)nF}$ assigned to cathodic and anodic peak potential according to Laviron (Laviron, 1979). The linear equations 4.2 - 4.3 and 4.4 - 4.5 fom the plot (graph not shown) were obtained for GCE/f-MWCNT/Fe_3O_4NPL and GCE/f-MWCNT/Fe_3O_4NPF, respectively. The linear equation (4.2 - 4.5) with the correlation coefficient value obtained from the plot is presented below:

$$Epa = 0.08443 \log v + 0.15333;\ R^2 = \ 0.92693 \quad (4.2)$$

$$Epc = -0.09296 \log v + 0.32814;\ R^2 = 0.94127 \quad (4.3)$$

GCE/f-MWCNT/Fe_3O_4NPL

$$Epa = 0.13081 \log v + 0.06927;\ R^2 = 0.95745 \quad (4.4)$$

$$Epc = -0.13361 \log v + 0.38341;\ R^2 = 0.95763 \quad (4.5)$$

GCE/f-MWCNT/Fe_3O_4NPF

Low regression values at GCE/f-MWCNT/Fe_3O_4NPL could possibly be due to a slower interfacial rate of electron transport resulting from the adsorption of reactants on the surface of the electrodes.

Epa and Epc is the anodic and cathodic peak potential respectively. Obtained slope values from the plot of Ep versus log v for GCE/f-MWCNT/Fe_3O_4NPL and GCE/f-MWCNT/Fe_3O_4NPF were 0.08443 and 0.13081 $Vdec^{-1}$ respectively base on the slope values in equation 4.2 - 4.5. Electron transfer coefficient (α) was found to be 0.47 and 0.44 for GCE/f-MWCNT/Fe_3O_4NPL and GCE/f-MWCNT/Fe_3O_4NPF respectively with one number of electrons calculated for the electrodes. Tafel value "b" was calculated to be 0.168 and 0.261 $Vdec^{-1}$ GCE/f-MWCNT/Fe_3O_4NPL and GCE/f-MWCNT/Fe_3O_4NPF using equation 4.6.

$$\text{Ep} = \frac{b}{2}\log v \ + constant \quad (4.6)$$

b values were quite higher than the theoretical value (0.118 $Vdec^{-1}$) for one–electron process in the rate determining process which was due to surface adsorption of reactants on the electrodes (Soderberg *et al.*, 2006).

Electron transfer rate constant (ks) for GCE/f-MWCNT/Fe_3O_4NPL and GCE/f-MWCNT/Fe_3O_4NPF were found to be 0.09 and 0.29 cms^{-1} respectively using equation 4.7.

$$\text{Ks} = \propto \log(1-\propto) + (1-\propto) log \ \propto - log \frac{RT}{nFv} - \propto (1-\propto) \frac{nF\Delta E_p}{2.3\text{RT}} \quad (4.7)$$

R is the gas constant (8.314 $Jmol^{-1}k^{-1}$), A is the surface area of glassy carbon electrode, T is the operating temperature (298K) and ΔEp is potential peak separation (Epa-Epc).

4.1.3.3 Electrochemical characterization of electrode using electrochemical impedance spectroscopy (EIS)

The process of electron transport at the electrode–electrolyte surface was further investigated using EIS via AUTOLAB FRA 32 PGSTART 302 with NOVA software version 1.10.19 in 0.1 M PBS containing 5 mM $K_3[Fe(CN)_6]$ at fixed $E_{1/2}$ 0.2 V versus Ag/AgCl, sat'd 3 M KCl in a frequency range of 100 kHz - 0.1 Hz. Ideal Nyquist plot obtained on fitting for the electrodes is shown in Figure 4.13a, b. Experimental impedance data were fitted with the Randle's current model of NOVA soft ware version 1.10.1.9 as presented in Figure 4.13c-e. R_s is the solution/electrolyte resistance, R_{ct} is electron transfer resistance reflected on the semi-circle diameter which relates to electron transport of $K_3[Fe(CN)_6]$ at the electrode surface (Choi *et al.*, 2020; Mazloum-Ardakani & Khoshroo, 2014). Zw is warburg impedance which appeared as a semi-circle-infinite linear diffusion (Choi *et al.*, 2020) while C_{dl} is the double layer capacitance, Q is the constant phase element. Summary of the fitted impedance data is shown in Table 4.4, where x^2 is the chi-square. The negative chi-square values and the percentage errors in parentheses confirmed successful fitting of EIS data. A large R_{ct} value of 1402 Ω was noticed at the bare GCE at the semicircle while smaller values of 345 Ω and 249 Ω were obtained for GCE/f-MWCNT/Fe_3O_4NPF and GCE/f-MWCNT/Fe_3O_4NPL (nanocomposite electrodes) suggesting a more rapid electron transport at the nanocomposite electrodes which is attributed to good conductivity of f-MWCNT which acted as an excellent electron conductor between Fe_3O_4NP and the electrode surface. From the result, it can be concluded that electron transport was much easier at the GCE/f-MWCNT-Fe_3O_4NPL electrode, which agrees with the cyclic voltammetry data.

Furthermore, electron transfer rate constant (k^0) and exchange current density (i_0) for the electrodes were determined using equation 4.8 and 4.9 respectively with estimated values represented in Table 4.4. EIS k^0 values were lower than that obtained via cyclic voltammetry (0.09, 0.29 cms^{-1}) for GCE/f-MWCNT/Fe_3O_4NPL and GCE/f-MWCNT/Fe_3O_4NPF which could possibly be alluded to a faster overall impedance. The exchange current density was highest at the nanocomposite electrode which correlates with the CV data.

$$R_{ct} = \frac{\mathrm{RT}}{n^2F^2ACk^0} \tag{4.8}$$

$$i_o = nFAk^0\mathrm{C} \tag{4.9}$$

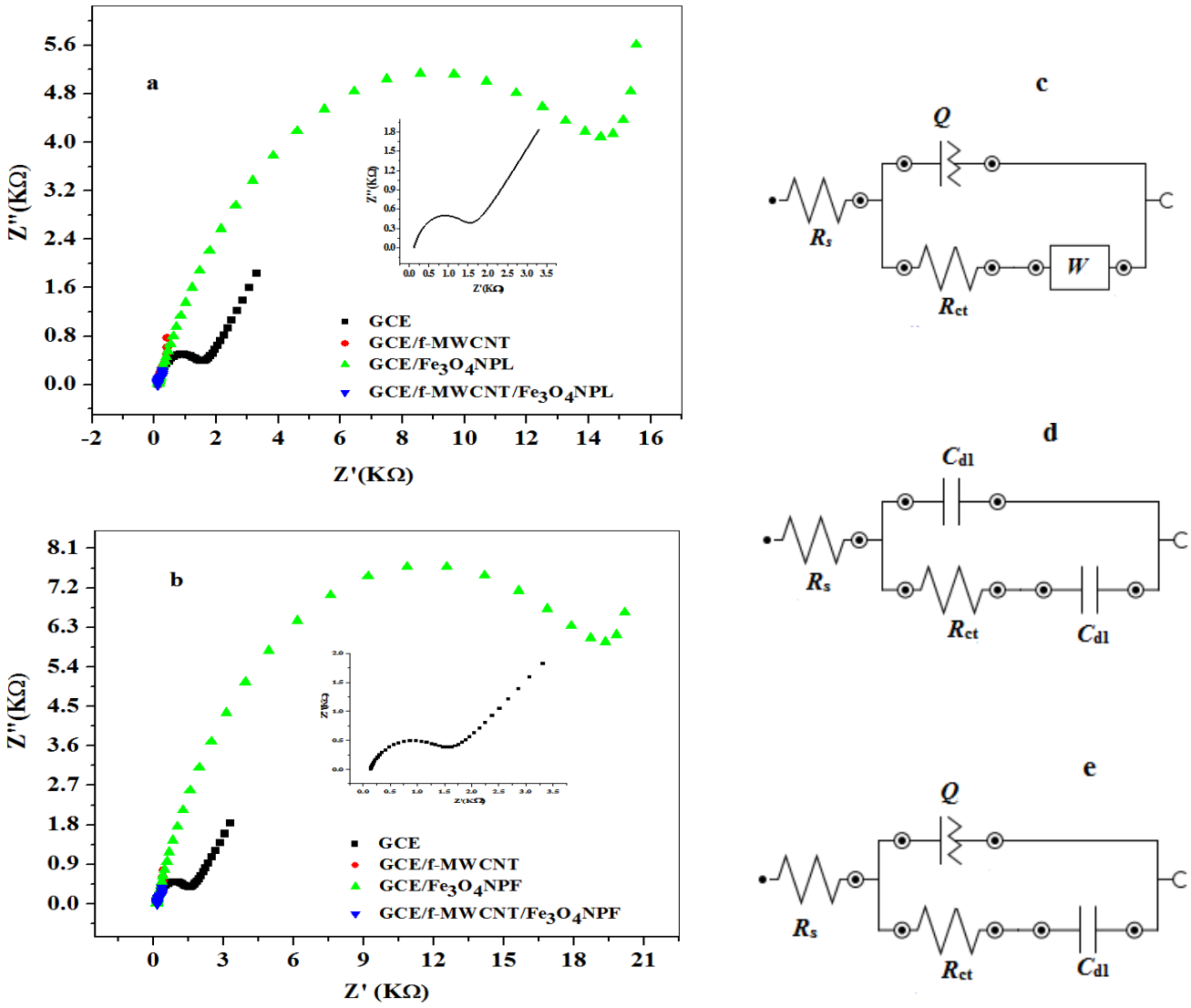

Figure 4.13: Nyquist plots obtained for (a, b) bare GCE and modified electrodes (c) circuit used in the fitting of EIS data of GCE (d) GCE/f-MWCNT, GCE/f-MWCNT/Fe_3O_4NPL, GCE/f-MWCNT/Fe_3O_4NPF and (e) GCE nanocomposite modified electrodes using NOVA 1.10.1.9 in 100 KHz and 0.1Hz frequency at a fixed 0.2 V vs Ag/AgCl potential in 10 m M PBS (pH 7.4) containing 5 mM $K_3[Fe(CN)_6]$.

Table 4.4: Impedance data for the GCE and modified electrodes in 5 mM $K_3[Fe(CN)_6]$ solution at 0.2 V (vs Ag/AgCl sat'd KCl). All values were acquired from the fitted impedance spectra

after several iterations of the circuits used. The values in parentheses are percentage errors of data fitting.

Electrodes	R_s **(Ω)**	R_{ct} **(Ω)**	k^0 **(cms^{-1})**	i_0 **(A/cm^2)**	x^2
GCE	123 (3.04)	1402 (4.74)	1.2×10^{-3}	3.63	0.404
GCE/Fe_3O_4NPF	132 (2.41)	22700 (3.67)	2.4×10^{-3}	7.2	0.298
GCE/Fe_3O_4NPL	116 (5.89)	22862 (6.96)	7.4×10^{-5}	0.224	0.906
GCE/MWCNT	123 (1.97)	699 (7.09)	7.4×10^{-4}	2.241	0.665
GCE/MWCNT/Fe_3O_4NPF	148 (1.57)	345 (14.6)	4.9×10^{-3}	14.845	0.431
GCE/MWCNT/Fe_3O_4NPL	114 (1.69)	249 (9.72)	6.8×10^{-3}	20.601	0.502

4.1.3.4 The influence of pH on the electrocatalytic activity of nanocomposite modified electrodes

The effect of the electrolyte solution pH on the electrochemical performance of modified nanocomposite electrodes (GCE/f-MWCNT/Fe_3O_4NPL and GCE/f-MWCNT/Fe_3O_4NPF) towards choline in 10 mM lithium chloride solution was investigated using cyclic voltammogram with various pH values ranging from 3.1 - 8.9. The aim of the investigation was to obtain the best oxidation peak resolution and utmost sensitivity in choline detection. A negative and positive shifts in both anodic and cathodic peaks potentials was noticed (Figure 4.14) with increasing pH of the electrolyte which suggest that, the redox reaction of choline involves some proton transferred at the modified nanocomposite electrodes (Zangeneh Kamali *et al.*, 2014). The anodic peak current of choline reach maximum value of pH 7.3 and then decreased gradually with increasing pH. Therefore, pH of 7.3 was used throughout the experiment. The cyclic peaks are not well defined (Figure 4.14 a, b) which could be due to the observed cross overs supposedly attributed to nucleation overpotential.

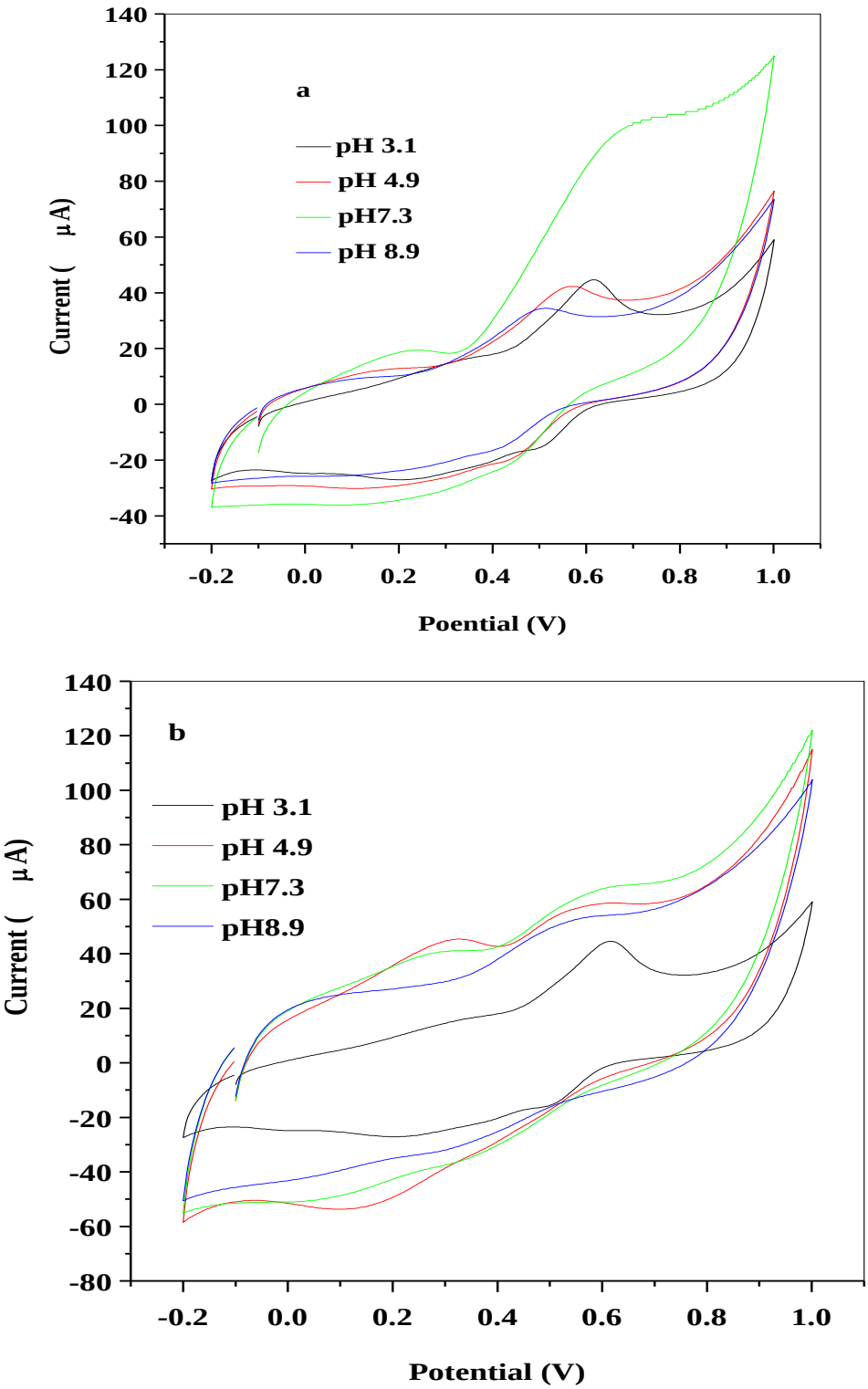

Figure 4.14: Cyclic voltammogram of (a) GCE/f-MWCNT/Fe_3O_4NPL and (b) GCE/f-MWCNT/Fe_3O_4NPF at scan rate of 25 mVs^{-1} in 2 mM choline prepared in LiCL at different pH.

4.1.3.5. Electrocatalysis of choline

The electrochemical properties of bare GCE, GCE/f-MWCNT, GCE/Fe_3O_4NPL, GCE/Fe_3O_4NPF, GCE/f-MWCNT/Fe_3O_4NPL, and GCE/f-MWCNT/Fe_3O_4NPF electrodes in 10

mM lithium chloride solution of pH 7.3, containing 2 mM choline (Cho) were performed using cyclic voltammetry at scan rate of 25 mVs^{-1} (Figure 4.15a, b) over same potential windows and step stated in section 4.3.1. Well defined choline oxidation peak was observed at anodic current and potentials at nanocomposites modified electrodes (GCE/f-MWCNT/Fe_3O_4NPL, and GCE/f-MWCNT/Fe_3O_4NPF) while bare and GCE/MWCNT showed no voltammetric response to choline but a capacitive current and redox peaks were absent on metal oxide (MO) nanoparticle modified electrodes. From the cyclic voltammetry experiments, Choline oxidation current (Ipa) and potential (Epa) were 0.58 V (47.8 µA) and 0.50 V (41.0 µA) for GCE/f-MWCNT/Fe_3O_4NPL, and GCE/f-MWCNT/Fe_3O_4NPF electrodes. Both electrodes had better electrocatalytic response towards the oxidation of choline than other electrodes owing to the electronic conductivity of nanocomposites (MWCNT and Fe_3O_4NP), their interaction with enhanced electrocatalytic properties, their biocompatibility with the analyte (choline) and their high surface area. However, a more vivid choline oxidation peak was observed at GCE/f-MWCNT/Fe_3O_4NPL resulting from rapid transfer of electron during oxidation of choline. A redox electrochemical process was observed in the voltammogram. Figure 4.16 represents possible electrochemical redox reaction mechanism for choline.

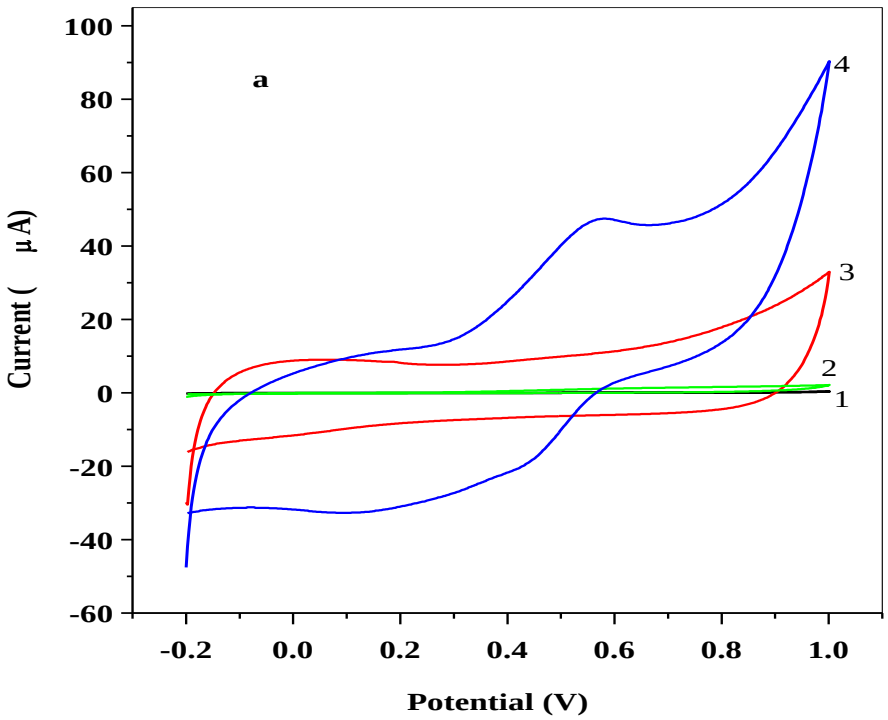

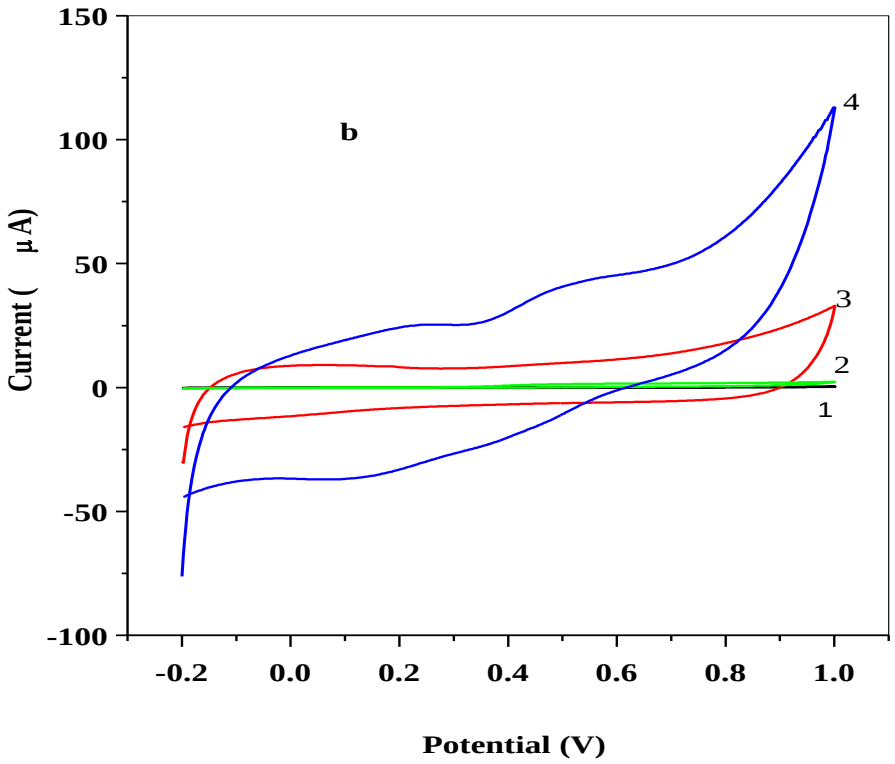

Figure 4.15: Cyclic voltammogram of (a,b1) bare GCE (a2) GCE/Fe_3O_4NPL (b2) GCE/Fe_3O_4NPF (a,b3) GCE/f-MWCNT (a4) GCE/f-MWCNT/Fe_3O_4NPL and (b4) GCE/f-MWCNT/Fe_3O_4NPF in 10 mM LiCl pH 7.3 containing 2 mM choline.

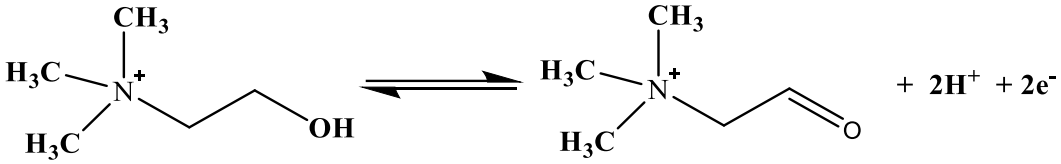

Figure 4.16: Possible mechanism of choline redox reaction at the surface of modified GCE/f-MWCNT/Fe_3O_4NP electrodes.

Further electrochemical studies were conducted using nanocomposites modified electrodes since they exhibited better electrochemical response towards choline.

4.1.3.6 Effects of varying scan rate at constant choline concentration (2 mM) in LiCl solution

The influence of scan rate variation at nanocomposite modified electrodes in 10 mM LiCl solution containing 2 mM choline (Cho) concentration was studied using cyclic voltammetry. A gradual increase of oxidation (anodic) peak current with a shift in peak potentials to a more positive was noticed with increase in scan rate in the range of 25 to 400 mVs^{-1} which confirmed a diffusion controlled process (Figure 4.17a, b). Disappearance of peak potentials (redox peaks) noticed from 250 mVs^{-1} scan rate in Figure 4.17b for GCE/f-MWCNT/Fe_3O_4NPF electrode could be ascribed to great polarization because the potential of the redox reaction exceeds the scan potential range (Qiu *et al.*, 2020), and saturation of choline at the electrode (Mphuthi *et al.*, 2016). ΔE increased in GCE/f-MWCNT/Fe_3O_4NPL (94 - 514 mV) and GCE/f-MWCNT/Fe_3O_4NPF (3.4 - 474 mV) with variation of scan rate suggesting a quasi- reversible process (Das *et al.*, 2016). From the result, the plot of peak current against square root of scan rate ($V^{1/2}$) showed the existence of a linear relationship with regression values of 0.99 and 0.99 for GCE/f-MWCNT/Fe_3O_4NPL and GCE/f-MWCNT/Fe_3O_4NPF respectively as can be seen in Figure 4.17c,d. Regression values further confirmed electrochemical process at the nanocomposites modified electrodes to be diffusion controlled. Diffusion coefficient for choline was calculated to be 3.90×10^{-4} and 7.46×10^{-4} cm^2s^{-1} for GCE/f-MWCNT/Fe_3O_4NPL and GCE/f-MWCNT/Fe_3O_4NPF electrodes from equation 2.2.

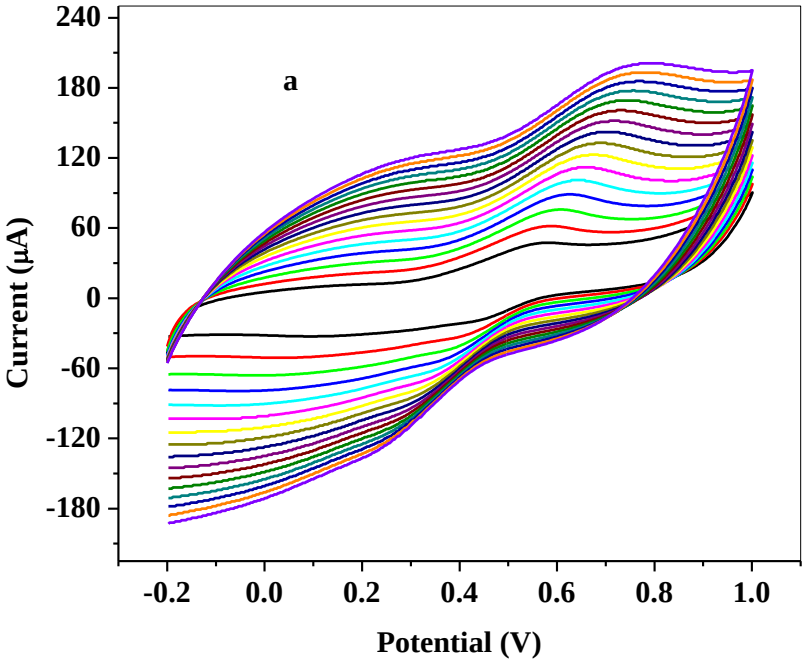

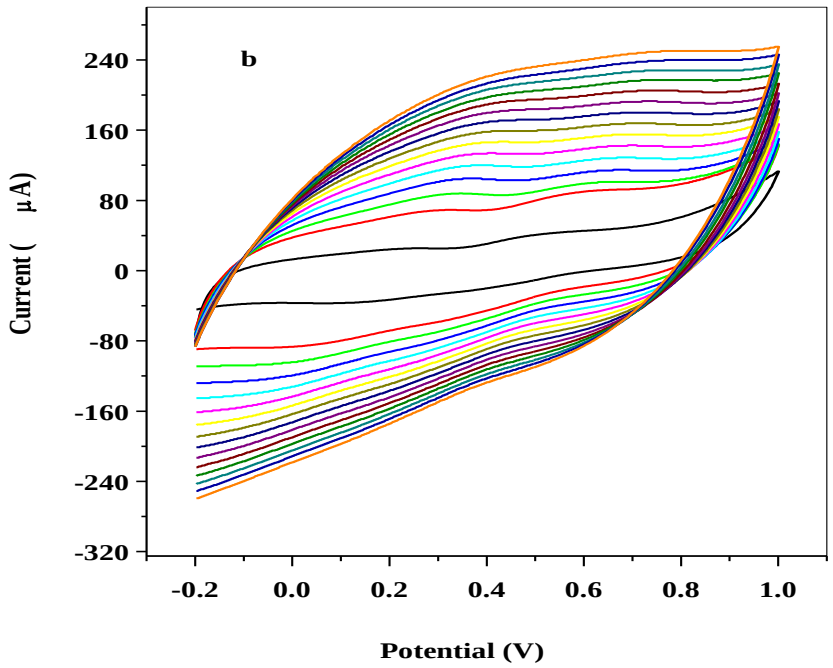
b
240
160
80
0
-80
-160
-240
-320
-0.2
0.0
0.2
0.4
0.6
0.8
1.0
Current (µA)
Potential (V)

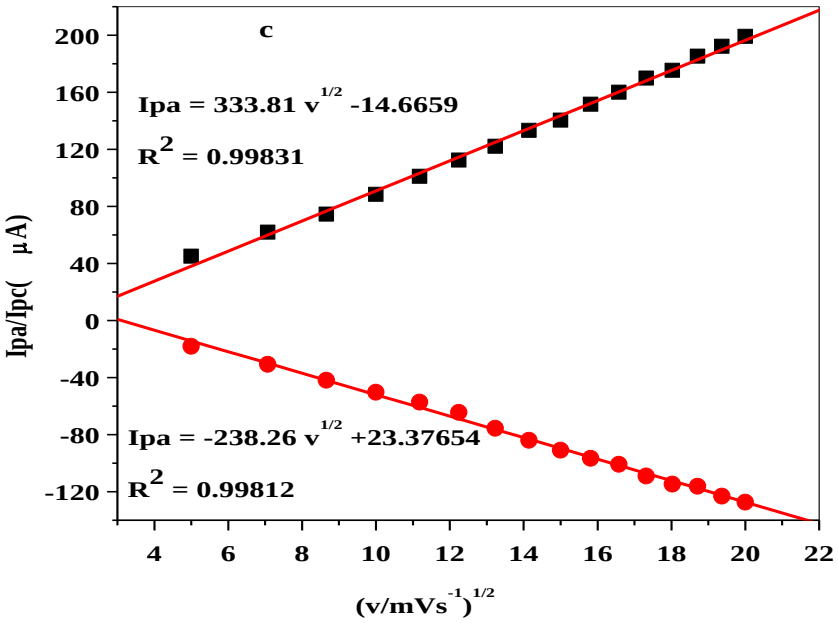
c
Ipa = 333.81 v^1/2 -14.6659
R^2 = 0.99831
Ipa = -238.26 v^1/2 +23.37654
R^2 = 0.99812
200
160
120
80
40
0
-40
-80
-120
4
6
8
10
12
14
16
18
20
22
Ipa/Ipc(µA)
(v/mVs^-1)^1/2

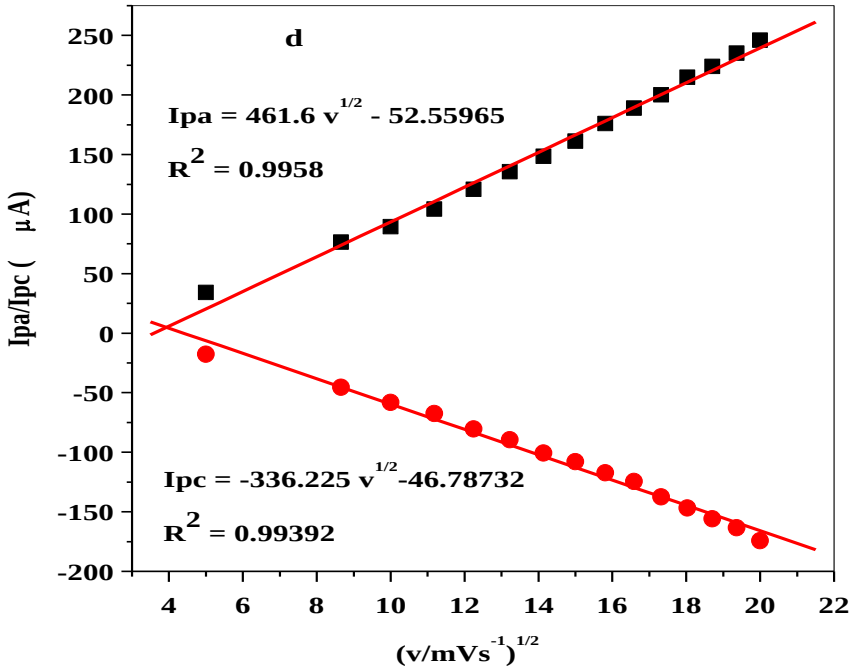

Figure 4.17: Cyclic voltammogram obtained for (a) GCE/f-MWCNT/Fe_3O_4NPL (b) GCE/f-MWCNT/Fe_3O_4NPF (25–400 mVs^{-1}; inner to outer) in 10 mM LiCl pH 7.3 containing 2 mM choline; linear plots of Ipa vs square root of scan rate $(v/mVs^{-1})^{1/2}$ of (c) GCE/f-MWCNT/Fe_3O_4NPL and (d) GCE/f-MWCNT/Fe_3O4NPF.

Surface concentration (Γ) of the electroactive specie (choline) was determined to be 0.013 and 0.018 $molcm^{-2}$ at the respective electrodes using equation 4.10 from the slope values of graph of peak current (Ip) versus scan rate (v) represented in Figure 4.18a, b.

$$I_p = \frac{n^2F^2\Gamma Av}{4RT} \qquad (4.10)$$

n is the number of electrons transferred (1), F is faraday constant (96500 C), R is the gas constant (8.314 $Jmol^{-1}k^{-1}$), A is the surface area of glassy carbon electrode (0.0314 cm^2), T is the operating temperature (298K).

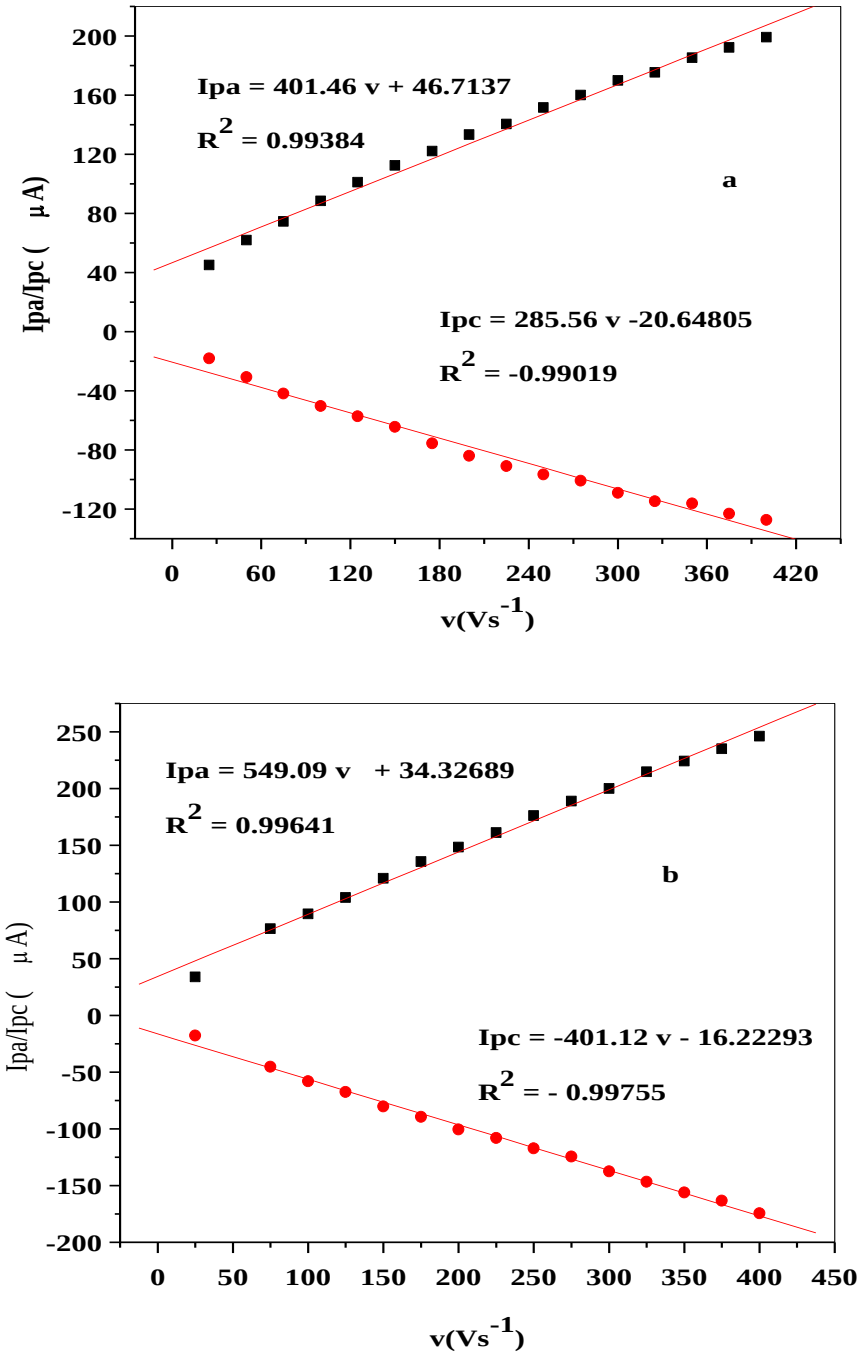

Figure 4.18: Linear plots of Ipa versus scan rate v(vs^{-1}) for (a) GCE/f-MWCNT/Fe_3O_4NPL and (b) GCE/f-MWCNT/Fe_3O4NPF in 10 mM LiCl of pH 7.3 containing 2 mM choline.

Furthermore, from the cyclic voltammetry experiments in Figure 4.17a, b, a plot of peak potentials (Ep) against logarithm of scan rate (log v) was plotted (graph not presented) with slope

Values 0.188/-0.18566; and 0.210/-0.2007 (Epa/Epc) for GCE/MWCNT/Fe3O4NPL and GCE/MWCNT/Fe3O4NPF electrodes respectively with linear equation and regression express in equation 4.11 and 4.14.

$$Epa = 0.18858 \log v + 0.24416;\ R^2 = 0.97436 \quad (4.11)$$

$$Epc = -0.18566 \log v + 0.73628;\ R^2 = -0.97872 \quad (4.12)$$

GCE/f-MWCNT/Fe_3O_4NPL

$$Epa = 0.21035 \log v + 0.09135;\ R^2 = 0.94025 \quad (4.13)$$

$$Epa = -0.20077 \log v + 0.76513;\ R^2 = -0.94721 \quad (4.14)$$

GCE/f-MWCNT/Fe_3O_4NPF

From slope values, charge transfer coefficient (α) at the anode was found to be 0.50 (GCE/f-MWCNT/Fe_3O_4NPL) and 0.51 (GCE/f-MWCNT/Fe_3O_4NPF). Number of electrons transferred at the electrodes was calculated to be 1 from the equation 4.15 and 4.16.

$$\text{Epa (slope)} = \frac{2.3RT}{(1-\propto)nF} \quad (4.15)$$

$$\text{Epc (slope)} = \frac{-2.3RT}{\propto nF} \quad (4.16)$$

Rate constant of electron transferred (Ks) was computed to be 0.10 and 0.01 cms^{-1} for GCE/f-MWCNT/Fe_3O_4NPL and GCE/f-MWCNT/Fe_3O_4NPF electrodes (equation 4.5). The disparity in Ks value is ascribed to different levels of catalysis at the nanocomposite modified electrodes surface (Adekunle *et al.*, 2011). Tafel slope (b) values (377 and 420 $mVdec^{-1}$) obtained for the respective electrodes employing equation 4.6 exceeded the theoretical value (118 $mVdec^{-1}$) which could be attributed to adsorption of choline on the surface of the electrodes.

4.1.3.7 Electrochemical impedance spectroscopic (EIS) study of choline at nanocomposite modified electrodes

Impedance measurement was conducted with metrohm AUTOLAB frequency response analyser (FRA 32) NOVA software version 1.10.1.9 between 100 kHz and 0.1 Hz to understand information on electron transfer mechanism and the behavior of the electrode-electrolyte interface during the oxidation of 2 mM choline at constant potential +0.50 V versus Ag/AgCl, single sine wave, and 0.01 V amplitude. Experimental data for GCE/f-MWCNT/Fe_3O_4NPF, and GCE/f-MWCNT/Fe_3O_4NPL were successfully fitted with Randle's circuit model same as Figure 4.13 d-([R(C[RC])], Circuit [R(Q[RC])] as presented in Figure 4.13e for bare GCE, GCE/f-MWCNT, GCE/Fe_3O_4NPL electrodes while [R(R[QC])] was used for GCE/Fe_3O_4NPF (Figure

4.19c) and Nyquist plot represented by Figure 4.19a, b. R_{ct} values of bare GCE was 349 kΩ as compared to GCE/f-MWCNT/Fe_3O_4NPF (0.795 kΩ) and GCE/f-MWCNT/Fe_3O_4NPL (0.587 kΩ) indicating exchange of electrons to be easier at the later electrode than former and this correlates with the obtained cyclic voltammogram (Figure 4.15a) (Magar *et al.*, 2017). The values of the double layer capacitance (C_{dl}) was higher at GCE/f-MWCNT/Fe_3O_4NPL (1040 µF) compared to the bare GCE (605 µF) and GCE/f-MWCNT/Fe_3O_4NPsF (213 µF) suggesting greater accumulation of charge and better conductivity (Magar *et al.*, 2017). The order of electron transfer process is GCE/f-MWCNT/Fe_3O_4NPL > GCE/f-MWCNT/Fe_3O_4NPF > GCE.

In addition, estimated rate of electron transferred –k0 (3.6×10-3, 4.4×10-3, 1.4×10-2 in cms-1) and exchange current density-i0 (10.9, 13.3, 44.2 Acm-2) for bare and nanocomposite modified electrodes accordingly were obtained applying equation 4.8 and 4.9 respectively. The magnitude of the determined k^0 differs with that calculated from cyclic voltammetric measurement which could probably be ascribed to rapid impedance (overall) at the electrode. i_0 was largest at GCE/f-MWCNT/Fe_3O_4NPL inferring a more rapid transfer of ions at the electrode which is in agreement with the cyclic voltammogram current response in Figure 4.15a.

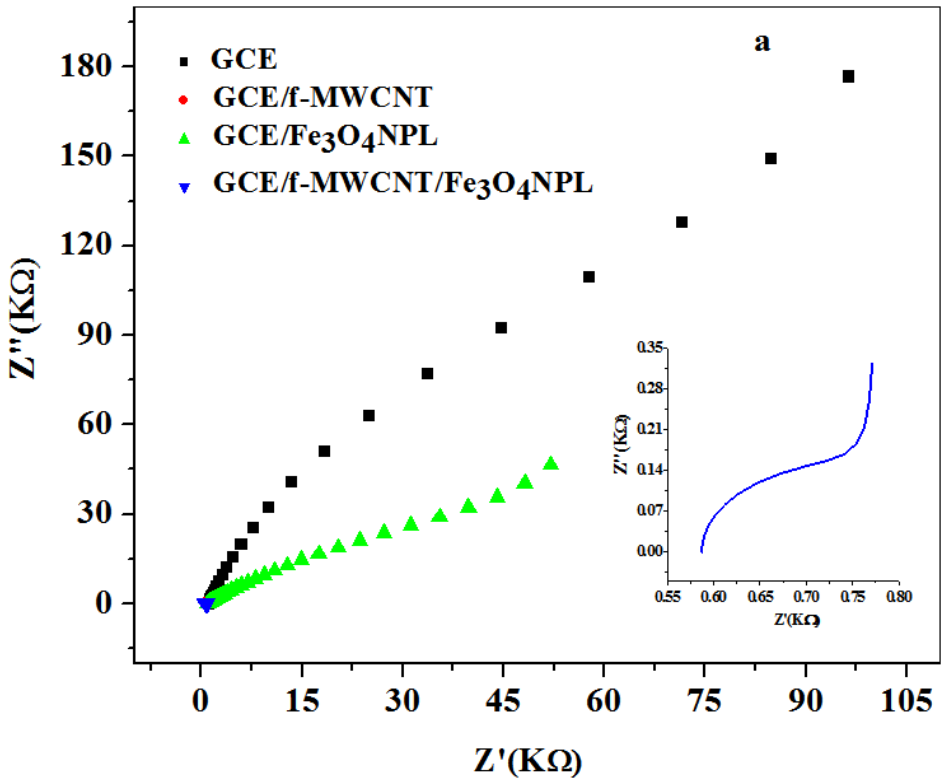

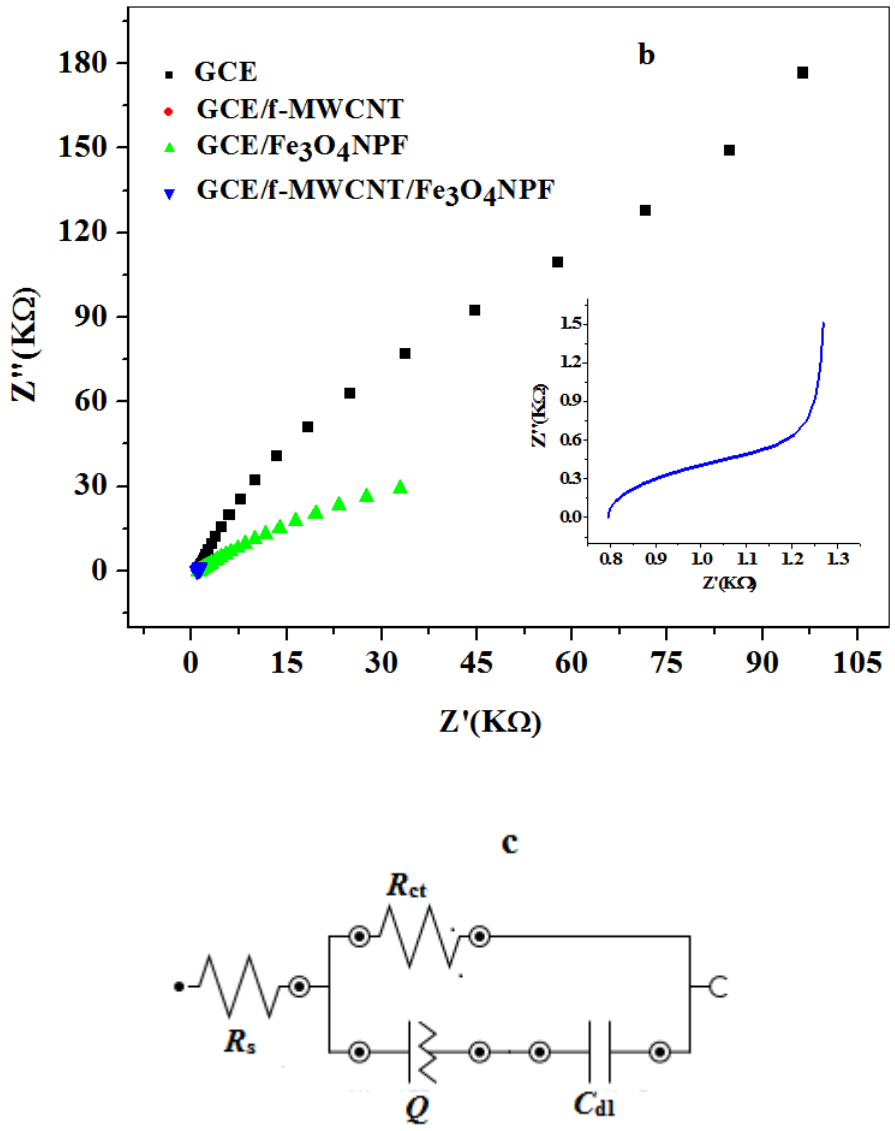

Figure 4.19: Nyquist plots a, b obtained for bare GCE and modified electrodes at a fixed +0.50 V potential in 2 mM choline prepared in 10 mM LiCl of pH 7.3 (c) circuit used in the fitting of EIS data.

Further investigations were conducted at GCE/f-MWCNT/Fe_3O_4NPL and GCE/f-MWCNT/Fe_3O_4NPF electrodes since they demonstrated better electrochemical response towards choline.

4.1.3.8 Electroanalysis of choline

The sensitivity of the proposed sensors was investigated via concentration study using square wave voltammetry (SWV) technique in 10 mM LiCl solution of pH 7.3 over 3×10^{-7} to 2.2×10^{-6} M choline concentrations range in triplicate from 0.2 to 0.8 V potential window with 0.005 V, 0.01 V, 25 Hz, 5 s, and +0.58 V versus Ag/AgCl sat'd 3 M KCl potential step, amplitude, frequency, equilibration time and applied potential respectively. The results obtained after subtraction of the supporting electrolyte (background current) is presented in Figure 4.20a, b. Choline (Cho) reduction current peak increased proportionally when series of choline concentrations were added to LiCl solution indicating the dependence of Cho oxidation peak currents on choline concentration. A linear graph of choline reduction peak current versus choline concentration was plotted with 0.91795 and 0.9906 regression value obtained at modified electrodes (Fig 4.20 c, d). Detection limit (LoD) for GCE/MWCNT/Fe_3O_4NPL and GCE/f- MWCNT/Fe_3O_4NPF was 0.83 µM and 0.36 µM using the relationship $\text{LoD} = \frac{3SD}{m}$. Where SD is the standard deviation of the intercept of the Y-coordinate from the line of best fit and m is the slope of same line. Sensitivity of GCE/f-MWCNT/Fe_3O_4NPL and GCE/f-MWCNT/Fe_3O_4NPF electrodes was 0.107 µA/µM and 0.673 µA/µM respectively. The best electrode based on the detection limit was GCE/f-MWCNT/Fe_3O_4NPF with well-defined peak current. The LoD values were compared with those reported in the literature using various electrochemical method and sensors (Table 4.6).

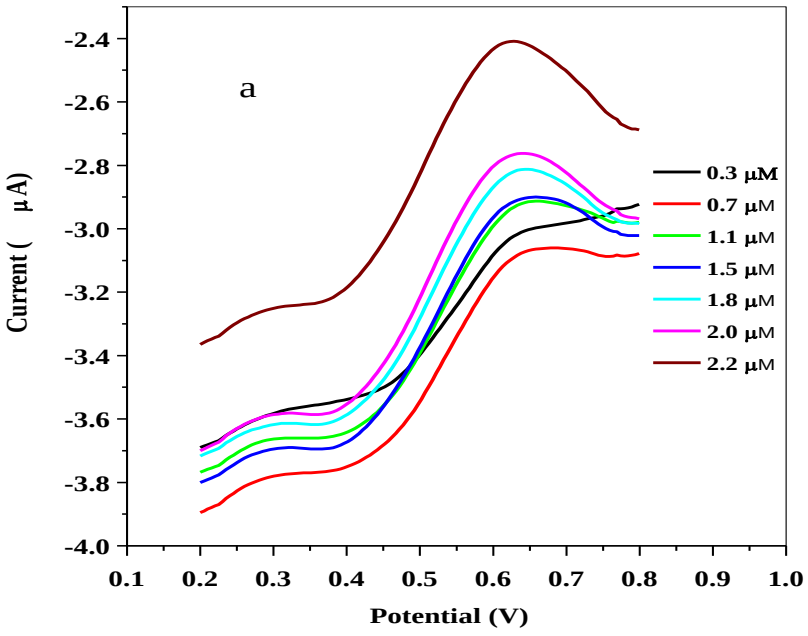

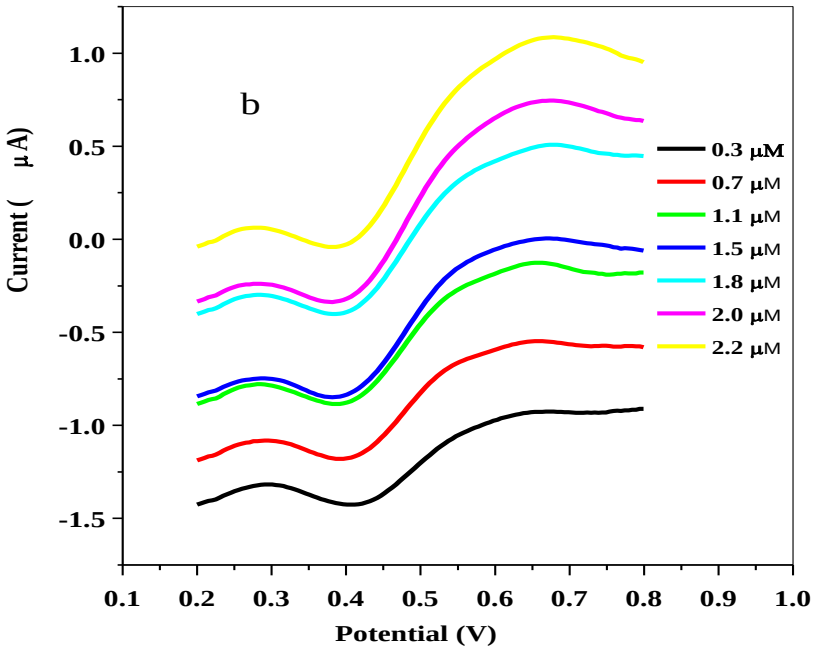
b
Current (µA)
Potential (V)
0.3 µM
0.7 µM
1.1 µM
1.5 µM
1.8 µM
2.0 µM
2.2 µM

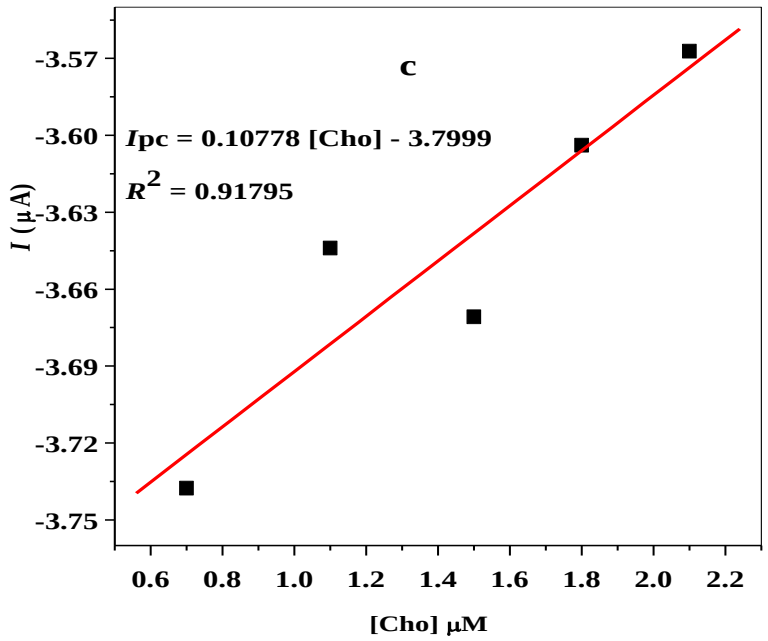
c
Ipc = 0.10778 [Cho] - 3.7999
R2 = 0.91795
I (µA)
[Cho] µM

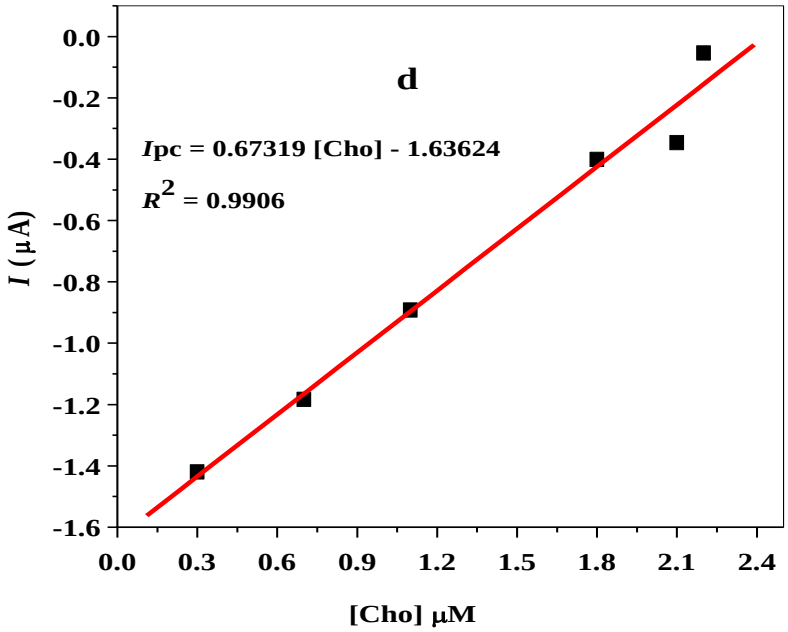

Figure 4.20: Background subtracted SWVs of (a) GCE/f-MWCNT/Fe_3O_4NPL (b) GCE/f-MWCNT/Fe_3O_4NPF at different choline concentrations (0.3 - 2.2 μM) from down top in LiCl solution, pH 7.3; linear plot of current against Cho concentration for (c) GCE/f-MWCNT/Fe_3O_4NPL and (d) GCE/f-MWCNT/Fe_3O_4NPF.

Chronoamperometric technique was also used to determine the applicability of the designed electrode for choline sensing. Figure 4.21a, b shows the chronoamperometric response (presented on histogram) of GCE/f-MWCNT/Fe_3O_4NPL and GCE/f-MWCNT/Fe_3O_4NPF electrodes upon stepwise addition of 0.1 mM choline into 10 mM LiCl (pH = 7.3) at an applied potential of 0.58 V base on the peak potential obtained from cyclic voltammetry. The decreased in current noticed with increasing choline concentration in the range of 1.19 – 7.45 μM could be ascribed to the fall in the diffuse layer of analyte (choline) at nanocomposite modified electrode surface. Figure 4.21 c, d suggests choline response to be linear in the choline concentration range with correlation coefficient value of 0.96138 and 0.98875 at GCE/f-MWCNT/Fe_3O_4NPL and GCE/f-MWCNT/Fe_3O_4NPF respectively. Similar linear response was obtained in the literature although with different electrodes (Deng *et al.*, 2013). A 0.16 and 0.05 μM LoD with 1.09 and 0.86 μA/μM sensitivity value was obtained at the respective modified electrodes. GCE/f-MWCNT/Fe_3O_4NPF also proved to be the best electrode considering the LoD value.

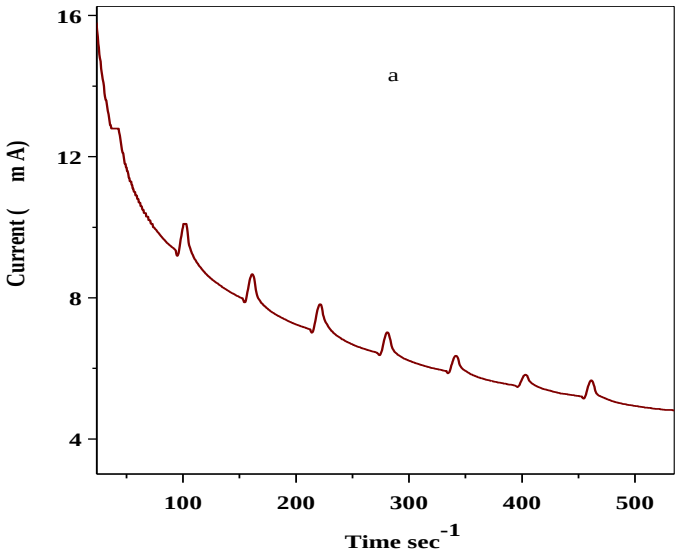
a
Current (mA)
Time sec-1
16
12
8
4
100
200
300
400
500

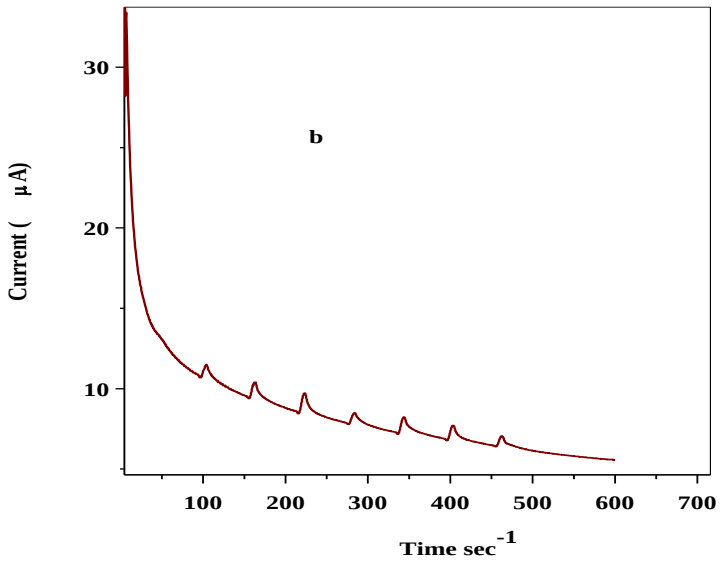
b
Current (µA)
Time sec-1
30
20
10
100
200
300
400
500
600
700

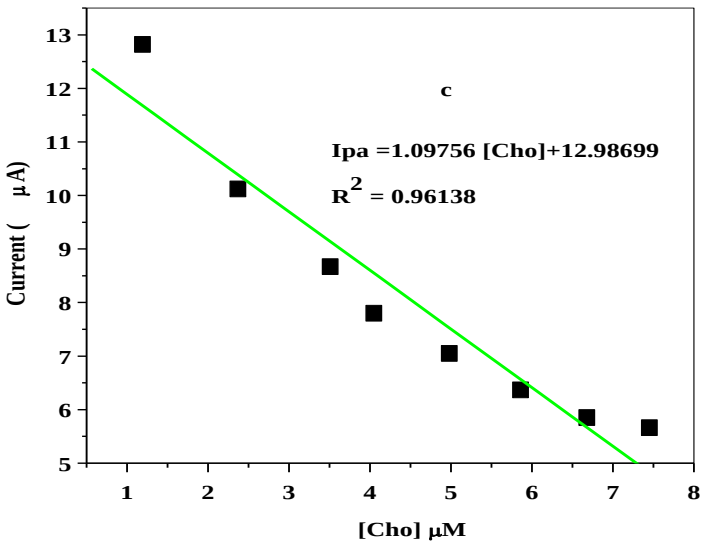
c
Ipa =1.09756 [Cho]+12.98699
R2 = 0.96138
Current (µA)
[Cho] µM
13
12
11
10
9
8
7
6
5
1
2
3
4
5
6
7
8

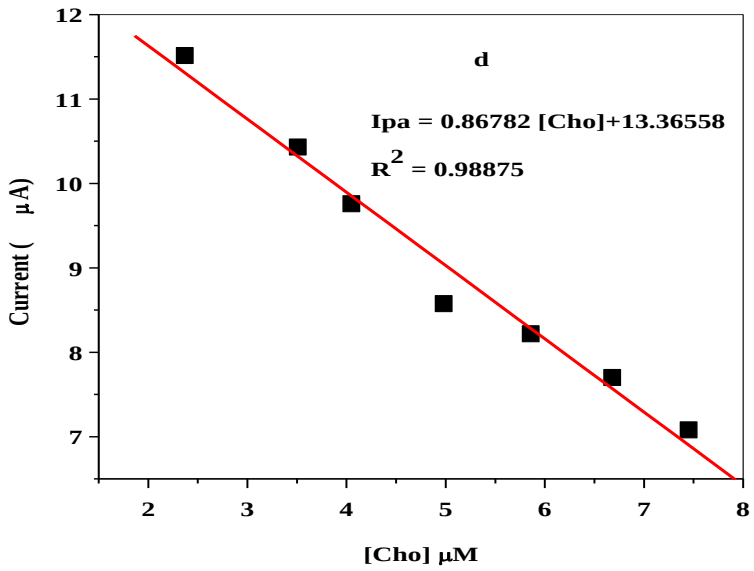

Figure 4.21: Current-time curve of (a) GCE/f-MWCNT/Fe_3O_4NPL and (b) GCE/f-MWCNT/Fe_3O_4NPF upon series of choline addition in 10mM LiCl solution, pH 7.3 at +0.58 V vs. Ag/AgCl; linear plot of current against Cho concentration for (c) GCE/f-MWCNT/Fe_3O_4NPL and (d) GCE/f-MWCNT/Fe_3O_4NPF.

Table 4.5: Comparison of designed sensors for choline detection with reported sensors.

Working electrodes	Methods	Linear range	LoD (µM)	Ref
ChOx[a]/GNP$_4$[b]/MWCNT[c]/GCE[d]	EIS[t]	3 – 120	0.6	(Magar *et al.*, 2017)
ChOx/MWCNT/Pt[e]	Amperometry	5 – 100	0.7	(Song *et al.*, 2006)
PVA[f]/Au[g]/ChOx/Pt	Amperometry	20 – 400	10	(Ren *et al.*, 2009)
ChOx/RTIL[h]/NH$_2$[i]-MWCNT/GCE	Amperometry	6.9 – 670	2.7	(Sajjadi *et al.*, 2012)
MCPE[j]/NiO[k]	Amperometry	250 – 6980	25.4	(Sattarahmady *et al.*, 2014)
Nano-W[l]/GEL/SIM[m]	DPSV[u]	1 – 100	0.92	(Xie *et al.*, 2017)
Nafion/ChOx/MnO$_2$[n]/GCE	CV[v]	8 – 1000	5	(Yu *et al.*, 2016)
ChOx/PDDA[o])n(PVS[p]/PAA[q])3 /MWCNTs/pt	Amperometry	5 – 100	0.7	(Qin *et al.*, 2009)
GCE/MWCNT/Fe$_3$O$_4$NPL[r]	SWV[w]	0.3 - 2.2	0.83	This work
	Chronoamperometry	1.19 - 7.45	0.16	
GCE/MWCNT/Fe$_3$O$_4$NPF[s]	SWV	0.3 - 2.2	0.36	This work
	Chronoamperometry	1.19 - 7.45	0.05	

a -choline oxidase, **b** -gold nanoparticles, **c**-Multi-walled carbon nanotube, **d**-glassy carbon electrode, **e** -platinum electrode, **f** - poly vinyl alcohol, **g** - gold nano rods, **h** - ionic liquid (1-Butyl-3-methylimidazolium), **i**- amine, **j**-modified carbon pencil paste electrode, **k** -nickel oxide, **l** –Wire, **m**-silica isoporous membrane, **n** -manganese (IV) oxide, **o** - poldiallyldimethlammonium, **p** -poly vinyl sulphate, **q** -poly allylamine, **r&s** - iron (III) oxide nanoparticles synthesized from *Callistemon viminalis* leaf and flower extract, **t** -electrochemical impedance spectroscopy, **u** -differential pulse stripping voltammetry, **v** -cyclic voltammetry, and **w** -Square wave voltammetry.

4.1.3.9 Selectivity of designed sensors

The common challenge in the electrochemical detection of choline is the interference from coexisting substances such as ascorbic acid (AA) and dopamine (DA). Selectivity of the designed electrochemical sensors in the presence of these possible interfering species was investigated using square wave voltammetry and chronoamperometry with +0.58 V applied potential.

Voltammetric response of choline in the presence of AA and DA was carried out using square wave voltammetry, within -0.4 – 1.6 V potential windows, 0.005 V, 0.01 V, 25 Hz, 5 sec, and + 0.58 V versus Ag/AgCl sat'd 3 M KCl potential step, amplitude, frequency, equilibration time and applied potential respectively in LiCl containing mixtures of 100 mM AA, 0.1 mM DA and

0.1 mM Cho. Three distinct oxidation response of each interferents: AA (Epa = 0.16; 0.10 V), DA (Epa = 0.31;0.48 V) was found to be more negative than that of Cho (Epa=0.40; 0.56 V) as shown in Figure 4.22a, b. Anodic potential peaks separation of 240; 460 mV, 190; 80 mV, and 150; 380 mV was observed between Cho and AA, Cho and DA, and AA and DA at GCE/f-MWCNT/Fe_3O_4NPL and GCE/f-MWCNT/Fe_3O_4NPF respectively. Therefore, the simultaneous detection of choline in the presence of AA and DA is possible on the designed sensor. The result also showed that 1000 and 1 fold of AA and DA did not interfere with choline oxidation signal.

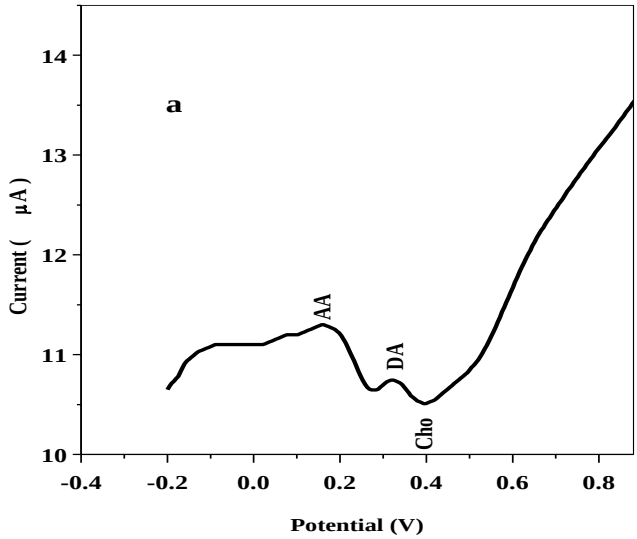

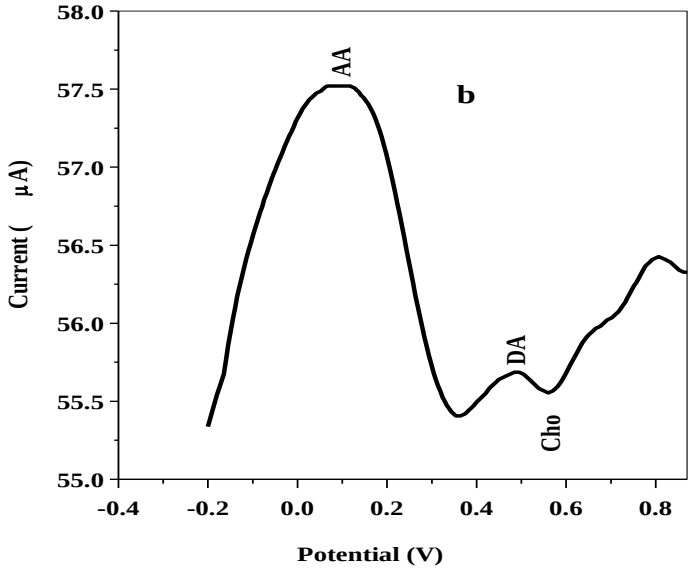

Figure 4.22: Background subtracted SW voltammogram of (a) GCE/f-MWCNT/Fe_3O_4NPL and (b) GCE/f-MWCNT/Fe_3O_4NPF in LiCl, pH 7.3 containing 100 mM AA, 0.1 mM DA, and 0.1 mM Cho solutions.

Figure 4.23 a, b presents histogram from the chronoamperometric current time curve recorded at applied potential set at +0.58 V vs. Ag/AgCl saturated KCl at modified f-MWCNT/Fe_3O_4 electrodes (GCE/f-MWCNT/Fe_3O_4NPL and GCE/f-MWCNT/Fe_3O_4NPF) upon successive addition of 1 ml of Cho (0.1 mM), AA (100 mM) and DA (0.1 mM). Choline response was determined before and after injection of each of AA and DA into 10 mM LiCl solution of pH 7.3. The result shows significant increase in current response of choline after the injection of several concentrations of AA and DA, indicating that AA and DA signal did not interfere with choline detection on the nanocomposites modified f-MWCNT/Fe_3O_4NP electrodes. Also, nanocomposite modified electrodes demonstrated high selectivity to choline in the presence of AA and DA at the applied potential. However, recovery current was better at GCE/f-MWCNT/Fe_3O_4NPF compared to GCE/f-MWCNT/Fe_3O_4NPL electrode.

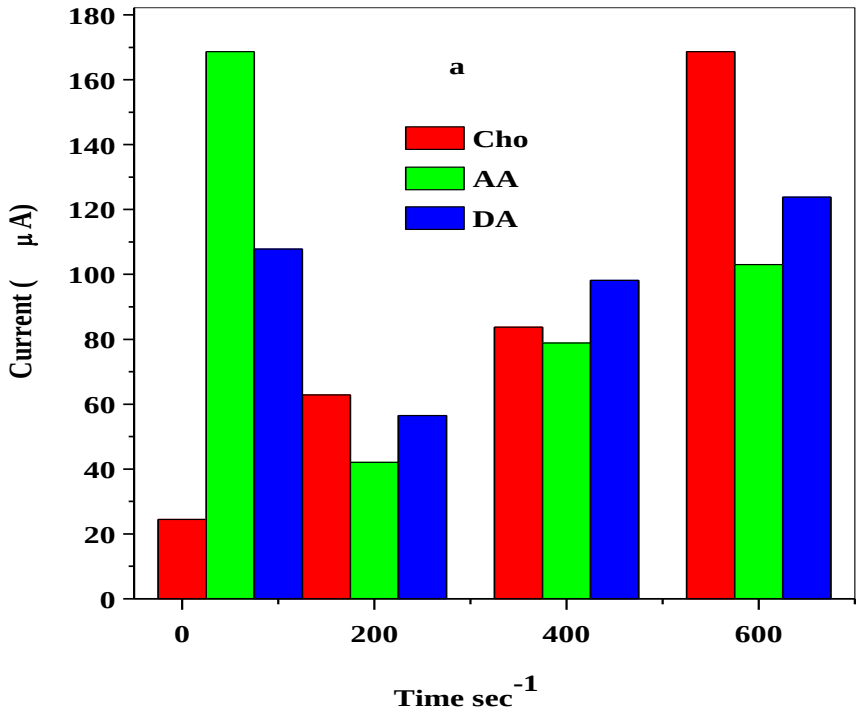

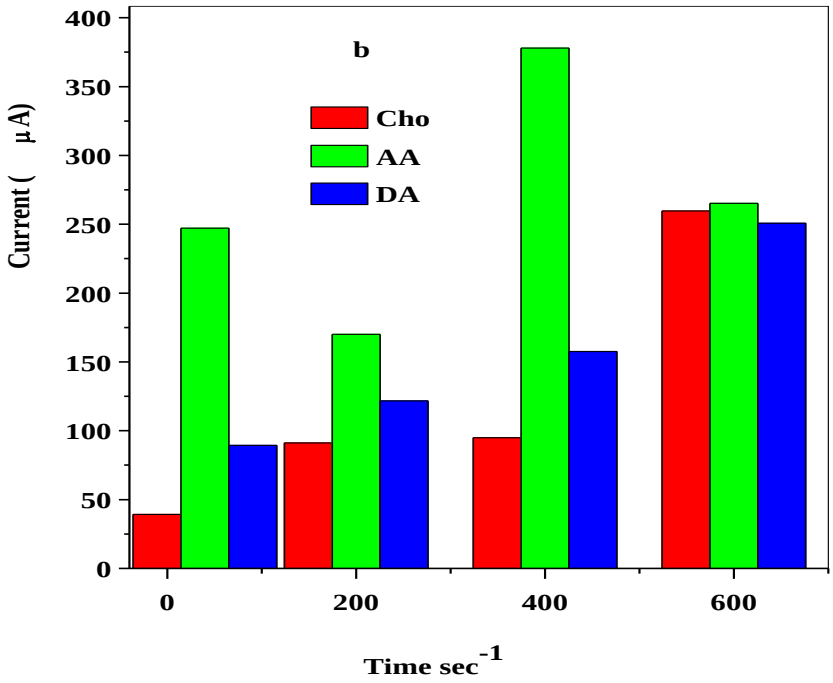

Figure 4.23: Histogram from current-time curves of (a) GCE/f-MWCNT/Fe_3O_4NPL and (b) GCE/f-MWCNT/Fe_3O_4NPF in 10 mM LiCl, pH 7.3 at + 0.58 V vs. Ag/AgCl at successive injection of 1ml 0.1 mM Cho, 100 mM AA and 0.1 mM DA.

4.1.3.10 Reproducibility and stability of designed sensors

The reproducibility of the electrochemical sensors to 2 mM choline in 10 mM LiCl was determined using cyclic voltammetry. The relative standard deviation (RSD) of the developed sensors was 6.2 and 4.5% respectively for GCE/f-MWCNT/Fe_3O_4NPL and GCE/f-MWCNT/Fe_3O_4NPF for six successive scans at 25 mVs^{-1} scan rate (Figure 4.24a, b). The RSD values indicate reasonable reproducibility of the proposed sensors and also the reliability of the sensor. GCE/f-MWCNT/Fe_3O_4NPF electrode demonstrated better reproducibility than GCE/f-MWCNT/Fe_3O_4NPL electrode. From the voltammograms, peaks are not well defined and not superimposed (oxidation and reduction) from the voltammogram (4.24 a,b) probably because of slight increase in oxidation and reduction current peaks despite at a fixed scan rate. the increase in current peaks could be due to increased electroactive surface with more interaction of the analyte at the electrode surface.

Storage stability of the proposed electrochemical sensors (GCE/f-MWCNT/Fe_3O_4NPL and GCE/f-MWCNT/Fe_3O_4NPF) was studied by monitoring their response to 2 mM choline in 10

mM LiCl, pH 7.3 at intervals of one week using square wave voltammetry technique. The sensors were stored under dry condition when not in use. After two weeks, there was no drop in response for GCE/f-MWCNT/Fe_3O_4NPL rather there was a 16.5% of its initial sensitivity was retained while 35% drop was observed for GCE/f-MWCNT/Fe_3O_4NPF connoting good stability at former than the later electrode.

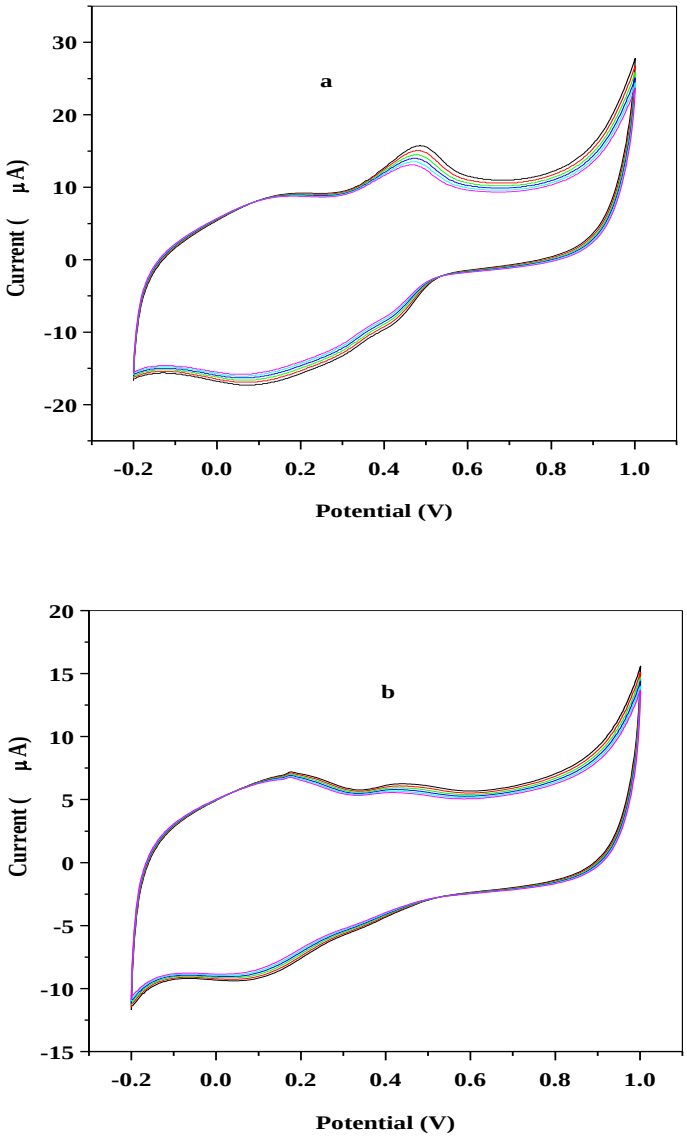

Figure 4.24: Repetitive cyclic voltammogram at 25 mVs^{-1} of (a) GCE/f-MWCNT/Fe_3O_4NPL (b) GCE/f-MWCNT/Fe_3O_4NPF in 10 mM LiCl of pH 7.3 containing 2 mM choline.

4.1.3.11 Analytical application of designed sensors in pharmaceutical samples

The feasibility of designed sensors for determination of choline in real samples was demonstrated with pharmaceutical samples (dietary supplements); CDP choline (citicholine) and choline bitartrate in super B energy injection fizzy tablet (choline bitartrate) using SWV. Standard addition experiment was conducted by addition of known amount of choline standard solution into prepared samples. Choline concentration was evaluated using SWV set at +0.58 V in potential range for +0.2 to 0.8 V. Table 4.6 shows the obtained result with recovery for n = 3.

The recovery values confirmed that the designed sensors are reliable for determining choline in real samples.

Table 4.6: Detection of choline in pharmaceutical samples at nanocomposite modified electrodes.

Sample	Working electrode	Added (µM)	Found (µM)	Recovery (%)	RSD (n = 3)
CDP choline	GCE/f-MWCNT/Fe_3O_4NPF	29.5	29.5	100	3.02
		44.0	46.3	105	2.91
		58.0	61.3	106	3.06
	GCE/f-MWCNT/Fe_3O_4NPL	29.5	23.7	80	1.60
		44.0	41.6	95	1.68
		58.0	60.7	105	1.75
Choline Bitartrate	GCE/f-MWCNT/Fe_3O_4NPF	14.8	15.0	100	1.61
		58.0	49.8	86	1.62
		72.2	76.6	100	1.83
	GCE/f-MWCNT/Fe_3O_4NPL	14.8	15.4	96	0.11
		58.0	67.8	116	0.09
		72.2	69.4	96	0.13

The results of t-test, F-test carried out at 95% confidence level signifies there was no significant difference in the results. The Q-test analysis indicated that the outliers (80, 86 recoveries) be retained since Qcal was < Qtab.

4.2 Zinc oxide nanoparticles/multi-walled carbon nanotubes nanocomposites modified electrode for choline detection: electrochemical study

Carbon nanotube (CNTs) nanocomposites are used as modifiers in preparation of electrode due to their ability to increase electron rate transport between biomolecules and the electrode surface

thus enhancing electrode kinetics (Thomas *et al.*, 2013). Multi-walled carbon nanotube (MWCNT) is a type of CNTs with high tensile strength, excellent electrical conductivity, stability (chemical), strong adsorptive ability on surface of electrode, high surface area with fast electron transfer ability between the electroactive specie and the electrode surface (Ahmed *et al.*, 2013; Magar *et al.*, 2017; Qu *et al.*, 2005; Rajarao *et al.*, 2014; Sahebian *et al.*, 2016; Savk *et al.*, 2019). Hence, there is a growing application of MWCNT in electrochemical sensors.

Zinc oxide nanoparticles (ZnONP) are one of the most studied and applied metal oxide nanoparticles in electrochemical studies due to its excellent catalytic activity, wide surface area and biocompatibility (Zhang *et al.*, 2014). Nanocomposites of MWCNT and zinc oxide nanoparticles have proven to be a potent method of improving the performance, stability and sensitivity of designed sensors owing to the interaction between the two materials (MWCNT and metal oxide nanoparticles) resulting in an improved quality. For example a mixture of MWCNT/ZnO was dope for sensing of dopamine and serotonin (Fayemi *et al.*, 2017). In another study, a sensor was fabricated using ZnOpc/MWCNT for detection of epinephrine and norepinephrine (Mphuthi *et al.*, 2016). Also, a different experiment developed an amperometric biosensor for choline and acetylcholine determination based on AChE/ZnO/MWCNT composite (Zhang *et al.*, 2014). In addition, MWCNTs-ZnO/chitosan on screen-printed electrode platform was employed for determining norepinephrine and serotonin (Wang *et al.*, 2015).

Choline is popularly seen in the mammalian peripheral and central nervous system and also in food (Bai *et al.*, 2007; Magar *et al.*, 2017; Phillips, 2012). Choline as a vital nutrient is implicated in several biological functions in the human body such as synthesis of some vital phospholipids (Lecithin, sphingomyelin), which provides structure to cell membrane and facilitates signalling within membranes, synthesis of neurotransmitter acetylcholine which plays a part in the cholinergic neural networks linked to memory, synthesis of phosphatidylcholine, oxidation of betaine in the kidney, and in pregnant women, choline is essential for foetal development and functioning of the liver, and placenta (He *et al.*, 2014; Magar *et al.*, 2017; Yu *et al.*, 2016; Zeisel, 2013). Choline is acquired endogenously within the body cell and via dietary supplementation (Phillips, 2012). Inadequate choline in the body results in haemorrhagic kidney necrosis, growth/neural disorders, death of liver cells and damage of muscles (Phillips, 2012; Zeisel, 2012).

Common methods for choline detection include chromatography (HPLC, Ls/Ms/MS) and amperometric biosensors. However, chromatography assays are expensive, time and labour intensive due to sample clean up, extraction and separation steps (Magar *et al.,* 2017; Pati *et al.*, 2007; Sattarahmady *et al.,* 2014; Yu *et al.,* 2016) while severe enzyme immobilization steps, instability and loss of enzyme are associated with amperometric biosensors (Power & Morrin, 2013; Sattarahmady *et al.,* 2014). It was therefore necessary to introduce an electrochemical sensor which involved the application of composites of ZnONPs and MWCNT in modifying glassy carbon electrode (GCE/MWCNT/ZnO) with aim of enhancing response, sensitivity, and selectivity. The electrochemical kinetics of the modified electrodes were investigated and then employed in the electrocatalytic oxidation and sensing of choline.

4.2.1 Characterization of zinc oxide nanoparticles and nanocomposites

4.2.1.1 Fourier transform infrared (FTIR) study of ZnONP

The FTIR result reveales the bonding properties and functional groups of compounds present in the extracts obtained from the leaves and flowers of C. viminalis and the synthesized ZnONP (Figure 4.25a). In the FTIR spectrum of leaf extracts of *C. viminalis* (graph not shown), vibration bands at 3460 cm^{-1}, 2967 cm^{-1} and 1725 cm^{-1} indicated the presence of alcohol/phenol O-H stretch, carboxylic acid O-H stretch and C ═ O of aldehyde, ketone and carboxylic acid respectively which are believed to be responsible for the formation of ZnONP obtained. FTIR spectrum of ZnONP synthesized using *C. viminalis* leaves extract (ZnONPL) revealed vibrations at 3368 cm^{-1}, 1485 cm^{-1} and 538 cm^{-1} (Figure 4.25 a) which correspond to alcohol/phenol O-H stretch/N-H stretching of aliphatic primary amine, C-H bending of alkane methylene group and Zn-O nanoparticles respectively. Vibrations at 3468 cm^{-1}, 2952 cm^{-1} and 1728 cm^{-1} corresponds to alcohol/phenol O - H stretch, carboxylic acid O - H stretch and aldehyde, ketone and carboxylic acid C ═ O stretch respectively were noticed in *C. viminalis* flowers extract spectrum (graph not shown). While ZnONPF spectrum showed vibrational bands at 3362 cm^{-1}, 1569 cm^{-1}, 1470 cm^{-1} and 533 cm^{-1} which were assigned to alcohol/phenol O - H stretch/N - H aliphatic primary amine stretch, C = C aromatic bend, C - H bending of alkane methylene group and Zn-O of nanoparticles respectively (Figure 4.25a).

FTIR spectra of Zn-O bond at 538 and 533 cm^{-1} in ZnONPL and ZnONPF respectively confirmed the synthesized zinc oxide nanoparticles (ZnONP). The vibrational bands were within the region assigned to Zn-O (400 - 600 cm^{-1}) as typical of ZnONP synthesized from different

plant extracts (Jafarirad *et al.*; Kalpana *et al.*, 2017; Sagar Raut & Thorat, 2015; Senthilkumar *et al.*, 2017). The mechanisms of the greenly synthesized nanoparticles (ZnONPL and ZnONPF) is probably due to the binding of bioactive compounds (polyphenols, carboxylic acid, and flavonoids) in the extracts to the surface of metal ion (Zn^{2+}) which triggered the formation of ZnONP by reducing Zn^{2+} to Zn^{0} (zero valence). The C = O and C = C functional groups aided the stabilization of the synthesized ZnONP (Jafarirad *et al.*). A difference in the FTIR spectra of ZnONPL and ZnONPF was observed. ZnONPF spectrum displayed intense stretching and vibrational bands compared to ZnONPL indicating great absorption of bioactive compounds on the surface of ZnONPF than ZnONPL. The current findings agreed with what was reported in the literature (Bala *et al.*, 2015; Jafarirad *et al.*).

Figure 4.25b, c represents the structural analysis of f-MWCNT/ZnONPL and f-MWCNT/ZnONPF via FTIR while Table 4.7 repesents the summary of the observed major peaks and their assigned functional groups.

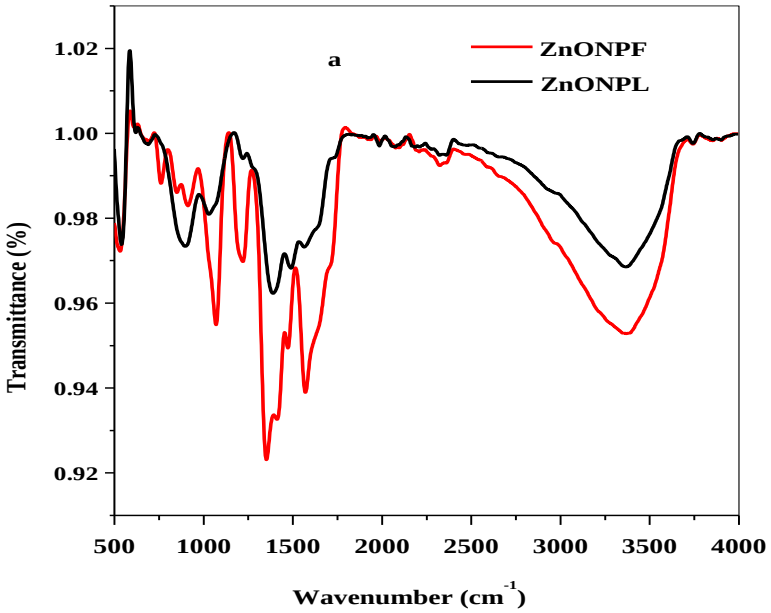

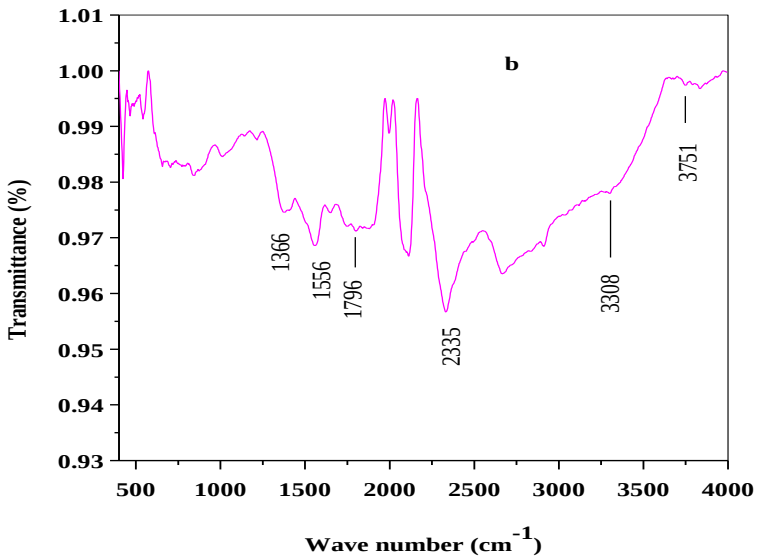

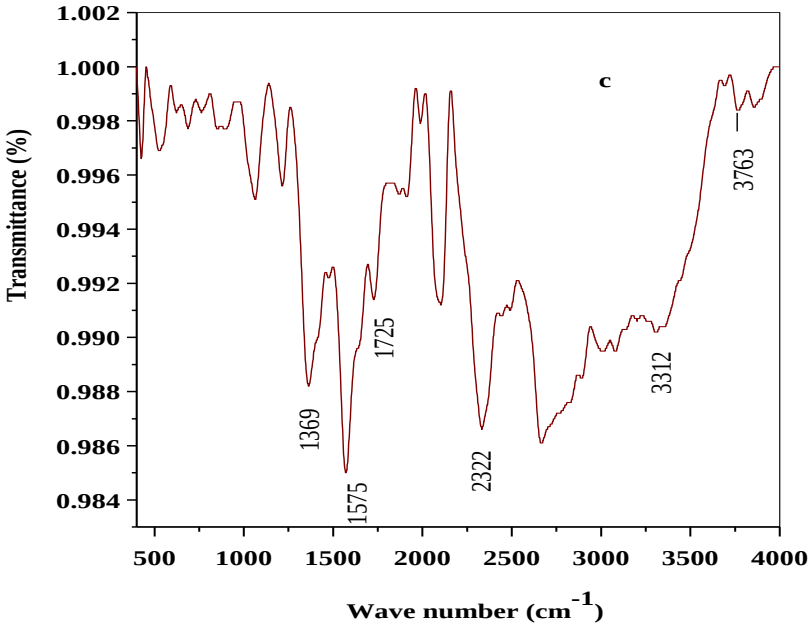

Figure 4.25: FTIR of (a) ZnONPL, ZnONPF (b) f-MWCNT/ZnONPL and (c) f-MWCNT/ZnONPF.

Table 4.7: FTIR vibration peaks and their corressponding funtional groups.

Raw MWCNT (cm^{-1})	f-MWCNT (cm^{-1})	f-MWCNT/ ZnONPL (cm^{-1})	f-MWCNT/ ZnONPF (cm^{-1})	Functional groups
3743	3772	3751	3763	Free hydroxyl group O-H
3298	3304	3308	3312	O-H stretch from carboxyl groups (O=C-OH and C-OH)
2351	2341	2335	2309	O-H stretch from strongly hydrogen –bonded-COOH
1735	1738	1743	1725	Stretching vibration of carboxylic group (C=O)
1510	1533	1556	1575	O-H deformation vibrations
1370	1378	1377	1375	Bending deformation in carboxylic groups (-COOH) due to the formation of CN bond in amino functional group.

Observed slight bathochromic shifts of O-H, -COOH, and C = O in raw and f-MWCNT spectra (Figure 4.3 c) and high intensity suggest increase in number of these groups on the surface of MWCNT after functionalization (Figure 4.3 c). In Figure 4.3b,c, the bathochromic and hypsochromic shifts of major peaks found in the f-MWCNT and the presence of new peaks around 545 - 1214 cm^{-1} confirmed the successful formation of MWCNT/ZnONP composite.

4.2.1.2 Ultraviolet-visible (UV-Vis) spectroscopy

UV-Visible spectroscopic analysis of synthesized ZnONP using *C. viminalis* leaves (ZnONPL) and flowers (ZnONPF) extract was performed within the range of 100 nm - 1200 nm. Absorption peaks at 371 and 323 nm were obtained respectively for ZnONPsL and ZnONPF as shown in Figure 4.26a, b. The absorption values were quite close to the reported value (Jamdagni *et al.*, 2018; Kavitha *et al.*, 2017). A shift in absorption peaks to a shorter wavelength was noticed in the UV-Vis spectra of f-MWCNT/ZnONPL (291 nm) and f-MWCNT/ZnONPF (293) connoting a good integration of ZnONP into f-MWCNT (Figure 4.26 c, d).

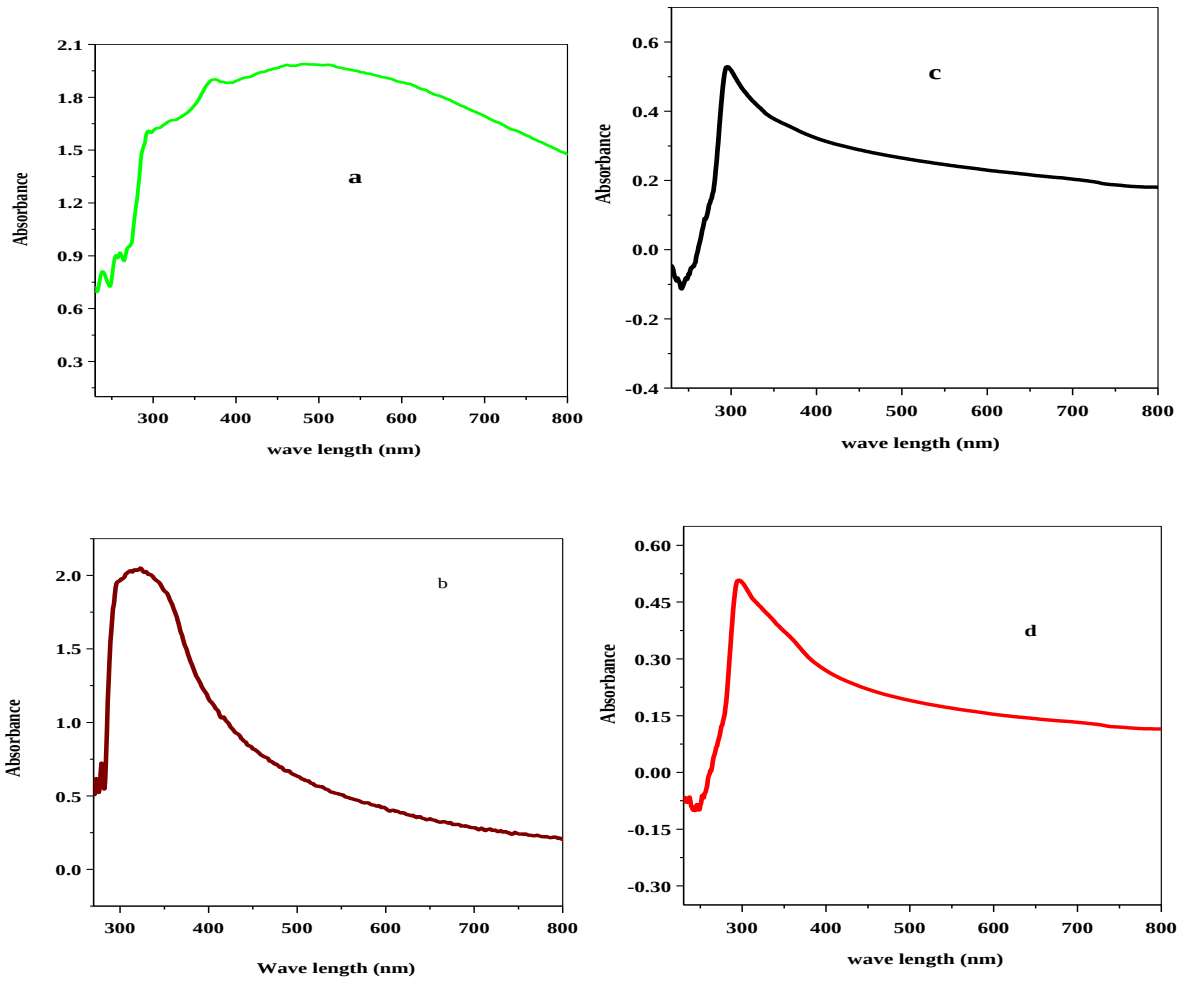

Figure 4.26: UV-visible spectra of (a) ZnONPL (b) ZnONPF (c) f-MWCNT/ZnONPL (d) f-MWCNT/ZnONPF.

4.2.1.3 X-ray diffraction analysis

The X-ray diffraction (XRD) pattern confirmed the presence of ZnONP peaks in the synthesized ZnONPL (black spectrum) and ZnONPL (red spectrum) as presented in Figure 4.27. The peaks correspond to wurtzite structure/hexagonal phase of ZnO. The peaks were sharp and narrow confirming the crystalline form of the synthesized ZnONP while the broadening of peaks noticed was as a result of crystalline finite size and strain (Debanath & Karmakar, 2013). Maximum diffraction peaks, which is ideal for ZnONP was noticed in 36.13 and 36.27 diffraction angles for respective synthesized nanoparticles (ZnONPL and ZnONPF) and their average crystalline particle size (10.15 and 13.71 nm) was estimated from the intense/maximum peaks using Debye Scherer formula (Equation 4.17)

$$D = \frac{0.89\lambda}{\beta Cos\theta} \qquad (4.17)$$

Where, 0.89 = Scherrer's constant,

λ = X-ray wavelength (0.154 nm)

β = FWHM (Full Width at Half Maximum) of the peak located in ZnONPL and ZnONPF spectra at 2θ (36.13 and 36.27) respectively

θ = Bragg's angle of diffraction in radians

Values of the crystalline particle size fell so close to that (10, 13.86 nm) reported in the previous studies with different plant extracts (Azizi *et al.*, 2017; Sagar Raut & Thorat, 2015).

Figure 4.27b shows XRD pattern of f-MWCNT/ZnONP with diffraction planes (100, 002, 101, 102, 110, 103) typical of ZnONP crystalline structure with particle size of 11.8 nm for f-MWCNT/ZnONPF and 11.9 nm for f-MWCNT/ZnONPL and reduced intensity and size indicating a successful incoporation of ZnONP into f-MWCNT.

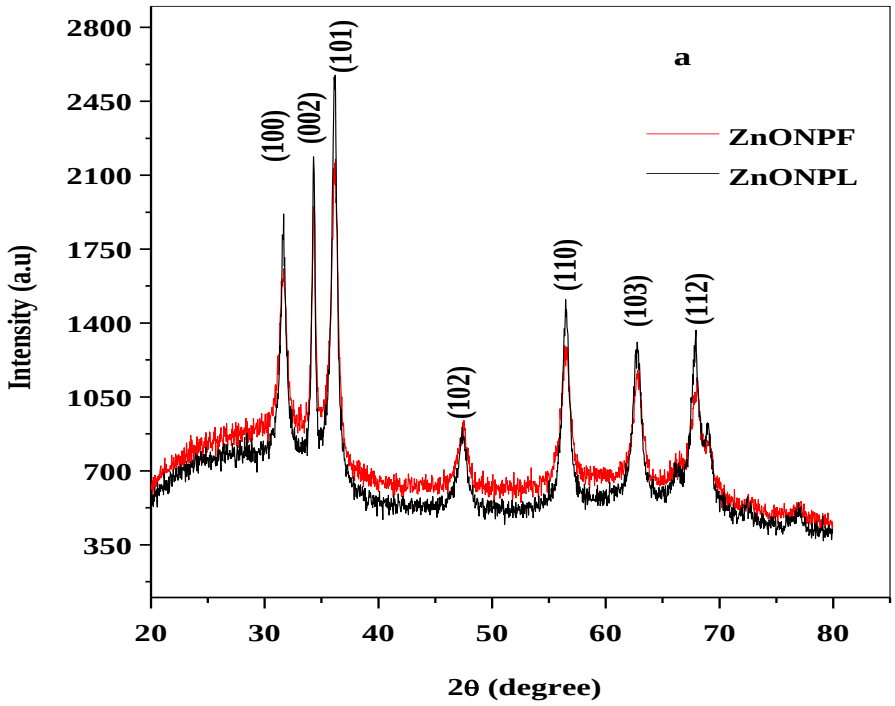

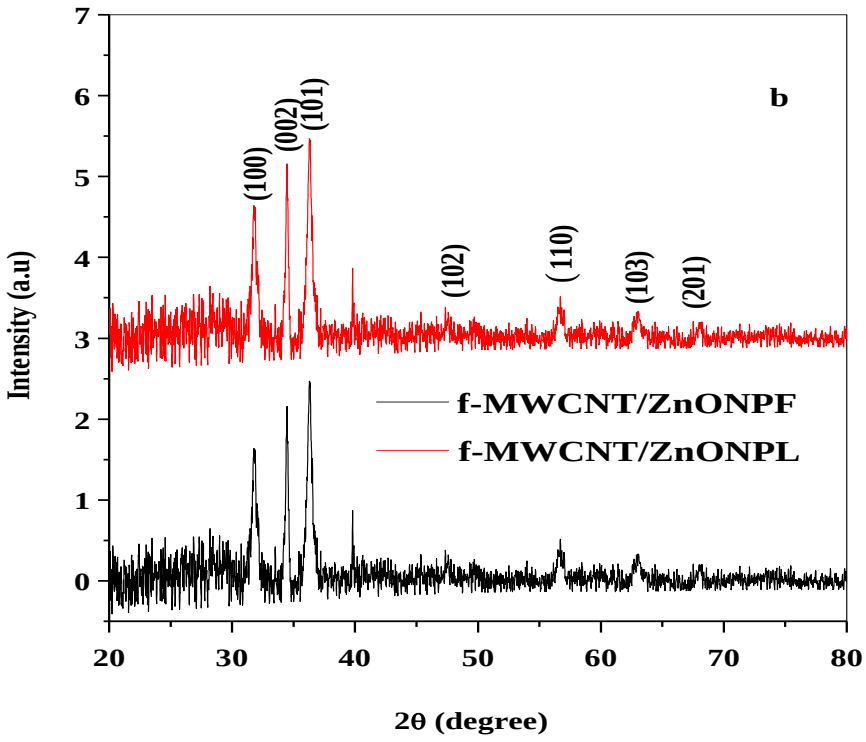

Figure 4.27: XRD pattern of (a) ZnONP and (b) f-MWCNT/ZnONP.

4.2.1.4 Transmission electron microscopic analysis

Figure 4.28 ai shows the TEM micrograph of ZnONPL with the size distribution on Figure 4.28 aii using image J software application. The TEM image of Zinc oxide nanoparticles mediated from leaves (ZnONPL) revealed a well dispersed particles as dark dots nearly spherical in shape with a mean diameter and average particle size of 1.020 ±0.67 for 6497 number of counts (N). Figure 4.28 bi shows a micrograph of ZnONP from flowers extract of *C. viminalis* (ZnONPF) with the size distribution (Figure 4.28 bii) using image J software application. The image showed a non dispersed nanoparticles as a dark dots with average particle size of 5.06 ± 1.695 and 5.06 nm (mean diameter, N = 948).

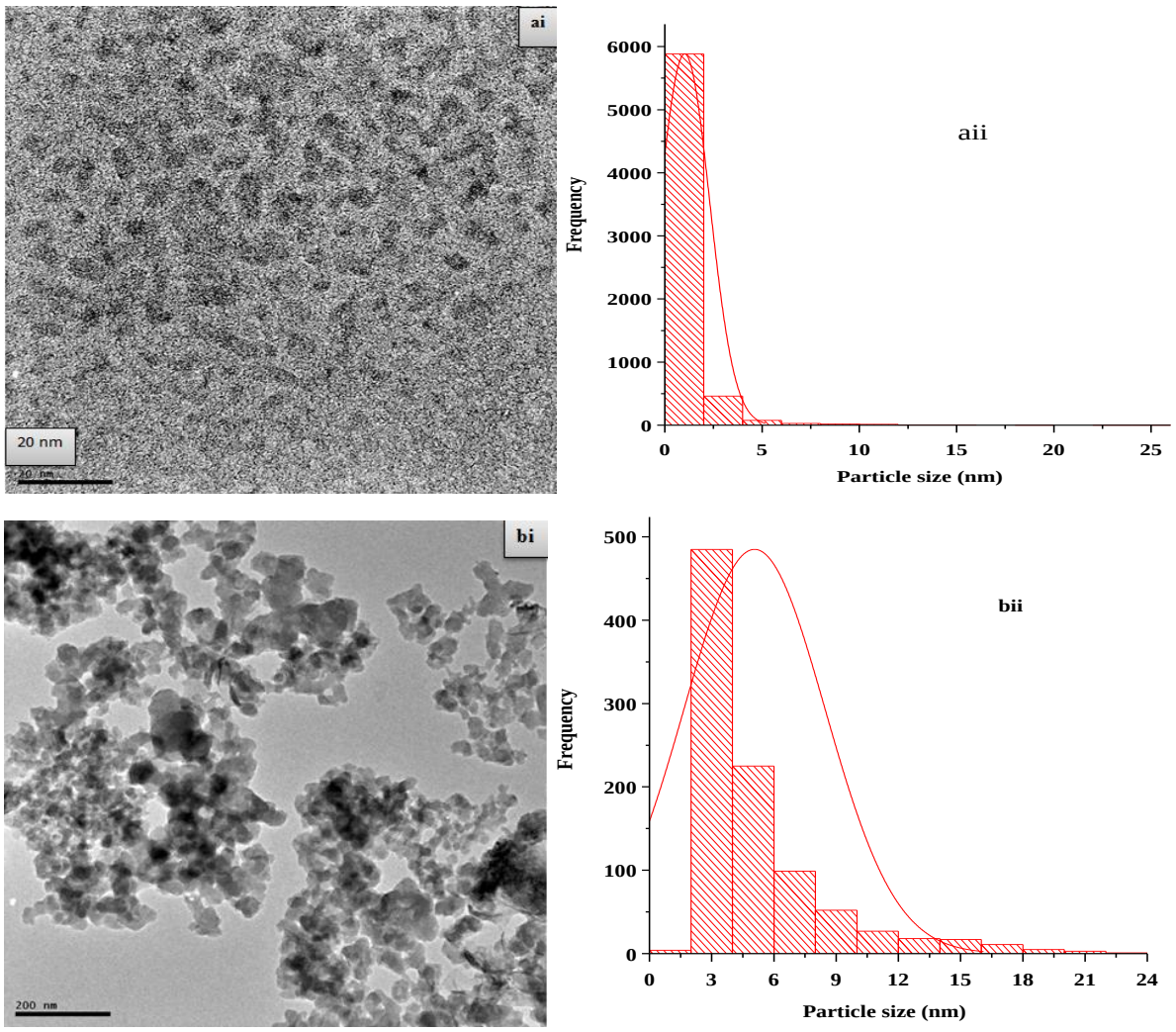

Figure 4.28: TEM Micrograph of (ai) ZnONPL (bi) ZnONPL (aii) size distribution of ZnONPL (bii) size distribution of ZnONPF.

4.2.1.5 Scaning electron microscopy (SEM)

Figure 4.29a revealed a well distributed net-like structure (reticular) and irregular flower shaped nano structured of f-MWCNT/ZnONPL while a rough nanostructure with a spatially distributed boulder like grain of ZnONPL on the morphology of f-MWCNT/ZnONPF composite is noticed on f-MWCNT/ZnONPF (Figure 4.29b).

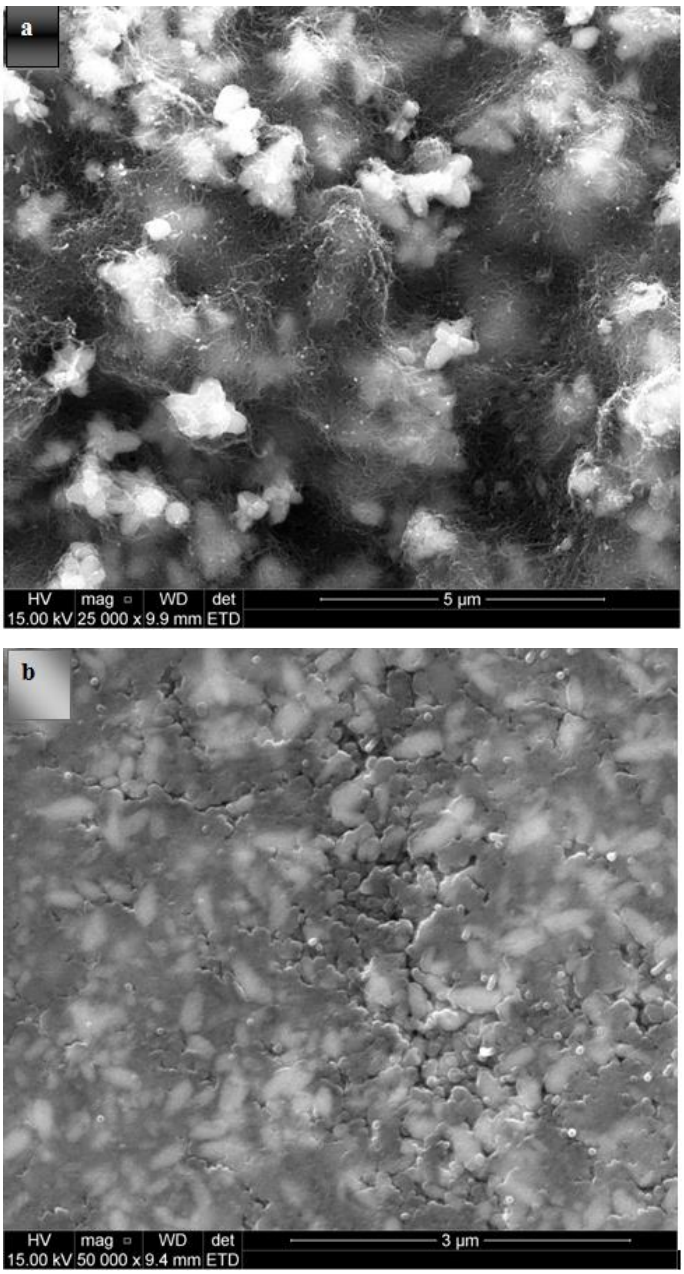

Figure 4.29: SEM images of (a) f-MWCNT/ZnONPL and (b) f-MWCNT/ZnONPF.

4.2.1.6 Thermogravimetry analysis

Thermogravimetric curves of synthesized ZnONP is shown in Figure 4.30. Percentage weight loss (0.3%, 4.6% and 23%) was observed at 53, 187 and 619 ^{o}C for ZnONP synthesized from flowers extract (ZnONPF) which are attributed to loss of moisture, water and organic compounds respectively. A slight weight loss (0.1%) though minute and 10% loss was noticed at 59 and 485 ^{o}C for ZnONPL. Stability of synthesized ZnONPF and ZnONPL was attained at 619 ^{o}C and 485 ^{o}C since there was no detectable weight loss after these temperatues. ZnONPL

seemed to be more stable than ZnONPF. The TGA curves obtained are quite similar to that in the litrature (Al-Shabib *et al.*, 2016; Chunduri *et al.*, 2017).

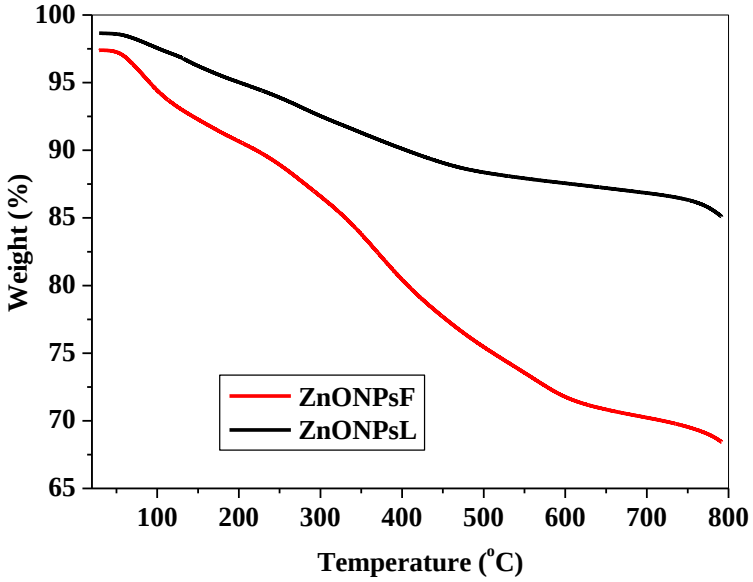

Figure 4.30: TGA curves of ZnONP.

4.2.1.7 Zeta potential analysis

Zeta potential, which could also be refer to electrokinetic potential with a Greek symbol (ζ) is a characteristics of nanoparticles suspended in or dispersed in fluid and is based on the interaction of dispersed or suspended particle in a fluid between the charged particle and applied field on give an insight on the type of electrical charge on the particle (negative or positive) and also the stability of synthesized ZnONP. From the zeta potential analysis of green mediated ZnONP from leaves and flowers of *C. viminalis* using Malvern zetasizer instrument version 7.11, Zeta potential values -15.1 mV and -35.2 mV was obtained for ZnONPL and ZnONPF respectively. Summary of the zeta potential analysis of ZnONPL and ZnONPF are shown in Figure 4.31a,b. The high negative zeta potential values (-15.1 and -35.2 mV) are indication of the existence of electrostatic forces of repulsion between the ZnONPs which resulted in an increased stability of the synthesized nanoparticles (Senthilkumar *et al.*, 2017). Hence, synthesized ZnONP are in good stability. However, A higher stability was observed in ZnONPF than ZnONPL due to the greater surface charge (-35.2 mV) which could be attributed to the existence of more dense electrostatic forces within the synthesized particles and compositions of the reducing agent in the *C. viminalis* flowers extract. Obtained zetal potential values were within the range of -13 and

-57.70 mV reported in zinc oxide nanoparticles (Al-Shabib *et al.*, 2016; Azizi *et al.*, 2017; Chunduri *et al.*, 2017; Song & Yang, 2016).

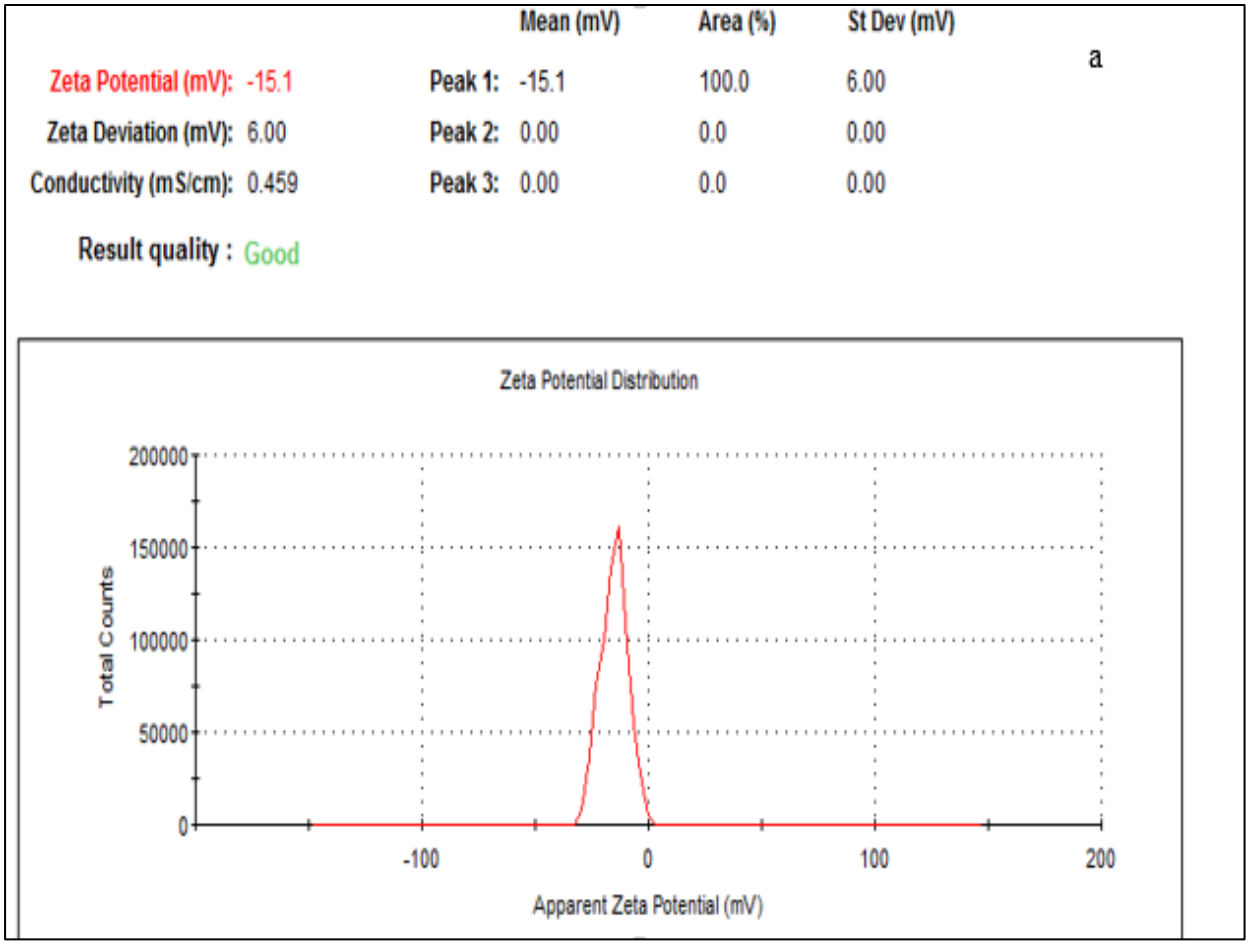

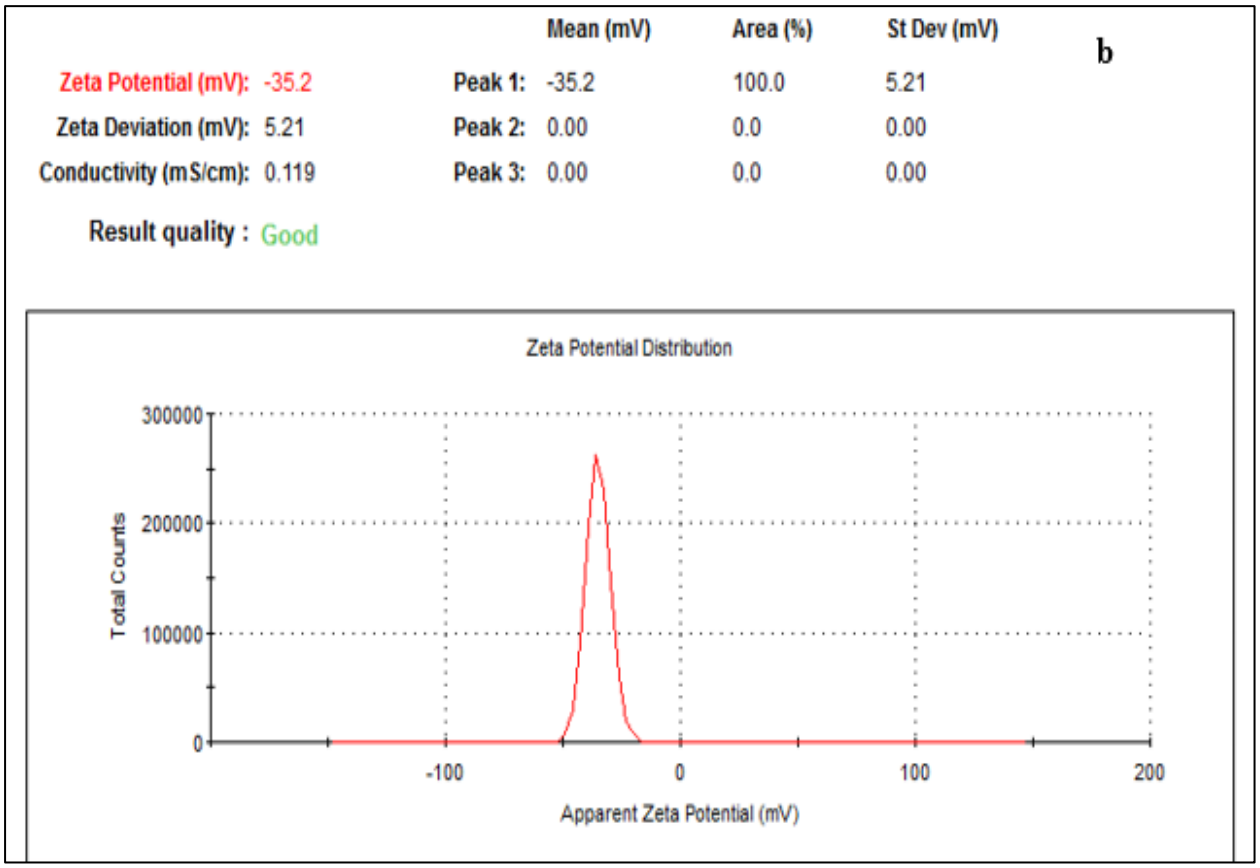

Figure 4.31: Zeta potential analysis (a) ZnONPL and (b) ZnONPF.

4.2.2 Electrochemical studies

4.2.2.1 Cyclic voltammetric characterization of modified GCE/f-MWCNT/ZnONP electrodes

The electron transport for the bare and modified electrodes were investigated using cyclic voltammetry (CV) experiments in 0.1 M phosphate buffer solution (PBS) containing $K_3[Fe(CN)_6]$ (probe solution) at 25 mVs^{-1} potential sweep. Redox peaks were observed in all the electrodes except modified nanoparticle electrodes (GCE/ZnONP) as shown in Figure 4.32a,b. The absence of the redox peaks on ZnONP modified electrode could probably be due to fast electron transport at the electrodes or overlap between $K_3[Fe(CN)_6]$ and ZnO redox peaks. The oxidation peak potential noticed on the nanocomposites modified electrode at about 0.35 V for GCE/f-MWCNT/ZnONPL is possibly due to overlap of Fe^{3+} from the probe solution and $Zn^{2+/}Zn$ redox process (Adekunle *et al.*, 2011). The less vivid probe peak on GCE/f-MWCNT/ZnONPF cyclic voltammogram could be ascribed to the capacitive nature of the electrode which favours charge storage. The anodic peak current responses for the electrodes are

in an ascending order: GCE (20.2 μA) < GCE/f-MWCNT/ZnONPL (39.0 μA) < GCE/f-MWCNT (47.4 μA) < GCE/f-MWCNT/ZnONPF (83.4 μA). High current response observed at nanocomposites modified electrodes compare with the bare GCE conceded with literature and is owed to the ionic interaction between f-MWCNT and ZnONP, the conductive nature of ZnONP and f-MWCNT, and the large surface area provided by f-MWCNT which allows free flow of electrolytes and charges between the base of electrode and electroactive species at the surface of the electrode. Comparing the cyclic voltammogram of the modified GCE/f-MWCNT/ZnONPL and GCE/f-MWCNT/ZnONPF electrodes (nanocomposites electrodes), current response at the later was twice higher than the former. Table 4.8 presents the electrochemical parameters obtained from CV measurement.

Table 4.8: Parameters determine from cyclic voltammetric measurements at bare and modified electrode.

Electrode type	Ipa (μA)	Ipc (μA)	Epa (V)	Epc (V)	ΔE (V)	$E_{1/2}$
GCE	20.2	- 29.5	0.266	0.180	0.086	0.043
GCE/f-MWCNT/ZnONPL	36.7	-112.6	0.352	0.286	0.066	0.033
GCE/f-MWCNT/ZnONPF	83.4	-37.21	0.192	0.313	0.121	0.0605

*Ipa = oxidation peak current; Ipc = reduction peak current; Epa = oxidation potential peak; Epc = reduction potential peak; ΔE = Epa, Epc separation and $E_{1/2}$ (forma potential) $= \frac{Epa-Epc}{2}$

Both nanocomposites modified electrode demonstrated a quasi-reversible reaction from ΔE value.

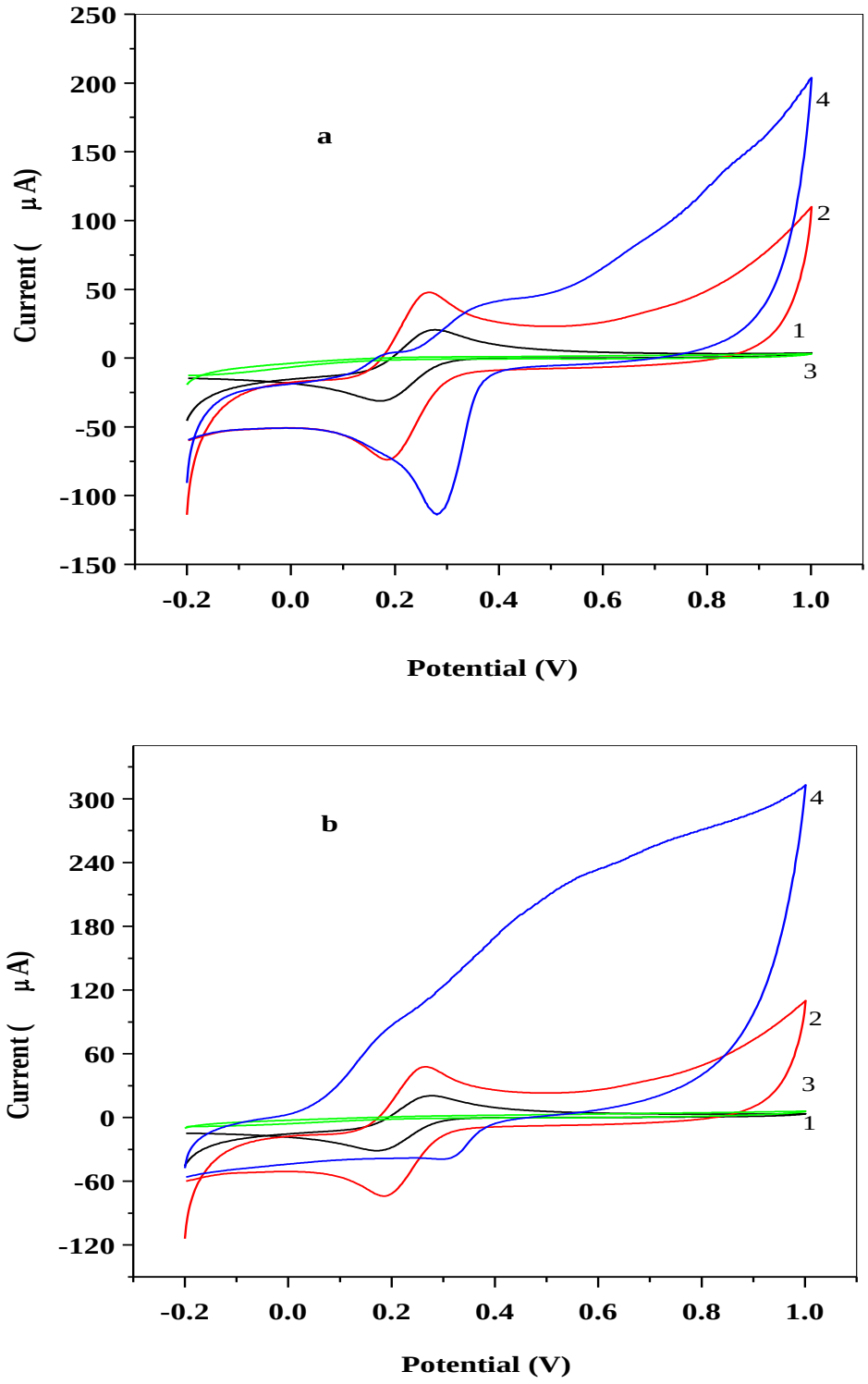

Figure 4.32: Cyclic voltammogram of (1) bare GCE (2a) GCE/ZnONPL (2b) GCE/ZnONPF (3a,b) GCE/MWCNT (4a) GCE/f-MWCNT/ZnONPL and (4b) GCE/f-MWCNT/ZnONPF in 10 mM PBS solution, pH 7.4 containing 5 mM $K_3[Fe(CN)_6]$.

4.2.2.2 Impact of varying scan rate

The effect of scan rate on potential and current peak for the modified nanocomposites electrodes was conducted in probe solution using CV technique. An increase in both anodic and cathodic peak current (Ipa, Ipc) with increasing scan rates (25 -500 mVs^{-1}) was noticed as presented in Figure 4.33a, b. In addition, there was an increment in ΔE values (9 - 232 mV) as the scan rate increased connoting a quasi -reversible reaction. The plot of Ipa/Ipc varied linearly with square root of scan rate (Figure 4.33c, d) with 0.98404 and 0.99339 regression values for GCE/f-MWCNT/ZnONPL and GCE/f-MWCNT/ZnONPF confirming diffusion controlled process. Active surface area was estimated to be 3.6×10^{-2} cm^2 (GCE/f-MWCNT/ZnONPL) and 3.1×10^{-2} cm^2 (GCE/f-MWCNT/ZnONPF) using equation 2.3.

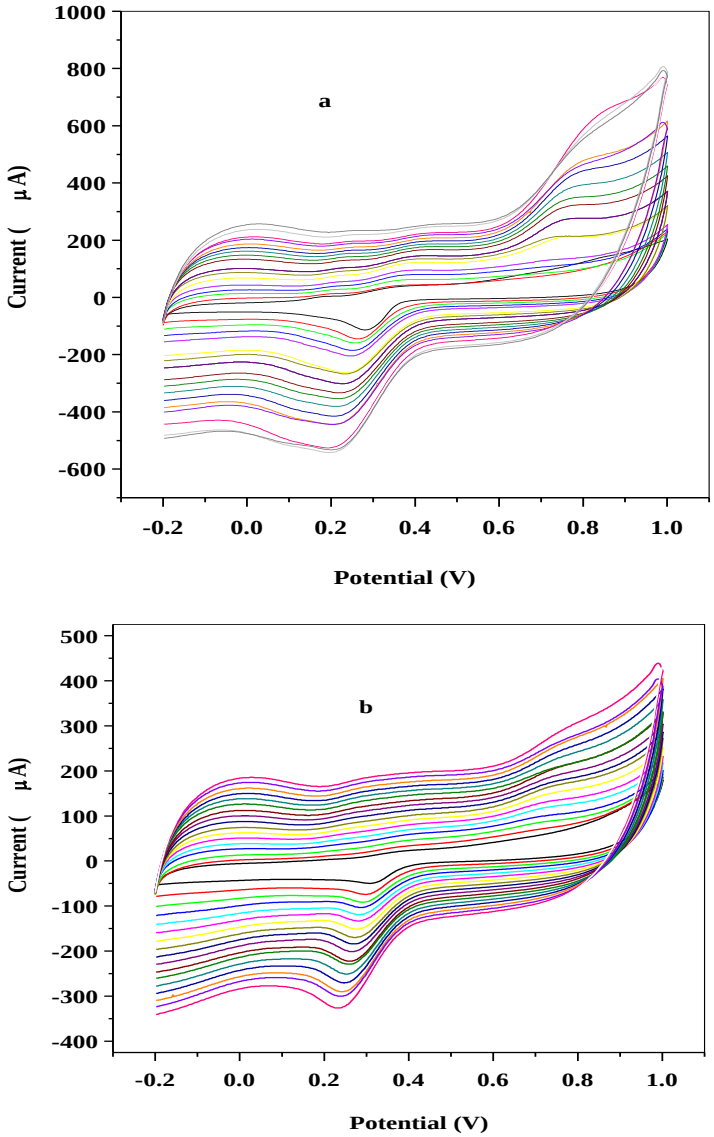

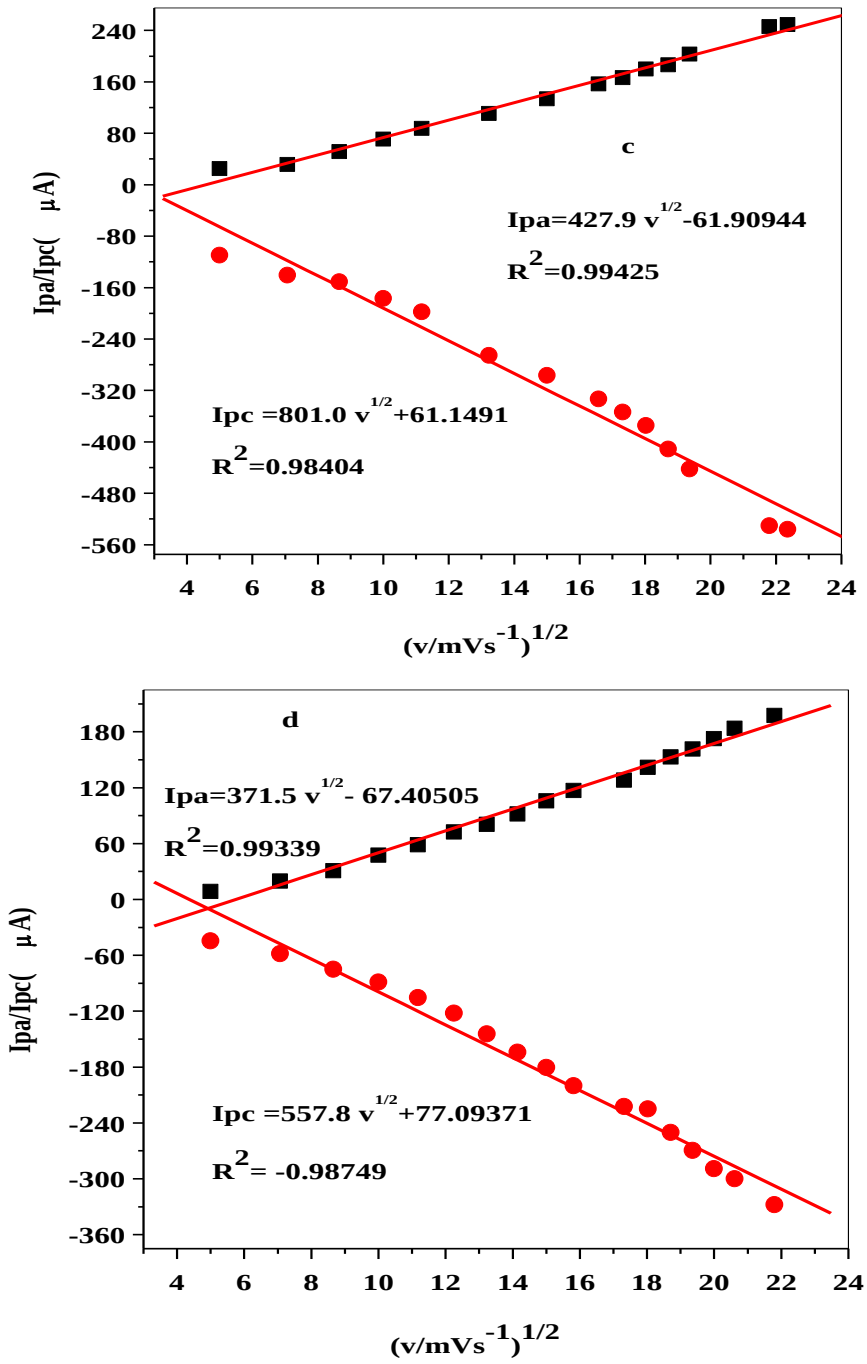

Figure 4.33: Cyclic voltammogram analysis of (a) GCE/f-MWCNT/ZnONPL and (b) GCE/f-MWCNT/ZnONPF in 5 mM $K_3[Fe(CN)_6]$ prepared in 10 mM PBS, pH 7.4; linear plot of current against square root of scan rate (v/mVs^{-1}) for (c) GCE/f-MWCNT/ZnONPL and (d) GCE/f-MWCNT/ZnONPF.

Furthermore, from the cyclic voltammetric experiment, anodic peak potentials was plotted against logarithm of scan rate (graph not shown) with resulting 0.08619 and 0.0816 $Vdec^{-1}$ slope values at the respective electrodes as expressed in the linear equation 4.18 to 4.21.

$$Epa = 0.08619 \log v + 0.16732;\ R^2 = 0.92261 \quad (4.18)$$

$$Epc = -0.07627 \log v + 0.40844;\ R^2 = -0.94837 \quad (4.19)$$

GCE/f-MWCNT/ZnONPL

$$Epa = 0.0816\ \log v + 0.15681;\ R^2 = 0.9248 \quad (4.20)$$

$$Epc = -0.08316 \log v + 0.48005;\ R^2 = -0.93981 \quad (4.21)$$

GCE/f-MWCNT/ZnONPF

Low regession value suggest a slow interfacial rate of electron transport due to adsorption of reactants intermediate at the electrode surface. Based on the slope values (0.08619, 0.0816), Tafel slope (b) was found to be 172 and 163 $mVdec^{-1}$ for the GCE/f-MWCNT/ZnONPL and GCE/f-MWCNT/ZnONPF electrodes employing equation 4.6. The b values suggest adsorption process on the modified nanocomposites electrodes surface since tafel values were > 118 $mVdec^{-1}$ (theoretical values). Electron transfer coefficient (α), number of electron (n) involved in the rate determining step were estimated to be 0.53 and 0.49; n = 1 using 4.11and 4.12 relationship with slope of linear equation (4.18- 4.21) equal to $\frac{-2.3RT}{\propto nF}$ and $\frac{2.3RT}{(1-\propto)nF}$ assigned to cathodic and anodic peak according to Laviron and 0.25 and 0.14 (cms^{-1}) ks (from equation 4.7) for GCE/f-MWCNT/ZnONPL and GCE/f-MWCNT/ZnONPF electrodes respectively.

4.2.2.3 Impedimetric characterization of the designed electrode

AUTOLAB frequency response analyser (FRA) GPES software version 4.9 between 100 kHz and 0.1 Hz was employed in investigating the interfacial properties of the electrodes in 5 mM $K_3[Fe(CN)_6]$ at fixed potential 0.2V vs Ag/AgCl sat'd KCl. The Nyquist plot obtained is shown in Figure 4.34a, b while circuit models used in the fitting of the impedance data for GCE, GCE/f-MWCNT and GCE/f-MWCNT/ZnONP is presented in Figure 4.34c, d and Table 4.9 presents the values of fitted equivalent circuit parameters. R_{ct}, which conforms to electron transfer kinetics of the redox probe at the electrode surface, is reflected on the arc diameter while Warburg impedance appeared as a linear line with 45° slope resulting from semi-infinite diffusion process (Choi *et al.*, 2020). The decrease in R_{ct} values in nanocomposites modified electrodes suggest an improved conductivity of the modified electrode as a result of the synergic effect of MWCNT and ZnONP on the electrode. Also, it connotes higher rate of interfacial

electron transfer of the Probe. High C_{dl} in GCE/f-MWCNT/ZnONPF indicates oxidation intermediates adsorption resulting in increased storage of charges related to the capacitive behavior noticed in cyclic voltammogram. See Table 4.9 for result summary.

Furthermore, electron transfer rate constant (k^0) and exchange current density (i_0) was determined via EIS using equation 4.6 and 4.7 respectively. Estimated values are presented in Table 4.9. There is no much significant different in the EIS and CV k^0 for GCE/f-MWCNT/ZnONPF as expected theoretically while CV- determined electron transfer rate constant for GCE/f-MWCNT/ZnONPL (2.5×10^{-1} cms^{-1}) was quite higher than EIS value which probably is associated with a faster overall impedance.

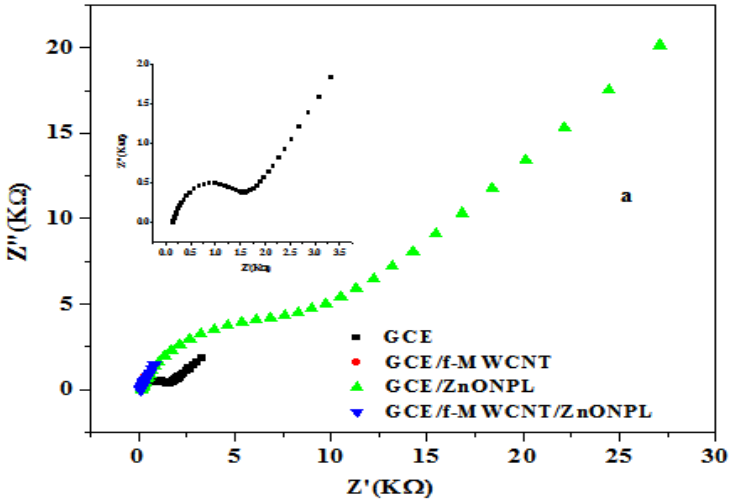

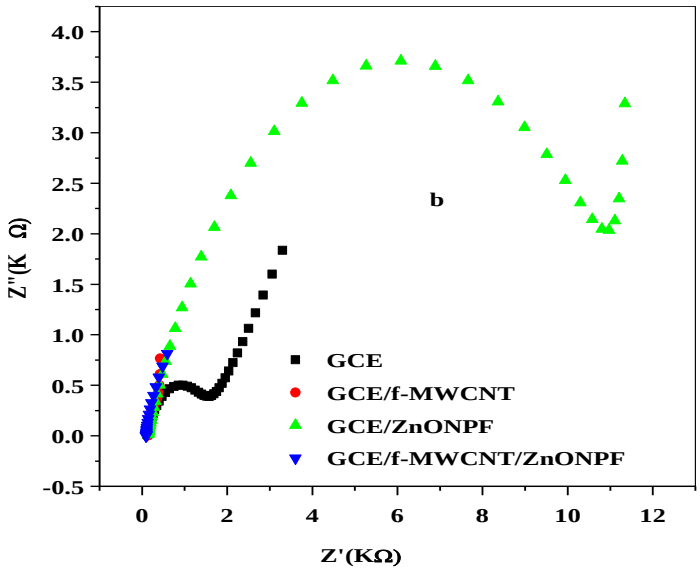

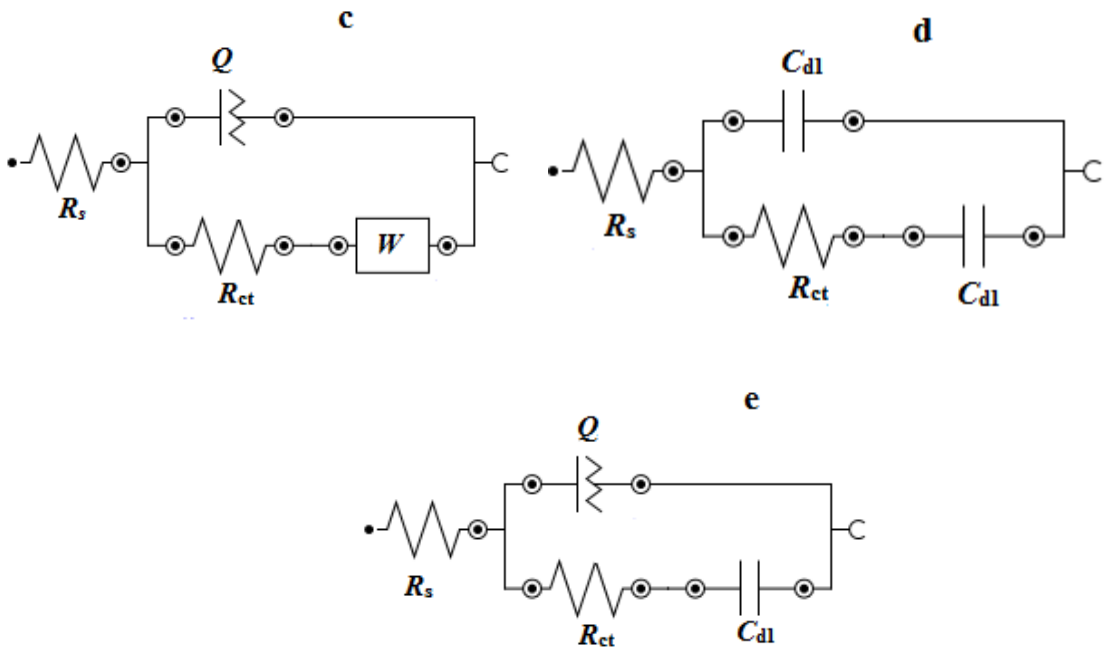

Figure 4.34: Nyquist plots of (a,b) bare GCE and modified electrodes in 0.1 M PBS, pH 7.4 containing 5 mM $K_3[Fe(CN)_6]$ and circuit models: (c) [R(Q[RW)] (d) [R(C[RC] and (e) [R(Q[RC] for GCE, GCE/f-MWCNT, GCE/f-MWCNT/ZnONP accordingly.

Table 4.9: Impedance data for bare, GCE/f-MWCNT and ZnO nanocomposite modified electrodes in 0.1 M PBS and $K_3[Fe(CN)_6]$ electrolyte at a constant potential of 0.2 V vs Ag/Ag/Cl Sat'd KCl.

Electrodes	R_s (Ω)	R_{ct} (Ω)	C_{dl} (μF)	k^0 (cm/s)	i_0 (a/cm^2)	Chi square
GCE	123 (3.04)	1402 (4.74)	-------	1.2×10^{-3}	3.63	0.404
GCE/ZnONPL	149 (4.29)	8500 (8.60)	-----	1.9×10^{-4}	0.575	0.5603
GCE/ZnONPF	136 (5.16)	11800 (4.50)	515 (33.4)	1.4×10^{-4}	0.424	0.7924
GCE/f-MWCNT	123(1.97)	664 (12.3)		2.4×10^{-3}	7.2	0.6657
GCE/f-MWCNT/ZnONPF	89(4.0)	14.5 (35.3)	685 (10.0)	1.2×10^{-1}	351	0.3078
GCE/f-MWCNT/ZnONPL	108(1.81)	17.2 (92.0)	125 (17.55)	9.8×10^{-2}	29.1	0.3075

4.2.2.4: pH optimization on the electrocatalysis of choline at modified nanocomposites

The effect of pH on the electrocatalysis of 2 mM choline was studied over the pH range of 3.1-8.9 in lithium chloride (LiCl) solution by cyclic voltammetry since the electrode reaction might be influenced by pH of the electrolyte (medium). Optimum response to choline was obtained at pH 7.3 as shown in Figure 4.35. Thus, pH 7.3 was selected for all the experiments.

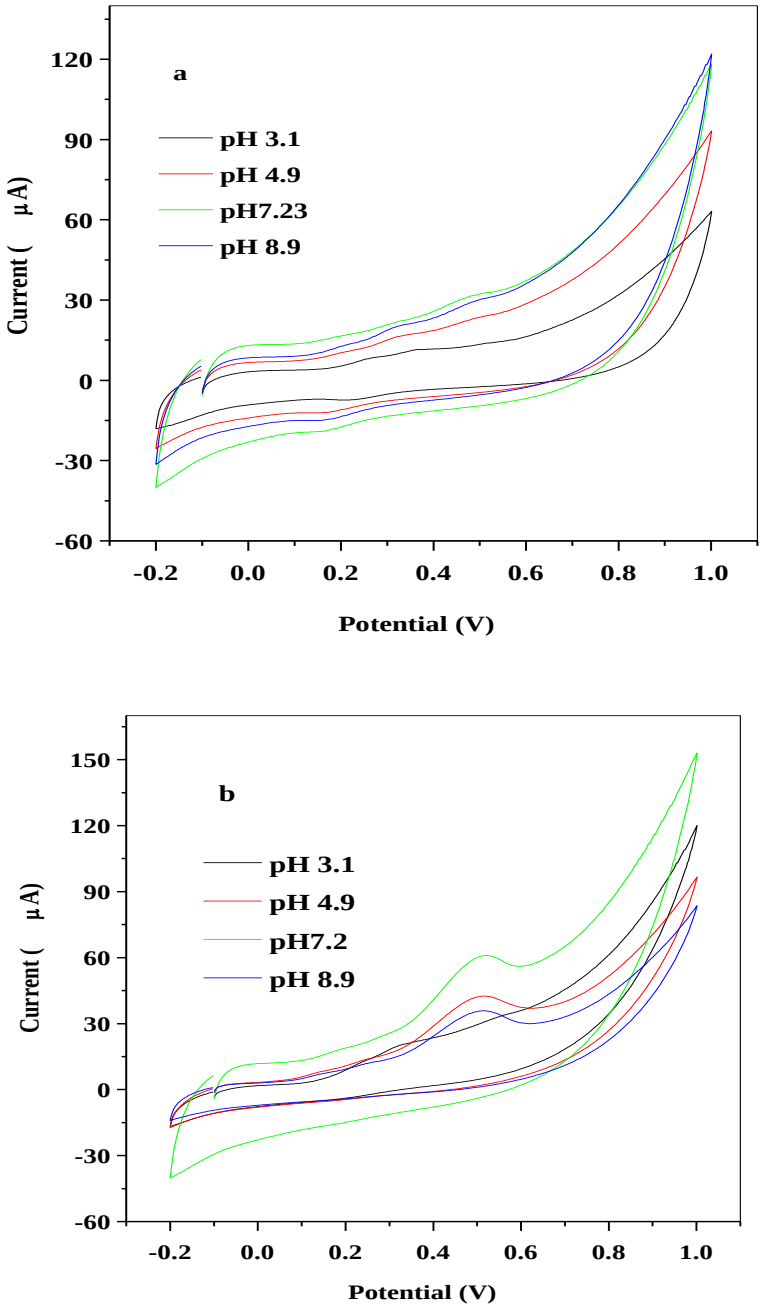

Figure 4.35: Cyclic voltammogram of (a) GCE/f-MWCNT/ZnONPL and (b) GCE/f-MWCNT/ZnONPF in 2 mM choline prepared in 10 mM LiCl of different pH.

4.2.2.5 Electrocatalysis of choline on modified nanocomposite electrodes surface

The electrochemical response of choline at bare (GCE), modified f-MWCNT/metal oxide (GCE/ZnONP) and nanocomposite (GCE/f-MWCNT/ZnONP) electrodes in 10 mM LiCl solution, pH 7.3 containing 2 mM of choline was studied using cyclic voltammetry with potential window -0.2 - 1.0 V. In Figure 4.36a, b, choline oxidation peaks (Ipa and Epa) were seen at 1.22 µA 0.32 V for GCE/ZnONPL, 1.19 µA (0.34 V) for GCE/ZnONPF, 20.1 µA (0.51 V) and 151.4 µA (0.67V) for GCE/f-MWCNT/ZnONPL and GCE/f-MWCNT/ZnONPF electrodes respectively while a capacitive current was noticed on GCE, GCE/f-MWCNT electrode. High current response at the latter electrode (GCE/f-MWCNT/ZnONPF) suggests better biocompatibility of choline with the nanocomposites. However, no peak was noticed in the reverse scan indicating an irreversible oxidation process (Gowda & Nandibewoor, 2014). The oxidation product on the electrode displayed no re-oxidized or reduced peak in succession at potential extended range which certifies that, the oxidation product was not electroactive (Gowda & Nandibewoor, 2014). Redox peak was noticed at GCE/f-MWCNT/ZnONPL electrodes with 396 mV (0.548 - 0.152) peak potential separation and oxidation/reduction peak current ratio was > 1 (2) suggesting quasi-reversible reaction (Espinoza *et al.*, 2019). Figure 4.37a, b represents possible redox process and electrochemical oxidation mechanism of choline for GCE/f-MWCNT/ZnONPL and GCE/f-MWCNT/ZnONPF.

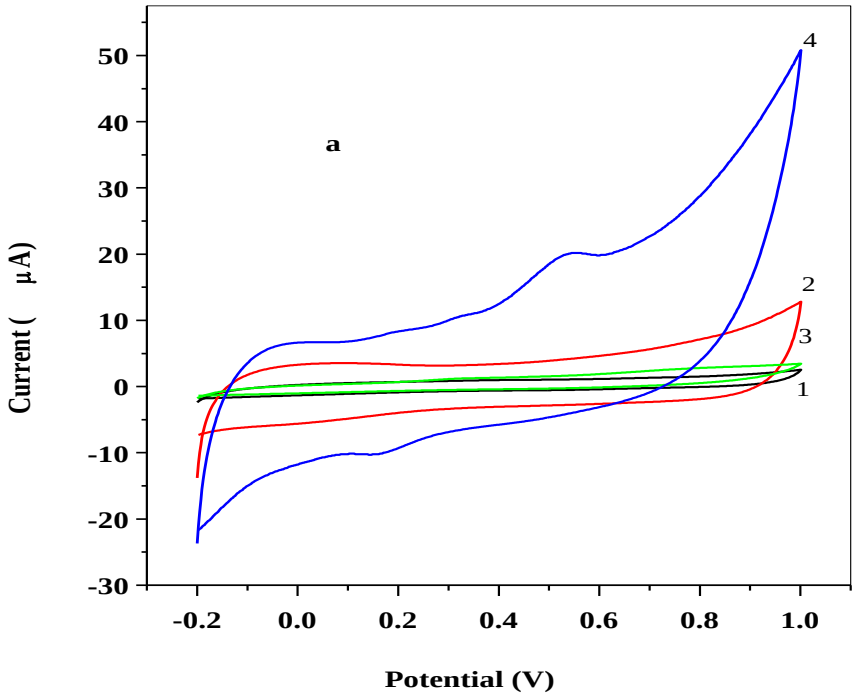

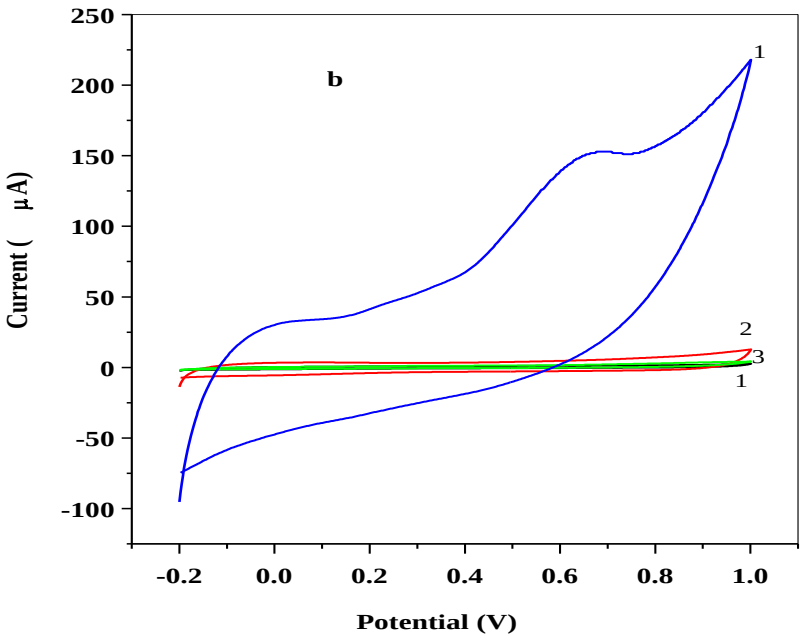

Figure 4.36: Cyclic voltammogram of (1a,b) bare GCE (2a) GCE/ZnONPL (2b) GCE/ZnONPF, (3a,b) GCE/f-MWCNT and (4a) GCE/f-MWCNT/ZnONPL, and (4b) GCE/f-MWCNT/ZnONPF in 10 mM LiCl pH 7.3.

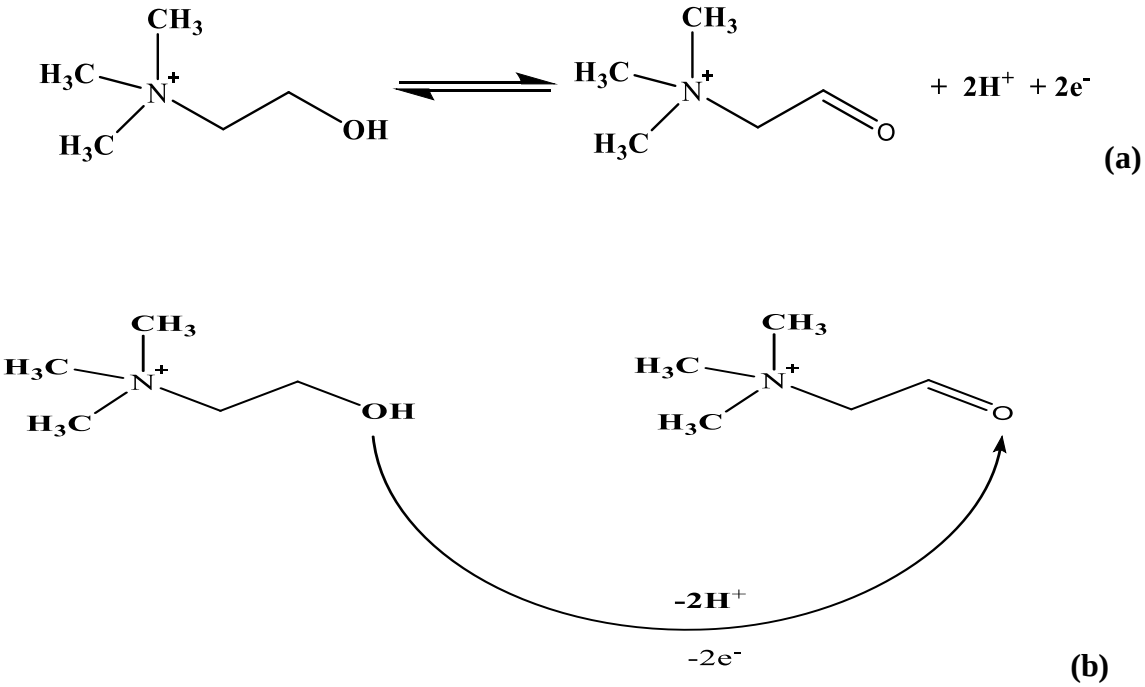

Figure 4.37: Possible electrochemical reaction mechanism for choline oxidation at the surface of (a) GCE/f-MWCNT/ZnONPL and (b) GCE/f-MWCNT/ZnONPF.

4.2.2.6 Effect of scan rate towards choline

The influence of scan rate potential on the electrochemical behavior of choline at modified nanocomposite electrode was studied using cyclic voltammetry with scan rate in the range of 25-400 mVs^{-1} in 2 mM choline as presented in Figure 4.38a, b. Scan rate studies were conducted to ascertain if the reaction on GCE/f-MWCNT/ZnONPL and GCE/f-MWCNT/ZnONPF was diffusion or adsorption controlled. GCE/f-MWCNT/ZnONPL voltammogram, a shift of anodic peak after the first scan at 25 mVs^{-1} to the negative, and then to the positive and an increasing oxidation current was noticed with increasing scan rate. In addition, peak potential separation (ΔE) increased from 80 - 446 mV with increasing scan rate, demonstrating quasi reversible reaction. Disappearance of peak potentials after the first scan observed for GCE/f-MWCNT/ZnONPF as seen in Figure 4.38a could probably be attributed to saturation of choline at the electrode surface (Mphuthi *et al.*, 2016). The plot of Ip against square root of scan rate ($V^{1/2}$) was linear for both electrodes with 0.99 regression coefficient (Figure 4.38i,ii) indicating diffusion controlled electrochemical process. From the slope values of Figure 4.38i,ii, diffusion coefficient was obtained for GCE/f-MWCNT/ZnONPL with equation 2.2 and 2.3 for GCE/f-MWCNT/ZnONPF.

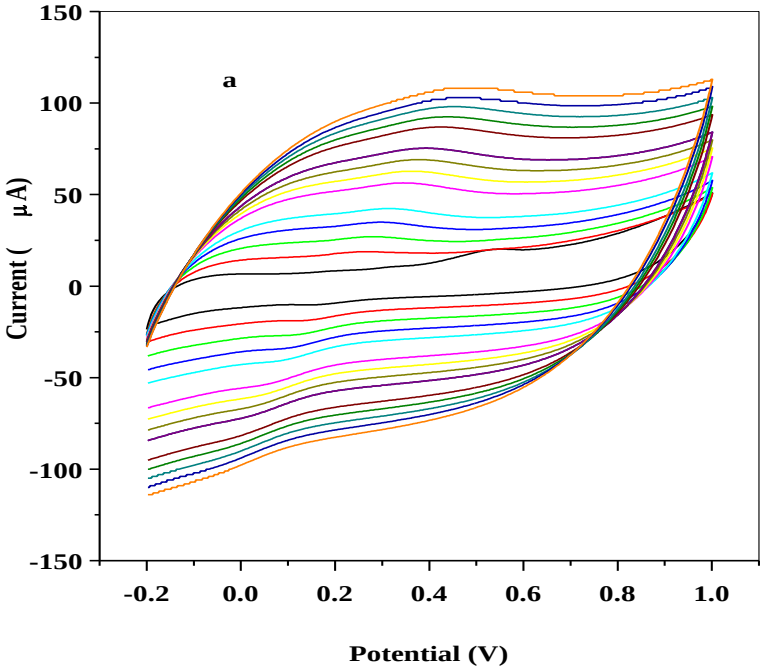

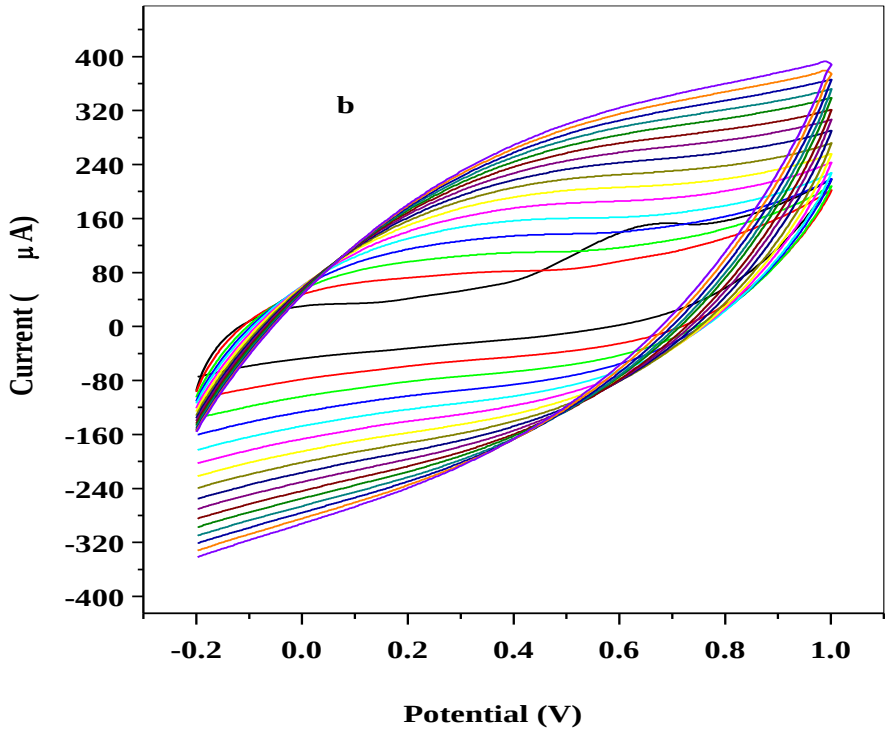
b
Current (µA)
Potential (V)
400
320
240
160
80
0
-80
-160
-240
-320
-400
-0.2
0.0
0.2
0.4
0.6
0.8
1.0

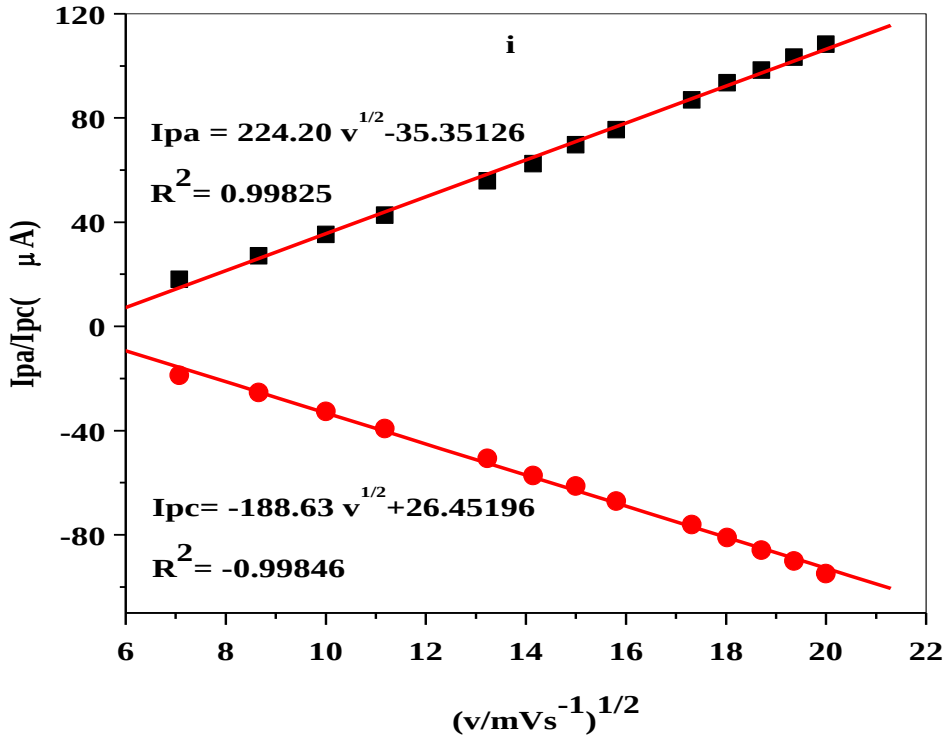
i
Ipa = 224.20 v^1/2 -35.35126
R^2 = 0.99825
Ipc= -188.63 v^1/2 +26.45196
R^2 = -0.99846
Ipa/Ipc(µA)
(v/mVs^-1)^1/2
120
80
40
0
-40
-80
6
8
10
12
14
16
18
20
22

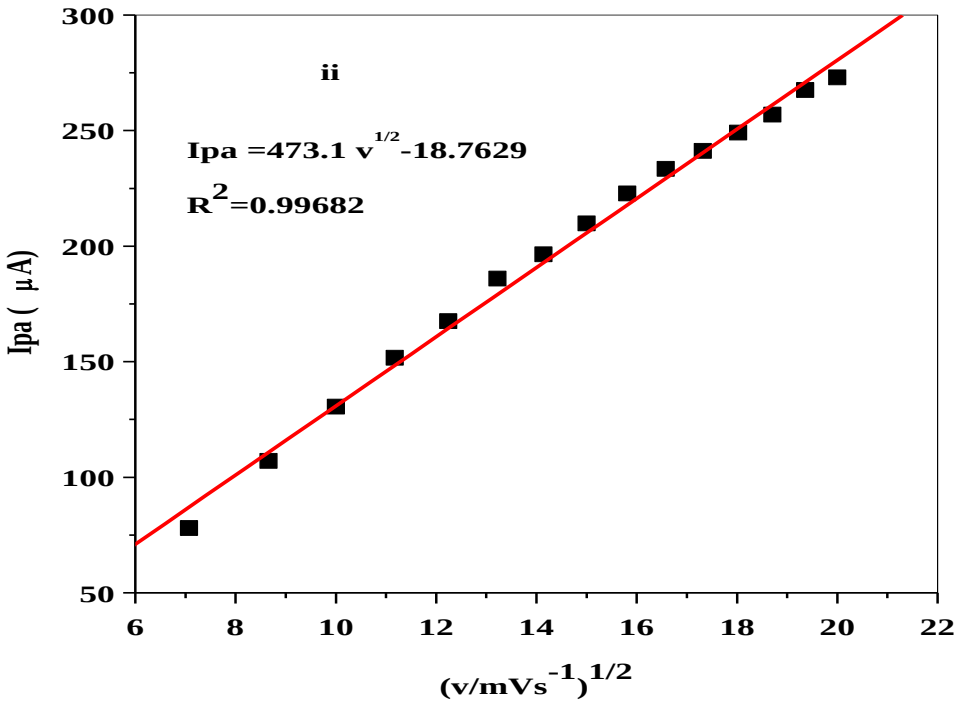

Figure 4.38: Cyclic voltammogram obtained for (a) GCE/f-MWCNT/ZnONPL (b) GCE/f-MWCNT/ZnONPF (25 – 400 mVs^{-1}; inner to outer); linear plots of Ipa versus square root of scan rate $(v/mVs^{-1})^{1/2}$ at (i) GCE/f-MWCNT/ZnONPL and (ii) GCE/f-MWCNT/ZnONPF in 10 mM LiCl pH 7.3 containing 2 mM choline.

Electroactive choline surface concentration (Γ) was calculated from slope values of Figure 4.39a, b (plot of peak current versus scan rate). The linear plot also confirmed a diffusion controlled reaction at the respective nanocomposite modified electrodes.

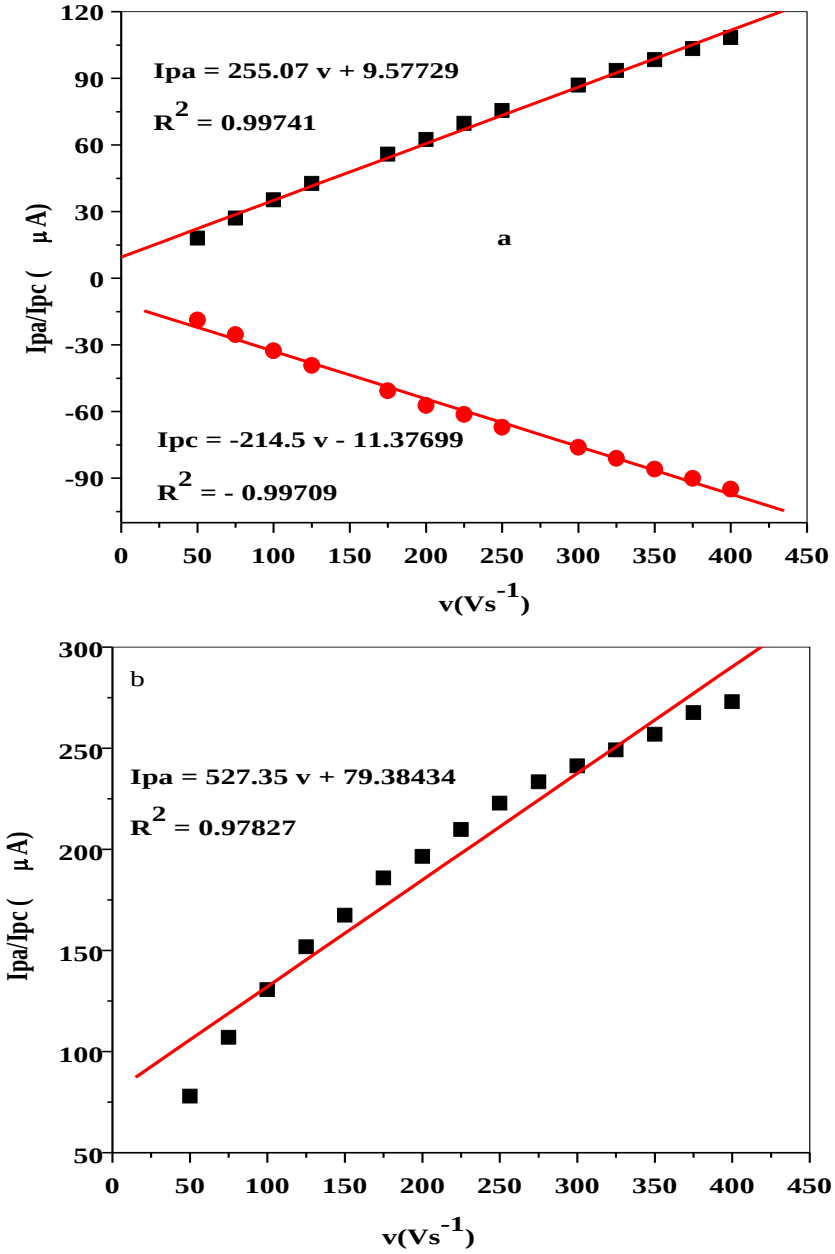

Figure 4.39: Linear plots of Ipa vs scan rate (v/Vs^{-1}) for (a) GCE/f-MWCNT/ZnONPL and (b) GCE/f-MWCNT/ZnONPF in 10 mM LiCl pH 7.3 containing 2 mM choline.

Furthermore, from the plot of logarithm of peak potential against logarithm of scan rate (plot not shown) with linear equation 4.22 - 4.25 below; the regression value further confirmed diffusion controlled process for GCE/f-MWCNT/ZnONPF while a mixed reaction (diffusion and adsorption) was observed for GCE/f-MWCNT/ZnONPL. The regression value (Epc = 1) suggest adsorption reaction (Fayemi *et al*, 2015).

$$\text{LogIpa}\ (\mu\text{A}) = 0.84818 \log v - 0.16042\ ;\ (R^2 = 0.999) \quad (4.22)$$

$$\text{LogIpc}\ (\mu\text{A}) = -0.78063 \log v + 0.04956;\ (R^2 = 1) \quad (4.33)$$

GCE/f-MWCNT/ZnONPL

$$\text{LogIpa}\ (\mu\text{A}) = 0.58501 \log v + 0.9356\ ;\ (R^2 = 0.999451) \quad (4.17)$$

GCE/f-MWCNT/ZnONPF

Linear equation from the plot of peak potential (Ep) logarithm of scan rate (graph not shown) is given below (equation 4.26 - 4.29):

$$\text{Epa} = 0.26411 \log v - 0.246\ ;\ (R^2 = 0.96903) \quad (4.26)$$

$$\text{Epc} = -0.14994 \log v + 0.42488;\ (R^2 = -0.98384) \quad (4.27)$$

(GCE/f-MWCNT/ZnONPL)

$$\text{Epa} = 0.14528 \log v + 0.0299;\ (R^2 = 0.98004) \quad (4.28)$$

(GCE/f-MWCNT/ZnONPF)

A 290 and 528 mVdec^{-1} Tafel (b) values was obtained at GCE/f-MWCNT/ZnONPL and GCE/f-MWCNT/ZnONPF) Epa slope values using equation 4.6 were quite higher than the theoretical value (118 mVdec^{-1}) stipulating adsorption of choline or its reaction intermediate at the electrodes surface. Also, from the slope, charge transfer coefficient (α), number of electron (n), and rate constant (ks) in the rate determining step were evaluated for the fabricated electrodes. Summary of the kinetics parameters for electroxidation of choline is shown in Table 4.10

Table 4.10: Kinetic parameters for choline redox reaction at GCE/f-MWCNT/ZnONPL and oxidation reaction at GCE/f-MWCNT/ZnONPF.

Electrode type	Diffusion coefficient (D) in cm^2/s	Surface concentration of cholne (Γ) in mol/cm^2	Number of electrons (n)	Electron transfer coefficient (α)	Electron rate constant (Ks) in cms^{-1}
GCE/f-MWCNT/ ZnONPL[a]	1.78×10^{-4}	8.64×10^{-7}	1	0.63	0.01
GCE/f-MWCNT/ ZnONPF[b]	1.54×10^{-3}	8.64×10^{-3}	1	0.59	0.0007

- Values of D for electrode a, and b was estimated using equation 2.2 and 2.3 respectively, while equations 4.7 and 4.10 was used for ks and Γ respectively.

4.2.2.7 Impedimetric studies on choline

The mechanism of the electron transport process during the oxidation of 2 mM choline at fixed 0.50 V potential vs Ag/AgCl sat'd 3 mole KCl and frequencies between 100 kHz and 0.1 Hz was monitored using impedance. Nyquist graph obtained are presented in Figure 4.40a while Figure 4.40c shows the equivalent circuit ([R(Q[RC]) applied in the fitting of impedance spectra and the values of the fitted equivalent circuit parameters is shown in Table 4.11. Lower R_{ct} values were obtained at nanocomposite modified electrode as compared with the bare GCE indicating that exchange of electrons was much easier at the electrodes (GCE/f-MWCNT/ZnONPF and GCE/f-MWCNT/ZnONPL). However, GCE/f-MWCNT/ZnONPF had the lowest charge transfer resistance (R_{ct}) value which probably was accountable for the high electron transfer performance exhibited during choline oxidation from the cyclic voltammetry experiment. Low C_{dl} values noticed at same electrodes indicates lesser charge storage at the electrodes which allowed rapid transport of ions during choline oxidation. The sequence of electron transport process is GCE< GCE/f-MWCNT< GCE/f-MWCNT/ZnONPL< GCE/f-MWCNT/ZnONPF.

Also, the rate constant of electron transfer (k^0) and exchange current density (i_0) as shown in Table 4.11 were determined for the unmodified and modified electrodes employing equation 4.6 and 4.7 respectively. EIS k^0 at GCE/f-MWCNT/ZnONPF was larger than cyclic voltammetric estimated value (7×10^{-4} cms^{-1}) which could be attributed to a lower overall impedance (Randviir, 2018) while vice versa for GCE/f-MWCNT/ZnONPL. Obtained i_0 was highest at the nanocomposite modified electrodes which agrees with the CV measurement indicating a fast rate of transfer of ions at the electrodes.

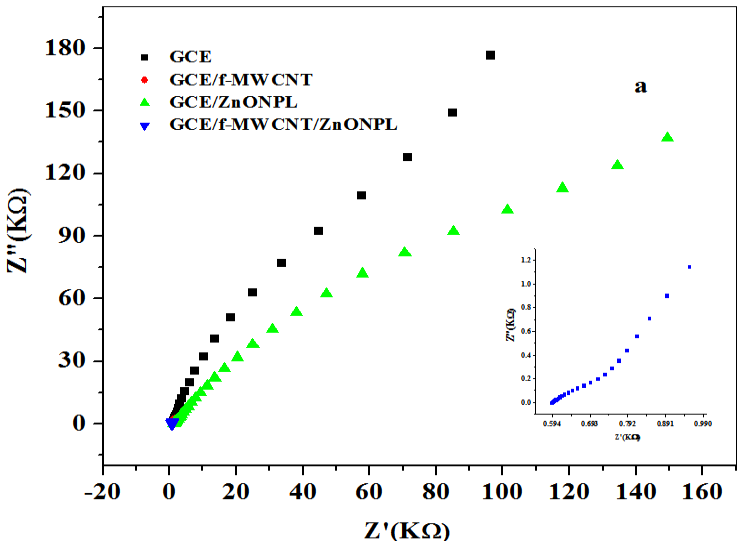

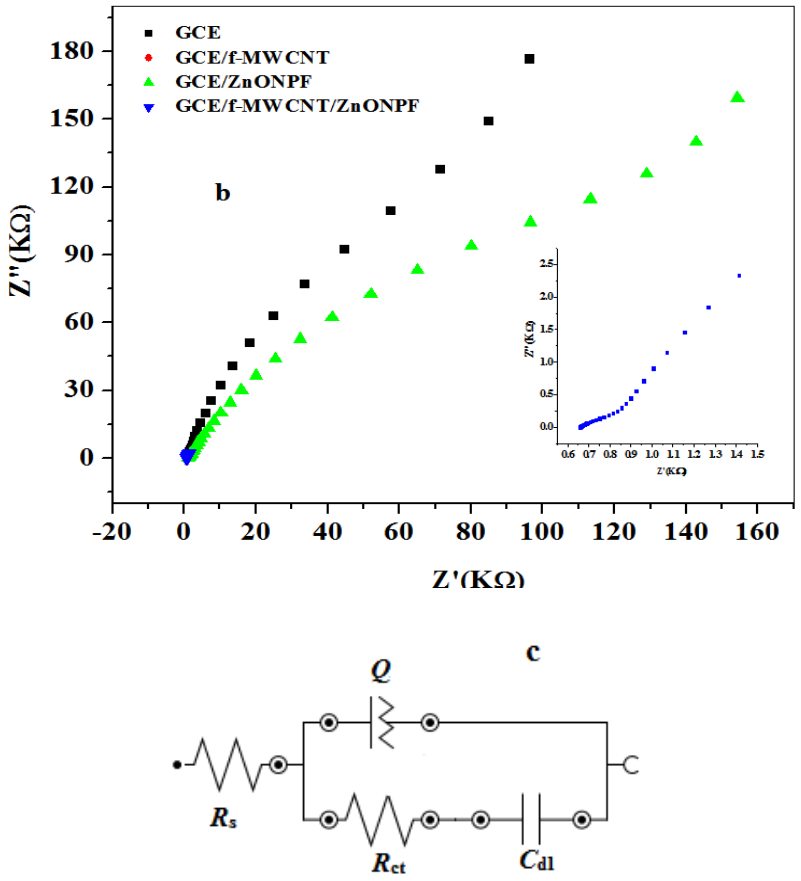

Figure 4.40: Nyquist plots of (a,b) bare and modified electrodes in 10 mM LiCl, pH 7.3 containing 2 mM choline and circuit model (c) bare and modified electrodes.

Table 4.11: Impedance data obtained for bare, GCE/f-MWCNT and ZnO nanocomposite modified electrodes in 10 mM LiCl containing 2 mM choline at a fixed potential 0.50V Ag/Ag/Cl sat'd KCl.

Electrodes	R_s **(kΩ)**	R_{ct} **(kΩ)**	C_{dl} **(μF)**	k^0 **(cms^{-1})**	i_0 **(A/cm^2)**	**Chi square**
GCE	1.17 (1.39)	349 (12.5)	6.05 (18.6)	3.6×10^{-3}	10.9	0.20346
GCE/ZnONPF	1.3 (1.71)	320 (7.94)	9.07 (18.5)	1.3×10^{-5}	0.03	0.21661
GCE/ZnONPL	1.28 (2)	365(9.71)	9.34 (24.8)	1.1×10^{-5}	0.03	0.25361
GCE/f-MWCNT	0.827(1.49)	1.13 (21.4)	296 (22.5)	3.7×10^{-3}	11.2	0.21939
GCE/f-MWCNT/ZnONPF	0.065 (1.19)	0.732 (29.9)	213 (21.2)	5.7×10^{-3}	17.2	0.1746
GCE/f-MWCNT/ZnONPL	0.592 (1.`6)	0.753 (5.18)	313 (49.9)	5.6×10^{-3}	16.9	0.372

4.2.2.8 Electroanalysis of choline

Further studies on the sensitivity and LoD of the electrodes towards choline was conducted via SWV with 0.005 V step potential, 25 Hz frequency at fixed potential +0.58 V vs Ag/AgCl saturated KCl with potential windows 0.2-0.8 V. Square wave voltammogram obtained for the nanocomposite modified electrodes after background subtraction is presented in Figure 4.41a,b. Based on the results, a calibration graph of current peaks versus concentration was obtained showing a linear increase in peak current as the concentration of choline increased from 3×10^{-7} to 2.2×10^{-6} M (Figure 4.41c) with a decrease in Figure 4.41d which could be attributed to limitation (instability of electrode with increasing choline concentrations) of electrode . LoD values for 3SD/m relationship were 0.06 and 0.45 μM for GCE/f-MWCNT/ZnONPL and GCE/f-MWCNT/ZnONPF and 0.23789 and 0.08027 μA/μM sensitivity at the respective electrodes. Table 4.6 and 4.12 represents summary of the designed electrodes with other sensors.

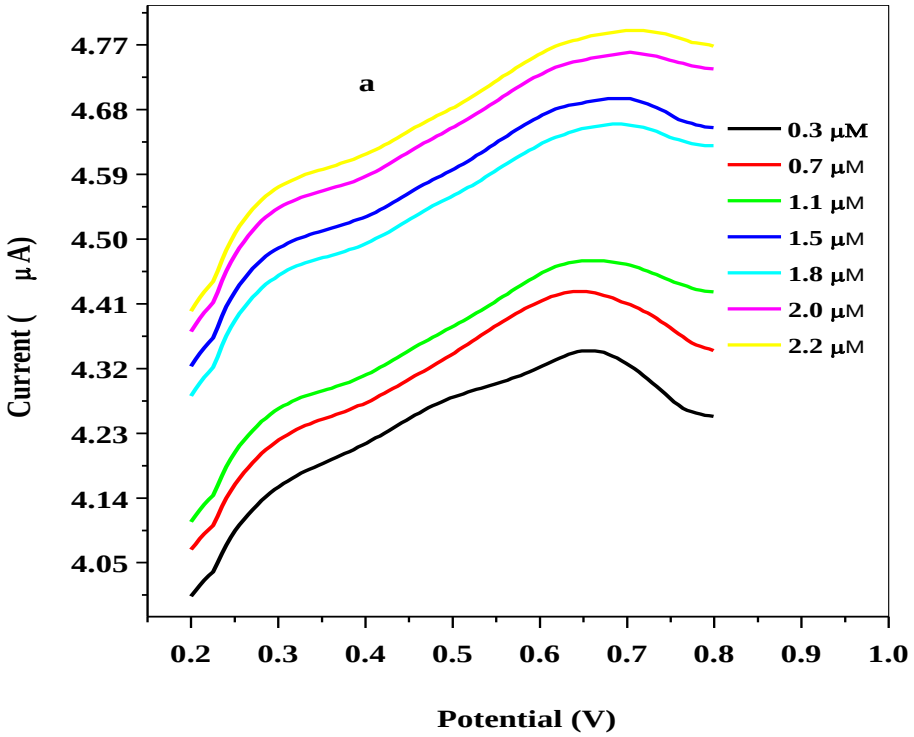

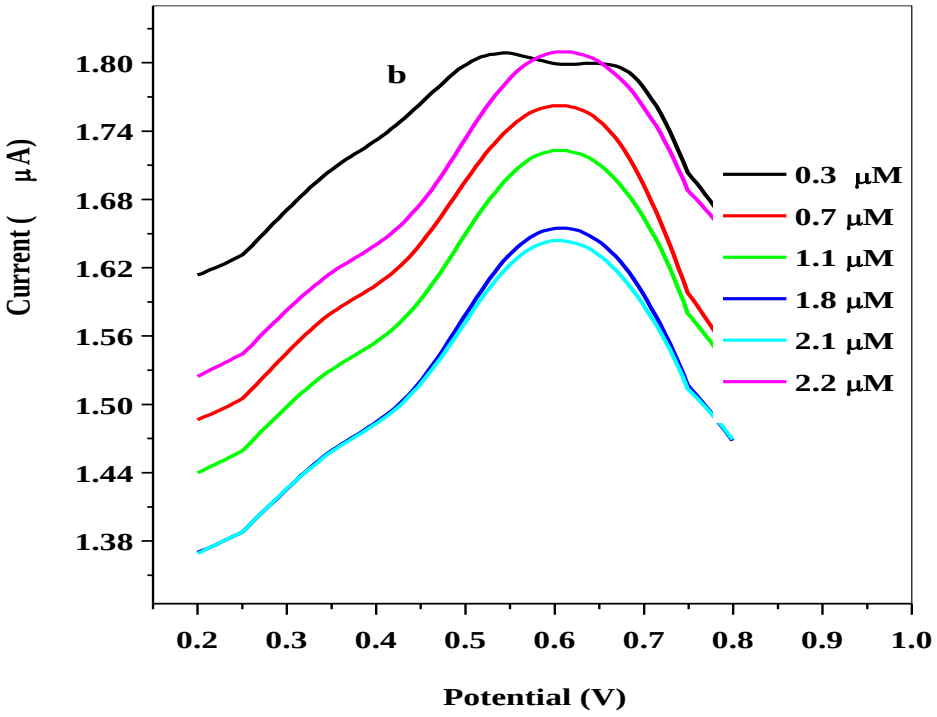
b
Current (µA)
1.80
1.74
1.68
1.62
1.56
1.50
1.44
1.38
0.2
0.3
0.4
0.5
0.6
0.7
0.8
0.9
1.0
Potential (V)
0.3 µM
0.7 µM
1.1 µM
1.8 µM
2.1 µM
2.2 µM

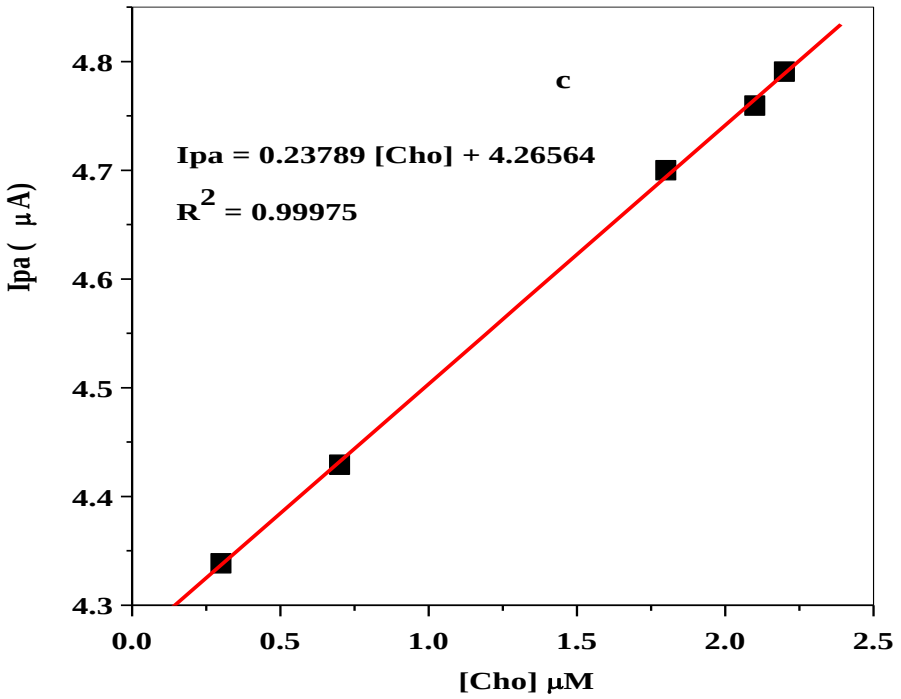
c
Ipa = 0.23789 [Cho] + 4.26564
R2 = 0.99975
Ipa (µA)
4.8
4.7
4.6
4.5
4.4
4.3
0.0
0.5
1.0
1.5
2.0
2.5
[Cho] µM

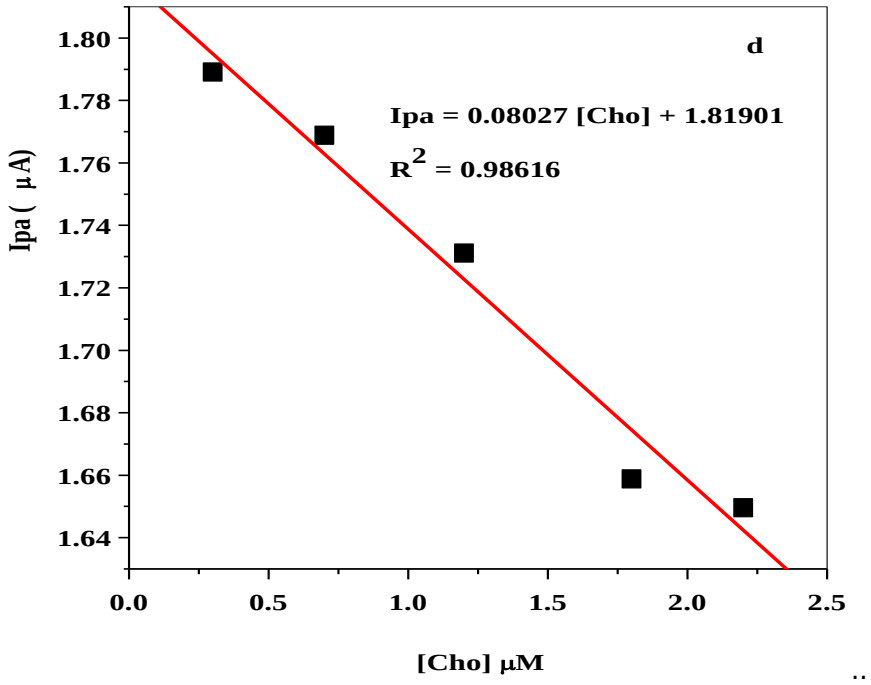

Figure 4.41: Background subtracted SWVs of (a) GCE/MWCNT/ZnONPL and (b) GCE/MWCNT/ZnONPF in different choline concentrations (0.3 - 2.2 µM) from down -up in LiCl solution, pH 7.3; linear plot of current peaks against choline concentration for (c) GCE/f-MWCNT/ZnONPL and (d) GCE/f-MWCNT/ZnONPF.

Down- up is a statement connoting the arrangement of the background subtracted SWVs obtained for GCE/MWCNT/ZnONPF. Suggesting higher to smaller concentration (from the down/last voltammogram)

4.2.2.9: Chronoamperometric detection of choline

Chronoamperometry technique was also employed for the investigation of sensitivity and LoD of designed electrodes in response to choline. Current time choline response curve on successive addition of choline in the range of 0.3 – 2.2 µm is presented in Figure 4.42a, b. The observed current decrease could possibly be due to fall in choline diffused layer at surfaces of the electrodes. Figure 4.42c, d shows the linear graph of peak current (Ipa) against choline concentration. LoD of 0.29 µM for GCE/f-MWCNT/ZnONPL and 0.32 µM for GCE/f-MWCNT/ZnONPF were compared with those in the literature as presented in Table 4.12.

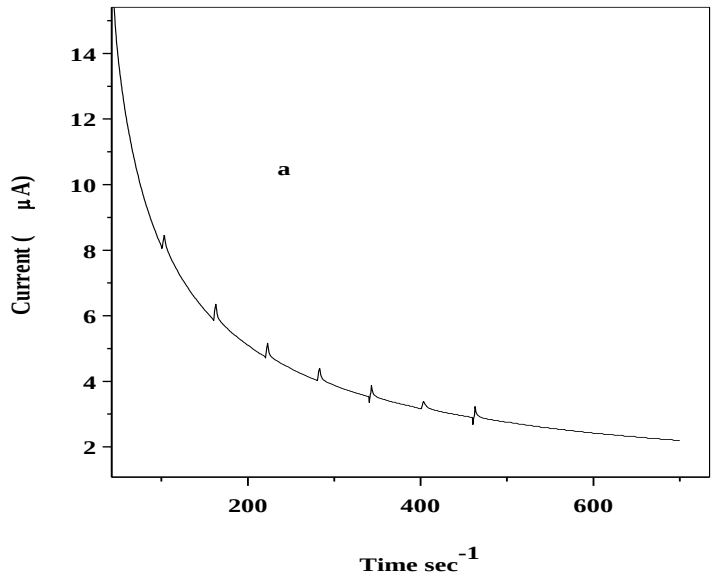
a
Current (µA)
Time sec-1
14
12
10
8
6
4
2
200
400
600

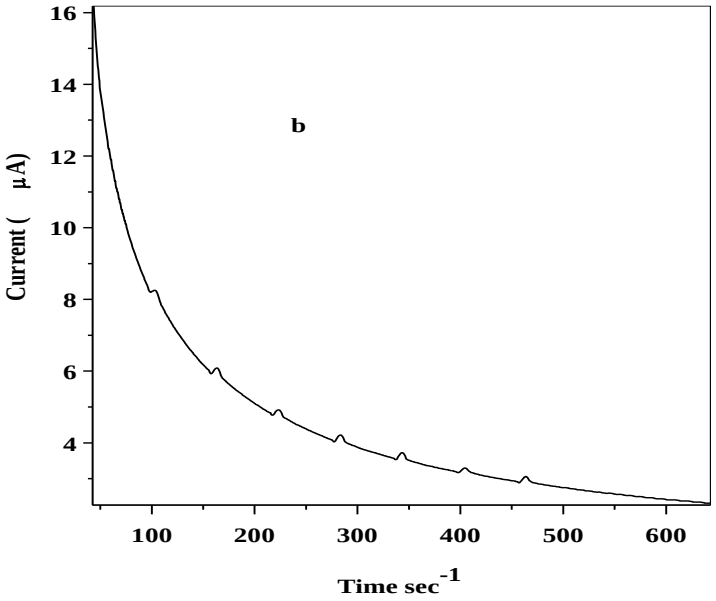
b
Current (µA)
Time sec-1
16
14
12
10
8
6
4
100
200
300
400
500
600

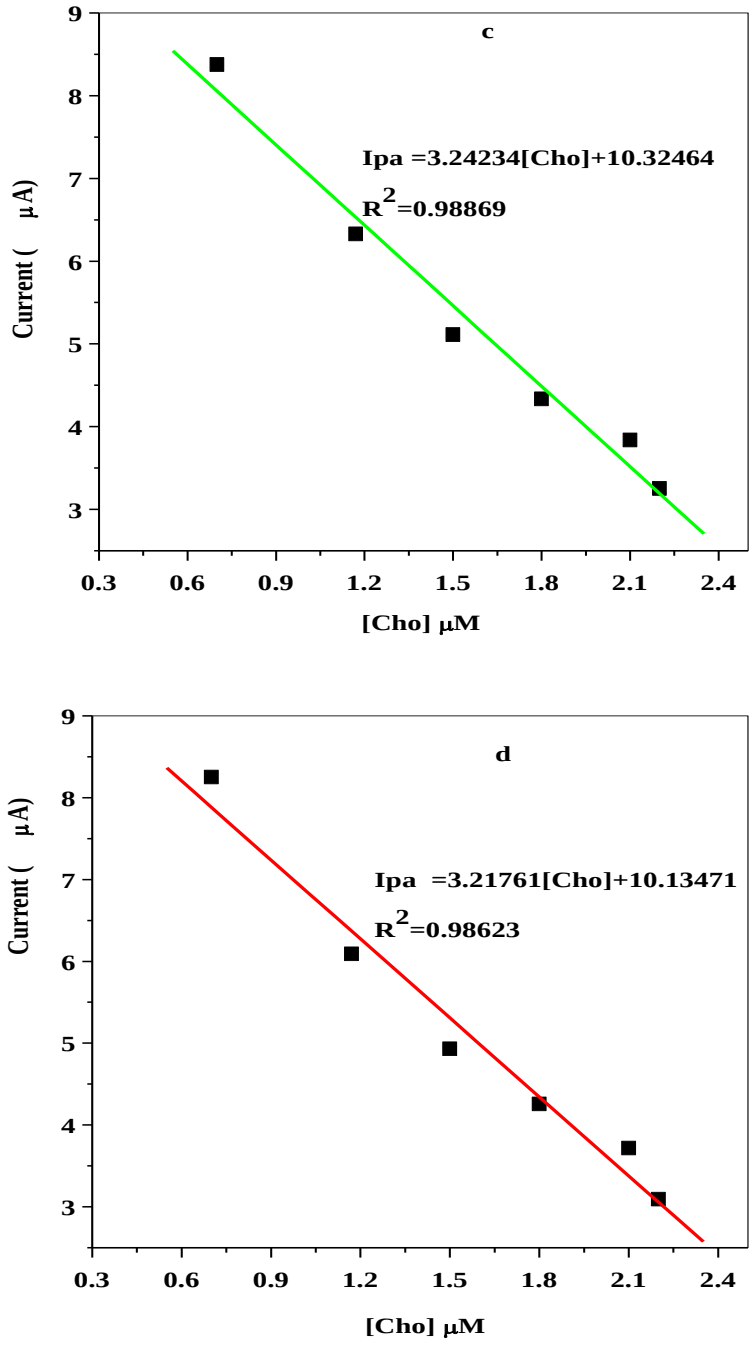

Figure 4.42: Current-time curve of (a) GCE/f-MWCNT/ZnONPL and (b) GCE/f-MWCNT/ZnONPF upon series of choline addition in 10mM LiCl solution, pH 7.3 at +0.58 V vs. Ag/AgCl; linear plot of current against choline concentrations for (c) GCE/f-MWCNT/ZnONPL and (d) GCE/f-MWCNT/ZnONPF.

Table 4.12: Comparison of the designed sensors with choline biosensors.

Electrodes	Methods	Linearity (µM)	LoD (µM)	
ChOx/Ni-PB/MWCNT-IL//GCE	Amperometry	0.45 - 100	0.45	(Keihan *et al.*, 2014)
ChOx/HRPsCPE	Amperometry	0.5 - 70	0.1	(Razola *et al.*, 2003)
GCE/f-MWCNT/ZnONPL	SWV	0.3 – 2.2	0.06	This work
	Chronoamperometry	0.3 - 2.2	0.29	
GCE/f-MWCNT/ZnONPF	SWV	0.3 – 2.2	0.45	This work
	Chronoamperometry	0.3 - 2.2	0.32	

Note: ChOx: choline oxidase; HRP: horseradish peroxidase; CPE: carbon paste electrode; IL– ionic liquid; PB: prussian blue.

4.2.2.10 Selectivity studies

Selectivity and sensitivity of the nanocomposite modified electrode for choline were investigated by comparing the electrochemical behaviour of choline (0.1 mM) in the presence of 100 mM of ascorbic acid (AA) and 0.1 dopamine (DA) prepared in 10 mM lithium chloride (LiCl) of pH 7.23 on GCE/MWCNT/ZnONPF and GCE/MWCNT/ZnONPL using chronoamperometry. Figure 4.43a,b shows the current-time curve response from chronoamperometry measurement presented in histogram for nanocomposite electrodes by successive injection of equal ml of choline AA and DA at +0.58 V potential versus Ag/AgCl in 50 mL LiCl solution and interval time of 0.5 sec. The interfering species did not affect choline oxidation signals produced at the nanocomposite modified electrode. This reveals the designed sensor to be highly selective for choline determination in the presence of AA present at higher concentration (1000 times).

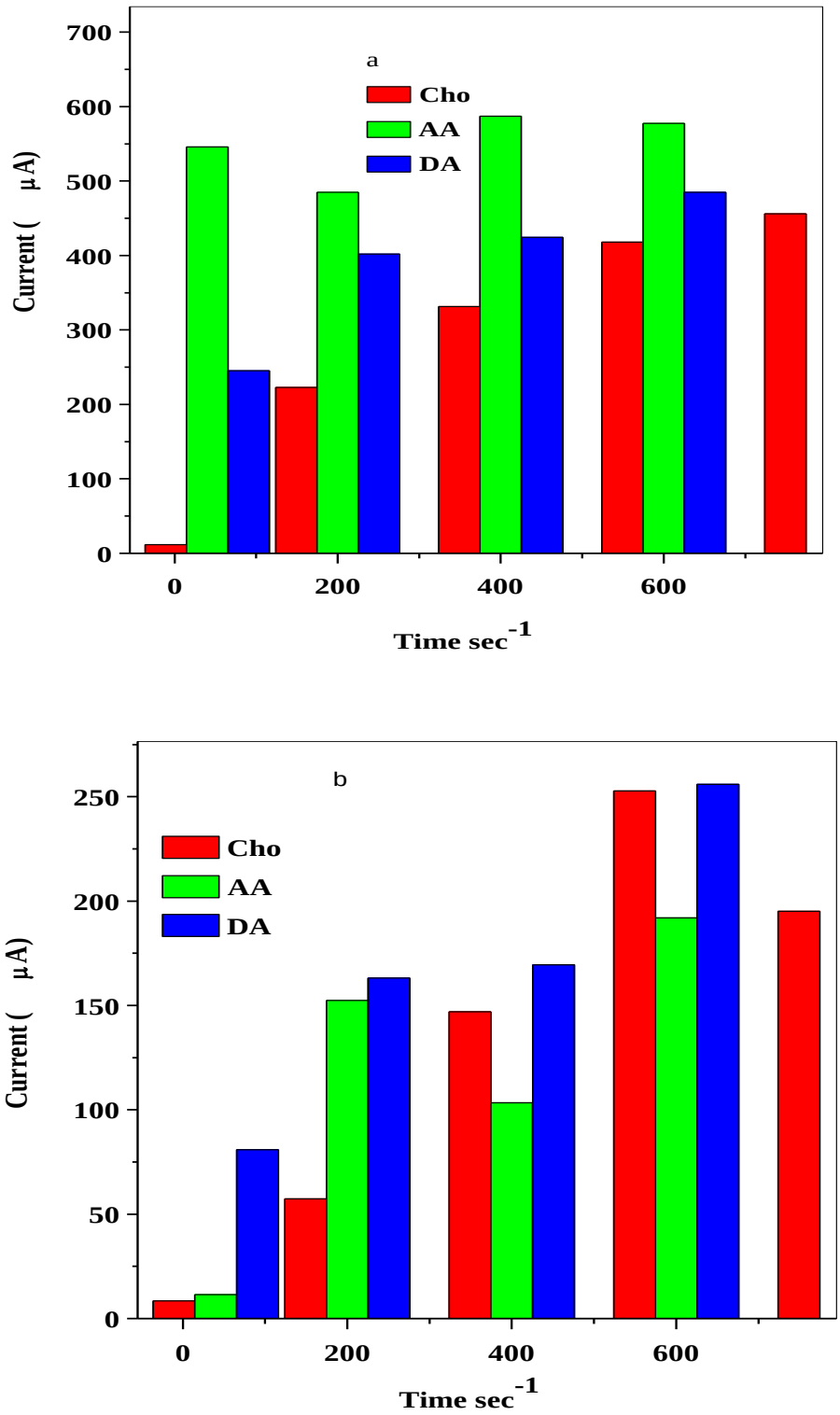

Figure 4.43: Current-time curves of (a) GCE/f-MWCNT/ZnONPL and (b) GCE/f-MWCNT/ZnONP in 10 mM LiCl, pH 7.3 at + 0.58 V vs. Ag/AgCl at successive injection of 0.1 mM Cho, 100 mM AA and 0.1 mM DA.

4.2.2.11 Reproducibility and stability studies

The reproducibility of the designed electrode was examined by measuring the current response of the electrodes (GCE/MWCNT/ZnONPL and GCE/MWCNT/ZnONPF) for seven successive 2 µM choline measurements using cyclic voltammetry (Figure 4.44a,b). Current drop was 26% and 17.2% obtained for respective electrode . In addition, storage stability was conducted by monitoring choline Ipa responses weekly. The sensor was stored dry in a cupboard. After two weeks storage, 6.4 and 9 % decrease of the initial sensitivity of GCE/f-MWCNT/ZnONPL and GCE/f-MWCNT/ZnONPF was observed accordingly while 99 % drop was observed which could be due to loss of the nanocomposites from the electrode.

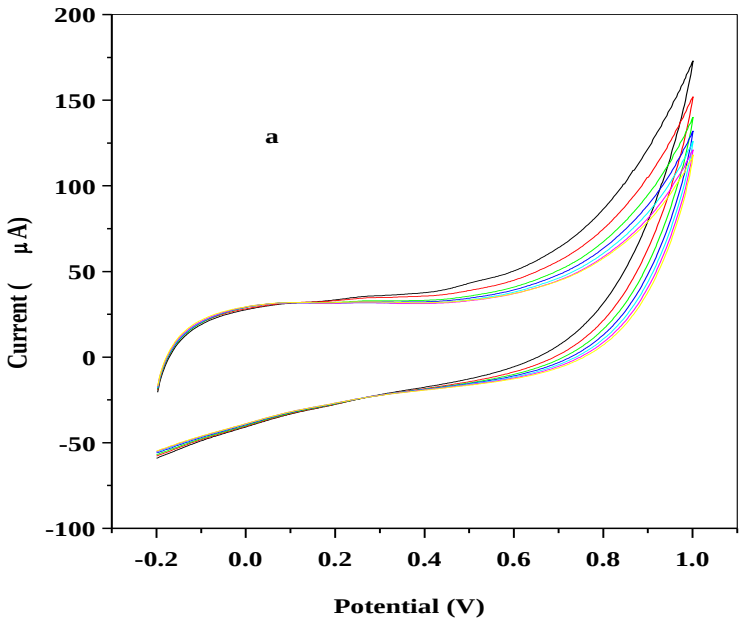

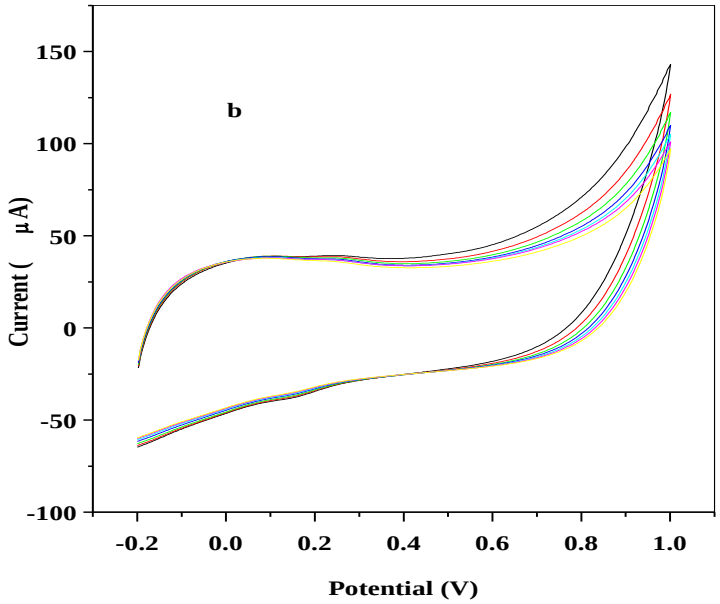

Figure 4.44: Repetitive cyclic voltammogram of (a) GCE/f-MWCNT/ZnONPL (b) GCE/f-MWCNT/ZnONPF in 10 mM LiCl of pH 7.3 containing 2 mM choline at 25 mVs^{-1} scan rate.

4.2.2.12 Real sample analysis

The analytical reliability and practical application of the proposed sensors in the detection of choline was evaluated by applying the nanocomposite modified electrodes in the sensing of choline in real pharmaceutical samples using SVW with 0.01 V amplitude and frequency of 25 Hz. The sensing behaviour of the developed sensor was examined using the same procedure mentioned in section 4.1.3.11. The obtained results are shown in Table 4.13.

Table 4.13: Recovery data for choline determination in pharmaceutical samples at modified electrodes (S/N = 3).

Samples	Working electrodes	Added (µM)	Found (µM)	RSD	% Recovery
CDP choline	GCE/f-MWCNT/ZnONPF	44.0	49.2	0.64	112
		58.0	60.7	0.24	105
		72.2	65.9	0.15	92
	GCE/f-MWCNT/ZnONPL	44.0	51.5	0.43	117
		58.0	62.3	0.10	107
		72.2	66.8	0.10	93
Choline bitartrate	GCE/f-MWCNT/ZnONPF	44.0	38.5	1.18	88
		58.0	58.5	1.29	100
		72.2	70.0	0.65	97
	GCE/f-MWCNT/ZnONPL	44.0	45.3	0.46	103
		58.0	60.9	0.28	105
		72.2	71.3	0.44	99

Validation of the results using t-test, and f-test at 95 % confidence level confirmed there were no significantly different results. Also Q-test on GCE/MWCNT/ZnONPF (choline bitartrate) suggests retainment of the outlier (recovery 88). It is evident that the developed sensors have great potential to sense choline from real samples with good recovery.

CONCLUSIONS AND RECOMMENDATIONS

5.1 Conclusions

This thesis described the green synthesis metal oxides MO (where MO = Fe_3O_4NPL, Fe_3O_4NPF, ZnONPL and ZnONPF) nanoparticles from *Callistemon viminalis* leaves and flowers extract supported on functionalized multi-walled carbon nanotubes (MWCNT) towards the electrocatalytic oxidation of acetylcholine precursor known as choline (Cho). It has been proven that glassy carbon electrode modified with functionalised MWCNT nanocomposites (GCE/f-MWCNT/Fe_3O_4NPL, GCE/f-MWCNT/Fe_3O_4NPF, GCE/f-MWCNT/ZnONPL and GCE/f-MWCNT/ZnONPF) exhibit enhanced electrochemical response towards electro-oxidation of the choline.

It is shown that the nanocomposite modified electrodes (GCE/f-MWCNT/Fe_3O_4NPL, GCE/f-MWCNT/Fe_3O_4NPF) gave better electron transport and choline response when compared with other electrodes investigated (GCE, GCE/Fe_3O_4NPL GCE/f-MWCNT). Electrocatalysis and electroanalysis of choline was diffusion controlled. The modified nanocomposites electrodes, GCE/f-MWCNT/Fe_3O_4NPF proved to be the best electrode in terms of detection limit and reproducibility while GCE/f-MWCNT/Fe_3O_4NPL exhibited greater choline oxidation current, selectivity and excellent storage stability. From the selectivity study, square wave voltammetric simultaneous detection of ascorbic acid (100 mM), dopamine (0.1 mM), and choline (0.1 mM) showed well resolved signals with anodic potential peak separation at 840, 690, 150 mV between Cho and AA, Cho and DA, and AA and DA at GCE/f-MWCNT/Fe_3O_4NPL electrode while 720, 330 and 390 mV was obtained at GCE/f-MWCNT/Fe_3O_4NPF respectively. Significant increase in current response of choline upon successive additions of 1 ml each of AA and DA was observed from the interference study using chronoamperometry connoting non-interference of AA and DA signal with that of choline. The designed sensors (GCE/f-MWCNT/Fe_3O_4NPL and GCE/f-MWCNT/Fe_3O_4NPF) were successfully applied for direct choline detection in real samples (choline dietary supplements) with good percentage recoveries (in the range of 80 -116 and 80 – 106 for the respective electrodes). The study shows that, the designed electrochemical sensors could be applied for detecting choline in pharmaceutical and physiological sample at low cost, fast response, and simple instrumentation.

Electrochemical behaviour of GCE/f-MWCNT/ZnONPF electrode in the probe solution showed an absence of oxidation peak suggesting the electrode to be capacitive due to high storage of charges which impedes fast electron transport. The capacitive nature of the electrode was confirmed from the electrochemical impedance spectroscopic (EIS) experiment with a high double layer capacitance value (685 μF) as compared to GCE/f-MWCNT/ZnONPL electrode (125 μF). Electrocatalytic activity of the electrodes towards choline revealed a reversible, and oxidation irreversible electrochemical process for GCE/f-MWCNT/ZnONPL and GCE/f-MWCNT/ZnONPF respectively using cyclic voltammetry. However, both nanocomposite electrodes displayed excellent response towards choline when compared with bare, nanoparticles, and functionalized multi-walled carbon nanotube modified (GCE, GCE/ZnONPL GCE/ZnONPF, and GCE/f-MWCNT) electrodes. GCE/f-MWCNT/ZnONPF electrode proved to be the best electrode in terms of selectivity to 0.1 mM choline with insignificant decrease in choline current response after successive droppings of 1 ml of interfering species (100 mM ascorbic acid and 0.1 mM dopamine) solutions using chronoamperometry. GCE/f-MWCNT/ZnONPL had the best detection limit. Electrocatalysis of choline on the GCE/f-MWCNT/ZnONPL and GCE/f-MWCNT/ZnONPF electrodes was diffusion controll. Practical applicability of the fabricated electrodes for real sample sensing of choline was successful with good recoveries and relative standard deviation (RSD). The study suggest that the nanocomposite modified electrodes can be used for in-vitro and in-vivo study of choline detection.

5.2 Recommendations

Base on the successful detection of choline at green mediated nanocomposite modified electrodes, the following recommendations are made for future choline detection.

1. More research on the use of a carbon based compound -ferromagnetic oxide anocomposite as electrode catalyst for choline detection
2. Use of bi-metal oxide (Fe_2O_3/CuO) in fabrication of electrode
3. Use of a chemical synthesized nanocomposite in the designing of sensors
4. Use of polymer-metal oxide composites
5. Use of metal/multiwalled carbon nanotube composite

REFERENCES

Adekunle, A.S., Ayenimo, J.G., Fang, X.-Y., Doherty, W.O., Arotiba, O.A. & Mamba, B.B. 2011. Electrochemical response and impedimetric behaviour of dopamine and epinephrine at platinum electrode modified with carbon nanotubes-gold nanocomposite. *Int. J. Electrochem. Sci*, 6:2826-2844.

Ahammad, A., Lee, J.- J. & Rahman, M. 2009. Electrochemical sensors based on carbon nanotubes. *Sensors*, 9(4):2289-2319.

Ahmed, D. S., Haider, A. J. & Mohammad, M. 2013. Comparesion of functionalization of multi-walled carbon nanotubes treated by oil olive and nitric acid and their characterization. *Energy Procedia*, 36:1111-1118.

Ahn, K.- J., Lee, Y., Choi, H., Kim, M. - S., Im, K., Noh, S. & Yoon, H. 2015. Surfactant-templated synthesis of polypyrrole nanocages as redox mediators for efficient energy storage. *Scientific reports*, 5:14097.

Allen, J. B. & Larry, R. F. 2001. Electrochemical methods fundamentals and applications: John Wiley & Sons.

Al-Ruqeishi, M. S., Mohiuddin, T. & Al-Saadi, L. K. 2019. Green synthesis of iron oxide nanorods from deciduous Omani mango tree leaves for heavy oil viscosity treatment. *Arabian Journal of Chemistry*, 12(8):4084-4090.

Al-Shabib, N.A., Husain, F.M., Ahmed, F., Khan, R.A., Ahmad, I., Alsharaeh, E., Khan, M. S., Hussain, A., Rehman, M. T., Yusuf, M., Hassan, I., Khan, J. M., Ashraf, G. M., Alsalme, A., Al-Ajmi, M.F., Tarasov, V.V. & Aliev, G. 2016. Biogenic synthesis of Zinc oxide nanostructures from Nigella sativa seed: Prospective role as food packaging material inhibiting broad-spectrum quorum sensing and biofilm. *Scientific reports* 6

Alagarasi, A. 2011. Chapter-Introduction To Nanomaterials.

Ampurdanés, J., Crespo, G.A., Maroto, A., Sarmentero, M. A., Ballester, P. & Rius, F. X. 2009. Determination of choline and derivatives with a solid-contact ion-selective electrode based on octaamide cavitand and carbon nanotubes. *Biosensors and Bioelectronics*, 25(2):344-349.

Andersen, Ø. 2006. ordheim M. The Anthocyanins: Flavonoids: Chemistry, Biochemistry and Applications. Boca Raton: CRC Press.

Aoki, K. J. & Chen, J. 2018. Tips of Voltammetry. Voltammetry. IntechOpen.

Atieh, M. A., Bakather, O.Y., Al-Tawbini, B., Bukhari, A.A., Abuilaiwi, F.A. & Fettouhi, M.B. 2010. Effect of carboxylic functional group functionalized on carbon nanotubes surface on the removal of lead from water. *Bioinorganic chemistry and applications*, 2010.

Atta, N.F., Galal, A. & Ahmed, R.A. 2011. Simultaneous determination of catecholamines and serotonin on poly (3, 4-ethylene dioxythiophene) modified Pt electrode in presence of sodium dodecyl sulfate. *Journal of The Electrochemical Society*, 158(4):F52.

Ayuk, E., Ugwu, M. & Aronimo, S.B. 2017. A review on synthetic methods of nanostructured materials. *Chemistry Research Journal*, 2(5):97-123.

Azizi, S., Mahdavi Shahri, M. & Mohamad, R. 2017. Green synthesis of zinc oxide nanoparticles for enhanced adsorption of lead ions from aqueous solutions: equilibrium, kinetic and thermodynamic studies. *Molecules*, 22(6):831.

Babaei, A., Taheri, A.R. & Aminikhah, M. 2013. Nanomolar simultaneous determination of levodopa and serotonin at a novel carbon ionic liquid electrode modified with Co (OH) 2 nanoparticles and multi-walled carbon nanotubes. *Electrochimica Acta*, 90:317-325.

Bai, Y - H., Du, Y., Xu, J.-J. & Chen, H.-Y. 2007. Choline biosensors based on a bi-electrocatalytic property of MnO2 nanoparticles modified electrodes to H2O2. *Electrochemistry Communications*, 9(10):2611-2616.

Bala, N., Saha, S., Chakraborty, M., Maiti, M., Das, S., Basu, R. & Nandy, P. 2015. Green synthesis of zinc oxide nanoparticles using Hibiscus subdariffa leaf extract: effect of temperature on synthesis, anti-bacterial activity and anti-diabetic activity. *RSC Advances*, 5(7):4993-5003.

Balamurughan, M. G., Mohanraj, S., Kodhaiyolii, S., & Pugalenthi, V. 2014. Ocimum sanctum leaf extract mediated green synthesis of iron oxide nanoparticles: spectroscopic and microscopic studies. *J. Chem. Pharm. Sci*, 4:201-204.

Banjari, I., Vukoje, I. & Mandić, M. L. 2014. Brain food: How nutrition alters our mood and behaviour. *Hrana u zdravlju i bolesti: znanstveno-stručni časopis za nutricionizam i dijetetiku*, 3(1):13-21.

Bardini, L. 2015. EIS 101, an introduction to electrochemical spectroscopy. What was a website is now available as a self-contained PDF.

Basu, T., Solanki, P.R. & Malhotra, B. 2008. Recent advances in carbon nanotubes based biosensors. *Sensors*, 8(s 2).

Batra, B., Kumari, S. & Pundir, C.S. 2014. Construction of glutamate biosensor based on covalent immobilization of glutmate oxidase on polypyrrole nanoparticles/polyaniline modified gold electrode. *Enzyme and microbial technology*, 57:69-77.

Berger, M., Gray, J.A. & Roth, B. L. 2009. The expanded biology of serotonin. *Annual review of medicine*, 60:355-366.

Bhattacharjee, S. 2016. DLS and zeta potential–what they are and what they are not? *Journal of Controlled Release*, 235:337-351.

Brownson, D. A. & Banks, C. E. 2014. Interpreting electrochemistry. The handbook of graphene electrochemistry. Springer. p. 23-77).

Buchanan, D.N., Fucek, F.R. & Domino, E.F. 1980. Paired-ion high-performance liquid chromatographic assay for plasma choline.

Bunaciu, A. A., UdriŞTioiu, E. G. & Aboul-Enein, H. Y. 2015. X-ray diffraction: instrumentation and applications. *Critical reviews in analytical chemistry*, 45(4):289-299.

Buzea, C., Pacheco, I. I. & Robbie, K. 2007. Nanomaterials and nanoparticles: sources and toxicity. *Biointerphases*, 2(4):MR17-MR71.

Carrera, V., Sabater, E., Vilanova, E. & Sogorb, M.A. 2007. A simple and rapid HPLC–MS method for the simultaneous determination of epinephrine, norepinephrine, dopamine and 5-hydroxytryptamine: Application to the secretion of bovine chromaffin cell cultures. *Journal of Chromatography B*, 847(2):88-94.

Carter, N. & Trenerry, V. C. 1996. The determination of choline in vitamin preparations, infant formula and selected foods by capillary zone electrophoresis with indirect ultraviolet detection. *ELECTROPHORESIS*, 17(10):1622-1626.

Chakraborty, D.S. 2016. Intrumentation of FTIR and its herbal applications. . *World J pharm pharmaceuticals sci*, 5(3):498-505.

Chang-Zhi, Z., Jia, Y., Gai-Shuang, Z. & Kui, J. 2011. Choline Biosensor Based on Poly (thionine)/H2O2 Photoelectrochemical Sensing Interface. *Chinese Journal of Analytical Chemistry*, 39(6):886-889.

Chao, M., Li, Y., Wu, G., Zhou, Z. & Yan, L. 2019. Functionalized Multiwalled Carbon Nanotube-Reinforced Polyimide Composite Films with Enhanced Mechanical and Thermal Properties. *International Journal of Polymer Science*, 2019.

Chau, R.M. & Patel, B.A. 2009. Determination of serotonin, melatonin and metabolites in gastrointestinal tissue using high-performance liquid chromatography with electrochemical detection. *Biomedical Chromatography*, 23(2):175-181.

Chauveau, J., Fert, V., Morel, A. & Delaage, M. 1991. Rapid and specific enzyme immunoassay of serotonin. *Clinical chemistry*, 37(7):1178-1184.

Chen, J.- L., Yan, X.- P., Meng, K. & Wang, S.- F. 2011. Graphene oxide based photoinduced charge transfer label-free near-infrared fluorescent biosensor for dopamine. *Analytical chemistry*, 83(22):8787-8793.

Chen, H.- C., Tsai, R.- Y., Chen, Y.- H., Lee, R.- S. & Hua, M. - Y. 2013. A colloidal suspension of nanostructured poly (N-butyl benzimidazole)-graphene sheets with high oxidase yield for analytical glucose and choline detections. *Analytica Chimica Acta*, 792:101-109.

Chimezie, A. B., Hajian, R., Yusof, N. A., Woi, P. M. & Shams, N. 2017. Fabrication of reduced graphene oxide-magnetic nanocomposite (rGO-Fe3O4) as an electrochemical sensor for trace determination of As (III) in water resources. *Journal of Electroanalytical Chemistry*, 796:33-42.

Choi, M. R., Kouyoumdzian, N. M., Mikusic, N. L. R., Kravetz, M. C., Rosón, M. I., Fermepin, M. R. & Fernández, B. E. 2015. Renal dopaminergic system: Pathophysiological implications and clinical perspectives. *World journal of nephrology*, 4(2):196.

Choi, W., Shin, H.- C., Kim, J. M., Choi, J.- Y. & Yoon, W.-S. 2020. Modeling and Applications of Electrochemical Impedance Spectroscopy (EIS) for Lithium-ion Batteries. *Journal of Electrochemical Science and Technology*, 11(1):1-13.

Chunduri, L. A., Kurdekar, A., Pradeep, B. E., Haleyurgirisetty, M.,Venkataramaniah, K. & Hewlett, I. 2017. Streptavidin conjugated ZnO nanoparticles for early detection of HIV infection. *Advance. Material. Letter.*, 8:472-480.

Dahman, Y. 2017. Nanotechnology and Functional Materials for Engineers: Elsevier.

de Oliveira, A. H. P., Nascimento, M. L. F. & de Oliveira, H. P. 2016. Carbon nanotube@ MnO2@ polypyrrole composites: chemical synthesis, characterization and application in supercapacitors. *Materials Research*, 19(5):1080-1087.

Das, M. C., Biswas, R., Akter, H., Haque, M., Bakshi, P. & Shaikh, A. 2016. Cyclic Voltammetric Study of the Interaction of Biologically Important Metal Ion with Proton Pump Inhibitors. *Dhaka University Journal of Science*, 64(1):25-30.

Debanath, M. & Karmakar, S. 2013. Study of blueshift of optical band gap in zinc oxide (ZnO) nanoparticles prepared by low-temperature wet chemical method. *Materials Letters*, 111:116-119.

Deng, K., Zhou, J. & Li, X. 2013. Noncovalent nanohybrid of ferrocene with chemically reduced graphene oxide and its application to dual biosensor for hydrogen peroxide and choline. *Electrochimica Acta*, 95:18-23.

Deshmukh, S., Kandasamy, G., Upadhyay, R.K., Bhattacharya, G., Banerjee, D., Maity, D., Deshusses, M.A. & Roy, S.S. 2017. Terephthalic acid capped iron oxide nanoparticles for sensitive electrochemical detection of heavy metal ions in water. *Journal of Electroanalytical Chemistry*, 788:91-98.

Dhand, C., Das, M., Datta, M. & Malhotra, B.D. 2011. Recent advances in polyaniline based biosensors. *Biosensors and Bioelectronics*, 26(6):2811-2821.

Dhand, C., Dwivedi, N., Loh, X.J., Ying, A.N.J., Verma, N. K., Beuerman, R. W., Lakshminarayanan, R. & Ramakrishna, S. 2015. Methods and strategies for the synthesis of diverse nanoparticles and their applications: a comprehensive overview. *Rsc Advances*, 5(127):105003-105037.

Duncan, M.W., Smythe, G.A., Nicholson, M.V. & Clezy, P.S. 1984. Comparison of high-performance liquid chromatography with electrochemical detection and gas chromatography—mass fragmentography for the assay of salsolinol, dopamine and dopamine metabolites in food and beverage samples. *Journal of Chromatography B: Biomedical Sciences and Applications*, 336(1):199-209.

Ebnesajjad, S. 2014. Chapter 4 - Surface and Material Characterization Techniques. *(In* Ebnesajjad, S., *ed.* Surface Treatment of Materials for Adhesive Bonding (Second Edition). Oxford: William Andrew Publishing. p. 39-75).

EFSA Panel on Dietetic Products, N. & Allergies. 2016. Dietary reference values for choline. *EFSA Journal*, 14(8):e04484.

El Ghandoor, H., Zidan, H., Khalil, M. M. & Ismail, M. 2012. Synthesis and some physical properties of magnetite (Fe3O4) nanoparticles. *Int. J. Electrochem. Sci*, 7(6):5734-5745.

Engbaek, F. & Voldby, B. 1982. Radioimmunoassay of serotonin (5-hydroxytryptamine) in cerebrospinal fluid, plasma, and serum. *Clinical chemistry*, 28(4):624-628.

Espinoza, E. M., Clark, J. A., Soliman, J., Derr, J. B., Morales, M. & Vullev, V.I. 2019. Practical aspects of cyclic voltammetry: How to estimate reduction potentials when irreversibility prevails. *Journal of The Electrochemical Society*, 166(5):H3175.

Fayemi O. E, A. A., Ebenso E. E 2015. Metal oxide nanoparticles/multi-walled carbon nanotube nanocomposite modified electrode for the detection of dopamine: comparative electrochemical study. *J. Biosens. Bioelectron* 6(4):190.

Fayemi, O. E., Adekunle, A. S. & Ebenso, E. E. 2017. Electrochemical determination of serotonin in urine samples based on metal oxide nanoparticles/MWCNT on modified glassy carbon electrode. *Sensing and Bio-Sensing Research*, 13:17-27.

Fayemi, O. E., Adekunle, A. S., Swamy, B. K. & Ebenso, E. E. 2018. Electrochemical sensor for the detection of dopamine in real samples using polyaniline/NiO, ZnO, and Fe3O4 nanocomposites on glassy carbon electrode. *Journal of Electroanalytical Chemistry*, 818:236-249.

Fenelon, A. M. & Breslin, C. B. 2002. The electrochemical synthesis of polypyrrole at a copper electrode: corrosion protection properties. *Electrochimica Acta*, 47(28):4467-4476.

Filik, H., Avan, A.A. & Aydar, S. 2014. Square-Wave Adsorptive Stripping Voltammetric Determination of Serotonin at Glassy Carbon Electrode Modified with Safranine O. *Int. J. Electrochem. Sci*, 9:2922-2933.

Fletcher, J. P., Best, C. H. & Solandt, O. M. 1935. The distribution of choline. *The Biochemical journal*, 29(10):2278-2284.

Fossati, T., Colombo, M., Castiglioni, C. & Abbiati, G. 1994. Determination of plasma choline by high-performance liquid chromatography with a postcolumn enzyme reactor and electrochemical detection. *Journal of Chromatography B: Biomedical Sciences and Applications*, 656(1):59-64.

Ferrer, N. 2012. Applications of Fourier transform infrared spectroscopy. *Handbook of Instrumental Techniques*.

Gao, F., Cai, X., Wang, X., Gao, C., Liu, S., Gao, F. & Wang, Q. 2013. Highly sensitive and selective detection of dopamine in the presence of ascorbic acid at graphene oxide modified electrode. *Sensors and Actuators B: Chemical*, 186:380-387.

Gao, F., Zhang, L. & Huang, S. 2010. Fabrication horizontal aligned MoO2/single-walled carbon nanotube nanowires for electrochemical supercapacitor. *Materials Letters*, 64(4):537-540.

Gelamo, R.V., Abbaspourrad, A., Verissimoa, C., Vaz, A.R., Rouxinol, F.P., Alves, O.L. and Moshkalev, S.A., . 2009. Multiwall carbon nanotubes decorated with metal oxide nanoparticles for gas sensing applications. *ECS Transactions*, 23(1):237-242.

Ghanbari, K. & Hajheidari, N. 2015. ZnO–CuxO/polypyrrole nanocomposite modified electrode for simultaneous determination of ascorbic acid, dopamine, and uric acid. *Analytical biochemistry*, 473:53-62.

Gibson, L.T. 2005. ARCHAEOMETRY AND ANTIQUE ANALYSIS | Metallic and Ceramic Objects. *(In* Worsfold, P., Townshend, A. & Poole, C., *eds*. Encyclopedia of Analytical Science (Second Edition). Oxford: Elsevier. p. 117-123).

Girault, H.H. 2010. Electrochemistry at liquid-liquid interfaces. Vol. 23: CRC Press Boca Raton, FL.

Glick, D. 1944. Concerning the reineckate method for the determination of choline. *Journal of Biological Chemistry*, 156:643-651.

Gossell-Williams, M., Fletcher, H., McFarlane-Anderson, N. & Jacob, A. 2005. Dietary intake of choline and plasma choline concentrations in pregnant women in Jamaica. *West indian medical journal*, 54(6):355-359.

Gowda, J.I. & Nandibewoor, S.T. 2014. Electrochemical behavior of paclitaxel and its determination at glassy carbon electrode. *Asian Journal of Pharmaceutical Sciences*, 9(1):42-49.

Guerfi, A., Trottier, J., Boyano, I., De Meatza, I., Blazquez, J., Brewer, S., Ryder, K., Vijh, A. & Zaghib, K. 2014. High cycling stability of zinc-anode/conducting polymer rechargeable battery with non-aqueous electrolyte. *Journal of Power Sources*, 248:1099-1104.

Guo, Z. & Dong, S. 2005. Electrogenerated Chemiluminescence Determination of Dopamine and Epinephrine in the Presence of Ascorbic Acid at Carbon Nanotube/Nafion-Ru (bpy) _3^2+

Composite Film Modified Glassy Carbon Electrode. *Electroanalysis: An International Journal Devoted to Fundamental and Practical Aspects of Electroanalysis*, 17(7):607-612.

Gupta, V.K. & Saleh, T.A. 2011. Synthesis of carbon nanotube-metal oxides composites; adsorption and photo-degradation. *Carbon NanotubesY From Research to Applications*.

Guy, O.J. & Walker, K.- A. D. 2016. Graphene functionalization for biosensor applications. Silicon Carbide Biotechnology. Elsevier. p. 85-141).

Han, H.S., Lee, H.K., You, J.-M., Jeong, H. & Jeon, S. 2014. Electrochemical biosensor for simultaneous determination of dopamine and serotonin based on electrochemically reduced GO-porphyrin. *Sensors and Actuators B: Chemical*, 190:886-895.

Han, H.S., You, J.-M., Jeong, H. & Jeon, S. 2013. Synthesis of graphene oxide grafted poly (lactic acid) with palladium nanoparticles and its application to serotonin sensing. *Applied surface science*, 284:438-445.

Haque, F., Rahman, M., Ahmed, E., Bakshi, P. & Shaikh, A. 2013. A cyclic voltammetric study of the redox reaction of Cu (II) in presence of ascorbic acid in different pH media. *Dhaka University Journal of Science*, 61(2):161-166.

Hasegawa, Y., Kunihara, M. & Maruyama, Y. 1982. Determination of picomole amounts of choline and acetylcholine in blood by gas chromatography-mass spectrometry equipped with a newly improved pyrolyzer. *Journal of Chromatography A*, 239:335-342.

He, B., Tang, Q., Wang, M., Ma, C. & Yuan, S. 2014a. Complexation of polyaniline and graphene for efficient counter electrodes in dye-sensitized solar cells: Enhanced charge transfer ability. *Journal of Power Sources*, 256:8-13.

He, S.-B., Wu, G.-W., Deng, H.-H., Liu, A.-L., Lin, X.-H., Xia, X.-H. & Chen, W. 2014b. Choline and acetylcholine detection based on peroxidase-like activity and protein antifouling property of platinum nanoparticles in bovine serum albumin scaffold. *Biosensors and Bioelectronics*, 62:331-336.

Hefni, M., McEntyre, C., Lever, M. & Slow, S. 2015. A Simple HPLC Method with Fluorescence Detection for Choline Quantification in Foods. *Food Analytical Methods*, 8(9):2401-2408.

Herlenius, E. & Lagercrantz, H. 2010. Neurotransmitters and neuromodulators. *The Newborn Brain: Neuroscience and Clinical Applications. Cambridge University Press, Cambridge*:99-119.

Holm, P. I., Ueland, P. M., Kvalheim, G. & Lien, E.A. 2003. Determination of choline, betaine, and dimethylglycine in plasma by a high-throughput method based on normal-phase chromatography–tandem mass spectrometry. *Clinical Chemistry*, 49(2):286.

Holmes, H.C., I. Snodgrass, G.J.A. & Iles, R. A. 2000. Changes in the choline content of human breast milk in the first 3 weeks after birth. *European Journal of Pediatrics*, 159(3):198-204.

Honeychurch, K. 2012. Printed thick-film biosensors. Printed Films. Elsevier. p. 366-409).

Hossain, M.A., Weli, A.M. & Ahmed, S.H. I. 2019. Comparison of total phenols, flavonoids and antioxidant activity of various crude extracts of Hyoscyamus gallagheri traditionally used for the treatment of epilepsy. *Clinical Phytoscience*, 5(1):20.

Hu, Y. & Guo, C. 2011. Carbon nanotubes and carbon nanotubes/metal oxide heterostructures: synthesis, characterization and electrochemical property. *Carbon nanotubes—growth and applications. InTech, Croatia*:3-34.

Huang, G., Lu, C.- H. & Yang, H.-H. 2019. Magnetic nanomaterials for magnetic bioanalysis. novel nanomaterials for biomedical, environmental and energy applications. Elsevier. p. 89-109).

Huang, M., Li, H., He, H., Zhang, X. & Wang, S. 2016. An electrochemical impedance sensor for simple and specific recognition of G–G mismatches in DNA. *Analytical Methods*, 8(40):7413-7419.

Huang, X. & Mazza, G. 2011. Simultaneous analysis of serotonin, melatonin, piceid and resveratrol in fruits using liquid chromatography tandem mass spectrometry. *Journal of Chromatography A*, 1218(25):3890-3899.

I. Takai, Z.M., M. K. Asman, S. A. K. Sekak,. 2019. Preparation and characterization of magnetite (Fe3O4) nanoparticles by sol-gel method. *Journal of Human Development and Communication.*, 12:37-46.

Ikarashi, Y. & Maruyama, Y. 1993. Liquid chromatography with electrochemical detection for quantitation of bound choline liberated by phospholipase D hydrolysis from phospholipids containing choline in rat plasma. *Journal of Chromatography B: Biomedical Sciences and Applications*, 616(2):323-326.

Immanuel, S., Aparna, T. & Sivasubramanian, R. 2019. Graphene–Metal Oxide Nanocomposite Modified Electrochemical Sensors. Graphene-Based Electrochemical Sensors for Biomolecules. Elsevier. p. 113-138).

Imming, P., Sinning, C. & Meyer, A. 2006. Drugs, their targets and the nature and number of drug targets. *Nature reviews Drug discovery*, 5(10):821-834.

Inam, M.A., Khan, R., Park, D.R., Lee, Y.-W. & Yeom, I.T. 2018. Removal of Sb (III) and Sb (V) by ferric chloride coagulation: Implications of Fe solubility. *Water*, 10(4):418.

Ishaq, S., Moussa, M., Kanwal, F., Ehsan, M., Saleem, M., Van, T.N. & Losic, D. 2019. Facile synthesis of ternary graphene nanocomposites with doped metal oxide and conductive polymers as electrode materials for high performance supercapacitors. *Scientific reports*, 9(1):1-11.

Jafarirad, S., Mehrabi, M. & pur, E.R. Classic synthesis of ZnO and CuO NPs using Rosa sahandina fruit broth. (*In* organised by.

Jamdagni, P., Khatri, P. & Rana, J. 2018. Green synthesis of zinc oxide nanoparticles using flower extract of Nyctanthes arbor-tristis and their antifungal activity. *Journal of King Saud University-Science*, 30(2):168-175.

Jiang, G., Gu, X., Jiang, G., Chen, T., Zhan, W. & Tian, S. 2015. Application of a mercapto-terminated binuclear Cu (II) complex modified Au electrode to improve the sensitivity and selectivity for dopamine detection. *Sensors and Actuators B: Chemical*, 209:122-130.

Jin, J., Muroga, M., Takahashi, F. & Nakamura, T. 2010. Enzymatic flow injection method for rapid determination of choline in urine with electrochemiluminescence detection. *Bioelectrochemistry*, 79(1):147-151.

Kalpana, V., Patra, R.R. & Rajeswari, V.D. 2017. Green synthesis of zinc oxide nanoparticles using fresh stem of Cissus quadrangularis extract and its various in vitro studies. *Asian J. Chem*, 29(6):1323.

Kanagasubbulakshmi, S., & Kadirvelu, K. 2017. Green synthesis of iron oxide nanoparticles using lagenaria siceraria and evaluation of its antimicrobial activity. *Defence Life Science Journal*, 2(4):422-427.

Karabiberoğlu, Ş.U., Koçak, Ç.C. & Dursun, Z. 2016. Carbon Nanotube-Conducting Polymer Composites as Electrode Material in Electroanalytical Applications. *Carbon Nanotubes: Current Progress of their Polymer Composites*:393.

Kanwal, F., Siddiqi, S.A., Batool, A., Imran, M., Mushtaq, W. & Jamil, T. 2011. Synthesis of polypyrrole–ferric oxide (Ppy–Fe2o3) composites and study of their structural and conducting properties. *Synthetic Metals*, 161(3-4):335-339.

Kavitha, S., Dhamodaran, M., Prasad, R. & Ganesan, M. 2017. Synthesis and characterisation of zinc oxide nanoparticles using terpenoid fractions of Andrographis paniculata leaves. *International Nano Letters*, 7(2):141-147.

Kecili, R. & Hussain, C.M. 2018. Mechanism of Adsorption on Nanomaterials. Nanomaterials in Chromatography. Elsevier. p. 89-115).

Keihan, A.H., Sajjadi, S., Sheibani, N. & Moosavi-Movahedi, A.A. 2014. A highly sensitive choline biosensor based on bamboo-like multiwall carbon nanotubes/ionic liquid/Prussian blue nanocomposite. *Sensors and Actuators B: Chemical*, 204:694-703.

Khan, I., Saeed, K. & Khan, I. 2017. Nanoparticles: Properties, applications and toxicities. *Arabian Journal of Chemistry*.

Khashan, S., Dagher, S., Tit, N., Alazzam, A. & Obaidat, I. 2017. Novel method for synthesis of Fe3O4@ TiO2 core/shell nanoparticles. *Surface and Coatings Technology*, 322:92-98.

Kim, J.S., Kim, W. J., Cho, N., Shukla, S., Yoon, H., Jang, J., & Lee, K. S. (2009). . Synthesis and properties of quantum dot-polypyrrole nanotube composites for photovoltaic application. . *Journal of nanoscience and nanotechnology*, 9(12):6957-6961.

Kim, S.K., Kim, D. & Jeon, S. 2012. Electrochemical determination of serotonin on glassy carbon electrode modified with various graphene nanomaterials. *Sensors and Actuators B: Chemical*, 174:285-291.

Klein, M.O., Battagello, D.S., Cardoso, A.R., Hauser, D.N., Bittencourt, J.C. & Correa, R.G. 2019. Dopamine: functions, signaling, and association with neurological diseases. *Cellular and molecular neurobiology*, 39(1):31-59.

Koc, H., Mar, M.-H., Ranasinghe, A., Swenberg, J.A. & Zeisel, S.H. 2002. Quantitation of choline and its metabolites in tissues and foods by liquid chromatography/electrospray ionization-isotope dilution mass spectrometry. *Analytical chemistry*, 74(18):4734-4740.

Kouhbanani, M.A.J., Beheshtkhoo, N., Amani, A.M., Taghizadeh, S., Beigi, V., Bazmandeh, A.Z. & Khalaf, N. 2018. Green synthesis of iron oxide nanoparticles using Artemisia vulgaris leaf extract and their application as a heterogeneous Fenton-like catalyst for the degradation of methyl orange. *Materials Research Express*, 5(11):115013.

Kouhbanani, M.A.J., Beheshtkhoo, N., Taghizadeh, S., Amani, A.M. & Alimardani, V. 2019. One-step green synthesis and characterization of iron oxide nanoparticles using aqueous leaf extract of Teucrium polium and their catalytic application in dye degradation. *Advances in Natural Sciences: Nanoscience and Nanotechnology*, 10(1):015007.

Kounaves, S.P. 1997. Voltammetric techniques. *Handbook of instrumental techniques for analytical chemistry*:709-726.

Koyun, A., Ahlatcolu, E., Koca, Y. & Kara, S. 2012. Biosensors and their principles. *A Roadmap of Biomedical Engineers and Milestones*:117-142.

Kumar, D. & Sharma, R. 1998. Advances in conductive polymers. *European polymer journal*, 34(8):1053-1060.

Kumar, R., Singh, S. & Yadav, B. 2015. Conducting polymers: synthesis, properties and applications. *International Advanced Research Journal in Science, Engineering and Technology*, 2(11):110-124.

Kumar, S. 2006. Spectroscopy of organic compounds. *Cosmic rays* 10:4.

Kwiecińska, B., Pusz, S. & Valentine, B.J. 2019. Application of electron microscopy TEM and SEM for analysis of coals, organic-rich shales and carbonaceous matter. *International Journal of Coal Geology*.

Laikhtman, M. & Rohrer, J.S. 1999. Determination of choline in infant formula by ion chromatography. *JOURNAL-AOAC INTERNATIONAL*, 82:1156-1162.

Lakshm, S., Roopa Bai, R., Sharanagouda, H., Ramachandra, C. & Kumar Nidoni, U. 2017. A review study of zinc oxide nanoparticles synthesis from plant extracts. *Green Chem. Technol. Lett*, 3(2):26-37.

Larrude, D., Ayala, P., Maia da Costa, M. & Freire, F. 2012. Multiwalled carbon nanotubes decorated with cobalt oxide nanoparticles. *Journal of Nanomaterials*, 2012.

Laviron, E. 1979. General expression of the linear potential sweep voltammogram in the case of diffusionless electrochemical systems. *Journal of Electroanalytical Chemistry and Interfacial Electrochemistry*, 101(1):19-28.

Lehmann, W., Schulten, H.R. & Schröder, N. 1978. Determination of choline and acetylcholine in distinct rat brain regions by stable isotope dilution and field desorption mass spectrometry. *Biomedical mass spectrometry*, 5(10):591-595.

Li, F., Yang, L., Zhao, C. & Du, Z. 2011a. Electroactive gold nanoparticles/polyaniline/polydopamine hybrid composite in neutral solution as high-performance sensing platform. *Analytical Methods*, 3(7):1601-1606.

Li, L., Liu, H., Shen, Y., Zhang, J. & Zhu, J.-J. 2011b. Electrogenerated chemiluminescence of Au nanoclusters for the detection of dopamine. *Analytical Chemistry*, 83(3):661-665.

Lima, J.L., Delerue-Matos, C. & Vaz, M.C.V. 2000. Enzymatic determination of choline in milk using a FIA system with potentiometric detection. *Analyst*, 125(7):1281-1284.

Lin, J.-Y., Wang, W.-Y. & Chou, S.-W. 2015. Flexible carbon nanotube/polypropylene composite plate decorated with poly (3, 4-ethylenedioxythiophene) as efficient counter electrodes for dye-sensitized solar cells. *Journal of Power Sources*, 282:348-357.

Lin, Y.-T., Chen, C.-H. & Lin, M.S. 2018. Enzyme-free amperometric method for rapid determination of histamine by using surface oxide regeneration behavior of copper electrode. *Sensors and Actuators B: Chemical*, 255:2838-2843.

Liu, C.-Y., Chou, Y.-C., Tsai, J.-H., Huang, T.-M., Chen, J.-Z. & Yeh, Y.-C. 2019. Tyrosinase/Chitosan/Reduced graphene oxide modified screen-printed carbon electrode for sensitive and interference-free detection of dopamine. *Applied Sciences*, 9(4):622.

Liu, J., Yuan, L. & Dong, X. 2015. Recent advances in analytical techniques for the determination of dopamine. *Int J Chem Stud*, 3(3):39-45.

Liu, M., Miao, Y.-E., Zhang, C., Tjiu, W.W., Yang, Z., Peng, H. & Liu, T. 2013. Hierarchical composites of polyaniline–graphene nanoribbons–carbon nanotubes as electrode materials in all-solid-state supercapacitors. *Nanoscale*, 5(16):7312-7320.

Liu, X., Zhu, H. & Yang, X. 2014. An electrochemical sensor for dopamine based on poly (o-phenylenediamine) functionalized with electrochemically reduced graphene oxide. *Rsc Advances*, 4(8):3706-3712.

Lozić-Đurić, M. 2015. Neurotransmitters in the central nervous system: Basic knowledge revisited. *Medicinski podmladak*, 66(2):12-15.

Luo, B., Li, X., Yang, J., Li, X., Xue, L., Li, X., Gu, J., Wang, M. & Jiang, L. 2014. Non-enzymatic electrochemical sensors for the detection of hydrogen peroxide based on Cu 2 O/Cu nanocomposites. *Analytical Methods*, 6(4):1114-1120.

Ma, X., Chao, M. & Wang, Z. 2012. Electrochemical detection of dopamine in the presence of epinephrine, uric acid and ascorbic acid using a graphene-modified electrode. *Analytical Methods*, 4(6):1687-1692.

Magar, H.S., Ghica, M.E., Abbas, M.N. & Brett, C.M.A. 2017. A novel sensitive amperometric choline biosensor based on multiwalled carbon nanotubes and gold nanoparticles. *Talanta*, 167:462-469.

Mahmoudian, M.R., Alias, Y., Basirun, W.J. & Yousefi, R. 2013. Synthesis and characterization of zinc/polypyrrole nanotube as a protective pigment in organic coatings. *Metallurgical and Materials Transactions A*, 44(7):3353-3363.

Mahvidi, S., Gharagozlou, M., Mahdavian, M. & Naghibi, S. 2017. Potency of ZnFe2O4 nanoparticles as corrosion inhibitor for stainless steel; the pigment extract study. *Materials Research*, 20(6):1492-1502.

Mahdavi, M., Ahmad, M.B., Haron, M.J., Namvar, F., Nadi, B., Rahman, M.Z.A. & Amin, J. 2013. Synthesis, surface modification and characterisation of biocompatible magnetic iron oxide nanoparticles for biomedical applications. *Molecules*, 18(7):7533-7548.

Malik, M.A., Wani, M.Y. & Hashim, M.A. 2012. Microemulsion method: A novel route to synthesize organic and inorganic nanomaterials: 1st Nano Update. *Arabian journal of Chemistry*, 5(4):397-417.

Manbohi, A. & Ahmadi, S.H. 2019. Sensitive and selective detection of dopamine using electrochemical microfluidic paper-based analytical nanosensor. *Sensing and Bio-Sensing Research*, 23:100270.

Marsalek, R. 2014. Particle size and zeta potential of ZnO. *APCBEE procedia*, 9:13-17.

Martinez, S.E.V. 1983. Simultaneous determination of choline and betaine in some fish materials. *Analyst*, 108(1290):1114-1119.

Maruyama, Y., Kusaka, M., Mori, J., Horikawa, A. & Hasegawa, Y. 1979. Simple method for the determination of choline and acetylcholine by pyrolysis gas chromatography. *Journal of Chromatography B: Biomedical Sciences and Applications*, 164(2):121-127.

Mazloum-Ardakani, M. & Khoshroo, A. 2014. High sensitive sensor based on functionalized carbon nanotube/ionic liquid nanocomposite for simultaneous determination of norepinephrine and serotonin. *Journal of Electroanalytical Chemistry*, 717:17-23.

Mirceski, V., Skrzypek, S. & Stojanov, L. 2018. Square-wave voltammetry. *ChemTexts*, 4(4):17.

Mostaço-Guidolin, L.B., and Luciano Bachmann. 2011. Application of FTIR spectroscopy for identification of blood and leukemia biomarkers: A review over the past 15 years.". *Applied Spectroscopy Reviews,*, 46(5):388-404.

Mphuthi, N.G., Adekunle, A.S. & Ebenso, E.E. 2016. Electrocatalytic oxidation of Epinephrine and Norepinephrine at metal oxide doped phthalocyanine/MWCNT composite sensor. *Scientific Reports*, 6:26938.

Mphuthi, N.G., Adekunle, A.S., Fayemi, O.E., Olasunkanmi, L.O. & Ebenso, E.E. 2017. Phthalocyanine doped metal oxide nanoparticles on multiwalled carbon nanotubes platform for the detection of dopamine. *Scientific reports*, 7:43181.

Muzzi, C., Bertocci, E., Terzuoli, L., Porcelli, B., Ciari, I., Pagani, R. & Guerranti, R. 2008. Simultaneous determination of serum concentrations of levodopa, dopamine, 3-O-methyldopa and α-methyldopa by HPLC. *Biomedicine & pharmacotherapy*, 62(4):253-258.

Nezhad, M.H., Tashkhourian, J. & Khodaveisi, J. 2010. Sensitive spectrophotometric detection of dopamine, levodopa and adrenaline using surface plasmon resonance band of silver nanoparticles. *Journal of the Iranian Chemical Society*, 7(2):S83-S91.

Nnamchi, P.S. & Obayi, C.S. 2018. Electrochemical Characterization of Nanomaterials. Characterization of Nanomaterials. Elsevier. p. 103-127).

Ngaboyamahina, E., Cachet, H., Pailleret, A. & Sutter, E. 2014. Photo-assisted electrodeposition of an electrochemically active polypyrrole layer on anatase type titanium dioxide nanotube arrays. *Electrochimica Acta*, 129:211-221.

Nguyen, D.N. & Yoon, H. 2016. Recent advances in nanostructured conducting polymers: from synthesis to practical applications. *Polymers*, 8(4):118.

Özcan, A. & İlkbaş, S. 2015. Poly (pyrrole-3-carboxylic acid)-modified pencil graphite electrode for the determination of serotonin in biological samples by adsorptive stripping voltammetry. *Sensors and Actuators B: Chemical*, 215:518-524.

Palanisamy, S., Ku, S. & Chen, S.-M. 2013. Dopamine sensor based on a glassy carbon electrode modified with a reduced graphene oxide and palladium nanoparticles composite. *Microchimica Acta*, 180(11-12):1037-1042.

Panfili, G., Manzi, P., Compagnone, D., Scarciglia, L. & Palleschi, G. 2000. Rapid assay of choline in foods using microwave hydrolysis and a choline biosensor. *Journal of agricultural and food chemistry*, 48(8):3403-3407.

Park, B.-w., Yang, L., Johansson, E.M., Vlachopoulos, N., Chams, A., Perruchot, C., Jouini, M., Boschloo, G. & Hagfeldt, A. 2013. Neutral, polaron, and bipolaron states in PEDOT prepared by photoelectrochemical polymerization and the effect on charge generation mechanism in the solid-state dye-sensitized solar cell. *The Journal of Physical Chemistry C*, 117(44):22484-22491.

Park, Y.H., Zhang, X., Rubakhin, S.S. & Sweedler, J.V. 1999. Independent optimization of capillary electrophoresis separation and native fluorescence detection conditions for indolamine and catecholamine measurements. *Analytical chemistry*, 71(21):4997-5002.

Pati, S., Palmisano, F., Quinto, M. & Zambonin, P.G. 2005. Quantitation of Major Choline Fractions in Milk and Dietary Supplements Using a Phospholipase D Bioreactor Coupled to a Choline Amperometric Biosensor. *Journal of Agricultural and Food Chemistry*, 53(18):6974-6979.

Pati, S., Quinto, M. & Palmisano, F. 2007. Flow injection determination of choline in milk hydrolysates by an immobilized enzyme reactor coupled to a selective hydrogen peroxide amperometric sensor. *Analytica Chimica Acta*, 594(2):234-239.

Patra, J.K. & Baek, K.-H. 2017. Green biosynthesis of magnetic iron oxide (Fe3O4) nanoparticles using the aqueous extracts of food processing wastes under photo-catalyzed condition and investigation of their antimicrobial and antioxidant activity. *Journal of Photochemistry and Photobiology B: Biology*, 173:291-300.

Patterson, K.Y., Bhagwat, S.A., Williams, J.R., Howe, J.C., Holden, J., Zeisel, S., Dacosta, K. & Mar, M. 2008. USDA database for the choline content of common foods, release two. *Nutrient Data Laboratory, Beltsville Human Nutrition Research Center, ARS, USDA*.

Peik-See, T., Pandikumar, A., Nay-Ming, H., Hong-Ngee, L. & Sulaiman, Y. 2014. Simultaneous electrochemical detection of dopamine and ascorbic acid using an iron oxide/reduced graphene oxide modified glassy carbon electrode. *Sensors*, 14(8):15227-15243.

Peterson, Z.D., Lee, M.L. & Graves, S.W. 2004. Determination of serotonin and its precursors in human plasma by capillary electrophoresis–electrospray ionization–time-of-flight mass spectrometry. *Journal of Chromatography B*, 810(1):101-110.

Phillips, M.M. 2012. Analytical approaches to determination of total choline in foods and dietary supplements. *Analytical and Bioanalytical Chemistry*, 403(8):2103-2112.

Power, A.C. & Morrin, A. 2013. Electroanalytical sensor technology. Electrochemistry. InTech Rijeka. p. 141-178).

Prasanna, S.S., Balaji, K., Pandey, S. & Rana, S. 2019. Metal Oxide Based Nanomaterials and Their Polymer Nanocomposites. Nanomaterials and Polymer Nanocomposites. Elsevier. p. 123-144).

Pundir, S., Chauhan, N., Narang, J. & Pundir, C. 2012. Amperometric choline biosensor based on multiwalled carbon nanotubes/zirconium oxide nanoparticles electrodeposited on glassy carbon electrode. *Analytical biochemistry*, 427(1):26-32.

Qian, T., Yu, C., Zhou, X., Wu, S. & Shen, J. 2014. Au nanoparticles decorated polypyrrole/reduced graphene oxide hybrid sheets for ultrasensitive dopamine detection. *Sensors and Actuators B: Chemical*, 193:759-763.

Qin, X., Wang, H., Wang, X., Li, S., Miao, Z., Huang, N. & Chen, Q. 2009. Amperometric choline biosensors based on multi-wall carbon nanotubes and layer-by-layer assembly of multilayer films composed of Poly (diallyldimethylammonium chloride) and choline oxidase. *Materials Science and Engineering: C*, 29(4):1453-1457.

Qin, X., Wang, H., Wang, X., Miao, Z., Chen, L., Zhao, W., Shan, M. & Chen, Q. 2010. Amperometric biosensors based on gold nanoparticles-decorated multiwalled carbon nanotubes-poly (diallyldimethylammonium chloride) biocomposite for the determination of choline. *Sensors and Actuators B: Chemical*, 147(2):593-598.

Qiu, B., Wang, J., Li, Z., Wang, X. & Li, X. 2020. Influence of Acidity and Oxidant Concentration on the Nanostructures and Electrochemical Performance of Polyaniline during Fast Microwave-Assisted Chemical Polymerization. *Polymers*, 12(2):310.

Qu, F., Yang, M., Jiang, J., Shen, G. & Yu, R. 2005. Amperometric biosensor for choline based on layer-by-layer assembled functionalized carbon nanotube and polyaniline multilayer film. *Analytical Biochemistry*, 344(1):108-114.

Quadri, T.W., Olasunkanmi, L.O., Fayemi, O.E., Solomon, M.M. & Ebenso, E.E. 2017. Zinc oxide nanocomposites of selected polymers: synthesis, characterization, and corrosion inhibition studies on mild steel in HCl solution. *ACS omega*, 2(11):8421-8437.

Rahmawati, R., Taufiq, A., Sunaryono, Yuliarto, B., Suyatman, Nugraha, Noviandri, I., Setyorini, D.A. & Kurniadi, D. 2018. The synthesis of Fe3O4/MWCNT nanocomposites from local iron sands for electrochemical sensors. (*In*. AIP Conference Proceedings organised by: AIP Publishing LLC. p. 020016).

Rajarao, R., Jayanna, R., Sahajwalla, V. & Bhat, B.R. 2014. GreenApproach to decorate multi-walled carbon nanotubes by metal/metal oxide nanoparticles. *Procedia Materials Science*, 5:69-75.

Ramesh, A., Rama Devi, D., Mohan Botsa, S. & Basavaiah, K. 2018. Facile green synthesis of Fe3O4 nanoparticles using aqueous leaf extract of Zanthoxylum armatum DC. for efficient adsorption of methylene blue. *Journal of Asian Ceramic Societies*, 6(2):145-155.

Rand, E., Periyakaruppan, A., Tanaka, Z., Zhang, D.A., Marsh, M.P., Andrews, R.J., Lee, K.H., Chen, B., Meyyappan, M. & Koehne, J.E. 2013. A carbon nanofiber based biosensor for simultaneous detection of dopamine and serotonin in the presence of ascorbicacid. *Biosensors and Bioelectronics*, 42:434-438.

Randviir, E.P. & Banks, C.E. 2013. Electrochemical impedance spectroscopy: an overview of bioanalytical applications. *Analytical Methods*, 5(5):1098-1115.

Randviir, E.P., 2018. A cross examination of electron transfer rate constants for carbon screen-printed electrodes using electrochemical impedance spectroscopy and cyclic voltammetry. *Electrochimica Acta*, 286:179-186.

Rauch, P., Ferri, E.N., Girotti, S., Rauchova, H., Carrea, G., Bovara, R., Fini, F. & Roda, A. 1997. A Chemiluminescent Flow Sensing Device for Determination of Choline and Phospholipase D Activity in Biological Samples. *Analytical Biochemistry*, 245(2):133-140.

Razola, S.S., Pochet, S., Grosfils, K. & Kauffmann, J. 2003. Amperometric determination of choline released from rat submandibular gland acinar cells using a choline oxidase biosensor. *Biosensors and Bioelectronics*, 18(2-3):185-191.

Reddaiah, K., Rao, K.S.V.K. & Reddy, T.M. 2018. Electrochemical Detection of Serotonin in Human Serum Sample and Simultaneous Resolution in Presence of Epinephrine. *Analytical & bioanalytical electrochemistry*, 10(2):175-191.

Ren, X., Tang, F., Liao, R. & Zhang, L. 2009. Using gold nanorods to enhance the current response of a choline biosensor. *Electrochimica acta*, 54(28):7248-7253.

Rezaei, B. & Irannejad, N. 2019. Electrochemical detection techniques in biosensor applications. Electrochemical Biosensors. Elsevier. p. 11-43).

Rubí, B. & Maechler, P. 2010. Minireview: new roles for peripheral dopamine on metabolic control and tumor growth: let's seek the balance. *Endocrinology*, 151(12):5570-5581.

Saboonchian, F., Jamei, R. & Sarghein, S.H. 2014. Phenolic and flavonoid content of Elaeagnus angustifolia L.(leaf and flower). *Avicenna journal of phytomedicine*, 4(4):231.

Sacramento, A.S., Moreira, F.T., Guerreiro, J.L., Tavares, A.P. & Sales, M.G.F. 2017. Novel biomimetic composite material for potentiometric screening of acetylcholine, a neurotransmitter in Alzheimer's disease. *Materials Science and Engineering: C*, 79:541-549.

Sadegh, H., Shahryari-ghoshekandi, R. & Kazemi, M. 2014. Study in synthesis and characterization of carbon nanotubes decorated by magnetic iron oxide nanoparticles. *International Nano Letters*, 4(4):129-135.

Sagar Raut, D.P. & Thorat, R. 2015. Green synthesis of zinc oxide (ZnO) nanoparticles using Ocimum tenuiflorum leaves. *International Journal of Science and Research*, 4(5):1225-1228.

Sahebian, S., Zebarjad, S., Khaki, J.V. & Lazzeri, A. 2016. The decoration of multi-walled carbon nanotubes with nickel oxide nanoparticles using chemical method. *International Nano Letters*, 6(3):183-190.

Saif, S., Tahir, A. & Chen, Y. 2016. Green synthesis of iron nanoparticles and their environmental applications and implications. *Nanomaterials*, 6(11):209.

Sajjadi, S., Ghourchian, H., Rafiee-Pour, H.-A. & Rahimi, P. 2012. Accelerating the electron transfer of choline oxidase using ionic-liquid/NH 2-MWCNTs nano-composite. *Journal of the Iranian Chemical Society*, 9(2):111-119.

Sarada, A. & Ramasastri, B. 1983. A simple thin layer chromatographic identification of choline in human semen. *Journal of the Forensic Science Society*, 23(3):233-236.

Sathishkumar, G., Logeshwaran, V., Sarathbabu, S., Jha, P.K., Jeyaraj, M., Rajkuberan, C., Senthilkumar, N. & Sivaramakrishnan, S. 2018. Green synthesis of magnetic Fe3O4 nanoparticles using Couroupita guianensis Aubl. fruit extract for their antibacterial and cytotoxicity activities. *Artificial cells, nanomedicine, and biotechnology*, 46(3):589-598.

Sattarahmady, N., Heli, H. & Vais, R.D. 2014. A flower-like nickel oxide nanostructure: synthesis and application for choline sensing. *Talanta*, 119:207-213.

Savk, A., Özdil, B., Demirkan, B., Nas, M.S., Calimli, M.H., Alma, M.H., Asiri, A.M. & Şen, F. 2019. Multiwalled carbon nanotube-based nanosensor for ultrasensitive detection of uric acid, dopamine, and ascorbic acid. *Materials Science and Engineering: C*, 99:248-254.

Schmitzer, V., Veberic, R., Osterc, G. & Stampar, F. 2010. Color and phenolic content changes during flower development in groundcover rose. *Journal of the American Society for Horticultural Science*, 135(3):195-202.

Seabra, A.B. & Duran, N. 2015. Nanotoxicology of metal oxide nanoparticles. *Metals*, 5(2):934-975.

Senthilkumar, N., Nandhakumar, E., Priya, P., Soni, D., Vimalan, M. & Potheher, I.V. 2017. Synthesis of ZnO nanoparticles using leaf extract of Tectona grandis (L.) and their anti-bacterial, anti-arthritic, anti-oxidant and in vitro cytotoxicity activities. *New Journal of Chemistry*, 41(18):10347-10356.

Series, M.E. & Heath, J. 2014. Front cover image courtesy of EDAX. EBSD map of a Partially Recrystallised Ferritic Steel. This color-coding indicates the crystal direction parallel to the surface normal which is superimposed on a greyscale image quality map.

Shadlaghani, A., Farzaneh, M., Kinser, D. & Reid, R.C. 2019. Direct Electrochemical Detection of Glutamate, Acetylcholine, Choline, and Adenosine Using Non-Enzymatic Electrodes. *Sensors*, 19(3):447.

Si, B. & Song, E. 2018. Recent advances in the detection of neurotransmitters. *Chemosensors*, 6(1):1.

Sidhu, J.S. & Zafar, T.A. 2018. Bioactive compounds in banana fruits and their health benefits. *Food Quality and Safety*, 2(4):183-188.

Siregar, C., Sudibyo Martono, and Abdul Rohman. . 2018. Application of Fourier transform infrared (FTIR) spectroscopy coupled with multivariate calibration for quantitative analysis of curcuminoid in tablet dosage form.". *Journal of Applied Pharmaceutical Science* 8(08):151-156.

Soderberg, J.N., Co, A.C., Sirk, A.H. & Birss, V.I. 2006. Impact of porous electrode properties on the electrochemical transfer coefficient. *The Journal of Physical Chemistry B*, 110(21):10401-10410.

Somani, P., Mandale, A. & Radhakrishnan, S. 2000. Study and development of conducting polymer-based electrochromic display devices. *Acta Materialia*, 48(11):2859-2871.

Sone, B., Manikandan, E., Gurib-Fakim, A. & Maaza, M. 2015. Sm2O3 nanoparticles green synthesis via Callistemon viminalis' extract. *Journal of Alloys and Compounds*, 650:357-362.

Song, Y. & Yang, J. 2016. Preparation and in-vitro cytotoxicity of zinc oxide nanoparticles against osteoarthritic chondrocytes. *Tropical Journal of Pharmaceutical Research*, 15(11):2321-2327.

Song, Z., Huang, J.-D., Wu, B.-Y., Shi, H.-B., Anzai, J.-I. & Chen, Q. 2006. Amperometric aqueous sol–gel biosensor for low-potential stable choline detection at multi-wall carbon nanotube modified platinum electrode. *Sensors and Actuators B: Chemical*, 115(2):626-633.

Soytaş, S.H., Oğuz, O. & Menceloğlu, Y.Z. 2019. Polymer Nanocomposites With Decorated Metal Oxides. Polymer Composites with Functionalized Nanoparticles. Elsevier. p. 287-323).

Sun, X., Sun, K. & Liang, Y. 2015. Hydrothermal synthesis of magnetite: investigation of influence of aging time and mechanism. *Micro & Nano Letters*, 10(2):99-104.

Suominen, T., Uutela, P., Ketola, R.A., Bergquist, J., Hillered, L., Finel, M., Zhang, H., Laakso, A. & Kostiainen, R. 2013. Determination of serotonin and dopamine metabolites in human brain microdialysis and cerebrospinal fluid samples by UPLC-MS/MS: discovery of intact glucuronide and sulfate conjugates. *PLoS One*, 8(6):e68007.

Szeitz, A. & Bandiera, S.M. 2018. Analysis and measurement of serotonin. *Biomedical Chromatography*, 32(1):e4135.

Tekes, K. 2008. HPLC determination of serotonin and its metabolites from human platelet-rich plasma; shift to 5-hydroxytryptophol formation following alcohol consumption. *Journal of chromatographic science*, 46(2):169-173.

Thomas, T., Mascarenhas, R.J., Swamy, B.K., Martis, P., Mekhalif, Z. & Sherigara, B. 2013. Multi-walled carbon nanotube/poly (glycine) modified carbon paste electrode for the determination of dopamine in biological fluids and pharmaceuticals. *Colloids and Surfaces B: Biointerfaces*, 110:458-465.

Toth, P.S. & Dryfe, R.A. 2015. Novel organic solvents for electrochemistry at the liquid/liquid interface. *Analyst*, 140(6):1947-1954.

Trinh, N., Saulnier, M., Lepage, D. & Schougaard, S. 2013. Conductive polymer film supporting LiFePO4 as composite cathode for lithium ion batteries. *Journal of Power Sources*, 221:284-289.

Umar, H., Kavaz, D. & Rizaner, N. 2019. Biosynthesis of zinc oxide nanoparticles using Albizia lebbeck stem bark, and evaluation of its antimicrobial, antioxidant, and cytotoxic activities on human breast cancer cell lines. *International journal of nanomedicine*, 14:87.

Umeda, S., Stagliano, G.W., Borenstein, M.R. & Raffa, R.B. 2005. A reverse-phase HPLC and fluorescence detection method for measurement of 5-hydroxytryptamine (serotonin) in Planaria. *Journal of pharmacological and toxicological methods*, 51(1):73-76.

Uwaya, G.E. & Fayemi, O.E. 2020. Electrochemical detection of serotonin in banana at green mediated PPy/Fe3O4NPs nanocomposites modified electrodes. *Sensing and Bio-Sensing Research*:100338.

Van Valkenburg, C., Tjaden, U., Van der Krogt, J. & Van der Leden, B. 1982. Determination of dopamine and its acidic metabolites in brain tissue by HPLC with electrochemical detection in a single run after minimal sample pretreatment. *Journal of neurochemistry*, 39(4):990-997.

Wang, F., Wu, Y., Lu, K. & Ye, B. 2013. A simple but highly sensitive and selective calixarene-based voltammetric sensor for serotonin. *Electrochimica acta*, 87:756-762.

Wang, Y., Wang, S., Tao, L., Min, Q., Xiang, J., Wang, Q., Xie, J., Yue, Y., Wu, S. & Li, X. 2015. A disposable electrochemical sensor for simultaneous determination of norepinephrine and serotonin in rat cerebrospinal fluid based on MWNTs-ZnO/chitosan composites modified screen-printed electrode. *Biosensors and Bioelectronics*, 65:31-38.

Wiedeman, A.M., Barr, S.I., Green, T.J., Xu, Z., Innis, S.M. & Kitts, D.D. 2018. Dietary choline intake: current state of knowledge across the life cycle. *Nutrients*, 10(10):1513.

Winther-Jensen, O., Desai, S., Shepherd, R.L., Innis, P.C., Winther-Jensen, B., Forsyth, M., Wallace, G.G. & MacFarlane, D.R. 2010. Ion effects in REDOX cycling of conducting polymer based electrochromic materials. *Electrochemistry communications*, 12(11):1505-1508.

Woollard, D.C. & Indyk, H.E. 2000. Determination of Choline in Milk and Infant Formulas by Enzymatic Analysis: Collaborative Study. *Journal of AOAC International*, 83(1):131-138.

Wu, D., Xie, H., Lu, H., Li, W. & Zhang, Q. 2016. Sensitive determination of norepinephrine, epinephrine, dopamine and 5-hydroxytryptamine by coupling HPLC with [Ag (HIO6) 2] 5−– luminol chemiluminescence detection. *Biomedical Chromatography*, 30(9):1458-1466.

Xie, L., Huang, X. & Su, B. 2017. Portable Sensor for the Detection of Choline and Its Derivatives Based on Silica Isoporous Membrane and Gellified Nanointerfaces. *ACS Sensors*, 2(6):803-809.

Xu, J., Yang, Y., Yu, J. & Jiang, Y. 2009. Ordered conducting polymer multilayer films and its application for hole injection layers in organic light-emitting devices. *Applied Surface Science*, 255(7):4329-4333.

Xue, C., Wang, X., Zhu, W., Han, Q., Zhu, C., Hong, J., Zhou, X. & Jiang, H. 2014. Electrochemical serotonin sensing interface based on double-layered membrane of reduced graphene oxide/polyaniline nanocomposites and molecularly imprinted polymers embedded with gold nanoparticles. *Sensors and Actuators B: Chemical*, 196:57-63.

Yang, M., Yang, Y., Liu, Y., Shen, G. & Yu, R. 2006. Platinum nanoparticles-doped sol–gel/carbon nanotubes composite electrochemical sensors and biosensors. *Biosensors and Bioelectronics*, 21(7):1125-1131.

Yao, D., Vlessidis, A.G. & Evmiridis, N.P. 2002. Development of an interference-free chemiluminescence method for monitoring acetylcholine and choline based on immobilized enzymes. *Analytica Chimica Acta*, 462(2):199-208.

Yu, G., Zhao, Q., Wu, W., Wei, X. & Lu, Q. 2016. A facile and practical biosensor for choline based on manganese dioxide nanoparticles synthesized in-situ at the surface of electrode by one-step electrodeposition. *Talanta*, 146:707-713.

Zablocka, I., Wysocka-Zolopa, M. & Winkler, K. 2019. Electrochemical detection of dopamine at a gold electrode modified with a polypyrrole–mesoporous silica molecular sieves (MCM-48) film. *International Journal of Molecular Sciences*, 20(1):111.

Zangeneh Kamali, K., Alagarsamy, P., Huang, N.M., Ong, B.H. & Lim, H.N. 2014. Hematite nanoparticles-modified electrode based electrochemical sensing platform for dopamine. *The Scientific World Journal*, 2014.

Zeisel, S.H. 1981. Dietary choline: biochemistry, physiology, and pharmacology. *Annual review of nutrition*, 1(1):95-121.

Zeisel, S.H. 2006. The fetal origins of memory: the role of dietary choline in optimal brain development. *The Journal of pediatrics*, 149(5):S131-S136.

Zeisel, S.H. 2012. Dietary choline deficiency causes DNA strand breaks and alters epigenetic marks on DNA and histones. *Mutation Research/Fundamental and Molecular Mechanisms of Mutagenesis*, 733(1):34-38.

Zeisel, S.H. 2013. Nutrition in pregnancy: the argument for including a source of choline. *International journal of women's health*, 5:193.

Zeisel, S.H., A Char, D. & A Sheard, N.F. 1986. Choline, Phosphatidylcholine and Sphingomyelin in Human and Bovine Milk and Infant Formulas. *The Journal of Nutrition*, 116(1): 50-58.

Zeisel, S.H., A da Costa, Kerry-Ann. 2009. Choline: an essential nutrient for public health. *Nutrition Reviews*, 67(11):615-623.

Zeisel, S.H. & DaCosta, K.A. 1990. Choline: determination using gas chromatography/mass spectrometry. *Journal of Nutritional Biochemistry*, 1(1):55-59.

Zhang, H., Yin, Y., Wu, P. & Cai, C. 2012. Indirect electrocatalytic determination of choline by monitoring hydrogen peroxide at the choline oxidase-prussian blue modified iron phosphate nanostructures. *Biosensors and Bioelectronics*, 31(1):244-250.

Zhang, L., Chen, J., Wang, Y., Yu, L., Wang, J., Peng, H. & Zhu, J. 2014a. Improved enzyme immobilization for enhanced bioelectrocatalytic activity of choline sensor and acetylcholine sensor. *Sensors and Actuators B: Chemical*, 193:904-910.

Zhang, L., Ning, L., Li, S., Pang, H., Zhang, Z., Ma, H. & Yan, H. 2016. Selective electrochemical detection of dopamine in the presence of uric acid and ascorbic acid based on a composite film modified electrode. *RSC advances*, 6(71):66468-66476.

Zhang, X., Wang, S., Lu, S., Su, J. & He, T. 2014b. Influence of doping anions on structure and properties of electro-polymerized polypyrrole counter electrodes for use in dye-sensitized solar cells. *Journal of Power Sources*, 246:491-498.

Zhao, D., Guo, X., Wang, T., Alvarez, N., Shanov, V.N. & Heineman, W.R. 2014. Simultaneous detection of heavy metals by anodic stripping voltammetry using carbon nanotube thread. *Electroanalysis*, 26(3):488-496.

Zhao, H.-X., Mu, H., Bai, Y.-H., Yu, H. & Hu, Y.-M. 2011. A rapid method for the determination of dopamine in porcine muscle by pre-column derivatization and HPLC with fluorescence detection. *Journal of pharmaceutical analysis*, 1(3):208-212.

Zhao, S., Huang, Y., Shi, M., Liu, R. & Liu, Y.-M. 2010. Chemiluminescence resonance energy transfer-based detection for microchip electrophoresis. *Analytical chemistry*, 82(5):2036-2041.

Zheng, Y., Wang, Y. & Yang, X. 2011. Aptamer-based colorimetric biosensing of dopamine using unmodified gold nanoparticles. *Sensors and Actuators B: Chemical*, 156(1):95-99.

Zhou, H. & Han, G. 2016. One-step fabrication of heterogeneous conducting polymers-coated graphene oxide/carbon nanotubes composite films for high-performance supercapacitors. *Electrochimica Acta*, 192:448-455.

Zhou, H., Han, G., Fu, D., Chang, Y., Xiao, Y. & Zhai, H.-J. 2014. Petal-shaped poly (3, 4-ethylenedioxythiophene)/sodium dodecyl sulfate-graphene oxide intercalation composites for high-performance electrochemical energy storage. *Journal of Power Sources*, 272:203-210.

Zhu, L., Li, Y. & Zhu, G. 2002. Flow injection determination of dopamine based on inhibited electrochemiluminescence of luminol. *Analytical letters*, 35(15):2527-2537.

Zhu, Y., Pan, D., Hu, X., Han, H., Lin, M. & Wang, C. 2017. An electrochemical sensor based on reduced graphene oxide/gold nanoparticles modified electrode for determination of iron in coastal waters. *Sensors and Actuators B: Chemical*, 243:1-7.

Zydroń, M., Baranowski, J., Białkowski, J. & Baranowska, I. 2005. HPLC-FL/ED in the Analysis of Biogenic Amines and their Metabolites in Urine. *Separation science and technology*, 40(15):3137-3148.

APPENDIX

Conferences attended

2018 - Poster presented in 43rd National convention of the South African Chemical Institute at CISR – ICC, Pretoria.

2019 - Poster presented in 70th Annual meeting of the international society of electrochemistry Durban, South Africa.

List of manuscripts based on this work

Gloria Ebube Uwaya; Omolola Fayemi; El-Sayed M. Sherif; Harri Junaedi; Eno Ebenso Synthesis, electrochemical studies and antimicrobial properties of Fe_3O_4 nanoparticles from Callistemon viminalis plant extracts has been accepted in Materials (ISSN 1996-1944) on 30 September 2020.

Gloria Ebube Uwaya, Omolola Esther Fayemi. Electrochemical detection of serotonin in banana at green mediated PPy/Fe_3O_4NPs nanocomposites modified electrodes. Sensing and Bio-Sensing Research, Volume 28, June 2020, 100338. https://doi.org/10.1016/ j.sbsr.2020.100338.